Manganese through time and other stories concerning Cyanobacteria and the world around them

Thesis by
Usha Farey Lingappa

In partial fulfillment of the requirements for the degree of Doctor of Philosophy

CALIFORNIA INSTITUTE OF TECHNOLOGY
Pasadena, California

2021
(Defended March 3, 2021)

To the Cyanobacteria, and all tiny creatures that impacted the world in big ways.
May we each realize our own powers for change.

Usha Farey Lingappa
ORCID: 0000-0001-5691-6788

ACKNOWLEDGEMENTS

This thesis would not have been possible without so many people, each of whom impacted my PhD work, education, and perspective in unique and valuable ways.

I would like to start by thanking the Caltech administrative and technical staff who supported me during my time here: Kacey Gibson, Janice Grancich, Julie Lee, Jen Shechet, Ruth Martinez, Julia Zuckerman, Leticia Calderon, Lisa Christiansen, Kathy Young, Emi Vasquez, Kristy Nguyen, Jennifer Leonardini, Alice Oh, Liz Boyd, and Mark Garcia, along with Stephanie Connon, Fenfang Wu, Chi Ma, and Yunbin Guan for lab and instrument support. A special thank you to Ricardo Valentino for keeping clean the lab and office spaces where I worked.

I feel immensely lucky to have had so many wonderful professors guiding my graduate education: Woody Fischer, Victoria Orphan, John Grotzinger, Dianne Newman, Jared Leadbetter, George Rossman, Hope Johnson, and Joan Valentine. Woody was the best thesis advisor I could have wished for. I am deeply grateful for all the ways he fostered my creativity and individuality as a scientist and helped me to explore and grow in so many directions. Victoria was an amazing role model, as a scientist, and also as a person. Her encouragement and caring really helped ground me during my PhD. One of the aspects of my graduate education that I value most is how much I grew as a field scientist; John catalyzed so much of that growth by providing me with spectacular fieldwork opportunities and sharing so much knowledge with me in the field. Dianne pushed me to excel as a scholar in ways I did not think I could. Because of her, I am much more rigorous than I ever would have been otherwise. Jared taught me so much, from his unparalleled skill and intuition as a microbiologist to profound truths about the nature of discovery. George always entertained my weird ideas and questions with boundless enthusiasm and patience; his attitude and approach to both teaching and research greatly enriched my education. Hope was like a second advisor to me on the manganese oxidation project. She and her group were a joy to work with and invaluable to the progression of that project. Joan taught me everything I know about manganese, her insights were central to guiding the course of my PhD, and her friendship and mentorship have meant the world to me.

I am also grateful for my brilliant science-big-sister-figures: Jena Johnson, Lizzy Trower, and Danie Potocek. Jena's PhD work laid the foundation that my manganese projects built on. Although we never formally overlapped at Caltech, she has been a wonderful resource and support to me throughout my time here. I worked closely with Lizzy and Danie when they were postdocs at Caltech, on the microbead/borer projects and manganese biogeochemistry projects, respectively. They were both super fun to work with and inspire me in so many ways.

Among all the other colleagues I got to work with at Caltech, Jim Hemp, Ted Present, Nathan Stein, Preston Kemeny, and John Magyar deserve special recognition. Jim helped me through the steep learning curve of getting my PhD work off the ground. Ted taught me so much, in the office, lab, and field (fieldwork with Ted on the Great Slave Lake was the absolute best), and was a consistent source of much needed encouragement. Nathan was my counterpart on the wild ride that was the Ambergris project, and I am so glad to have shared that with him. Preston's camaraderie as a classmate, labmate, and friend has been so important to me. The discussions and ideas born out of the Fischer lab subgroup (and friends) known as Manganese Club were a vital aspect of my PhD; John was the glue that kept those meetings happening.

It has been an honor to share this journey with the other members of my pit cohort: Hao Xie, Lee Saper, Sujung Lim, Alex Phillips, Maddie Lewis, and Joe Biasi. Shout-out to Hao, for being my first friend at Caltech and a delightful officemate for the full duration of my time here, and to Alex, for the countless commiseration sessions over coffee/wine/Harry Potter that got us through the more frustrating parts of grad school.

So many other friends, classmates, and labmates have influenced me throughout my years at Caltech, and I feel gratitude for each of them: Sarah Slotznick, Elizabeth Trembath-Reichert, David Case, Stephen Cox, Hank Yu, Lewis Ward, Daven Quinn, Sean Mullin, Amber Witkosky, Giuliana Viglione,

Cody Finke, Chanel Valiente, Kyle Metcalfe, Dan Johnson, Jieun Shin, Elise Tookmanian, Brigitte Rooney, Celeste Labedz, Madison Douglas, Renee Wang, Daniela Osorio Rodriguez, Dustin Morris, Makayla Betts, Shaelyn Silverman, Phillip Woods, Elliot Mueller, Sergio Parra, Holly Barnhart, Justin Nghiem, Hannah Dion-Kirschner, Calvin Rusley, Vlada Stamenkovic, Ben Smith, Miquela Ingalls, Tony Wang, Mark Torres, Eryn Eitel, Roland Hatzenpichler, Kat Dawson, Ally Pasulka, Daan Speth, Alon Philosof, Ranjani Murali, Haley Sapers, Yamini Jangir, Kriti Sharma, Ella Yanay, Reto Wijker, Yoni Goldsmith, and many others. An especially heartfelt thanks to Aditi Narayanan, Sarah Zeichner, Leah Sabbeth, and Cecilia Sanders; finding such kindred spirits at a place like Caltech made all the difference.

I had the pleasure of advising three summer students during my PhD, and learned a lot from working with each of them: Kabir Mohammed, Jenny Ji, and Josh Phelan.

My work was also greatly enriched by collaborators outside of Caltech: Nina Lanza, Chris Yeager, Brian Hoffman, Ajay Sharma, Yang Liu, Jaeheung Cho, Bohee Kim, Nic Beukes, Birger Rasmussen, and Dave Britt. A special thank you to Sam Webb, Sharon Bone, Nick Edwards, and Courtney Roach for making synchrotron work so much fun.

I benefitted immensely from the Agouron Institute's advanced geobiology field course which kickstarted my work on Little Ambergris Cay. In addition to those already mentioned I would like to thank the other participants on that project: Maya Gomes, Marjorie Cantine, Emily Orzechowski, Justin Strauss, Leigh Anne Riedman, Shane O'Reilly, Hannah Grotzinger, Andy Knoll, Mel Simon, Julien Alleon, Anelize Bahniuk, Elizabeth Sibert, Michael Thorpe, Max Tarika, Shana Goffredi, Bethany Ehlmann, Rob Phillips, Sarah Jamison-Todd, Taleen Mahseredijian, Irina Overeem, and Cecilia Howard. And of course, none of our work on Little Ambergris would have been possible without Paul Mahoney and James Seymore.

I tried to do a PhD on Cyanobacteria without anyone close at hand with much expertise in growing and manipulating them, and encountered huge technical challenges and pitfalls that I was completely unprepared to overcome by myself. The help, insight, and commiseration that I received from the greater photosynthesis research community was an incredible gift. For this, a huge thank you to my photosynthesis friends: Jeff Cameron, Patrick Shih, Rick Debus, Kevin Redding, Chris Gisriel, Rob Burnap, Anton Avramov, Neil Miller, Avi Flamholz, Kapil Amarnath, Nate Glasser, Arthur Grossman, Devaki Bhaya, Sabeeha Merchant, Himadri Pakrasi, and Govindjee.

I would also like to thank my previous mentors: Lynn Miller, Herb Bernstein, Jason Tor, Rayane Moreira, and Oana Marcu, for helping to set me on the path that brought me to this point.

Outside of science, I would like to thank the CCID, especially Taso Dimitriadis and Erin-Kate Escobar; the CTLO, especially Kitty Cahalan; Jim Barry and the Caltech visual arts program; and Catrelia Magee and the PCC dance department; all of whom improved my life at Caltech substantially.

Even from far away, Casey and Malcolm Andrews have been the best friends I could ask for, and I am very grateful for them.

My partner, Gray Chadwick, has been there for me in so many ways. Sharing the last few years with him has been a delight.

Both of my grandmothers—Yamuna Lingappa and Gwen Farey—saw me start my PhD but not finish it. They were amazing women, who blazed new paths that in so many ways are why I am here writing this thesis. I hope they would be proud of this work. So above all, I would like to thank them, along with the rest of my family: Anuradha Lingappa, Krista Farey, Vishwanath Lingappa, Jaisri Lingapa, Patrick Tompkins, Jairam Lingappa, Catherine Staunton, Elli Lingappa, Kiran Lingappa, Alan Ismach, Kevin Farey, Mahea Uchiyama, Emily Dunster-Farey, Hoku Uchiyama, Anna Mkhikian, David McCoard, and so many more extended family members. I love you all so much. Thank you for your endless support.

Finally, this thesis also would not have been possible without my cats: Cuzzy, Ripple, Kosh, and Kala.

ABSTRACT

This thesis is a collection of investigations concerning the interplay between Cyanobacteria and the inorganic/physical world. Chapters II-VI focus on manganese, an element Cyanobacteria have been intimately entangled with for billions of years. Chapter II is a review/perspective paper on the dynamics of manganese in the environment through time and the many ways manganese interfaces with dioxygen. Chapter III deciphers environmental and biological signatures recorded in ancient rocks from the pivotal moment in Earth history when oxygenic photosynthesis first evolved. Chapter IV explores the ecology of desert varnish, and provides an adaptive physiological mechanism underpinning manganese enrichment. Chapter V examines the ability of modern Cyanobacteria to catalyze manganese oxidation. Chapter VI explains as kindly as possible that the field of manganese aquatic chemistry has fundamentally misunderstood the chemistry of Mn(III) and highlights how the current methods being used are problematic because of this misunderstanding. Chapters VII and VIII are not about manganese and instead concern other aspects of the physical world and their interface with Cyanobacteria. Chapter VII is about the impact of Hurricane Irma on a cyanobacterial mat ecosystem. Chapter VIII is about the use of ooids as an environmentally friendly replacement for plastic microbeads in facial scrubs, in which Cyanobacteria make a cameo as endoliths that facilitate ooid dissolution.

PUBLISHED CONTENT AND CONTRIBUTIONS

Lingappa, U. F., D. Monteverde, J. Magyar, J. S. Valentine, W. W. Fischer. “How manganese empowered life with dioxygen (and vice versa).” *Free Radical Biology and Medicine* 140:113-125 (2019).

UFL participated in idea development and wrote the manuscript.

Lingappa, U. F., W. W. Fischer. “Oxygenic Photosynthesis.” In: Gargaud M. *et al*. (eds) *Encyclopedia of Astrobiology*. Springer, Berlin, Heidelberg (2019).

UFL wrote the entry.

TABLE OF CONTENTS

LIST OF FIGURES AND TABLES

CHAPTER V

CHAPTER VI

CHAPTER VII

CHAPTER VIII

APPENDIX I

CHAPTER I

Introduction

Cyanobacteria are really important. Around 2.4 billion years ago, their ancestors evolved oxygenic photosynthesis—the ability to use light and water and carbon dioxide to make oxygen and organic matter—and with it they changed the world. This metabolic revolution caused the biggest impact life has ever had on the environment and completely redirected life's evolution, unleashing the biosphere to previously inconceivable limits and enabling the development of large, complex creatures like us.

This thesis is a collection of investigations concerning these extraordinary microbes and their relationship with the Earth. We begin with the origin of oxygenic photosynthesis because it is such a quintessential example of the reciprocal interplay between life and the world around it. Life is shaped by its surroundings; it evolves to thrive in whatever habitats are available. In turn, life impacts its surroundings. Over time, even the smallest creatures can remodel their environment. The environmental context of ancient Cyanobacteria gave rise to the evolution of oxygenic photosynthesis; with oxygenic photosynthesis, Cyanobacteria transformed the planet.

Evolving this ability required overcoming some immense challenges. Chemically speaking, pulling electrons off of water and then using them to fix carbon is spectacularly difficult. On top of that, producing oxygen is dangerous—oxygen causes oxidative stress, which can wreak havoc on biological systems. Life as we know it today has sophisticated mechanisms for combating this havoc (nonetheless it remains a threat; too much oxidative stress, like that induced by exposure to ionizing radiation or even just elevated partial pressures of oxygen, and you're toast), but since most such defenses did not exist when oxygenic photosynthesis first evolved, its inception probably precipitated a devastating mass extinction event. That life 1) developed this ability at all and 2) actually survived it, is incredible.

Much of the work in the first half of this thesis was motivated by trying to understand that pivotal moment in the history of life on Earth.

The connate roles of manganese in the natural history of Cyanobacteria

Oxygenic photosynthesis is not the only version of phototrophy—a metabolism that harnesses energy from light—that exists, and it wasn't the first. Phototrophy using electron sources other than water, such as hydrogen and iron, preceded oxygenic photosynthesis by up to a billion years. Oxygenic photosynthesis evolved from those earlier forms. However, the leap between them is big, for two reasons. First, oxidizing water requires much higher reduction potentials than oxidizing hydrogen, iron, or any of the other electron sources used by known forms of phototrophy. Because of that, the existing biochemical machinery used to access those other electron sources was not strong enough to access electrons from water. Second, phototrophy is fundamentally a single-electron process but oxidizing water is a four-electron process. This means that using water as an electron source for phototrophy not only requires reaching extremely high potentials, but also requires the ability to store up four electrons worth of oxidizing power. Manganese was the stepping stone for overcoming both of those hurdles.

The ancient waters in which oxygenic photosynthesis evolved contained high concentrations of dissolved manganese. For early phototrophs severely limited by their reliance on geochemical trickles of hydrogen and iron as electron sources, this dissolved manganese presented an enticing electron reservoir. Manganese has similarly high reduction potentials to water but is amenable to single-electron reactions. Therefore, the ecological niche offered by unlocking the ability to access electrons from manganese necessitated the development of high potential phototrophy but not the four-electron bridge—a halfway point between the earlier forms of low potential phototrophy and oxygenic photosynthesis. Put another way, manganese characterized the environmental context that incentivized the evolutionary trajectory which ultimately led to oxygenic photosynthesis. Along the way, a version of phototrophy based on manganese oxidation was a key intermediate. To complete the transition, the four-electron hurdle was overcome by the stabilization of four manganese atoms as a cofactor that cycles through oxidation states

to store up oxidizing power. To this day, all oxygenic photosynthesis requires this tetra-manganese cofactor.

Manganese was likely also the reason the ancestors of Cyanobacteria survived the sudden and severe levels of oxidative stress they inflicted upon themselves by producing the first oxygen. Manganese can be a potent antioxidant; many organisms that are particularly resistant to oxidative stress—such as *Deinococcus radiodurans*, which can survive over 1000x the radiation dose that would kill a human—hoard it to exploit this chemistry. The fact that manganese provided a critical stepping stone for the evolution of oxygenic photosynthesis meant that the organisms involved were already expressly interested in manganese. As a result, they had a built-in antioxidant system. To this day, cyanobacterial cells take in extraordinary amounts of manganese and appear to utilize its antioxidant properties.

The manganese oxidation mechanism that was the precursor to oxygenic photosynthesis did not disappear afterward. Today, no known phototrophs solely use manganese as their electron source, but Cyanobacteria seem to have retained the ability to use manganese in addition to water. Furthermore, Cyanobacteria can catalyze manganese oxidation by at least two other separate mechanisms. By any or all of these pathways, they generate reactive oxidized manganese products. Such products are dynamic players in the biogeochemical manganese cycle and connect to many other important ecosystem processes notably including the degradation of recalcitrant organic matter. The understanding that Cyanobacteria began oxidizing manganese over two billion years ago, and continue to do so today, implicates them as deeply entwined with these processes.

Exposed rock surfaces in the desert often develop a dark coating known as rock varnish[*], which is characterized by high concentrations of manganese and provides a neat ecological case study further

[*] Varnish has been remarked upon in the scientific literature for over 200 years (featured in the writings of Humboldt, Darwin, Lucas, and others) and engaged with by indigenous peoples for much longer than that—an interaction demonstrated by prehistoric petroglyphs carved into varnished surfaces. I wish I had knowledge of their understanding of varnish; I suspect it was profound. I have contacted dozens of tribal representatives, cultural preservation organizations, museums, and archivists, to try to find out how indigenous peoples have thought about this material, but have not yet been successful in finding this information. Western scientists, though, were stumped. Varnish was a long-standing geological mystery.

highlighting how the enduring connections between Cyanobacteria and manganese remain relevant today. Although such desert surfaces are extremely harsh environments subject to high levels of oxidative stress, certain Cyanobacteria have adapted to thrive there. Their use of manganese as an antioxidant system both enables their survival in this harsh setting and also explains how varnish ends up with such high manganese content—varnish development can be understood as the slow buildup of a residue left by Cyanobacteria stockpiling manganese as a survival strategy. Thus, varnish encapsulates the interplay of life shaped by the demands of environmental conditions in turn remodeling the environment itself.

Chapters II-VI tell this manganese story (Fig. 1*A*-*E*). Chapter II is a review/perspective paper that explains the aspects of manganese chemistry that made it so uniquely important in the evolution of photosynthesis, and describes the intimately entwined histories of manganese and oxygen. Chapter III deciphers the history recorded in a package of ancient rocks in South Africa known as the Transvaal Supergroup—truly one of the great wonders of the world—that captures the origin of oxygenic photosynthesis and accompanying changes in paleoenvironment. Chapter IV comes back to the modern world to examine varnish. Chapter V investigates the ability of modern Cyanobacteria to oxidize manganese. Chapter VI exposes problems with current methods and understandings applied to manganese chemistry in the environment.

The other stories

Beyond manganese, this thesis contains two other glimpses into the interplay between Cyanobacteria and the world around them (Fig. 1*F*-*G*).

Chapter VII concerns a cyanobacterial mat ecosystem reminiscent of those that ruled the Earth for over a billion years between the origin of oxygenic photosynthesis and the rise of animals and plants. In 2017, this ecosystem was hit by the eyewall of Hurricane Irma, one of the strongest hurricanes in recorded history. Although severely disrupted by the storm, the mat communities bounced back with remarkable resilience, an expression of how such ecosystems and the Cyanobacteria that build them have time and time again outlasted the environments they evolved to thrive in and adapted to new conditions.

Chapter VIII is an exploration of the material properties characterizing an ideal exfoliating microbead for cosmetic products (long story) but also offers a small window into the intriguing relationship between Cyanobacteria and carbonate minerals. Oxygenic photosynthesis as a bulk process tends to drive carbonate precipitation; however, certain Cyanobacteria are also able catalyze carbonate dissolution and use this ability to bore into carbonate mineral substrates, contributing to ocean-atmosphere-lithosphere carbon dynamics in unexpected ways.

Finally, the appendix provides an overview of oxygenic photosynthesis.

ଓ

Taken together, I hope this thesis paints a picture of the myriad and intricately beautiful ways the constant interactions between life and the environment play out. The studies presented here examine this relationship from numerous different perspectives: the geological record of Earth history, microbial physiology, microbial ecology, inorganic chemistry, and Earth surface processes. In that regard, there is something in this thesis for everyone: geologists, biologists, chemists, all or none of the above. Whoever you are, dear reader, having found your way here, I leave you with this wish: I hope that you find something in these pages that interests you, something that you never thought of before but that changes, in some small but meaningful way, how you see the natural world.

History does not end with us and the models that we understand the world through will inevitably be replaced as new ways of knowing enable better ones. For now, I have done my best, with the data and understandings available to me, to do justice to these stories. I feel deeply honored to have been a part of discovering and telling them.

Usha Farey Lingappa
February 2021

Figure

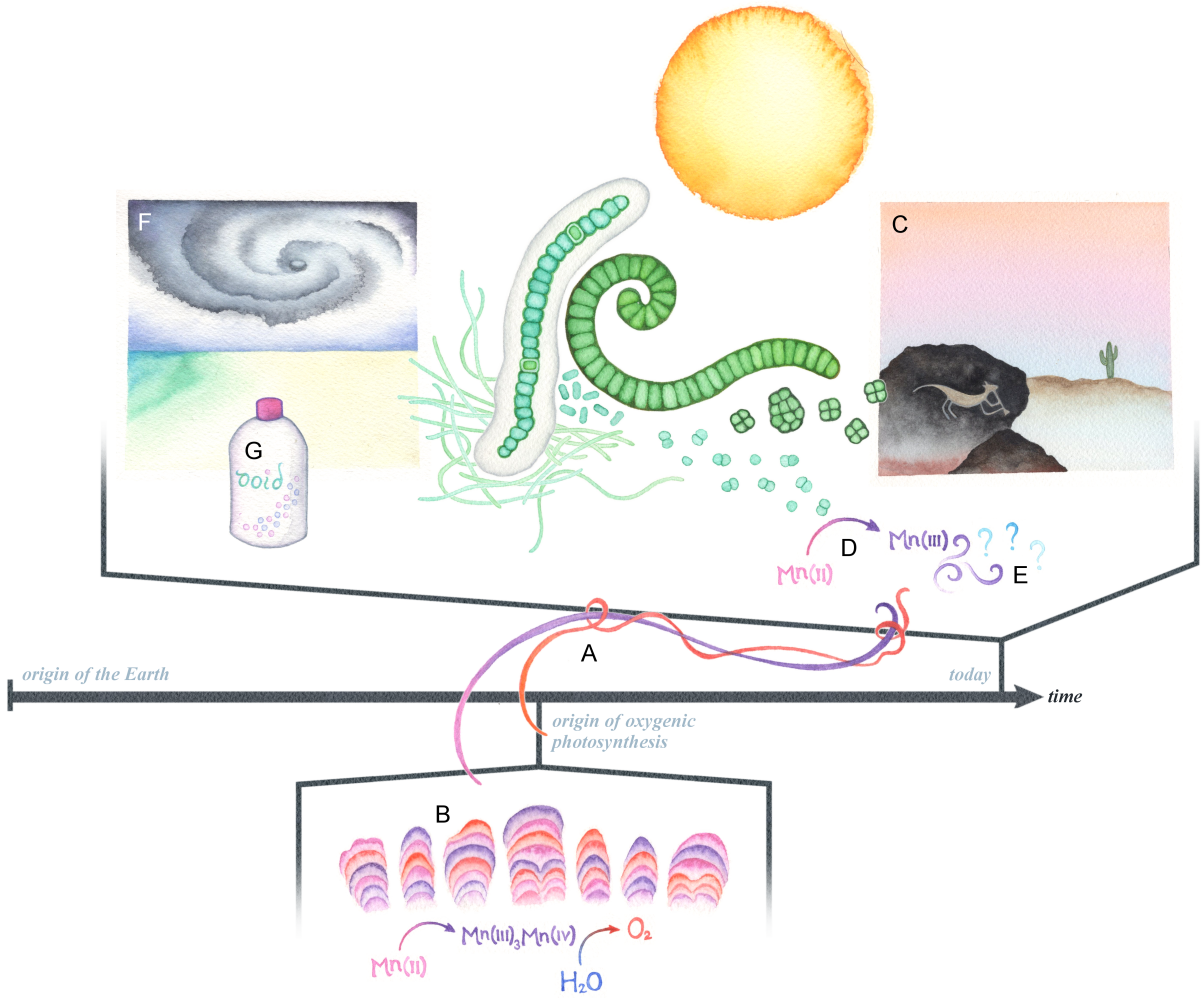

Figure 1. Thesis overview as a watercolor collage. ***A.*** The histories of manganese and O_2 are intimately entwined (Chapter II). ***B.*** Manganese oxidizing phototrophic communities evolved oxygenic photosynthesis (Chapter III). ***C.*** Desert varnish is a product of the relationship between Cyanobacteria and manganese (Chapter IV). ***D.*** Cyanobacteria oxidize manganese (Chapter V). ***E.*** Soluble Mn(III) complexes are important but elusive players in manganese biogeochemistry (Chapter VI). ***F.*** Hurricane Irma over Little Ambergris Cay (Chapter VII). ***G.*** Wash your face with ooids not plastic (Chapter VIII).

CHAPTER II

How manganese empowered life with dioxygen (and vice versa)

Usha F. Lingappa[1], Danielle R. Monteverde[1], John S. Magyar[1], Joan Selverstone Valentine[1,2], Woodward W. Fischer[1]

1. Div. of Geological & Planetary Sciences, California Institute of Technology, Pasadena, CA 91125 USA

2. Dept. of Chemistry & Biochemistry, University of California Los Angeles, Los Angeles, CA 90095 USA

Abstract

Throughout the history of life on Earth, abiotic components of the environment have shaped the evolution of life, and in turn life has shaped the environment. The element manganese embodies a special aspect of this collaboration; its history is closely entwined with those of photosynthesis and O_2—two reigning features that characterize the biosphere today. Manganese chemistry was central to the environmental context and evolutionary innovations that enabled the origin of oxygenic photosynthesis and the ensuing rise of O_2. It was also manganese chemistry that provided an early, fortuitous antioxidant system that was instrumental in how life came to cope with oxidative stress and ultimately thrive in an aerobic world. Subsequently, the presence of O_2 transformed the biogeochemical dynamics of the manganese cycle, enabling a rich suite of environmental and biological processes involving high-valent manganese and manganese redox cycling. Here, we described insights from chemistry, biology, and geology, to examine manganese dynamics in the environment, and its unique role in the history of life.

Introduction

The rise of dioxygen, O_2, ~2.35 billion years ago (Ga) registers as the single biggest influence of life on the environment (1). This defining moment in Earth history, widely attributed to the invention of oxygenic photosynthesis in the ancestors of modern Cyanobacteria, transformed the environmental redox landscape dramatically and irreversibly, impacted all global biogeochemical cycles, and was fundamental to the course of evolution to life as we know it today (2). Harnessing the ability to pull electrons from water released early autotrophs from the limitations of available geochemical electron donors, e.g., Fe(II), H_2, and H_2S, allowing for a huge increase in primary production (3). The buildup of significant amounts of O_2 in the atmosphere led to the evolution of aerobic biochemistries, and opened the door to new degrees of oxidative stress (4–6).

The element manganese is central to the production of O_2 because it plays a critical role at the active site of photosystem II (PSII) (7), which is comprised of a Mn_4CaO_5 cluster, sometimes referred to as the water-oxidizing complex (WOC) (8, 9). The WOC is one of the key features that set PSII apart

from all other anoxygenic phototrophic reaction centers and is the catalyst that enables PSII to use water as an electron donor for oxygenic photosynthesis. The manganese atoms in the WOC cycle through multiple oxidation states, allowing it to couple the one-electron process of photochemical charge separation with the four-electron process of splitting water to make O_2. Emerging geological, biochemical, and comparative biological data support the hypothesis that, prior to the origin of oxygenic photosynthesis, Mn^{2+}, rather than water, served as an electron donor to the ancestor of PSII in a manganese-based version of anoxygenic phototrophy, which led to the evolution of the WOC (10–13); this evidence is summarized further below.

Manganese also plays an important role in cellular protections against oxidative stress. Manganese ions are found as cofactors in some of the key enzymes involved in the detoxification of the reactive oxygen species (ROS) superoxide and hydrogen peroxide, i.e., manganese superoxide dismutase (MnSOD) and manganese catalase. Low molecular weight coordination complexes of manganese ions can also react catalytically with superoxide and hydrogen peroxide, and such species represent an important non-enzymatic antioxidant system in many organisms (14–18). Furthermore, manganese can replace iron in metalloenzymes, retaining catalytic activity, while conferring resistance to oxidative damage (19). Taken together, these antioxidant properties along with the importance of manganese in the evolution of photosynthesis reveal that manganese played a central role in both the production of O_2 and the strategies by which the first life to encounter O_2 survived the severe oxidative stress induced by its presence (4).

In Earth surface environments today, O_2 enables a diverse suite of processes that involve manganese redox chemistry. The standard reduction potentials of manganese redox couples are higher than those of most other common environmental species, which means that the oxidized forms of manganese are among the strongest oxidants found in the environment (20). O_2 and species derived from it, such as peroxides and hydroxyl radicals, are the only oxidants able to oxidize Mn^{2+} under environmentally relevant conditions. Accordingly, the biogeochemistry of manganese is uniquely sensitive to the presence or absence of these species. The introduction of O_2 provided a way to unlock the

rich redox chemistry of manganese, allowing it to participate in numerous important biochemical and ecological processes as a powerful oxidant.

Biology and geology provide two different yet complementary perspectives on the long cross talk between the evolution of life and its environment. Examining extant organisms can provide detailed mechanistic insight into biological processes as well as a way to develop hypotheses about the evolutionary relationships between different taxa and what traits can be considered ancestral (21–23). However, inferences gleaned from comparative biology can only place evolutionary processes in the framework of relative time, and using extant life to understand the ancient biosphere is hampered by the omnipresent effects of extinction—even for microbes (24). On the other hand, observations of physical and chemical fingerprints preserved in sedimentary rocks can provide a direct, albeit coarse, record of the life and environments that at one time existed. In this work, we incorporated both of these approaches to examine the intimately connected histories of manganese and O_2 and their interactions with the evolving biosphere.

Manganese speciation and reactivity in the modern environment

The biogeochemical dynamics of manganese are defined by its unique redox chemistry. Elemental Mn is a first row transition metal with the outer shell electronic configuration $3d^5 4s^2$. There are seven valence electrons, two electrons completely filling the 4s orbital and one each in the five 3d orbitals, half filling the 3d level. This electron configuration makes it possible for manganese to have formal oxidation states ranging from -3 to +7, providing the largest number of accessible oxidation states of any 3d transition metal (25). In biological and environmental systems, however, the main oxidation states are limited to Mn(II), Mn(III), and Mn(IV) (26). Other oxidation states may exist transiently as reactive intermediates, e.g., Mn(V) just prior to O-O bond formation during photosynthetic water splitting (27), but they never accumulate in natural systems. The fate of manganese in the environment, from its sources in weathering rocks to its sinks in sedimentation and subduction, is characterized by redox transformations.

Mn(II) is abundant in the Earth's crust (0.1 wt% MnO (28)) as a common minor constituent substituting for Fe(II) in igneous minerals (29). In sedimentary and supergene (ore produced from oxidative weathering of Mn(II)-bearing rocks) deposits, manganese can be found in much higher concentrations, largely as Mn(II) in carbonate salts and Mn(III)/Mn(IV) in oxides (30). These geological sources are mobilized by various processes of erosion or weathering (hydrolysis and dissolution) and transported as windborne dust particles and suspended or dissolved species in rivers (26). In natural waters, soils, and sediments, both abiotic and biologically mediated processes can contribute to manganese redox cycling. Table 1 contains an overview of manganese species found in the environment, and Figure 1 summarizes the major sources, sinks and conversions in the modern manganese cycle.

The geochemistry of manganese is often compared and contrasted with that of iron (31). Both are redox active in Earth surface environments today. Both of their reduced cations, i.e., Mn^{2+} and Fe^{2+}, are divalent and soluble in water; and both form insoluble oxide and oxyhydroxide minerals under redox conditions that favor their oxidation. Unlike manganese, Fe(II) and Fe(III) are the only biologically and environmentally stable oxidation states of iron, whereas Fe(IV) may exist transiently but does not accumulate in the environment. The dramatic difference in the relative stabilities of the trivalent and tetravalent oxidation states of manganese and iron, respectively, is a consequence of the differences in their outer shell d-electron configurations and the extra degree of stabilization that is predicted by quantum mechanics and observed experimentally for electronic configurations in which each of the five 3d orbitals contains one electron, i.e., $3d^5$. While elemental manganese has the outer shell electron configuration $3d^54s^2$, elemental iron has an additional d-electron, i.e., $3d^64s^2$. Thus the divalent ions have the outer shell configurations $3d^5$ for Mn(II) and $3d^6$ for Fe(II). The result is that it is relatively easy to oxidize Fe(II), $3d^6$, to Fe(III), $3d^5$, but relatively difficult to oxidize Mn(II), $3d^5$, to Mn(III), $3d^4$. Indeed, unless Mn(III) is stabilized by its ligand environment in a coordination complex or in an ionic solid, it takes less energy to remove two electrons from a single Mn(II) species to form a Mn(IV) species than to remove two electrons from two Mn(II) species to form two Mn(III) species (Figure 2*A*). Consequently, Mn(III) species generated in an environment lacking sufficient ligand stabilization will react rapidly with

themselves in a bimolecular reaction by disproportionation, i.e., 2Mn(III) → Mn(II) + Mn(IV) (32, 33). Due to this relative instability of Mn(III), for many years the classical paradigm for manganese speciation in the environment was a dichotomy of soluble Mn(II) species and insoluble Mn(III)- and Mn(IV)-containing oxide minerals.

Breaking with this classical view, we now know that Mn(III) species can persist in solution when coordinated by suitable stabilizing ligands. Mn^{3+} and Fe^{3+} show similar ligand preferences due to their high positive charge and small ionic radii. Anions are preferred over neutral ligands (e.g., HO^- versus H_2O), and chelating anionic ligands with oxygen donor atoms are particularly favored. In the case of Mn^{3+}, the large degree of stabilization provided by chelating ligands can stabilize that relatively unstable oxidation state with respect to its disproportionation reaction, allowing Mn(III) species to persist in solution and participate in other reactions. Ligand stabilization can also significantly change the standard reduction potential of manganese redox couples, thereby changing the energetics of electron transfer reactions (Figure 2*B*).

The exact identities of the ligands that stabilize Mn(III) in natural systems are often unknown. Nevertheless, the properties of these species can be predicted, to an extent, based on studies of known Mn(III) complexes that have been chemically characterized in aqueous solution. Some particularly instructive examples of such Mn(III) complexes were described by Klewicki and Morgan for the Mn(III) complexes of pyrophosphate, EDTA, and citrate (34). When these Mn(III) complexes decompose, it is not solely due to Mn(III) disproportionation, but also due to instabilities of the metal-bound ligands. In the case of pyrophosphate, complexation to Mn(III) is expected to enhance the reactivity of the bound pyrophosphate ligand with water resulting in the disappearance of the pyrophosphate by hydrolysis to give two phosphate ions (34, 35). In the case of EDTA and citrate, the Mn(III) complexes decompose due to internal (i.e., intramolecular) electron transfer from the ligands to Mn(III), thus producing Mn(II) and products that result from ligand oxidation. Another instructive example is the Mn(III) complex of desferrioxamine B (DFOB), studied by Duckworth and Sposito (36). At pH < 7, $Mn(III)DFOB^+$ decomposes slowly by internal electron transfer to give Mn(II) and the oxidized ligand, similar to the

Mn(III) complexes of EDTA and citrate. The reactivity of Mn(III) complexes is an important branch of manganese biogeochemistry, participating in major ecosystem processes including the oxidative breakdown of recalcitrant organic matter like lignocellulose—the most abundant organic compound on Earth (37).

The occurrence of significant amounts of high-valent manganese has been documented in the soluble fractions in many environmental systems and attributed to the presence of soluble, ligand-bound Mn(III) complexes (38–41). However, it is important to note here that environmental studies typically define "dissolved species" operationally based on filtration (e.g., anything that passes through a 0.2 μm or 0.45 μm filter). Colloidal or nanoparticulate matter can include insoluble manganese oxide minerals, and will typically be present in the environmental fractions classified as operationally soluble. The abundance of colloidal or nanoparticulate manganese in the environment is largely unknown, however the few studies that have measured it revealed that it can be substantial. For instance, one study found that in parts of the San Francisco Bay, up to 20% of operationally dissolved manganese fell within a colloidal fraction (defined as any particles > 10 kDa and < 0.2 μm) (42). Another study on the Loire River Watershed found 80% of operationally dissolved manganese to be colloidal (defined as particles > 0.01 μm and < 0.45 μm) (43). A better understanding of the distribution, diversity, and reactivity of both Mn(III)-ligand complexes and oxide mineral nanoparticles is required to improve our understanding of manganese redox dynamics in natural waters, soils, and sediments.

In minerals, the coordination of the higher oxidation states Mn^{3+}, Mn^{4+}, and Fe^{3+} is dominated by oxide ligands. Water molecules become extremely acidic when coordinated to these highly charged cations and dissociation of protons to give HO^- and/or O^{2-} can be suppressed only at very low pH. These hydroxo and oxo ligands are excellent bridging ligands and polymerization via M-O(H)-M or M-O-M bridging leads to the precipitation of insoluble metal oxides, which can take on a wide array of crystalline forms (44). The relative stabilities of the higher oxidation states of the metal ions in either manganese- or iron-containing minerals are hugely variable, depending on crystal form, degree of crystallinity, and particle size, in addition to pH and total metal concentration (45).

Oxidations of either Fe^{2+} or Mn^{2+} by O_2 to give oxides of Fe^{3+} or Mn^{4+} are thermodynamically favorable for either metal (26), but the reactions of Fe^{2+} with O_2 tend to be fast in most cases whereas the reactions of Mn^{2+} with O_2 can be prohibitively slow in the absence of a suitable catalyst (typically more than four orders of magnitude slower than Fe for homogeneous oxidation by O_2) (46). The kinetic barrier for the oxidation of aqueous Mn^{2+} with O_2 arises from the instability of the Mn(III) oxidation state in a homogeneous environment where water molecules are the only ligands. However, this kinetic barrier can be overcome with the presence of Mn(III) stabilizing ligands such as hydroxide, pyrophosphate, or citrate, or with the presence of a variety of metal oxides surfaces like iron, manganese, or aluminum oxides (47–49). The binding of the Mn^{2+} ion to the metal oxide surface also allows stabilization of the Mn(III) oxidation state, similar to the coordination of chelating ligands. The ability of manganese oxides to catalyze the oxidation of Mn^{2+} to manganese oxides means that, upon generating sufficient product, the reaction becomes autocatalytic.

In natural waters at circumneutral pH, the abiotic oxidation of Mn^{2+} with O_2 has been considered of relatively minor importance, due to the kinetic limitations of the homogeneous reaction. However, the presence of colloidal or nanoparticulate metal oxides in the water column may significantly promote heterogeneous oxidation. Furthermore, nanoparticles have also been shown to exhibit different surface atomic structures than their larger-scale bulk counterparts—this leads to exotic chemistries with important implications, including the ability to catalyze Mn^{2+} oxidation at much faster rates (50). Thus, in certain settings, abiotic oxidations of Mn^{2+} with O_2 may hold a more significant role in environmental manganese cycling than previously appreciated.

The reaction of Mn^{2+} with superoxide, O_2^-, has been given considerable attention, and once again the outcome is dependent upon the presence or absence of stabilizing ligands (16, 20, 51). Superoxide reacts with Mn^{2+} to form a transient MnO_2^+ intermediate, which can dissociate to give Mn^{3+} and H_2O_2. This reaction is readily reversible, and the transient MnO_2^+ intermediate can also be observed in the reaction of Mn^{3+} with H_2O_2, which results in manganese reduction back to Mn^{2+} (16). This equilibrium (Reaction 1) can be pulled to the right toward accumulation of the Mn(III) product by removal of the

H_2O_2 product, thus preventing its back-reaction with Mn^{3+}. For example, the enzyme catalase, which catalyzes the degradation of H_2O_2, has been implicated in Mn^{2+} oxidation by superoxide, a phenomenon discussed further below (52, 53). The presence of chelating anionic ligands that significantly stabilize Mn(III), for example pyrophosphate or citrate, can also limit the extent of the back-reaction with H_2O_2, resulting in the accumulation of Mn(III)-ligand complexes. However, in the presence of monodentate anionic ligands like carbonate or phosphate, the MnO_2^+ intermediate is sufficiently stabilized to enable a new bimolecular reaction that ultimately results in the catalysis of the disproportionation of two O_2^- to give H_2O_2 and O_2, regenerating Mn^{2+} in the process (Reaction 2) (16, 51). This catalytic removal of O_2^-, with no net Mn^{2+} oxidation, has been proposed to be the basis for the antioxidant activity of the Mn(II)-small molecule complexes (4).

Reaction 1. $Mn^{2+} + O_2^- + 2H^+ \rightleftarrows MnO_2^+ + 2H^+ \rightleftarrows Mn^{3+} + H_2O_2$

Reaction 2. $MnO_2^+ + MnO_2^+ + 2H^+ \rightarrow 2Mn^{2+} + H_2O_2 + O_2$

Hydrogen peroxide, H_2O_2, can serve as both an oxidant for Mn(II), and a reductant for Mn(III) or Mn(IV). The rates of these reactions are also ligand dependent. Similar to the phenomenon discussed above for O_2^-, the disproportionation of H_2O_2 can also be effectively catalyzed by Mn^{2+} (54). For this reason, the enzymes MnSOD and manganese catalase are unusual relative to other metalloenzymes in that the metal ion alone, in this case Mn^{2+}, in the absence of any protein, is an effective catalyst of the same reactions catalyzed by the metalloenzymes (16, 55).

Manganese and modern biology

In modern environments, manganese redox chemistry interfaces with biology in a myriad of ways. Manganese is an essential trace element with numerous biochemical roles within cells (26), and geochemical redox cycling affects the bioavailability of manganese, thereby controlling the biological processes dependent upon it—including photosynthesis (56). Conversely, manganese redox transformations in the environment, both oxidation and reduction, are often microbially mediated (20). These microbial manganese transformations can be either direct enzymatic reactions or indirect reactions

occurring via the biological production of a chemical species that reacts with manganese, and/or impact on local solution chemistry in a way that accelerates abiotic oxidation (like autotrophs taking up CO_2 and thereby raising pH). Biological catalysis can greatly increase the fluxes and decrease the timescales that are relevant for these reactions, adding to their ecological significance (56). In the case of manganese oxidation, the kinetic limitations of the abiotic reaction have led to the widely held premise that the dominant processes of manganese oxidation in the environment are biological (57). While this assumption may not accurately account for the extent of oxide nanoparticles and their role in heterogeneous abiotic manganese oxidation, there are many known bacteria and fungi (although no known archaea) that do oxidize Mn(II), and account for significant fluxes of oxidized manganese species in the environment. Notably, no organisms have been discovered to date with a metabolism based solely on manganese oxidation, although such chemolithotrophic or photolithotrophic metabolisms are thermodynamically plausible based on the redox potentials of certain high-valent manganese species (Figures 2*B* and 4*A*).

Among the bacteria, two enzyme families have been identified with members that carry out direct Mn(II) oxidation coupled to O_2 reduction: the multicopper oxidases, and the peroxidase cyclooxygenases. These enzymes are typically extracellular or outer membrane proteins, and the manganese oxidation reactions they catalyze are not thought to be involved directly in energy conservation. The multicopper oxidases have been identified in a diverse set of manganese oxidizing bacteria, including *Bacillus* sp. SG-1 (58–61), *Pseudomonas putida* GB-1 (62, 63), *Leptothrix discophora* SS-1 (64, 65), and *Pedomicrobium* sp. ACM 3067 (66). The peroxidase cyclooxygenases (formerly animal heme peroxidases (67)) have been identified in *Erythrobacter* sp SD21 (68), *Aurantimonas manganoxydans* SI85-9A1 (69), and *Pseudomonas putida* GB-1 (70). Both of these enzymes oxidize Mn^{2+} via single electron transfer steps to form a Mn(III) intermediate, which is then further oxidized or disproportionates to form Mn(IV) (60, 71, 72).

A third flavor of bacterial manganese oxidation was described in *Roseobacter* sp. AxwK-3b. In this system, an NADH oxidoreductase has been hypothesized to produce superoxide. The superoxide then oxidizes Mn(II), while another enzyme with sequence similarity to MopA, the peroxidase cyclooxygenase

in *Erythrobacter*, acts as a catalase to disproportionate the hydrogen peroxide produced by superoxide reduction (52, 53). The catalase activity draws down the concentration of hydrogen peroxide, thereby pulling the equilibrium discussed earlier (Reaction 1) towards the accumulation of oxidized manganese product, minimizing the back reaction of manganese reduction by hydrogen peroxide. Like the other modes of bacterial manganese oxidation discussed here, manganese oxidation by *Roseobacter* is an extracellular phenomenon, with no role in energy conservation.

Fungi are also known to oxidize manganese by both direct and indirect mechanisms. Similar to the *Roseobacter* system, fungi have been shown to oxidize manganese indirectly using superoxide that is produced by NADPH oxidoreductase (e.g. Nox family) enzymes as a signaling molecule during cell differentiation (73). Fungi also have mechanisms of direct enzymatic manganese oxidation—conducted by manganese peroxidase, a heme peroxidase found in a wide range of fungi involved in plant litter decomposition (74). Manganese peroxidase catalyzes successive single-electron oxidations of two Mn(II) to produce two Mn(III), coupled to the reduction of hydrogen peroxide or an organic peroxide. The Mn(III) product is stabilized by ligands—predominantly oxalate—to create a diffusible oxidant which plays a critical ecological role in environmental lignin degradation (37).

The only known mode of manganese oxidation where the electrons definitively go into the electron transport chain involved in an organism's energy metabolism is during the assembly of the WOC of PSII in Cyanobacteria and the plastids of algae and plants. The WOC is synthesized biologically via a process known as photoassembly, which involves the direct photochemical oxidation of Mn^{2+} by PSII (75). During photoassembly, four Mn(II) atoms are oxidized over five light-induced charge separation events to $Mn(III)_3Mn(IV)$ to generate the S_0 baseline oxidation state of the WOC. During the catalytic cycle, the cluster is further oxidized over four more light induced charge separation events to a hypothesized $Mn(IV)_3Mn(V)$ state, and then regenerated to the S_0 state with the four-electron oxidation of H_2O to O_2. Notably, this is the only known mechanism of biological manganese oxidation that does not use O_2 or other reactive oxygen species as an oxidant.

Unlike manganese oxidation, manganese reduction has been well documented as a form of microbial metabolism that conserves energy—namely as the final electron acceptor for anaerobic respiration. In extant organisms, manganese reduction is not known to be an obligate metabolism; generally organisms capable of respiring manganese are also capable of using other electron acceptors such as other metal oxides, dioxygen, nitrate, organic compounds, or sulfur compounds (76). In anaerobic environments with abundant manganese oxides, manganese reduction can theoretically yield more energy than other forms of respiration and represents an important pathway of organic carbon remineralization (20). The best studied organisms that respire manganese oxides are *Shewanella oneidensis* MR-1 (77), and *Geobacter sulfurreducens* (78), both of which employ extensive networks of multiheme cytochromes that transport electrons from the periplasmic membrane to extracellular electron acceptors, via either direct outer membrane electron transfer enzymes or small molecule electron shuttles like humics, flavins, or phenazines (79). Incubations done with environmental samples also suggest that manganese reduction may be syntrophically coupled to other microbial metabolisms such as the anaerobic oxidation of methane (80).

Intracellularly, manganese is found as both high molecular weight species bound to proteins and low molecular weight species bound to small molecules, including ortho- and polyphosphates, carbonates, and organics (14). In proteins, manganese is used both as a structural element and catalytically, both as a Lewis acid and as a redox cofactor (32, 81). Beyond O_2 production (PSII) and reactive oxygen species detoxification (MnSOD and manganese catalase), enzymes that contain manganese perform a diverse suite of functions, ranging from DNA synthesis to carbohydrate metabolism. In addition to magnesium, manganese exhibits the highest diversity of enzyme functional requirements spanning all six enzyme commission class designations and representing over 125 unique manganese enzymes (as listed in the protein database ExPASy) (82). These enzymes utilize manganese at mono-, bi-, and tetranuclear sites (83). No known trinuclear manganese proteins exist, although the tetramanganese cluster of the WOC is comprised of a trimanganese distorted cubane structure bound to the fourth, so called ‘dangler’

manganese by an oxo bridge (8, 11, 84). Table 2 presents a representative list of known manganese enzymes, with a focus on those that are redox active (for a more complete list see reference (85)).

Some enzymes have absolute requirements for manganese (e.g., PSII), while others are cambialistic and allow Mn^{2+} to substitute for other divalent cations like Zn^{2+}, Cu^{2+}, Fe^{2+}, Ni^{2+}, Co^{2+}, Mg^{2+}, and Ca^{2+} and yield a functioning enzyme (e.g., cytochrome *c* oxidase, xylose isomerase) (86). The most common of these substitutions is between Mn^{2+} and Mg^{2+} due to similarities in ionic radii and ionization potential, despite the fact that manganese typically has four orders of magnitude lower cellular concentration (10^{-7} M manganese versus 10^{-3} M magnesium (81), though manganese concentrations can vary significantly between organisms, and reach as high as 10^{-3} M (17, 87)). For example, cytochrome *c* oxidase (i.e. complex IV, heme-copper O_2 reductase), which pumps protons across the mitochondrial membrane and catalyzes the reduction of dioxygen to water, contains a number of redox active iron-copper centers as well as two non-redox active divalent metal centers typically composed of Zn^{2+} and Mg^{2+} (85). However, in some bacteria (e.g., the alphaproteobacterium *Paracoccus denitrificans*) up to 20% of the Mg^{2+} is replaced by Mn^{2+} (85, 88). It is currently unknown if this substitution plays a catalytic role or if the divalent metal only serves a structural role, although some evidence shows that the Mg/Mn site may be responsible for transport of the product waters and advected protons (89). Another intriguing example of a metal site sometimes occupied by Mg^{2+} and sometimes by Mn^{2+} is found in ribulose-1,5-biphosphate carboxylase/oxygenase (or RuBisCO)—the premier carbon fixation enzyme in the Calvin Cycle and most abundant protein on Earth. While the role of this substitution is also currently unknown, hypotheses have been proposed that it could regulate the notorious oxygenase activity of RuBisCO (90).

All of the known enzymes that use manganese in a redox capacity touch O_2 in some way, either as a direct product of the reactions they catalyze (e.g., PSII, catalase) or as an oxidant used to generate a catalytic Mn(III) or Mn(IV) center or product (e.g., oxalate decarboxylase, manganese peroxidase, multicopper oxidase MnxG). Thus O_2 enables manganese redox activity, greatly expanding the diversity of uses for manganese by biology. While the evolutionary history of specific proteins can be difficult to assess when they are subject to horizontal gene transfer and rapid evolutionary rates, we infer that all of

these proteins that interface with manganese redox chemistry postdate the rise of O_2—with the single, salient exception of PSII (discussed further below).

Manganese in the history of Earth and life

O_2 was not present on the early Earth in any meaningful amounts prior to the Great Oxygenation Event that occurred at ~2.35 Ga, following the origin of oxygenic photosynthesis. Multiple proxies in the geological record constrain earlier O_2 levels to exceedingly low. For example, the presence of weathered detrital grains of redox-sensitive minerals like pyrite and uraninite deposited in river sediments constrains O_2 levels to $< 10^{-5}$ atm (4, 91), and a mass-independent fractionation signal in the sulfur isotopic composition of sedimentary rocks caused by SO_2 photochemistry (enhanced by absence of an ozone layer) constrains O_2 levels to $< 10^{-10}$ atm (92–94). Both of these proxies are widespread in strata deposited prior to the rise of O_2, and completely absent in younger strata. Thus, both the advantages and disadvantages provided by O_2 were not available to ancient biochemistry.

Manganese was abundant in natural waters on the early Earth. Mn(II) hosted in igneous rocks was easily released by silicate weathering, which, combined with hydrothermal sources of Mn(II), led to an accumulation of Mn^{2+} in the oceans (Figure 3*A*). Because Mn(II) does not readily form sulfide or disulfide minerals as Fe(II) does, the only significant manganese-bearing phases that formed were carbonate salts. Thus, before the rise of O_2, the primary sink of Mn^{2+} was as a minor constituent of carbonate salts (aragonite, calcite, and dolomite) precipitated from seawater, where Mn^{2+} can substitute for Ca^{2+} (4, 95). Archean age (> 2.5 Ga) marine calcite cements contain substantial amounts of Mn(II), in contrast to their modern equivalents, which reflects the high abundance of dissolved Mn^{2+} prior to the onset of manganese redox cycling and oxidative removal of manganese from the water column (95–101). An equilibrium partition coefficient provides a means of estimating the amount of Mn^{2+} that was present in the ancient ocean from observations of the Mn:Ca ratio in well-preserved marine herringbone calcite cements—a rock type/texture that grew slowly and provides a meaningful proxy for aspects of ancient seawater chemistry (102) (Figure 3*C*). The Mn:Ca ratio in these rocks is many orders of magnitude

greater than occurs in younger rocks (Figure 3*D*), and suggests Mn^{2+} concentrations of up to 120 μM characterized seawater prior to the rise of O_2 (4, 103); this is in stark contrast to the nanomolar concentrations typical of modern open oceans (26). This Mn^{2+} was a prospective resource for the early anaerobic biosphere—the biochemical challenge was figuring out how to access it.

In spite of the high manganese concentrations in natural waters, all available evidence suggests that if Archean biology used manganese at all it was as a divalent cation with no redox activity. From a geological perspective, no Archean age rocks display robust evidence of the presence of oxidized manganese mineral phases. Evidence for meaningful manganese redox cycling first appears in the geologic record in Paleoproterozoic strata (~2.4 Ga) shortly before the rise of O_2 (10). And from a biological perspective, enzymes that use manganese that could have been present in Archean organisms employ Mn(II) in roles that do not solicit its redox chemistry. Without the high potential oxidants supplied by O_2 or PSII, none of the known biological mechanisms for manganese redox chemistry would have been accessible.

The onset of manganese redox cycling was accompanied by a tremendous change in the style of sedimentary manganese deposition, as the precipitation of insoluble manganese oxides is the only mechanism that can generate highly concentrated manganese ores (95, 104). Primary minerals deposited in poorly consolidated sediments commonly undergo a suite of post-depositional alteration processes as the sediment is lithified into rock; this means that the primary mineral phases are often lost, and instead a complex mixture of secondary and tertiary mineral products end up preserved in the geologic record. Accordingly, understanding the diagenetic history and petrogenesis of manganese deposits has been a valuable source of data to reconstruct past processes of manganese redox cycling at different times in Earth history. The manganese-bearing minerals preserved in sedimentary deposits appear to follow a similar pattern, where primary Mn(IV) oxide minerals like birnessite accumulate in shallow sediments, but then during burial these are reduced by organic carbon in sedimentary porewaters—a process likely catalyzed by manganese-reducing microbes (105), to form secondary phases of mixed valence Mn(III)-bearing minerals like braunite or Mn(II)-bearing carbonates like kutnohorite (Table 1), which can be

further recrystallized and metamorphosed to form tertiary phases like rhodochrosite and rhodonite (95). Therefore, high concentrations of Mn(II)-bearing minerals in sedimentary rocks can provide evidence for the initial deposition of insoluble Mn(IV) resulting from oxidative processes in the overlying water column or locally at the seabed.

For most of geologic time, the history of manganese oxide deposition reflects the history of O_2, as O_2 and other species derived from it are the only meaningful oxidants for Mn^{2+}. However, the earliest authigenic manganese deposit is found in the Koegas Formation, a package of sedimentary rocks in the Transvaal Supergroup in South Africa, which was deposited at ~2.4 Ga (106). Careful comparison of the onset of manganese deposition with independent proxies that constrain the amount of O_2 demonstrated that these manganese deposits predate the rise of O_2 (10). Evidence from other coeval Paleoproterozoic sedimentary basins preserved in Australia and Canada support a similar history of manganese deposition (11, 95, 107, 108). These observations suggest a novel mechanism of manganese oxidation occurring just before the invention of oxygenic photosynthesis and fluxes of dioxygen in surface environments.

Oxygenic photosynthesis evolved from anoxygenic phototrophy, simpler versions of light-driven metabolism that use electron donors other than water. Both geological observations and constraints from comparative biochemistry indicate that anoxygenic phototrophy evolved very early in Earth history—likely sometime prior to 3.4 Ga, predating oxygenic photosynthesis substantially (13, 109). To convert light energy to chemical energy that fuels electron transport chains, modern anoxygenic phototrophs use biochemical machinery (reaction centers) that share distant homology to the photosystems of oxygenic photosynthesis, indicating a common evolutionary history (13, 110, 111). Today, organisms conducting these metabolisms exist in niche environments where high concentrations of their electron donors are available; these environments are often anaerobic, and the microorganisms that live there are adapted to extreme temperature or chemical conditions where they have less ecological competition. However, prior to the origin of oxygenic phototrophy, anoxygenic phototrophs were likely more prevalent in ancient surface environments (109, 112–114).

All known forms of anoxygenic phototrophy use electron donors that are accessible to reaction center electron acceptors with moderately high reduction potentials, ~250-500 mV; this is much lower than the reduction potential needed to access the H_2O/O_2 couple, which is accomplished by PSII with substantial overpotentials estimated at ~1250 mV. The extremely high potential of PSII must have evolved prior to the origin of oxygenic photosynthesis, as it is required to oxidize water. This implies an evolutionary missing link: a high-potential version of anoxygenic phototrophy bridging the canonical versions of lower-potential anoxygenic phototrophy with oxygenic phototrophy. Indeed, comparative biology of the D1 and D2 proteins of PSII with the analogous L and M subunits of the closest related anoxygenic reaction centers indicated that an ancestral version of PSII used a high potential electron donor (which must have been a small molecule, and not the single electron protein carriers employed by typical reaction center donors of cytochrome *c*, cupredoxin, or high-potential iron-sulfur protein) for anoxygenic phototrophy before the evolution of the WOC (13). Mn^{2+} is the only plausible electron donor to this ancestral version of PSII (13).

The hypothesis that Mn^{2+} served as an electron donor to ancestral PSII leading up to the evolution of oxygenic photosynthesis provides a natural explanation for the onset of manganese oxidation observed in the geologic record shortly before the rise of O_2 (10). Capturing light energy to generate a strong biochemical electron acceptor is the only known mechanism for manganese oxidation in the absence of a chemical electron acceptor, i.e., O_2, and therefore the most conceivable mechanism for that earliest manganese oxidation. Furthermore, using Mn^{2+} as an electron donor is exactly what modern PSII does during the assembly of the WOC (75). Thus, all biological water oxidation first requires phototrophic manganese oxidation, and as such, phototrophic manganese oxidation must have preceded the ability to oxidize water (11).

The high concentrations of dissolved Mn^{2+} in the ancient oceans provided an enticing ecological opportunity. Prior to gaining the ability to use the abundant resource of water as an electron donor, rates of primary productivity by the biosphere were not nutrient limited as they are today, but rather they were electron limited, with the most abundant sources of electrons coming from a geological trickle of rock-

weathering derived electron donors like H_2, sulfur compounds, and Fe(II) (3, 11). While Fe(II) represents the largest available geochemical electron source, iron appears to have had already developed a redox cycle and empirical observations show that Fe^{2+} was largely depleted from Late Archean surface waters (98, 113). At the same time, surface waters were rich in Mn^{2+}, water, and light. Therefore, Mn^{2+} represented a valuable untapped electron reservoir, providing a tangible incentive to evolve a much higher-potential reaction center capable of manganese oxidation—an evolutionary trajectory that would ultimately pave the way to oxygenic photosynthesis.

With the origin of oxygenic photosynthesis came the first appearance of meaningful sources of O_2. For biology, O_2 is a double-edged sword—it enabled the development of aerobic respiration, the most energy-rich form of metabolism, but it also brought the risk of devastating oxidative stress. Thus the appearance of O_2 in the environment imparted strong new selection pressures on life. Today, effective systems for combating oxidative stress are thoroughly integrated in biochemistry, but prior to the introduction of O_2 there would have been little use for such systems, and therefore little reason for them to have already evolved. As such, the first organisms to encounter oxidative stress had to rely on the antioxidant properties of molecules that served other functions intracellularly or pre-existed in the environment. The ability of Mn^{2+} complexes to catalytically quench reactive oxygen species (16, 54), along with the ability of Mn^{2+} to confer resistance to oxidative damage by replacing Fe^{2+} in metalloenzymes (19), makes manganese a key example of such a fortuitous antioxidant system. The concentrations of Mn^{2+} in ancient seawater were sufficiently high that manganese antioxidant chemistry could be considered naturally built-in to the environment. That O_2 production evolved in organisms that were already conducting a manganese-based version of phototrophy, and therefore already inclined to accumulate manganese intracellularly, means that those cells were readily poised to co-opt this manganese-based antioxidant system. Genomic analyses demonstrate that aerobic respiration evolved subsequent to oxygenic photosynthesis in the ancestors of Cyanobacteria (115). Early antioxidant systems would have been a critical ingredient that allowed these cells that had just learned how to produce O_2 to

survive, and eventually evolve more complex strategies of coping with, and ultimately exploiting the energy available in O_2.

Manganese and humans

The manganese chemistry unlocked by O_2 enabled a suite of novel processes that have proven valuable in the uses of manganese materials by humans. Humans have been present for only a tiny fraction (< 0.5 Ma) of the ~4 Ga history of life on this planet, but we are another species that left a disproportionate impact on the environment (116–118), like the Cyanobacteria that changed the atmosphere forever with the introduction of O_2—albeit in our case through societal and technological innovations rather than biochemical ones. As such, it seems appropriate to briefly discuss the role of manganese in human society in this history of manganese in the co-evolution of life and the environment.

Hominids have interacted with manganese for at least tens of millennia, as archaeological evidence for the use of manganese oxides has been found at numerous Middle Paleolithic sites. A common interpretation is that these materials were used as pigments, for both cave art and body decoration. However, the unique redox chemistry of high-valent manganese minerals may have provided another, more specific, use. Heyes *et al.* showed that manganese oxides can promote fire ignition under conditions where it otherwise would not ignite; gases derived from wood pyrolysis are oxidized by MnO_2, causing the reductive decomposition of the MnO_2, which releases O_2, lowering the ignition temperature of the wood. Taken together with archeological evidence of MnO_2 associated with fire pits, this data suggests that Neanderthals used MnO_2 to ease fire making, an innovation that may have been critical during the glacial periods of the Paleolithic (119).

Today, human activities contribute substantially to the redistribution of manganese in the environment, with 50,000,000 metric tons of manganese ore produced every year (120), and anthropogenic emissions accounting for a significant flux of manganese to natural waters and the atmosphere (121, 122). The biggest industrial use of manganese is in steel production (44). Manganese is requisite in modern steel making, both as a refining additive and also as an essential alloy. It lends unique

properties to the steel, such as a considerable increase in tensile strength. There is no known satisfactory substitute for manganese in metallurgy, and as such it is considered a critical mineral commodity (123). Beyond steel, manganese is used in a staggeringly diverse array of other applications (124, 125). It is used as a pigment in glass, ceramics and paints. It is used as an oxidizing agent in the chemical synthesis of a wide range of products, from dyes and fragrances to yellow-cake uranium. It is used as a scavenger in water treatment, and as an octane booster/anti-knock agent in unleaded gasoline. Manganese was used as an electron acceptor in the earliest Leclanché type primary cell batteries, and continues to be used to this day in zinc/manganese primary and secondary cell batteries (126). Thus, this strange and wonderful element[*] has been repurposed by the biosphere once again—this time via the evolution of human creativity.

Conclusion

In the ancient, anaerobic world, manganese redox chemistry was not accessible until after the evolution of a phototrophic reaction center with a high enough reduction potential to oxidize manganese—this was the direct ancestor to PSII. Unlocking manganese redox chemistry shattered the previous ceiling of redox space available to biology and was a crucial evolutionary bridge that led to the origin of oxygenic photosynthesis and the rise of environmental O_2 (Figure 4). The fact that the production of O_2 evolved in organisms with a keen interest in manganese meant that the first organisms to encounter significant fluxes of O_2 had a built-in fortuitous antioxidant system, thanks to the ability of manganese complexes to catalytically quench dangerous reactive oxygen species like superoxide and hydrogen peroxide (Figure 4*F*). The antioxidant properties of Mn^{2+} along with its high concentrations in ancient oceans may have been the key to life surviving and ultimately thriving in an aerobic world.

As life discovered O_2 through manganese—and manganese continues to be the requisite catalyst for O_2 production—by reciprocity O_2 opened a doorway into a world of rich redox chemistry, enabling a

[*] The etymology of manganese comes from the Greek root *mangania*, or magic (127)

diverse suite of processes that use high-valent manganese. O_2 provided chemical species with even higher reduction potentials than manganese, further raising the ceiling of redox space available to biology and enabling energetically-favorable manganese oxidation without the input of light energy. Manganese redox chemistry was harnessed by enzymes with a wide range of functions (Table 2); some of these allow cells to cope with reactive oxygen species (e.g. catalase), while others enable important ecological processes like lignin degradation (Mn peroxidase). All manganese redox-active proteins interact with O_2 or species derived thereby, and appear to have only evolved in the wake of the rise of O_2. With its redox cycle, manganese would come to play an essential role in the function of biogeochemical cycles and participate in numerous redox and sorption processes affecting the availability and distribution of other key elements. Diverse components of the modern biosphere, from niche microbes to human industry, still exploit these relationships between O_2 and the biogeochemical dynamics of manganese.

Acknowledgements
We wish to acknowledge that in a number of ways this work has its origins at a small four day meeting on dioxygen held in Santa Fe in 2005, sponsored and organized by John Abelson and Mel Simon and the Agouron Institute. The participants were a broad mix of chemists and biochemists, molecular biologists, and Earth scientists, but this meeting was so valuable because it initiated meaningful cross-talk between the different disciplines studying how life came to first produce and then cope with dioxygen (WWF as a young graduate student, JSV as a chemist studying superoxide). We would also like to thank Jaeheung Cho and Kevin Barnese for valuable feedback on this manuscript. Support for this work was provided by the Simons Collaboration on the Origins of Life (WWF), the David and Lucile Packard Foundation (WWF), NASA Exobiology award "Discovering biosignatures in manganese deposits on Mars with rover payload instruments" (WWF), NSF IOS proposal # 1833247 (WWF), NSF Graduate Research Fellowship (UFL).

Author contributions
All authors contributed to idea development. UFL wrote the manuscript with input from JSV and WWF.

References

1. A. H. Knoll, The geological consequences of evolution. *Geobiology* **1**, 3–14 (2003).

2. W. W. Fischer, J. Hemp, J. E. Johnson, Evolution of Oxygenic Photosynthesis. *Annu. Rev. Earth Planet. Sci.* **44**, 647–683 (2016).

3. L. M. Ward, B. Rasmussen, W. W. Fischer, Primary Productivity was Limited by Electron Donors Prior to the Advent of Oxygenic Photosynthesis. *J. Geophys. Res. Biogeosciences*, in press. (2018).

4. W. W. Fischer, J. Hemp, J. S. Valentine, How did life survive Earth's great oxygenation? *Curr. Opin. Chem. Biol.* **31**, 166–178 (2016).

5. J. Raymond, D. Segrè, The effect of oxygen on biochemical networks and the evolution of complex life. *Science* **311**, 1764–1767 (2006).

6. J. A. Imlay, The molecular mechanisms and physiological consequences of oxidative stress: lessons from a model bacterium. *Nat. Rev. Microbiol.* **11**, 443–454 (2013).

7. W. W. Fischer, J. Hemp, J. E. Johnson, Manganese and the Evolution of Photosynthesis. *Orig. Life Evol. Biosphere J. Int. Soc. Study Orig. Life* **45**, 351–357 (2015).

8. J. P. McEvoy, G. W. Brudvig, Water-splitting chemistry of photosystem II. *Chem. Rev.* **106**, 4455–4483 (2006).

9. Y. Umena, K. Kawakami, J.-R. Shen, N. Kamiya, Crystal structure of oxygen-evolving photosystem II at a resolution of 1.9 \AA. *Nature* **473**, 55–60 (2011).

10. J. E. Johnson, *et al.*, Manganese-oxidizing photosynthesis before the rise of cyanobacteria. *Proc. Natl. Acad. Sci. U. S. A.* **110**, 11238–11243 (2013).

11. W. W. Fischer, J. Hemp, J. E. Johnson, Manganese and the Evolution of Photosynthesis. *Orig. Life Evol. Biosphere J. Int. Soc. Study Orig. Life* **45**, 351–357 (2015).

12. J. Hemp, *et al.*, Genomics of a phototrophic nitrite oxidizer: insights into the evolution of photosynthesis and nitrification. *ISME J.* (2016) https:/doi.org/10.1038/ismej.2016.56.

13. W. W. Fischer, J. Hemp, J. E. Johnson, Evolution of Oxygenic Photosynthesis. *Annu. Rev. Earth Planet. Sci.* **44**, 647–683 (2016).

14. V. C. Culotta, M. J. Daly, Manganese Complexes: Diverse Metabolic Routes to Oxidative Stress Resistance in Prokaryotes and Yeast. *Antioxid. Redox Signal.* **19**, 933–944 (2013).

15. A. Sharma, *et al.*, Across the tree of life, radiation resistance is governed by antioxidant Mn^{2+}, gauged by paramagnetic resonance. *Proc. Natl. Acad. Sci.* **114**, E9253–E9260 (2017).

16. K. Barnese, E. B. Gralla, J. S. Valentine, D. E. Cabelli, Biologically relevant mechanism for catalytic superoxide removal by simple manganese compounds. *Proc. Natl. Acad. Sci.* **109**, 6892–6897 (2012).

17. M. J. Daly, A new perspective on radiation resistance based on Deinococcus radiodurans. *Nat. Rev. Microbiol.* **7**, 237–245 (2009).

18. M. J. Daly, *et al.*, Small-Molecule Antioxidant Proteome-Shields in Deinococcus radiodurans. *PLoS ONE* **5**, e12570 (2010).

19. J. A. Imlay, R. Sethu, S. K. Rohaun, Evolutionary adaptations that enable enzymes to tolerate oxidative stress. *Free Radic. Biol. Med.* **140**, 4–13 (2019).

20. C. M. Hansel, “Manganese in Marine Microbiology” in *Advances in Microbial Physiology*, (Elsevier, 2017), pp. 37–83.

21. L. A. Johnson, L. A. Hug, Distribution of reactive oxygen species defense mechanisms across domain bacteria. *Free Radic. Biol. Med.* **140**, 93–102 (2019).

22. L. M. Ward, P. M. Shih, The evolution and productivity of carbon fixation pathways in response to changes in oxygen concentration over geological time. *Free Radic. Biol. Med.* **140**, 188–199 (2019).

23. A. K. Garcia, B. Kaçar, How to resurrect ancestral proteins as proxies for ancient biogeochemistry. *Free Radic. Biol. Med.* **140**, 260–269 (2019).

24. S. Louca, *et al.*, Bacterial diversification through geological time. *Nat. Ecol. Evol.* **2**, 1458–1467 (2018).

25. F. A. Armstrong, Why did Nature choose manganese to make oxygen? *Philos. Trans. R. Soc. Lond. B. Biol. Sci.* **363**, 1263-70-discussion 1270 (2008).

26. J. J. Morgan, Manganese in natural waters and earth’s crust: its availability to organisms. *Met. Ions Biol. Syst.* **37**, 1–34 (2000).

27. R. D. Britt, D. L. M. Suess, T. A. Stich, An Mn(V)–oxo role in splitting water? *Proc. Natl. Acad. Sci.* **112**, 5265–5266 (2015).

28. R. L. Rudnick, S. Gao, “Composition of the Continental Crust” in *Treatise on Geochemistry*, (Elsevier, 2003), pp. 1–64.

29. K. K. Turekian, K. H. Wedepohl, Distribution of the Elements in Some Major Units of the Earth’s Crust. *Geol. Soc. Am. Bull.* **72**, 175 (1961).

30. B. Cairncross, N. J. Beukes, *The Kalahari manganese field: the adventure continues* (Random House Struik, 2013).

31. D. E. Canfield, *Aquatic geomicrobiology* (Elsevier, 2005).

32. J. R. R. F. da Silva, R. J. P. Williams, *The biological chemistry of the elements: the inorganic chemistry of life* (Clarendon Press ; Oxford University Press, 1991).

33. P. F. Lang, B. C. Smith, Ionization Energies of Atoms and Atomic Ions. *J. Chem. Educ.* **80**, 938 (2003).

34. J. K. Klewicki, J. J. Morgan, Kinetic Behavior of Mn(III) Complexes of Pyrophosphate, EDTA, and Citrate. *Environ. Sci. Technol.* **32**, 2916–2922 (1998).

35. R. B. Stockbridge, R. Wolfenden, Enhancement of the Rate of Pyrophosphate Hydrolysis by Nonenzymatic Catalysts and by Inorganic Pyrophosphatase. *J. Biol. Chem.* **286**, 18538–18546 (2011).

36. O. W. Duckworth, G. Sposito, Siderophore−Manganese(III) Interactions II. Manganite Dissolution Promoted by Desferrioxamine B. *Environ. Sci. Technol.* **39**, 6045–6051 (2005).

37. M. Keiluweit, *et al.*, Long-term litter decomposition controlled by manganese redox cycling. *Proc. Natl. Acad. Sci.* **112**, E5253–E5260 (2015).

38. A. S. Madison, B. M. Tebo, A. Mucci, B. Sundby, G. W. Luther, Abundant Porewater Mn(III) Is a Major Component of the Sedimentary Redox System. *Science* **341**, 875–878 (2013).

39. R. E. Trouwborst, Soluble Mn(III) in Suboxic Zones. *Science* **313**, 1955–1957 (2006).

40. V. E. Oldham, A. Mucci, B. M. Tebo, G. W. Luther, Soluble Mn(III)–L complexes are abundant in oxygenated waters and stabilized by humic ligands. *Geochim. Cosmochim. Acta* **199**, 238–246 (2017).

41. V. E. Oldham, M. R. Jones, B. M. Tebo, G. W. Luther, Oxidative and reductive processes contributing to manganese cycling at oxic-anoxic interfaces. *Mar. Chem.* **195**, 122–128 (2017).

42. S. A. Sañudo-Wilhelmy, I. Rivera-Duarte, A. R. Flegal, Distribution of colloidal trace metals in the San Francisco Bay estuary. *Geochim. Cosmochim. Acta* **60**, 4933–4944 (1996).

43. M. Baalousha, *et al.*, Suspended particulate matter determines physical speciation of Fe, Mn, and trace metals in surface waters of Loire watershed. *Environ. Sci. Pollut. Res.* (2018) https:/doi.org/10.1007/s11356-018-1416-5 (November 27, 2018).

44. J. E. Post, Manganese oxide minerals: Crystal structures and economic and environmental significance. *Proc. Natl. Acad. Sci.* **96**, 3447–3454 (1999).

45. C. E. Levar, C. L. Hoffman, A. J. Dunshee, B. M. Toner, D. R. Bond, Redox potential as a master variable controlling pathways of metal reduction by Geobacter sulfurreducens. *ISME J.* **11**, 741–752 (2017).

46. J. J. Morgan, Kinetics of reaction between O2 and Mn(II) species in aqueous solutions. *Geochim. Cosmochim. Acta* **69**, 35–48 (2005).

47. S. H. R. Davies, J. J. Morgan, Manganese(II) oxidation kinetics on metal oxide surfaces. *J. Colloid Interface Sci.* **129**, 63–77 (1989).

48. W. Sung, J. J. Morgan, Oxidative removal of Mn(II) from solution catalysed by the γ-FeOOH (lepidocrocite) surface. *Geochim. Cosmochim. Acta* **45**, 2377–2383 (1981).

49. D. E. Wilson, Surface and complexation effects on the rate of Mn(II) oxidation in natural waters. *Geochim. Cosmochim. Acta* **44**, 1311–1317 (1980).

50. M. F. Hochella, *et al.*, Nanominerals, Mineral Nanoparticles, and Earth Systems. *Science* **319**, 1631–1635 (2008).

51. K. Wuttig, M. I. Heller, P. L. Croot, Reactivity of Inorganic Mn and Mn Desferrioxamine B with O_2, O_2^-, and H_2O_2 in Seawater. *Environ. Sci. Technol.*, 130822151350003 (2013).

52. D. R. Learman, B. M. Voelker, A. I. Vazquez-Rodriguez, C. M. Hansel, Formation of manganese oxides by bacterially generated superoxide. *Nat. Geosci.* **4**, 95–98 (2011).

53. P. F. Andeer, D. R. Learman, M. McIlvin, J. A. Dunn, C. M. Hansel, Extracellular haem peroxidases mediate Mn(II) oxidation in a marine Roseobacter bacterium via superoxide production. *Environ. Microbiol.* **17**, 3925–3936 (2015).

54. E. R. Stadtman, B. S. Berlett, P. B. Chock, Manganese-dependent disproportionation of hydrogen peroxide in bicarbonate buffer. *Proc. Natl. Acad. Sci. U. S. A.* **87**, 384–388 (1990).

55. K. Barnese, E. B. Gralla, D. E. Cabelli, J. Selverstone Valentine, Manganous Phosphate Acts as a Superoxide Dismutase. *J. Am. Chem. Soc.* **130**, 4604–4606 (2008).

56. B. M. Tebo, H. A. Johnson, J. K. McCarthy, A. S. Templeton, Geomicrobiology of manganese(II) oxidation. *Trends Microbiol.* **13**, 421–428 (2005).

57. B. M. Tebo, *et al.*, Biogenic Manganese Oxides: Properties and Mechanisms of Formation. *Annu. Rev. Earth Planet. Sci.* **32**, 287–328 (2004).

58. C. N. Butterfield, A. V. Soldatova, S.-W. Lee, T. G. Spiro, B. M. Tebo, Mn(II,III) oxidation and MnO2 mineralization by an expressed bacterial multicopper oxidase. *Proc. Natl. Acad. Sci.* **110**, 11731–11735 (2013).

59. L. Tao, *et al.*, Mn(II) Binding and Subsequent Oxidation by the Multicopper Oxidase MnxG Investigated by Electron Paramagnetic Resonance Spectroscopy. *J. Am. Chem. Soc.*, 150813153632003 (2015).

60. A. V. Soldatova, *et al.*, Mn(II) oxidation by the multicopper oxidase complex Mnx: A coordinated two-stage Mn(II)/(III) and Mn(III)/(IV) mechanism. *J. Am. Chem. Soc.* (2017) https:/doi.org/10.1021/jacs.7b02772.

61. A. V. Soldatova, *et al.*, Mn(II) oxidation by the multicopper oxidase complex Mnx: A binuclear activation mechanism. *J. Am. Chem. Soc.* (2017) https:/doi.org/10.1021/jacs.7b02771.

62. G. J. Brouwers, *et al.*, cumA, a gene encoding a multicopper oxidase, is involved in Mn2+ oxidation in Pseudomonas putida GB-1. *Appl. Environ. Microbiol.* **65**, 1762–1768 (1999).

63. K. Geszvain, J. K. McCarthy, B. M. Tebo, Elimination of Manganese(II,III) Oxidation in Pseudomonas putida GB-1 by a Double Knockout of Two Putative Multicopper Oxidase Genes. *Appl. Environ. Microbiol.* **79**, 357–366 (2013).

64. P. L. A. M. Corstjens, J. P. M. de Vrind, T. Goosen, E. W. de V. Jong, Identification and molecular analysis of the *Leptothrix discophora* SS-1 *mofA* gene, a gene putatively encoding a manganese-oxidizing protein with copper domains. *Geomicrobiol. J.* **14**, 91–108 (1997).

65. G. J. Brouwers, P. L. A. M. Corstje, Stimulation of Mn^{2+} Oxidation in *Leptothrix discophora* SS-1 by Cu^{2+} and Sequence Analysis of the Region Flanking the Gene Encoding Putative Multicopper Oxidase MofA. *Geomicrobiol. J.* **17**, 25–33 (2000).

66. J. P. Ridge, *et al.*, A multicopper oxidase is essential for manganese oxidation and laccase-like activity in Pedomicrobium sp. ACM 3067. *Environ. Microbiol.* **9**, 944–953 (2007).

67. M. Zámocký, *et al.*, Independent evolution of four heme peroxidase superfamilies. *Arch. Biochem. Biophys.* **574**, 108–119 (2015).

68. K. Nakama, *et al.*, Heterologous Expression and Characterization of the Manganese-Oxidizing Protein from Erythrobacter sp. Strain SD21. *Appl. Environ. Microbiol.* **80**, 6837–6842 (2014).

69. C. R. Anderson, *et al.*, Mn(II) oxidation is catalyzed by heme peroxidases in "Aurantimonas manganoxydans" strain SI85-9A1 and Erythrobacter sp. strain SD-21. *Appl. Environ. Microbiol.* **75**, 4130–4138 (2009).

70. K. Geszvain, L. Smesrud, B. M. Tebo, Identification of a Third Mn(II) Oxidase Enzyme in Pseudomonas putida GB-1. *Appl. Environ. Microbiol.* **82**, 3774–3782 (2016).

71. S. M. Webb, G. J. Dick, J. R. Bargar, B. M. Tebo, Evidence for the presence of Mn(III) intermediates in the bacterial oxidation of Mn(II). *Proc. Natl. Acad. Sci. U. S. A.* **102**, 5558–5563 (2005).

72. H. A. Johnson, B. M. Tebo, In vitro studies indicate a quinone is involved in bacterial Mn(II) oxidation. *Arch. Microbiol.* **189**, 59–69 (2008).

73. C. M. Hansel, C. A. Zeiner, C. M. Santelli, S. M. Webb, Mn(II) oxidation by an ascomycete fungus is linked to superoxide production during asexual reproduction. *Proc. Natl. Acad. Sci. U. S. A.* **109**, 12621–12625 (2012).

74. M. Hofrichter, Review: lignin conversion by manganese peroxidase (MnP). *Enzyme Microb. Technol.* **30**, 454–466 (2002).

75. H. Bao, R. L. Burnap, Photoactivation: The Light-Driven Assembly of the Water Oxidation Complex of Photosystem II. *Front. Plant Sci.* **7** (2016).

76. D. R. Lovley, D. E. Holmes, K. P. Nevin, Dissimilatory Fe(III) and Mn(IV) reduction. *Adv. Microb. Physiol.* **49**, 219–286 (2004).

77. C. R. Myers, K. H. Nealson, Bacterial Manganese Reduction and Growth with Manganese Oxide as the Sole Electron Acceptor. *Science* **240**, 1319–1321 (1988).

78. D. R. Lovley, E. J. Phillips, Novel mode of microbial energy metabolism: organic carbon oxidation coupled to dissimilatory reduction of iron or manganese. *Appl. Environ. Microbiol.* **54**, 1472–1480 (1988).

79. J. A. Gralnick, D. K. Newman, Extracellular respiration. *Mol. Microbiol.* **65**, 1–11 (2007).

80. E. J. Beal, C. H. House, V. J. Orphan, Manganese- and iron-dependent marine methane oxidation. *Science* **325**, 184–187 (2009).

81. C. Andreini, I. Bertini, G. Cavallaro, G. L. Holliday, J. M. Thornton, Metal ions in biological catalysis: from enzyme databases to general principles. *JBIC J. Biol. Inorg. Chem.* **13**, 1205–1218 (2008).

82. P. Artimo, *et al.*, ExPASy: SIB bioinformatics resource portal. *Nucleic Acids Res.* **40**, W597–W603 (2012).

83. N. A. Law, M. T. Caudle, V. L. Pecoraro, "Manganese Redox Enzymes and Model Systems: Properties, Structures, and Reactivity" in *Advances in Inorganic Chemistry*, (Elsevier, 1998), pp. 305–440.

84. J. Yano, V. Yachandra, Mn4Ca cluster in photosynthesis: where and how water is oxidized to dioxygen. *Chem. Rev.* **114**, 4175–4205 (2014).

85. A. Sigel, H. Sigel, Eds., *Manganese and its role in biological processes* (Marcel Dekker, 2000).

86. J. D. Crowley, D. A. Traynor, D. C. Weatherburn, Enzymes and proteins containing manganese: an overview. *Met. Ions Biol. Syst.* **37**, 209–278 (2000).

87. N. Keren, M. J. Kidd, J. E. Penner-Hahn, H. B. Pakrasi, A light-dependent mechanism for massive accumulation of manganese in the photosynthetic bacterium Synechocystis sp. PCC 6803. *Biochemistry* **41**, 15085–15092 (2002).

88. C. Ostermeier, A. Harrenga, U. Ermler, H. Michel, Structure at 2.7 A resolution of the Paracoccus denitrificans two-subunit cytochrome c oxidase complexed with an antibody FV fragment. *Proc. Natl. Acad. Sci.* **94**, 10547–10553 (1997).

89. L. Florens, B. Schmidt, J. McCracken, S. Ferguson-Miller, Fast Deuterium Access to the Buried Magnesium/Manganese Site in Cytochrome *c* Oxidase †. *Biochemistry* **40**, 7491–7497 (2001).

90. A. J. Bloom, K. M. Lancaster, Manganese binding to Rubisco could drive a photorespiratory pathway that increases the energy efficiency of photosynthesis. *Nat. Plants* **4**, 414–422 (2018).

91. J. E. Johnson, A. Gerpheide, M. P. Lamb, W. W. Fischer, O_2 constraints from Paleoproterozoic detrital pyrite and uraninite. *Geol. Soc. Am. Bull.* **126**, 813–830 (2014).

92. null Farquhar, null Bao, null Thiemens, Atmospheric influence of Earth's earliest sulfur cycle. *Science* **289**, 756–759 (2000).

93. G. Paris, J. F. Adkins, A. L. Sessions, S. M. Webb, W. W. Fischer, Neoarchean carbonate-associated sulfate records positive $\Delta^{33}S$ anomalies. *Science* **346**, 739–741 (2014).

94. M. A. Torres, G. Paris, J. F. Adkins, W. W. Fischer, Riverine evidence for isotopic mass balance in the Earth's early sulfur cycle. *Nat. Geosci.* **11**, 661–664 (2018).

95. J. E. Johnson, S. M. Webb, C. Ma, W. W. Fischer, Manganese mineralogy and diagenesis in the sedimentary rock record. *Geochim. Cosmochim. Acta* **173**, 210–231 (2016).

96. W. W. Fischer, J. Hemp, J. S. Valentine, How did life survive Earth's great oxygenation? *Curr. Opin. Chem. Biol.* **31**, 166–178 (2016).

97. G. Shields, J. Veizer, Precambrian marine carbonate isotope database: Version 1.1: Carbonate isotope database. *Geochem. Geophys. Geosystems* **3**, 1 of 12–12 12 (2002).

98. N. J. Beukes, Facies relations, depositional environments and diagenesis in a major early Proterozoic stromatolitic carbonate platform to basinal sequence, Campbellrand Subgroup, Transvaal Supergroup, Southern Africa. *Sediment. Geol.* (1987).

99. J. Veizer, J. Hoefs, D. R. Lowe, P. C. Thurston, Geochemistry of Precambrian carbonates: II. Archean greenstone belts and Archean sea water. *Geochim. Cosmochim. Acta* **53**, 859–871 (1989).

100. D. Y. Sumner, Carbonate precipitation and oxygen stratification in late Archean seawater as deduced from facies and stratigraphy of the Gamohaan and Frisco formations, Transvaal Supergroup, South Africa. *Am. J. Sci.* **297**, 455–487 (1997).

101. D. Y. Sumner, J. P. Grotzinger, Implications for Neoarchaean ocean chemistry from primary carbonate mineralogy of the Campbellrand-Malmani Platform, South Africa - Sumner - 2004 - Sedimentology - Wiley Online Library. *Sedimentology* (2004).

102. K. C. Lohmann, J. C. G. Walker, The δ^{18} O record of phanerozoic abiotic marine calcite cements. *Geophys. Res. Lett.* **16**, 319–322 (1989).

103. A. Mucci, Manganese uptake during calcite precipitation from seawater: Conditions leading to the formation of a pseudokutnahorite. *Geochim. Cosmochim. Acta* **52**, 1859–1868 (1988).

104. S. E. Calvert, T. F. Pedersen, Sedimentary geochemistry of manganese; implications for the environment of formation of manganiferous black shales. *Econ. Geol.* **91**, 36–47 (1996).

105. J. E. Johnson, *et al.*, Real-Time Manganese Phase Dynamics during Biological and Abiotic Manganese Oxide Reduction. *Environ. Sci. Technol.* **50**, 4248–4258 (2016).

106. S. Schröder, D. Bedorf, N. J. Beukes, J. Gutzmer, From BIF to red beds: Sedimentology and sequence stratigraphy of the Paleoproterozoic Koegas Subgroup (South Africa). *Sediment. Geol.* (2011).

107. K. H. Williford, M. J. Van Kranendonk, T. Ushikubo, R. Kozdon, J. W. Valley, Constraining atmospheric oxygen and seawater sulfate concentrations during Paleoproterozoic glaciation: In situ sulfur three-isotope microanalysis of pyrite from the Turee Creek Group, Western Australia. *Geochim. Cosmochim. Acta* **75**, 5686–5705 (2011).

108. Y. Sekine, E. Tajika, R. Tada, T. Hirai, K. T. Goto, Manganese enrichment in the Gowganda Formation of the Huronian Supergroup: A highly oxidizing shallow-marine environment after the last Huronian glaciation. *Earth Planet. Ldots* (2011).

109. M. M. Tice, D. R. Lowe, Photosynthetic microbial mats in the 3,416-Myr-old ocean. *Nature* **431**, 549–552 (2004).

110. G. S. Orf, C. Gisriel, K. E. Redding, Evolution of photosynthetic reaction centers: insights from the structure of the heliobacterial reaction center. *Photosynth. Res.* **138**, 11–37 (2018).

111. S. Sadekar, J. Raymond, R. E. Blankenship, Conservation of distantly related membrane proteins: photosynthetic reaction centers share a common structural core. *Mol. Biol. Evol.* **23**, 2001–2007 (2006).

112. M. M. Tice, D. R. Lowe, Hydrogen-based carbon fixation in the earliest known photosynthetic organisms (2006).

113. W. W. Fischer, A. H. Knoll, An iron shuttle for deepwater silica in Late Archean and early Paleoproterozoic iron formation. *Geol. Soc. Am. Bull.* **121**, 222–235 (2009).

114. A. Kappler, C. Pasquero, K. O. Konhauser, D. K. Newman, Deposition of banded iron formations by anoxygenic phototrophic Fe(II)-oxidizing bacteria. *Geology* **33**, 865 (2005).

115. R. M. Soo, J. Hemp, D. H. Parks, W. W. Fischer, P. Hugenholtz, On the origins of oxygenic photosynthesis and aerobic respiration in Cyanobacteria. *Science* **355**, 1436–1440 (2017).

116. S. L. Lewis, M. A. Maslin, Defining the Anthropocene. *Nature* **519**, 171 (2015).

117. P. J. Crutzen, Geology of mankind. *Nature* **415**, 23 (2002).

118. S. Govorushko, *Human Impact on the Environment* (Springer International Publishing, 2016) https:/doi.org/10.1007/978-3-319-24957-5 (November 26, 2018).

119. P. J. Heyes, *et al.*, Selection and Use of Manganese Dioxide by Neanderthals. *Sci. Rep.* **6** (2016).

120. L. A. Corathers, Manganese. *USGS 2014 Miner. Yearb.* (2017).

121. H. Rollin, "Manganese: Environmental Pollution and Health Effects" in *Encycolpedia of Environmental Health*, (Burlington, Elsevier), pp. 617–629.

122. P. D. Howe, H. M. Malcolm, S. Dobson, *Manganese and its compounds: environmental aspects* (World Health Organization, 2004).

123. L. A. Corathers, Manganese. *USGS Miner. Commod. Summ.*, 104–105 (2018).

124. J. E. Spencer, The Artillery Manganese District in West-Central Arizona. *Ariz. Geol.* **21**, 9–12 (1991).

125. S. A. Weiss, *Manganese: The other uses* (Metal Bulletin Books Ltd, 1977).

126. R. Dell, Batteries fifty years of materials development. *Solid State Ion.* **134**, 139–158 (2000).

127. G. Cotzias, Manganese in health and disease. *Physiol. Rev.* **38**, 503–532 (1985).

128. A. A. Frost, Oxidation Potential-Free Energy Diagrams. *J. Am. Chem. Soc.* **73**, 2680–2682 (1951).

129. W. M. Latimer, *The Oxidation States of the Elements and their Potentials in Aqueous Solutions* (Prentice-Hall, Inc., New York., 1952).

130. J. D. Hem, Chemical Equilibria and Rates of Manganese Oxidation. *Geol. Surv. Water-Supply Pap. 1667-A* (1963).

131. K. S. Yamaguchi, D. T. Sawyer, The Redox Chemistry of Manganese(III) and -(IV) Complexes. *Isr. J. Chem.* **25**, 164–176 (1985).

132. W. W. Fischer, *et al.*, SQUID-SIMS is a useful approach to uncover primary signals in the Archean sulfur cycle. *Proc Natl Acad Sci USA* **111**, 5468–5473 (2014).

133. Dawn Y. Sumner, John P. Grotzinger, Herringbone Calcite: Petrography and Environmental Significance. *SEPM J. Sediment. Res.* **Vol. 66** (1996).

134. R. B. King, R. H. Crabtree, C. M. Lukehart, D. A. Atwood, R. A. Scott, Eds., "Electrode Potentials" in *Encyclopedia of Inorganic Chemistry*, (John Wiley & Sons, Ltd, 2006) https:/doi.org/10.1002/0470862106.id264 (August 23, 2018).

135. D. C. Harris, *Quantitative chemical analysis*, 7th ed, 3rd printing (W. H. Freeman, 2007).

136. M. T. Madigan, T. D. Brock, Eds., *Brock biology of microorganisms*, 12. ed., internat. ed (Pearson/Benjamin Cummings, 2009).

137. L. J. Bird, V. Bonnefoy, D. K. Newman, Bioenergetic challenges of microbial iron metabolisms. *Trends Microbiol.* **19**, 330–340 (2011).

138. J. A. Hayden, E. R. Farquhar, L. Que, J. D. Lipscomb, M. P. Hendrich, NO binding to Mn-substituted homoprotocatechuate 2,3-dioxygenase: relationship to O2 reactivity. *JBIC J. Biol. Inorg. Chem.* **18**, 717–728 (2013).

139. J. P. Emerson, E. G. Kovaleva, E. R. Farquhar, J. D. Lipscomb, L. Que, Swapping metals in Fe- and Mn-dependent dioxygenases: Evidence for oxygen activation without a change in metal redox state. *Proc. Natl. Acad. Sci.* **105**, 7347–7352 (2008).

140. J. A. Cotruvo, J. Stubbe, Class I Ribonucleotide Reductases: Metallocofactor Assembly and Repair In Vitro and In Vivo. *Annu. Rev. Biochem.* **80**, 733–767 (2011).

Figures

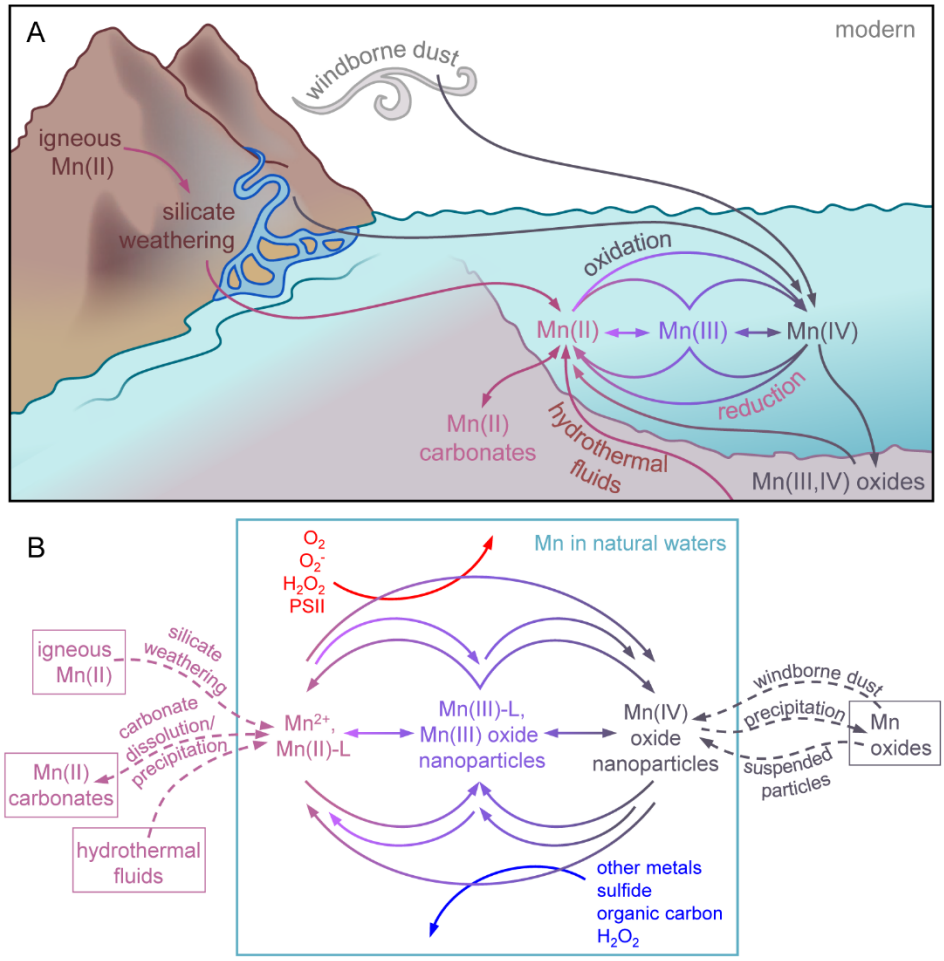

Figure 1. Manganese cycling in modern environments. Geological sources of manganese include manganese as a minor constituent of igneous rocks, and sedimentary deposits of Mn(II) in carbonates and Mn(III)/(IV) in oxides. These geological sources are liberated by processes of weathering and erosion, including by rivers and wind. In natural waters, manganese cycles between the Mn(II), Mn(III), and Mn(IV) oxidation states—biology plays a range of important roles in this cycling.

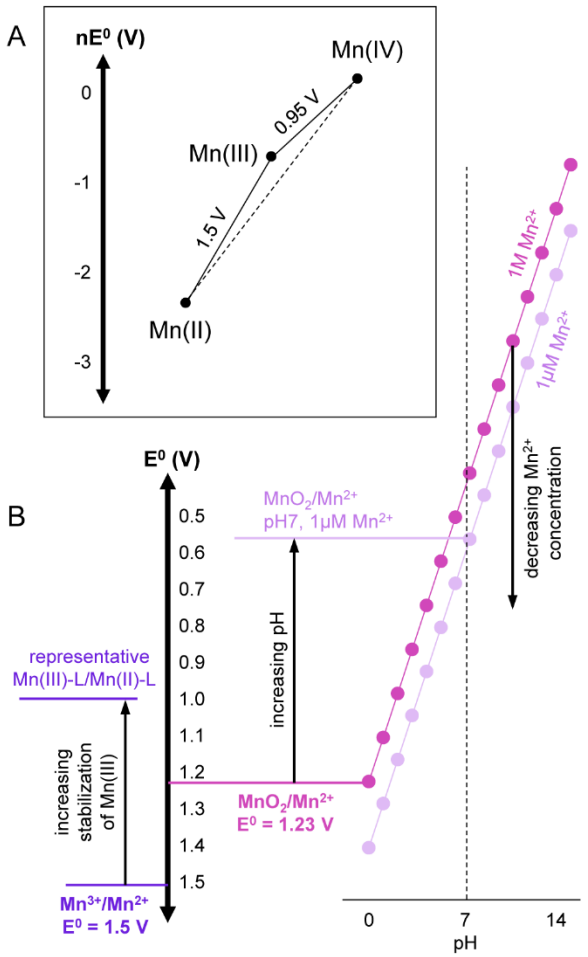

Figure 2. The breadth of manganese redox chemistry. ***A.*** Frost diagram of manganese in acidic solution (128). The slope of the line connecting two points represents the reduction potential for that redox couple. A state that is offset from the line connecting the states above and below it, i.e., Mn(III), is unstable with respect to disproportionation. ***B.*** Redox tower showing reduction potentials for different manganese species. The standard electrode potentials (E^0) vs. SHE for the Mn(III)/Mn(II) and Mn(IV)/Mn(II) couples are very high (129–131). However, pH, concentration, and coordination environment can affect the reduction potentials considerably, and therefore these are critical factors in determining the energetics of manganese redox transformations in the environment. For instance, the MnO_2/Mn^{2+} redox couple decreases by 0.82 V when adjusted to pH 7 and increases by 0.18 V when adjusted to 1 µM Mn^{2+}. E^0 was converted to redox potentials under environmentally relevant conditions using the Nernst equation:

$$Eh = E^0 + \frac{RT}{nf}\ln Q = E^0 + \frac{0.059}{n}\log_{10} Q$$

For a reaction $xA_{ox} + yH^+ \leftrightarrow zA_{red} + H_2O$; $Q = \frac{[A_{ox}]^x[H^+]^y}{[A_{red}]^z}$

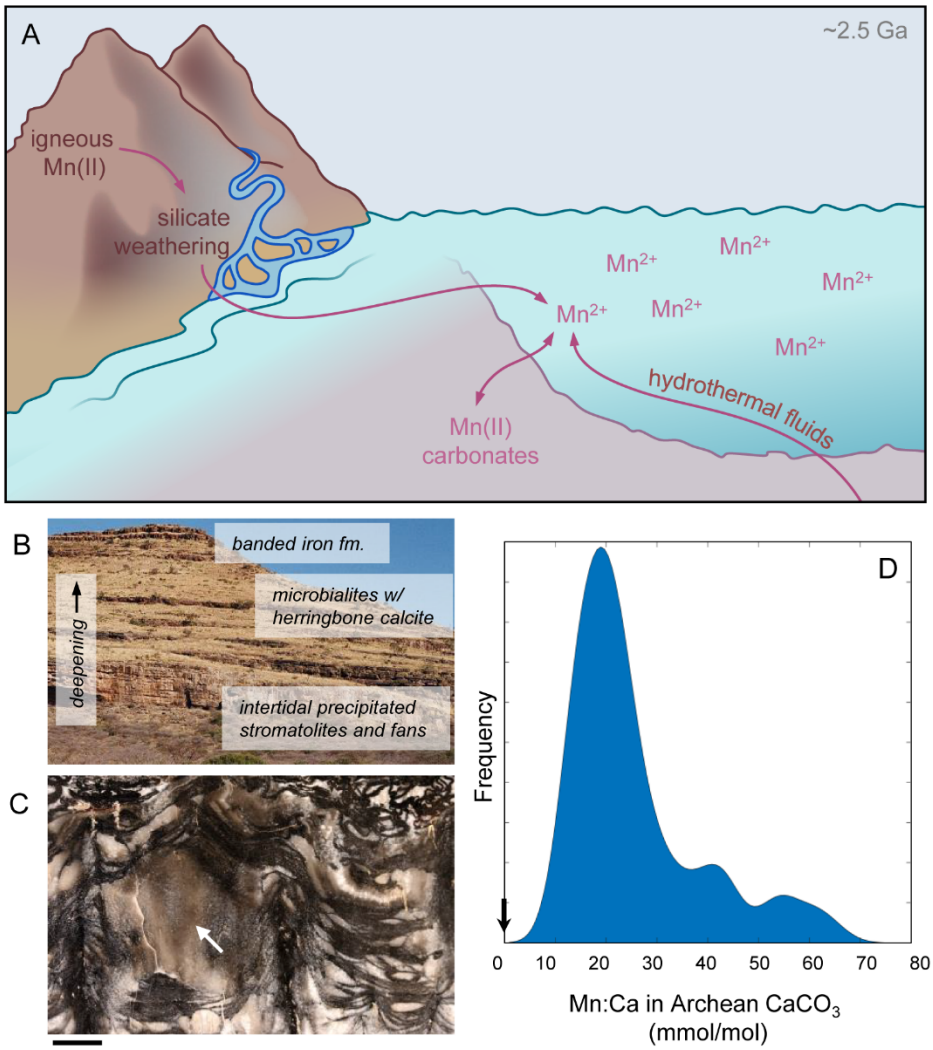

Figure 3: A simple manganese cycle on the early Earth—prior to the rise of O_2. ***A.*** Manganese is present in the crust exclusively as Mn(II) where it substitutes for Fe(II) in a range of igneous minerals. Both low temperature and high temperature (hydrothermal) silicate weathering sources dissolved Mn^{2+} to surface waters where it ultimately accumulates to substantial levels in the oceans, with the only meaningful sink as a minor constituent of marine calcium carbonate salts. ***B.*** Geological strata of a 2.5 Ga carbonate platform, deposited at a time prior to the appearance of any dioxygen in the atmosphere or oceans (96, 113, 132). These strata contain abundant marine calcite ($CaCO_3$) cements—including a specific texture termed 'herringbone calcite' that precipitated from subtidal seawater (133). ***C.*** Close up view of herringbone calcite (white arrow) deposited on ancient microbialites. These $CaCO_3$ cements contain substantial concentrations of Mn(II) (4). ***D.*** Kernel density estimate of 90 measurements of the Mn:Ca ratio in Archean carbonates show very high Mn(II) contents. These are many orders of magnitude higher than seen in carbonates after the rise of oxygen (typical modern value shown by the black arrow) and reflect very high concentrations of Mn^{2+} in seawater at this time—levels that would have naturally provided some oxidative stress resistance in marine environments (14, 16, 96).

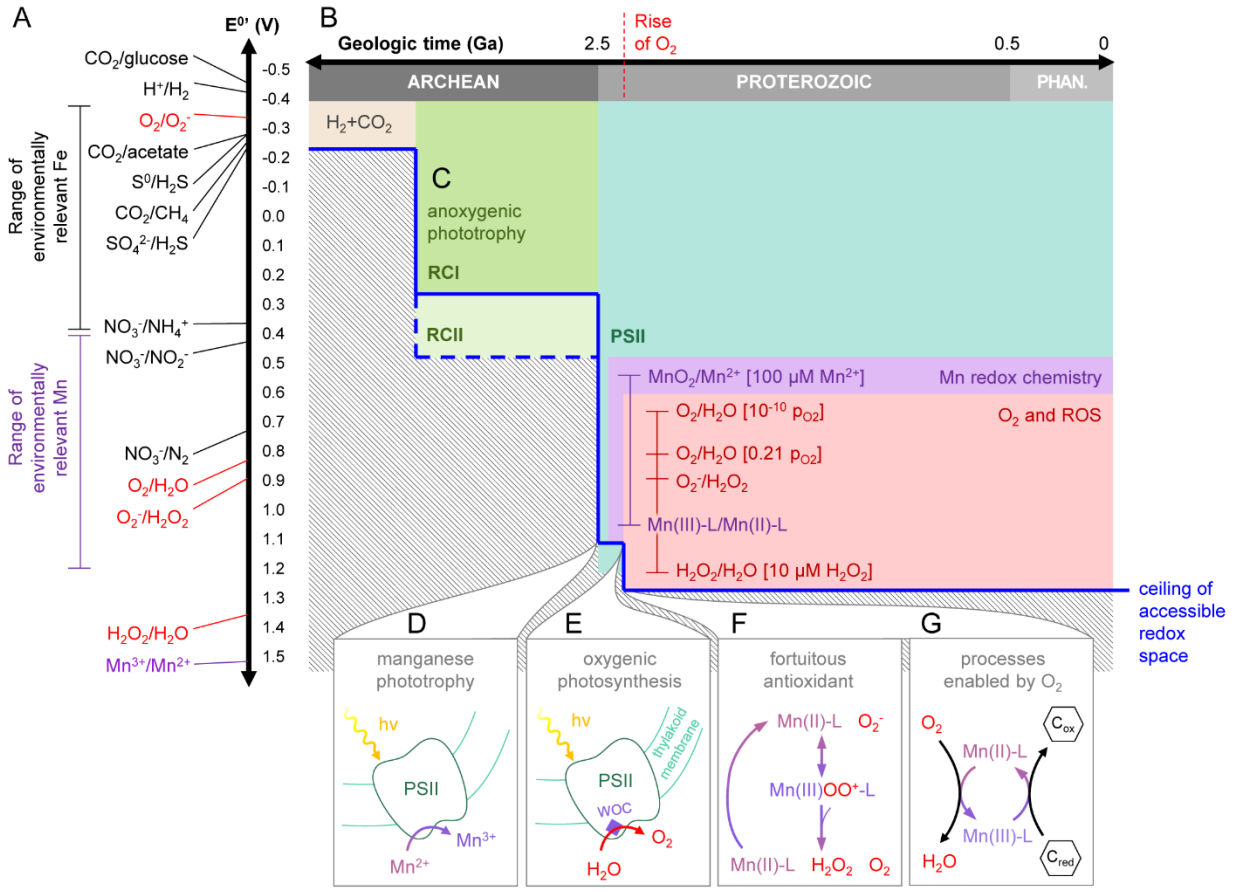

Figure 4. The breadth of redox chemistry exploited by the biosphere through time ***A.*** Redox tower showing midpoint reduction potentials at pH 7 ($E^{0'}$) for a selection of biologically and geochemically relevant species (26, 129–131, 134–137). Manganese redox couples occupy a range of redox space that is typically higher on the tower than most other environmentally and biologically relevant species—a range that overlaps with O_2 and other reactive oxygen species. ***B.*** Geologic timeline, illustrating how manganese expanded the high-potential limit of accessible redox chemistry. The earliest redox chemistry exploited by life depended on pre-existing thermodynamic disequilibria in the environment, allowing microbial metabolisms like H_2-CO_2 methanogenesis and acetogenesis (3). ***C.*** Phototrophy, the ability to capture and transduce the energy in visible light to create strong biochemical oxidants and reductants, enabled redox chemistry that was previously inaccessible; anoxygenic phototrophy was one of the most important early developments in high-potential metabolism (e.g., energy conservation around complex III). ***D.*** The evolution of a version of phototrophy with a high enough potential to oxidize Mn(II) introduced a source of high-valent manganese to the environment, and provided a stepping stone for the evolution of oxygenic photosynthesis (10, 11). ***E.*** The evolution of the WOC endowed the biosphere with the ability for photosynthetic water-splitting, and the rise of O_2 ensued. ***F.*** The introduction of O_2 and ROS further raised the ceiling of accessible redox space, defining the redox landscape in aerobic cells and environments today. Today the antioxidant properties of manganese are a critical feature of cellular protections against oxidative stress; the high Mn(II) concentrations in early environments and within cells would have been available as fortuitous (non-enzymatic) antioxidant systems that allowed life to cope and thrive with the rise of O_2. ***G.*** In the modern, aerobic world, manganese redox chemistry is involved in numerous biogeochemical processes. Enzymes with diverse functions incorporate redox-active

manganese cofactors, and manganese redox cycling plays a key role in ecological processes, such as the oxidative degradation of recalcitrant organic matter.

Tables

	Mn(II)	Mn(III)	Mn(IV)
Aqueous species	$Mn^{2+}(H_2O)_6$ $Mn^{2+}(OH)^{+}$ Mn(II)-L[a]	Mn(III)-L[a] Mn(III) oxide nanoparticles	Mn(IV) oxide nanoparticles
Mineral species	Mn^{2+} as a trace constituent in igneous minerals kutnohorite/ manganoan calcite $(Mn^{2+},Ca^{2+})CO_3$ rhodochrosite $Mn^{2+}CO_3$ rhodonite $Mn^{2+}SiO_3$	bixbyite $(Mn^{3+},Fe^{3+})_2O_3$ braunite $Mn^{2+}Mn^{3+}_6(SiO_4)O_8$ hausmanite $Mn^{2+}Mn^{3+}_2O_4$	Mn(IV) oxide $Mn^{4+}O_2$ Common polymorphs include pyrolusite, todorokite, hollandite, cryptomelane and birnessite [b]

[a] Known ligands that form aqueous manganese complexes include pyrophosphate, (bi)carbonate, citrate, tartrate, and humic acids. In general, the diversity and distribution of Mn-L species in the environment remains poorly constrained.
[b] Can include some Mn(III).

Table 1. Major manganese species and minerals found in the environment.

Enzyme	No. of Mn	Redox active Mn	Mn valence	EC no.	Enzyme class/function	Overall reaction	Distribution
PSII	4	Y	II/III/IV/ (V)	1.10.3.9	Oxidoreductase; Catalyzes oxidation of water to release dioxygen	$2\ H_2O + 2$ plastoquinone + 4 light $\rightarrow O_2 +$ 2 plastoquinol	Cyanobacteria, chloroplasts
Mn catalase	2	Y	II/III	1.11.1.6	Oxidoreductase; Catalyzes the disproportionation of hydrogen peroxide to water and dioxygen	$2H_2O_2 \rightarrow 2H_2O + O_2$	Bacteria
Mn Superoxide Dismutase (MnSOD)	1	Y	III	1.15.1.1	Oxidoreductase; Redox enzyme; acts on superoxide radical	$2O_2^- + 2H^+ \rightarrow H_2O_2 + O_2$	Mitochondria, chloroplasts, bacteria
Oxalate Oxidase	1	Y	II/III	1.2.3.4	Oxidoreductase; Aides in carbohydrate metabolism by catalyzing conversion of oxalate and dioxygen to hydrogen peroxide and carbon dioxide	$(COOH)_2 + O_2 \rightarrow H_2O_2 + 2CO_2$	Plants, bacteria
Oxalate Decarboxylase	1	Y	II/III	4.1.1.2	Lyase; Aides in carbohydrate metabolism by catalyzing cleavage of oxalate into formate and carbon dioxide	$(COOH)_2 + H^+ \rightarrow HCOO^- + CO_2$	Bacteria
Arginase	2	N	II	3.5.3.1	Hydrolase; Catalyzes the final step in the Urea Cycle	L-arginine + $H_2O \rightarrow$ L-ornithine + urea	Yeast, bacteria, mammals
Xylose Isomerase	1 or 2	N	II	5.3.1.5	Isomerase: Catalyzes the interconversion of aldose and ketose sugars with broad substrate specificity	D-xylopyranose $\rightarrow$ D-xylulose	Bacteria
Mn Dioxygenase	1 or 2	Y/N[a]	II/ possibly III(139)	1.13.11.39	Oxidoreductase; Catalyzes the degradation of catechol through incorporation of O_2	Biphenyl-2,3-diol + $O_2 \rightarrow$ 2-hydroxy-6-oxo-6-phenylhexa-2,4-dienoate	Bacteria
Type Ib Ribonucleotide reductase (RNR)	2	N[b]	III	1.17.4.1	Oxidoreductase; Catalyzes the reduction of ribonucleotide diphosphates to corresponding deoxyribonucleotides via reductive elimination of 2-hydroxyl	2'-deoxyribonucleoside diphosphate + thioredoxin disulfide + $H_2O \rightarrow$ ribonucleoside diphosphate + thioredoxin	Bacteria
Mn Peroxidase (MnP)[c]	-	Y	II/III	1.11.1.13	Peroxidase; Redox enzyme, degrades lignin	$2Mn^{2+} + 2H^+ + H_2O_2 \rightarrow 2Mn^{3+} + 2\ H_2O$	Fungi
Manganese - Oxidizing Multicopper Oxidase (MnxG)[c]	-	Y	II/III	1.16.3.3	Oxidoreductase; Oxidizes soluble Mn^{2+} to insoluble manganese oxides; typically located on the outer surface of the cell resulting in encrustation of the cells by the oxides.	$4\ Mn^{2+} + 2\ O_2 + 4\ H_2O \rightarrow 4\ MnO_2^+ + 8\ H^+$	Bacteria
Mn-Oxidizing Protein (MopA)[c]	-	Y	II/III	Unknown	Oxidoreductase; Extracellularly oxidizes soluble Mn^{2+} to Mn^{3+} via single electron transfer, which then accumulates as a soluble species (ligand unknown) or disproportionates to form Mn^{4+}	Exact reaction currently pathway unknown[d]	Bacteria

[a] Some studies have shown that extradiol dioxygenases that require Mn^{2+} or Fe^{2+} may not go through a redox change while undergoing oxygen activation (139)

[b] While the Mn in Type Ib RNR is not known to be redox active in the reduction of RNA to DNA, the biosynthesis of the protein does require oxidation of the $2Mn^{2+}$ into the final active cofactor MnIIIMnIII-tyrosyl radical. Two proposed protein assembly schemes for the active cofactor are: (1) $2Mn^{2+}$ + Tyrosine + $2H_2O_2 + e^- + H^+ \rightarrow$ MnIIIMnIII + Tyrosyl radical + $2H_2O$ / (2) $2Mn^{2+}$ + Tyrosine + $O_2^- + H^+ \rightarrow$ MnIIIMnIII + Tyrosyl radical (140)

[c] MnP, MnxG and MopA are proteins that perform manganese oxidation and do not require or use Mn as a cofactor in the enzyme.

[d] Based on sequence similarity the protein is known to fall in the peroxicin subfamily of the peroxidase cyclooxygenase superfamily (68). O_2 is required for the reaction to proceed and therefore is postulated to be the likely terminal electron acceptor to form Mn(III) as the product.

Table 2. Selection of known manganese-bearing metalloproteins, including redox-active and nonredox-active enzymes that require manganese for catalytic functioning, and also enzymes known to perform manganese oxidation but that do not use manganese as a cofactor. **No. of Mn** shows the number of manganese atoms required for protein function; **Redox-active Mn** defines whether or not the manganese cofactor (or substrate in the case of MnxG and MopA) undergoes a redox state change during the course of the reaction; **Mn valence** indicates the valence state manganese will exist or transition through during the reaction cycle; **EC no.** indicates the enzyme commission number. One can infer that the redox-active proteins that oxidize or reduce manganese either as innate metal center(s) or a substrate all evolved after the rise of O_2, and that manganese-bearing metalloproteins prior to the rise of oxygen were likely limited to performing simpler chemistry, e.g. laboring as hydrolases or isomerases.

CHAPTER III

Manganese cycling communities at the dawn of the Great Oxygenation Event

Usha F. Lingappa[1], Nic Beukes[2], Birger Rasmussen[3], Stefan Lalonde[4], Theodore M. Present[1], John S. Magyar[1], Chi Ma[1], Sam Webb[5], Roger Summons[6], Joan Selverstone Valentine[1,7] Woodward W. Fischer[1]

1. Div. of Geological & Planetary Sciences, California Institute of Technology, Pasadena, CA 91125, USA

2. Dept. of Geology, University of Johannesburg, Auckland Park 2006, South Africa

3. School of Earth Sciences, University of Western Australia, Perth, WA 6009, Australia

4. CNRS-UMR 6538 Laboratoire Géosciences Océan, European Institute for Marine Studies, 29280 Plouzané, France

5. Stanford Synchrotron Radiation Lightsource, Stanford University, Menlo Park, CA 94025, USA

6. Dept. of Earth, Atmospheric, & Planetary Sciences, Massachusetts Institute of Technology, Cambridge, MA 02139, USA

7. Dept. of Chemistry & Biochemistry, University of California Los Angeles, Los Angeles, CA 90095, USA

Abstract

The origin of oxygenic photosynthesis was a critical turning point in the evolution of life and dramatically altered Earth surface environments by introducing O_2. This metabolic innovation is hypothesized to have evolved from an anoxygenic version of photosynthesis based on manganese oxidation. Here we examined new drill cores through Paleoproterozoic sediments of the Transvaal Supergroup, South Africa, using detrital pyrite grains and manganese oxidation as two independent proxies for constraining the history of photosynthesis and accompanying onset of oxidative processes. We observed detrital pyrite grains in the Makganyene Formation, suggesting that if the Makganyene glaciation was triggered by O_2, this climatic consequence manifested extremely rapidly—before signatures of oxidative weathering were expressed in sediments. Systematic searches for such grains in the Duitschland Formation were unsuccessful, consistent with previous interpretations that deposition of the Duitschland Formation coincided with the Great Oxygenation Event. Examining the manganese record further refined this understanding—we observed no evidence of oxidative manganese deposition during a major weathering interval at the base of the Duitschland Formation; slightly higher up in the Duitschland Formation, we described a stromatolitic unit characterized by substantial oxidative manganese deposition. These stromatolites provide the first physical evidence of the hypothesized manganese oxidizing organisms responsible for evolving oxygenic photosynthesis. Taken together, this work sheds new light on the timing and tempo of how O_2 transformed the Earth and demonstrates the existence of manganese cycling communities during this pivotal transition.

Introduction

The rise of O_2—attributed to the evolution of oxygenic photosynthesis—was a singularly transformative turning point in Earth history that forever changed the face of the planet and with it the course of life's evolution (1). This marked transition is recorded in Paleoproterozoic sedimentary rocks by the Great Oxygenation Event (GOE), a shift expressed by numerous proxies demonstrating the oxidation of Earth surface environments and accompanying changes to biogeochemical cycles (2–19). Changes in

the sulfur and iron cycles are exhibited by the loss of mass independent fractionation of sulfur isotopes (S-MIF), the disappearance of detrital pyrite grains, the appearance of bedded sulfate deposits, and the retention of iron in paleosols. Each of these signals reflects a specific consequence of O_2-derived chemistry; therefore, their histories are closely tied to the history of O_2.

The manganese record tells a story concerning the evolution of oxygenic photosynthesis that is subtly distinct from the rise of O_2 itself (20). Manganese species have unusually high redox potentials and therefore require exceptionally high potential oxidants for their oxidation. Chemically, this is limited to O_2 and O_2-derived reactive oxygen species. However, a biological mode of manganese oxidation driven by light energy rather than a chemical oxidant—manganese oxidizing phototrophy (MOP)—is thought to have been the immediate evolutionary precursor to oxygenic photosynthesis. MOP prior to oxygenic photosynthesis explains evidence for oxidative manganese deposition in sediments that predate the GOE (21, 22).

Deciphering the events, timing, and environmental context leading up to the evolution of oxygenic photosynthesis and through the GOE remains an ongoing effort. The initial accumulation of O_2 in the atmosphere, climatic consequences such as global cooling due to the collapse of a methane greenhouse, and impacts on Earth surface processes such as weathering may each have manifested on different timescales. While S-MIF has been our premier record for pinpointing the GOE, each of the myriad other proxies that demonstrate Earth's oxygenation offers a different lens into the impacts of O_2 on the environment. Here we present data from the Transvaal Supergroup that augments the existing S-MIF record by providing new glimpses into the sedimentary archives of manganese biogeochemistry and the onset of oxidative weathering.

Geologic setting

The Transvaal Supergroup is a Neoarchean to Paleoproterozoic succession of sedimentary and volcanic rocks deposited on the Kaapvaal Craton (Fig. 1). It is preserved in two major subbasins in South Africa—the Griqualand West subbasin (GWS) to the southwest and the Transvaal subbasin (TS) to the

northeast. The base of this succession forms a mixed siliciclastic-carbonate ramp that grades upward into the extensive Campbellrand-Malmani carbonate platform, with margin to slope facies preserved in GWS and more proximal environments preserved in TS (23). A major marine transgression ~2.5 Ga triggered by platform subsidence resulted in platform drowning followed by the deposition of banded iron formation (BIF) (24). In GWS, the Koegas Subgroup records the onset of manganese oxidation prior to the GOE, interpreted as evidence for MOP before oxygenic photosynthesis (22). An erosional hiatus separates the Ghaap and Postmasburg Groups/Chuniespoort and Pretoria Groups in GWS/TS, respectively (25).

In GWS, the lower Postmasburg Group is characterized by glaciomarine deposits of the Makganyene Formation, which is conformably overlain by volcanics of the Ongeluk Formation dated to 2426 ± 3 Ma (26). Above the Ongleuk Formation sits BIF of the Hotazel Formation—which hosts the world's largest manganese deposits (27)—followed by the Mooidraai carbonate platform. Paleomagnetic data that the Makganyene glaciation reached low latitudes indicates a snowball Earth interval (28). This has been interpreted as a climatic consequence of atmospheric oxygenation, with the subsequent BIF and manganese deposits of the Hotazel Formation reflecting a post-melting bloom of biological productivity and O_2 production resulting in rapid oxidative deposition of iron and manganese (29, 30). That the Hotazel Formation postdates the rise of O_2 is undisputed; however, the relative timing of the GOE and deposition of the Makganyene and Ongeluk formations is less clear. Trace metal weathering signatures inherited from the upper continental crust have suggested that the Makganyene glaciation may in fact predate the GOE (31, 32).

In TS, the rise of O_2 is thought to have occurred during deposition of the Duitschland Formation, which hosts a wide variety of lithologies including glacial diamictites, conglomerates, coarsening upward cycles of shales to sandstones, and carbonates. A conglomerate member known as Bevetts, derived from karstic weathering of the underlying Malmani platform, sits at the base of the Duitschland Formation (33). An unconformity defines the mid-Duitschland sequence boundary, across which the loss of S-MIF indicates the GOE (4, 5, 34). The Duitschland Formation is overlain by the Timeball Hill Formation. In

the Carltonville area (southwest TS), the Rooihoogte Formation sits between the Malmani platform and the Timeball Hill Formation and also records the loss of S-MIF (5). Whether the Duitschland and Rooihoogte formations are stratigraphically correlative or the Rooihoogte Formation overlies the Duitschland Formation has been disputed (34, 35).

Results

Manganese stromatolites of the Duitschland Formation

New scientific drill cores from the Agouron Transvaal Drilling Campaign revealed authigenic manganese deposits in the Duitschland Formation just above the mid-Duitschland sequence boundary. Whole core X-ray fluorescence (XRF) scans illustrated the extremely high manganese enrichment of these deposits (Fig. 2). These deposits are comprised of microdigitate columnar stromatolites (Figs. 3*A*-*B*, S2) and are sufficiently unique that they were designated as the primary marker unit for correlation between the AGP-1 and AGP-2 cores. Indeed, stromatolites mineralized in manganese are not a common lithotype (36); to our knowledge, nothing similar to these deposits has been described elsewhere.

To understand better the origin of these manganese stromatolites, we examined them in petrographic thin section using scanning electron microscopy (SEM). Although diagenetic recrystallization textures overprint original depositional textures (diagenetic fabrics shown in Figs. 3*D*-*M* and S3*C*-*F*), some key features remain clear that support the interpretation of these stromatolites as the remains of microbial mat structures (36, 37). Laminae that thicken over the stromatolite apex reflects the growth of microbial mat layers (Figs. 3*D*, S3*C*), as opposed to abiotic crystal growth that would produce isopachous layers or the deposition of allochthonous organic material that would preferentially settle in topographic lows. Detrital grains sitting at higher angles than ~30°, the angle of repose for loose sediment, are indicative of microbial trapping and binding (Figs. 3*F*, S3*D*).

Energy dispersive spectroscopy (EDS) revealed that these stromatolites are comprised of carbonate minerals with variable mixtures of Mn^{2+} and Ca^{2+}, and to a lesser extent Fe^{2+}, as the dominant cation, along with chert, muscovite, and rare grains of Ti/Fe oxides, apatite, and zircon. The laminae are

broadly defined by composition, alternating between manganese carbonate (cation content up to 90% Mn^{2+}), carbonate with subequal cation mixtures (individual crystals exhibit Ca^{2+} or Fe^{2+} content up to 70%), and chert (Fig. 3*C*). Diagenetic textures suggested that this cation segregation is related to recrystallization, and samples from further down core were distinguished by larger domains of Mn^{2+} vs. Ca^{2+} cation segregation (Fig. S2, Fig. 3 vs. Fig S3). Nonetheless, carbonate material associated with exogenous textures such as detrital grains or later veins often exhibited the lowest manganese content (up to 95% Ca^{2+}). Synchrotron X-ray absorption near-edge structure (XANES) spectroscopy and mapping at the manganese K-edge confirmed that the manganese content of these stromatolites is present entirely as Mn^{2+} in carbonates (Fig. 4, Fig. S3*G-I*). Slight differences in the XANES spectra observed are consistent with manganese carbonates differing in other cation constituents and degree of self-absorption (38).

Carbonate $\delta^{13}C$ values in these samples are remarkably low (-16.4 to -19.2‰ VPDB), strongly depleted relative to seawater dissolved inorganic carbon (DIC) (~0‰ (39, 40)) (Fig. 5). Taken together with diagenetic textures, this isotopic signature suggests that these carbonate phases are secondary rather than primary and their carbon derives from the remineralization of organic matter in sedimentary porewater rather than from seawater DIC. Deposits with similar mineralogy, manganese content, and isotopic signatures in the Koegas Subgroup and Hotazel Formation have been interpreted to reflect the respiration of organic matter coupled to the reduction of manganese oxides (22, 41). Therefore, we propose that these stromatolites were likely originally mineralized with manganese oxides.

Detrital pyrite of the Makganyene Formation

The disappearance of redox-sensitive detrital grains from sediments has long been recognized as one of the clearest signatures of the GOE (19). Minerals such as pyrite and uraninite are highly sensitive to O_2—in the absence of O_2 they behave like sand grains, weathering slowly during sediment transport; in the presence of O_2 rapid oxidative degradation precludes their transport and deposition. Therefore, the sedimentary presence of rounded detrital grains of such minerals provides a simple and reliable proxy for the absence of O_2 in paleoenvironments.

We observed detrital pyrite grains in samples of the Makganyene Formation from two different GWS drill cores (Erin-3 (42) and GTF01 (22)) (Figs. 6, S5), implicating Makganyene sediments as predating the GOE. To further characterize these pyrites we measured multiple sulfur isotope ratios using *in situ* secondary ion mass spectrometry (SIMS), which allowed us to make isotopic measurements mapped onto petrographic textures, i.e., to distinguish detrital grains from later diagenetic pyrite (Fig. 6*G*). The pyrite grains we observed were not uniform in their isotopic compositions, suggesting multiple different provenances. Grains without any substantial fractionation signal were consistent with an igneous pyrite source (Fig. 6 grains A & C), while grains exhibiting a $\Delta^{33}S$ MIF signal indicated a sedimentary pyrite source predating the GOE (Fig. 6 grain B). Additionally, some of the grains examined featured post-depositional euhedral overgrowths that were isotopically distinct from the primary grain (Fig. 6 grains C & D). The overgrowths expressed slight $\Delta^{33}S$ signals that could be consistent with predating the GOE; however, this signal could also be inherited from remobilized older sulfur.

In seven thin sections of sandstones and shales taken from throughout the Duitschland Formation, including samples with heavy mineral laminae, we did not observe detrital pyrite (Fig. S6). This observation contrasts strongly with similar facies in underlying units that exhibit abundant detrital pyrite (19), supporting the interpretation that the Duitschland Formation postdates the GOE. However, the detrital pyrite proxy is diagnostic in its presence, not its absence, and therefore we refrain from drawing definitive conclusions based on this observation.

Manganese mobility as an oxidative weathering proxy

Archaean marine carbonates, such as those comprising the Campbellrand-Malmani platform, contain trace manganese content reflecting the manganese concentrations of Archean oceans—up to ~100 μM, much higher than the nM concentrations of modern oceans (20, 43). Therefore, although the manganese content of the Campbellrand-Malmani platform is negligible relative to the extreme manganese content of subsequent deposits reflecting the deposition of manganese oxides (such as those seen in the Koegas, Hotazel, and now Duitschland), it is not insubstantial. This manganese is mobilized

through carbonate dissolution during weathering, and soluble as long as it stays reduced. In the modern, oxic environment it is readily oxidized and precipitates as oxide minerals leading to supergene enrichment. This weathering signature is so dramatic that livestock on farms where these carbonates outcrop are susceptible to Vryburg hepatosis, a unique form of geophagic disease caused by manganese toxicity from supergene manganese nodules in the soil—a disease that does not occur anywhere else in the world (44). Therefore, an additional proxy for oxidative weathering can be inferred from the behavior of manganese mobilized by weathering of the Campbellrand-Malmani platform.

The Bevetts conglomerate member of the Duitschland Formation represents a major interval of weathering during Paleoproterozoic time of those same carbonate platform rocks. Bevetts is a chert pebble conglomerate, reflecting silicification of the original carbonate. Unlike the modern soil nodules, which are comprised of manganese oxides and therefore highly enriched in manganese, Bevetts retained almost no manganese; what little there is is present as a trace constituent of silicate minerals (Fig. 7). This suggests that the manganese mobilized during this weathering interval remained reduced and therefore soluble, carried away by fluids. The lack of any evidence for manganese enrichment reflects a lack of oxidative manganese deposition.

Discussion

Manganese played a fundamental role in the evolution of oxygenic photosynthesis. Not only is MOP thought to represent a critical evolutionary intermediate on the way to a photosystem capable of oxidizing water (20–22), the antioxidant activity of manganese small molecules provides an explanation for how the first organisms to generate O_2 survived the sudden and acute degree of oxidative stress it must have engendered, long before the evolution of sophisticated biochemical antioxidant systems (20, 43). Therefore, the microbial communities that evolved and sustained oxygenic photosynthesis must have been expressly interested in manganese. Our analyses described the Duitschland manganese stromatolites as the vestiges of a phototrophic microbial community that was mineralized in manganese oxides and suggested that the ecology of this community was strongly characterized by manganese cycling—with

primary production fueled by MOP, and heterotrophic carbon remineralization fueled by manganese reduction. This unit, from right around the time of the rise of O_2, provides the first example of what the hypothesized communities that evolved oxygenic photosynthesis might have looked like.

The oxidative weathering proxies presented here provided new insights that refine our understanding of how the GOE fits into the Transvaal Supergroup stratigraphy. On the GWS side, the 2426 ± 3 Ma age for the Ongeluk magmatism was previously interpreted as post-GOE and therefore constraining the GOE as older than that (26). However, if the Makganyene Formation actually predates the GOE, as our detrital pyrite data suggests, then that date for the Ongeluk can be interpreted as predating the GOE—a scenario which is much more congruent with the ~2.33 Ga estimate for the disappearance of S-MIF from TS (5). Therefore, we place the GOE between the Ongeluk and Hotazel Formations in GWS (Fig. 1*B*). In TS, the stark contrast between the behavior of manganese during modern weathering of the Campbellrand-Malmani platform and the weathering interval represented by Bevetts suggests that Bevetts predates the GOE; therefore, we place the GOE above Bevetts but relatively low in the Duitschland Formation, consistent with the S-MIF record (5) and absence of detrital pyrite.

The understanding that the Makganyene Formation predates the GOE raises important questions regarding the implications of the Makganyene glaciation. Based on the current data, two scenarios are plausible—the glacial interval predated the evolution of oxygenic photosynthesis and was therefore unrelated to O_2; alternatively, the glacial interval was precipitated by O_2 as previously proposed (29, 30), but the presence of O_2 was so incipient that surface processes did not yet reflect its influence. In the latter case, our data have profound implications for the relative tempos with which different consequences of introducing O_2 to the environment were expressed. If the Makganyene glaciation was related to O_2, the climatic consequence of global cooling manifested much more quickly than the impact of O_2 on sediments.

The history of manganese recorded in the Duitschland Formation provides an interesting contrast to the deeper water environments preserved in GWS. The Koegas Subgroup exhibits a clear signal of oxidative manganese deposition attributed to MOP (22). This biogenic MOP signature is distinct from

oxidative weathering; in the Koegas, that distinction is demonstrated by the co-occurrence of detrital pyrite grains demonstrating the absence of O_2. Assuming stratigraphic correlation of the erosional hiatus between the lower and middle Transvaal sequences in GWS and TS, our Bevetts data further strengthens this interpretation of the Koegas by demonstrating that oxidative manganese deposition did not occur during a weathering interval that postdates the Koegas deposition. Further up in the Duitschland Formation, the first instance of oxidative manganese deposition is the manganese stromatolite unit. While not demonstrably pre-GOE, the stromatolites instead provide textural evidence for MOP communities, unlike the deeper water facies of the Koegas which record only the product of such communities, not their physical form.

Methods

Whole core XRF

Whole core XRF scans at cm-scale resolution were taken at the European Institute for Marine Studies using an Avaatech XRF corescanner in two separate passes with excitation energies of 10 and 30 kV, respectively.

Sampling & thin sections

Cores were sampled at the University of Johannesburg. Thin sections were prepared by David Mann at High Mesa Petrographics (Los Alamos, NM).

Optical microscopy

Thin sections were examined on a Leica polarizing light microscope in both reflected and transmitted light.

SEM/EDS

SEM and EDS analyses were conducted in the Caltech Geological and Planetary Sciences Division Analytical Facility on a ZEISS 1550VP Field Emission SEM, with both secondary electron and Robinson-type backscatter electron detectors and an Oxford X-Max SDD X-ray EDS system. Petrographic thin sections were coated with 20 nm graphite using a Turbo carbon evaporator and imaged with accelerating voltages of 10 to 20 kV and working distances of 5 to 15 mm.

Synchrotron X-ray spectroscopy

Synchrotron analyses were conducted at the Stanford Synchrotron Radiation Lightsource on mesoprobe beamline 10-2 for full thin section maps and microprobe beamline 2-3 for high resolution maps and point spectra at the manganese K-edge. The beam was energy calibrated using the pre-edge feature of $KMnO_4$ at 6543.34 eV. XRF maps of manganese distribution were collected at 11000 eV; multiple energy maps for mapping manganese speciation were collected at 6551, 6552, 6553, and 6554 eV to capture subtle differences between the carbonate phases, along with 6558 and 6562 to capture spectral features diagnostic of higher valent oxides. Analyses at the sulfur K-edge were conducted on microprobe beamline 14-3, energy calibrated using the pre-edge feature of $Na_2S_2O_3$ at 2472.02 eV. Maps of sulfur distribution were collected at 2499 eV. Spectra and maps were reduced using the SIXPACK (45) and SMAK (46) software packages respectively (https://www.sams-xrays.com/). Colormaps were converted to viridis using fixthejet (https://fixthejet.ecrlife.org/).

Isotope analyses

Sulfur isotope ratios were determined by SIMS in the Caltech Microanalysis Center using a Cameca 7f-GEO. Petrographic thin sections were coated with 40 nm gold using a Cressington HR metal sputtering coater and interrogated with a primary beam current of ~ 3 nA and raster size was 5 x 5 µm. ^{32}S, ^{33}S, and ^{34}S were measured using Faraday cup detectors; ^{36}S was measured using an electron multiplier detector with deadtime correction. Instrument mass fractionation was corrected using an in-house pyrite standard calibrated to VCDT.

For carbonate $\delta^{13}C$ and $\delta^{18}O$ analyses, approximately 100 µg of microdrilled carbonate textures were sealed into 12 mL round-bottom borosilicate vials and flushed with helium gas. CO_2 was generated by reaction with 100 µL > 100% H_3PO_4 at 72°C for 1 hour in a Thermo Fisher Scientific Gasbench II CO_2 prepatory system. Isotopic compositions were determined on a Delta V Plus continuous flow mass spectrometer by standardization relative to NBS-18, NBS-19, and three in-house reference standards. Oxygen isotopic compositions are reported using the dolomite-CO_2 acid fractionation factor (47); this may result in a 1-2‰ $\delta^{18}O$ accuracy bias for extremely high manganese samples.

Acknowledgements
This research was supported by the Agouron Institute, the Simons Foundation collaboration on the origins of life, NSF grant IOS-1833247 (UFL and WWF), and the NSF GRFP (UFL). Use of the Stanford Synchrotron Radiation Lightsource, SLAC National Accelerator Laboratory, was supported by the DOE Office of Basic Energy Sciences under Contract No. DE-AC02-76SF00515, and the SSRL Structural Molecular Biology Program supported by the DOE Office of Biological and Environmental Research and the NIH, NIGMS (P41GM103393). This research also benefited from use of instrumentation made available by the Caltech Microanalysis Center and Caltech Geological and Planetary Sciences Division Analytical Facility. We thank Yunbin Guan for help with SIMS measurements, Fenfang Wu for help with Gasbench measurements, Sharon Bone and Nick Edwards for support at SSRL, George Rossman for providing manganese mineral standards, and Jena Johnson for helpful discussions and insight.

Author contributions
WWF, NB, BR, and UFL designed research. SL performed whole core XRF analyses. UFL and BR performed optical microscopy. UFL and CM performed SEM/EDS analyses. UFL, JSM, and SMW performed synchrotron analyses. UFL, JSM, and WWF performed SIMS analyses. UFL and TMP performed carbonate isotope analyses. UFL wrote the manuscript with input from WWF and JSV.

References

1. W. W. Fischer, J. Hemp, J. E. Johnson, Evolution of Oxygenic Photosynthesis. *Annu. Rev. Earth Planet. Sci.* **44**, 647–683 (2016).

2. P. E. Cloud, Atmospheric and hydrospheric evolution on the primitive earth. Both secular accretion and biological and geochemical processes have affected earth's volatile envelope. *Science* **160**, 729–736 (1968).

3. H. D. Holland, *The chemical evolution of the atmosphere and oceans* (Princeton University Press, 1984).

4. Q. Guo, H. Strauss, A. J. Kaufman, S. Schröder, Reconstructing Earth's surface oxidation across the Archean-Proterozoic transition. *Geology* **37**, 399–402 (2009).

5. G. Luo, *et al.*, Rapid oxygenation of Earths atmosphere 2.33 billion years ago. *Sci. Adv.* **2**, e1600134–e1600134 (2016).

6. R. Rye, H. D. Holland, Paleosols and the evolution of atmospheric oxygen: a critical review. *Am. J. Sci.* **298**, 621–672 (1998).

7. P. K. Pufahl, E. E. Hiatt, Oxygenation of the Earth's atmosphere–ocean system: A review of physical and chemical sedimentologic responses. *Mar. Pet. Geol.* (2012).

8. S. M. Roscoe, The Huronian Supergroup, a Paleoaphebian succession showing evidence of atmospheric evolution. *Geol. Assoc. Can.* (1973).

9. S. M. Roscoe, Huronian rocks and uraniferous conglomerates in the Canadian Shield. *Geol. Surv. Can. Pap.* **68–40**, 205pp (1969).

10. E. M. Cameron, Sulphate and sulphate reduction in early Precambrian oceans. *Nature* **296**, 145–148 (1982).

11. N. J. Beukes, H. Dorland, J. Gutzmer, M. Nedachi, H. Ohmoto, Tropical laterites, life on land, and the history of atmospheric oxygen in the Paleoproterozoic. *Geology* **30**, 491 (2002).

12. W. W. Fischer, A. H. Knoll, An iron shuttle for deepwater silica in Late Archean and early Paleoproterozoic iron formation. *Geol. Soc. Am. Bull.* **121**, 222–235 (2009).

13. H. E. Frimmel, Archaean atmospheric evolution: evidence from the Witwatersrand gold fields, South Africa. *Earth-Sci. Rev.* (2005).

14. D. E. Grandstaff, Origin of uraniferous conglomerates at Elliot Lake, Canada and Witwatersrand, South Africa: Implications for oxygen in the Precambrian atmosphere. *Precambrian Res.* **13**, 1–26 (1980).

15. N. Prasad, S. M. Roscoe, Evidence of anoxic to oxic atmospheric change during 2.45-2.22 Ga from lower and upper sub-Huronian paleosols, Canada. *CATENA* **27**, 105–121 (1996).

16. M. El Tabakh, K. Grey, F. Pirajno, B. Charlotte Schreiber, Pseudomorphs after evaporitic minerals interbedded with 2.2 Ga stromatolites of the Yerrida basin, Western Australia: Origin and significance. *Geology* **27**, 871 (1999).

17. S. Utsunomiya, T. Murakami, M. Nakada, Iron oxidation state of a 2.45-Byr-old paleosol developed on mafic volcanics. *Ldots Cosmochim. Acta* (2003).

18. A. Bekker, *et al.*, Dating the rise of atmospheric oxygen. *Nature* **427**, 117–120 (2004).

19. J. E. Johnson, A. Gerpheide, M. P. Lamb, W. W. Fischer, O_2 constraints from Paleoproterozoic detrital pyrite and uraninite. *Geol. Soc. Am. Bull.* **126**, 813–830 (2014).

20. U. F. Lingappa, D. R. Monteverde, J. S. Magyar, J. S. Valentine, W. W. Fischer, How manganese empowered life with dioxygen (and vice versa). *Free Radic. Biol. Med.*, 113–125 (2019).

21. W. W. Fischer, J. Hemp, J. E. Johnson, Manganese and the Evolution of Photosynthesis. *Orig. Life Evol. Biosphere J. Int. Soc. Study Orig. Life* **45**, 351–357 (2015).

22. J. E. Johnson, *et al.*, Manganese-oxidizing photosynthesis before the rise of cyanobacteria. **110**, 11238–11243 (2013).

23. D. Y. Sumner, N. J. Beukes, Sequence Stratigraphic Development of the Neoarchean Transvaal carbonate platform, Kaapvaal Craton, South Africa. *South Afr. J. Geol.* **109**, 11–22 (2006).

24. J. E. Johnson, S. M. Webb, C. B. Condit, N. J. Beukes, W. W. Fischer, Effects of metamorphism and metasomatism on manganese mineralogy: Examples from the Transvaal Supergroup. *South Afr. J. Geol.* **122**, 489–504 (2019).

25. P. G. Eriksson, *et al.*, The transvaal sequence: an overview. *J. Afr. Earth Sci. Middle East* **16**, 25–51 (1993).

26. A. P. Gumsley, *et al.*, Timing and tempo of the Great Oxidation Event. *Proc. Natl. Acad. Sci.* **114**, 1811–1816 (2017).

27. B. Cairncross, N. J. Beukes, *The Kalahari manganese field: the adventure continues* (Random House Struik, 2013).

28. D. A. Evans, N. J. Beukes, J. L. Kirschvink, Low-latitude glaciation in the Palaeoproterozoic era. *Nature* **386**, 262–266 (1997).

29. R. E. Kopp, J. L. Kirschvink, I. A. Hilburn, C. Z. Nash, The Paleoproterozoic snowball Earth: a climate disaster triggered by the evolution of oxygenic photosynthesis. *Proc. Natl. Acad. Sci. U. S. A.* **102**, 11131–11136 (2005).

30. J. L. Kirschvink, *et al.*, Paleoproterozoic snowball earth: extreme climatic and geochemical global change and its biological consequences. *Proc. Natl. Acad. Sci. U. S. A.* **97**, 1400–1405 (2000).

31. R. M. Gaschnig, *et al.*, Onset of oxidative weathering of continents recorded in the geochemistry of ancient glacial diamictites. *Earth Planet. Sci. Lett.* **408**, 87–99 (2014).

32. S. Li, R. M. Gaschnig, R. L. Rudnick, Insights into chemical weathering of the upper continental crust from the geochemistry of ancient glacial diamictites. *Geochim. Cosmochim. Acta* **176**, 96–117 (2016).

33. C. R. Anhaeusser, S. Maske, Geological Society of South Africa, Eds., *Mineral deposits of Southern Africa*, 1st ed (Geological Society of South Africa, 1986).

34. M. R. Warke, S. Schröder, Synsedimentary fault control on the deposition of the Duitschland Formation (South Africa): Implications for depositional settings, Paleoproterozoic stratigraphic correlations, and the GOE. *Precambrian Res.* **310**, 348–364 (2018).

35. B. Rasmussen, A. Bekker, I. R. Fletcher, Correlation of Paleoproterozoic glaciations based on U–Pb zircon ages for tuff beds in the Transvaal and Huronian Supergroups. *Earth Planet. Sci. Lett.* **382**, 173–180 (2013).

36. J. P. Grotzinger, A. H. Knoll, Stromatolites in Precambrian carbonates: evolutionary mileposts or environmental dipsticks? *Annu. Rev. Earth Planet. Sci.* **27**, 313–358 (1999).

37. A. C. Allwood, *et al.*, Controls on development and diversity of Early Archean stromatolites. *Proc. Natl. Acad. Sci. U. S. A.* **106**, 9548–9555 (2009).

38. J. E. Johnson, S. M. Webb, C. Ma, W. W. Fischer, Manganese mineralogy and diagenesis in the sedimentary rock record. *Geochim. Cosmochim. Acta* **173**, 210–231 (2016).

39. W. W. Fischer, *et al.*, Isotopic constraints on the Late Archean carbon cycle from the Transvaal Supergroup along the western margin of the Kaapvaal Craton, South Africa. *Precambrian Res.* **169**, 15–27 (2009).

40. M. Bau, R. L. Romer, V. Lüders, N. J. Beukes, Pb, O, and C isotopes in silicified Mooidraai dolomite (Transvaal Supergroup, South Africa): implications for the composition of Paleoproterozoic seawater and 'dating' the increase of oxygen in the Precambrian atmosphere. *Earth Planet. Sci. Lett.* **174**, 43–57 (1999).

41. H. Tsikos, N. J. Beukes, J. M. Moore, C. Harris, Deposition, Diagenesis, and Secondary Enrichment of Metals inthe Paleoproterozoic Hotazel Iron Formation, Kalahari Manganese Field, SouthAfrica. *Econ. Geol.* **98**, 1449–1462 (2003).

42. B. Rasmussen, J. R. Muhling, N. J. Tosca, H. Tsikos, Evidence for anoxic shallow oceans at 2.45 Ga: Implications for the rise of oxygenic photosynthesis. *Geology* **47**, 622–626 (2019).

43. W. W. Fischer, J. Hemp, J. S. Valentine, How did life survive Earth's great oxygenation? *Curr. Opin. Chem. Biol.* **31**, 166–178 (2016).

44. J. A. Neser, *et al.*, The possible role of manganese poisoning in enzootic geophagia and hepatitis of calves and lambs : to the editor. *J. S. Afr. Vet. Assoc.* **68**, 4–6 (1997).

45. S. M. Webb, SIXPack a Graphical User Interface for XAS Analysis Using IFEFFIT. *Phys. Scr.*, 1011 (2005).

46. S. M. Webb, I. McNulty, C. Eyberger, B. Lai, The MicroAnalysis Toolkit: X-ray Fluorescence Image Processing Software. *AIP Conf. Proc.* **1365**, 196–199 (2011).

47. S.-T. Kim, T. B. Coplen, J. Horita, Normalization of stable isotope data for carbonate minerals: Implementation of IUPAC guidelines. *Geochim. Cosmochim. Acta* **158**, 276–289 (2015).

Figures

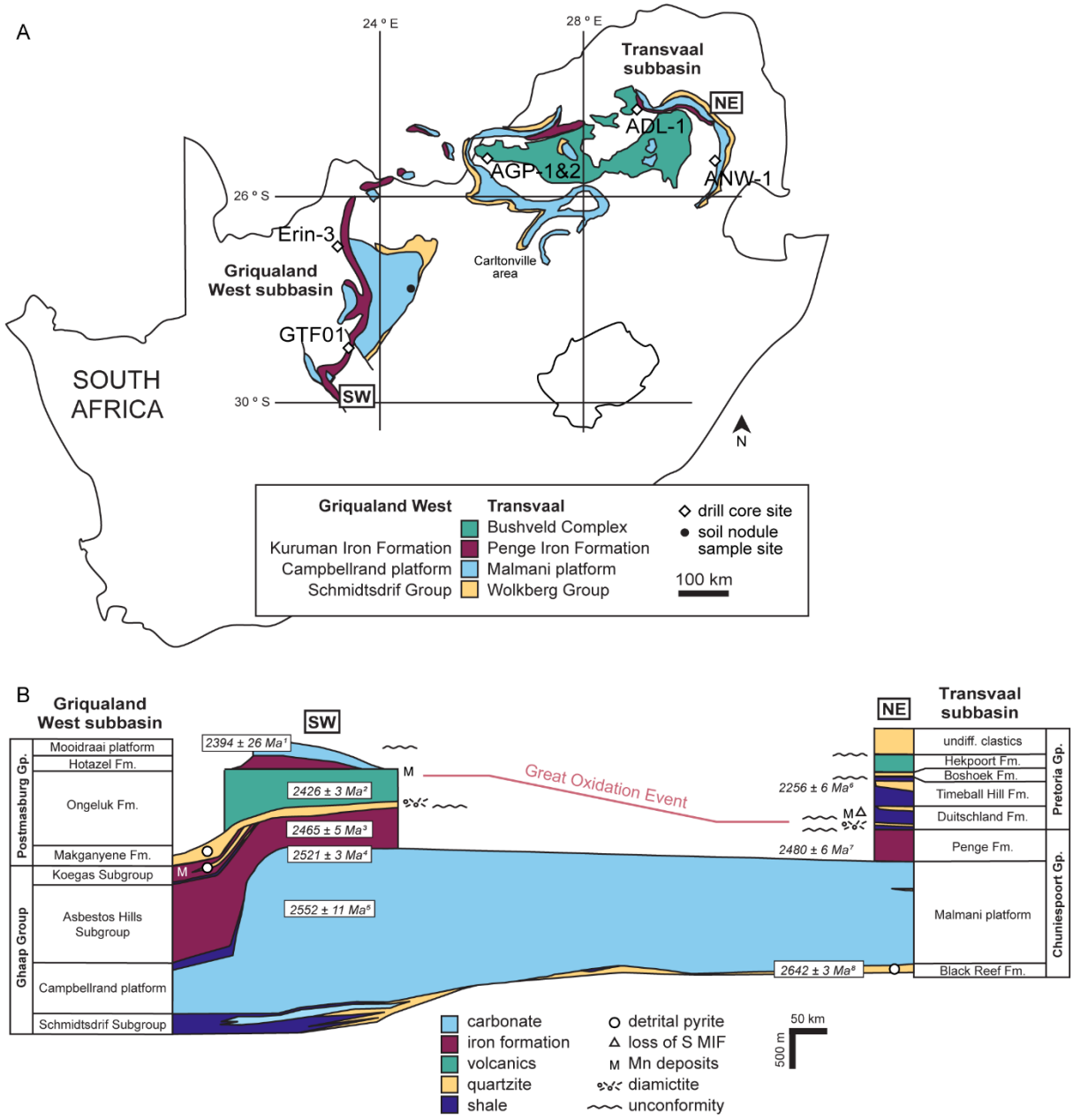

Figure 1. The Transvaal Supergroup. ***A.*** Geologic map showing exposures of the Griqualand West and Transvaal subbasins in South Africa, annotated with drill core and sample sites featured in this study. ***B.*** Stratigraphic cross section from the southwest to northeast of the Transvaal supergroup. Stratigraphy based on Sumner & Beukes, 2006; Cairncross & Beukes, 2013; Johnson *et al*, 2014. Age dates from 1. Bau *et al*, 1999 (Pb/Pb); 2. Gumsley *et al*, 2016 (U/Pb); 3. Pickard, 2003 (U/Pb); 4. Sumner & Bowring, 1996 (U/Pb); 5. Barton *et al*, 1994 (U/Pb); 6. Rasmussen *et al*, 2013 (Pb/Pb); 7. Nelson *et al*, 1999 (U/Pb); 8. Walraven *et al*, 1999 (U/Pb). Detrital pyrite from England *et al*, 2002; Hoffman *et al*, 2009; Johnson *et al*, 2013. S-MIF from Guo *et al*, 2009; Luo *et al*, 2016. Manganese depositis from Tsikos *et al*., 2003; Johnson *et al*, 2013; this study. We place the GOE between the Ongeluk and Hotazel Formations in GWS, and within the Duitschland Formation in TS.

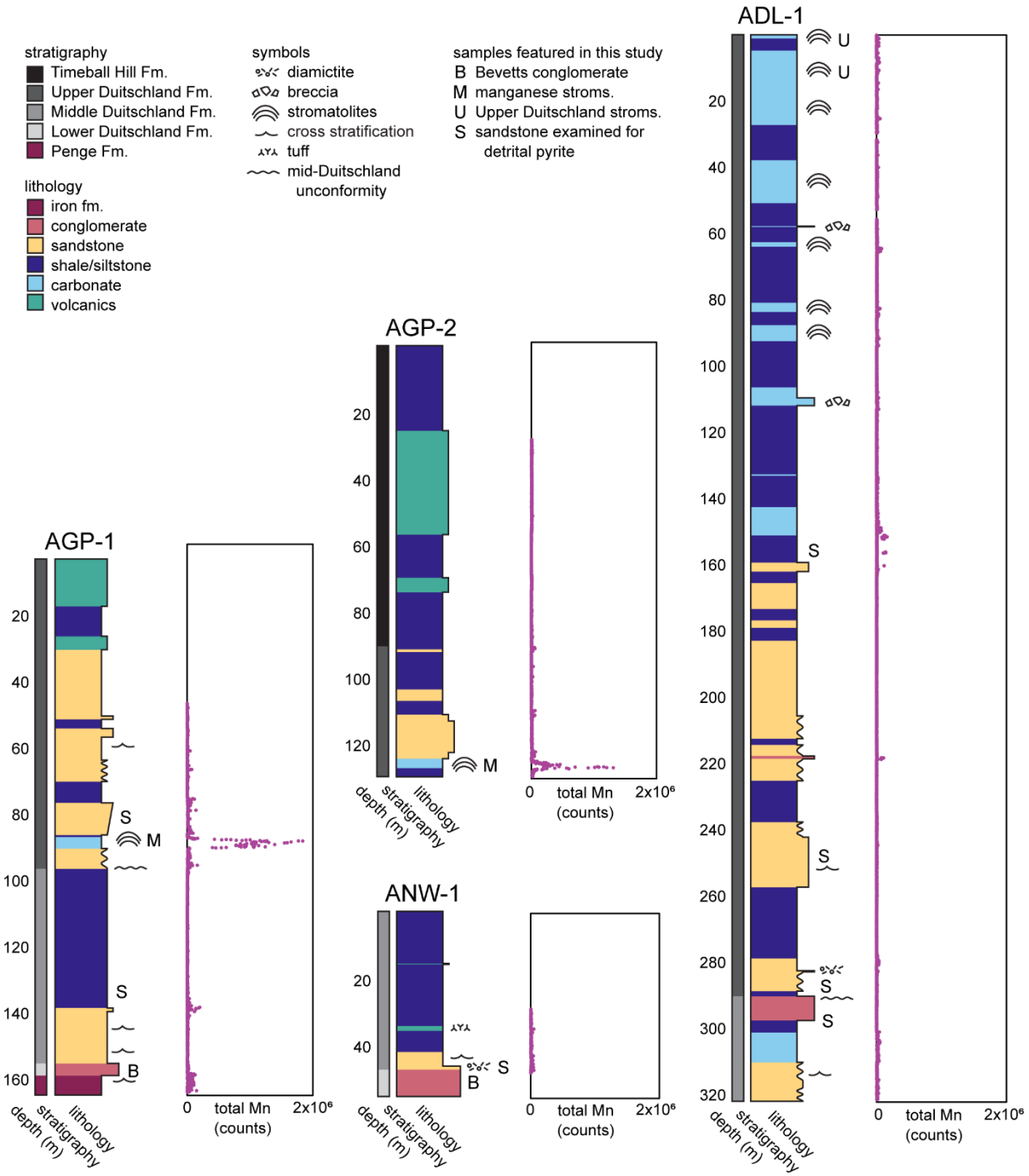

Figure 2. Stratigraphic columns of Agouron drill cores though the Duitchland Formation, annotated to indicate the samples featured in this study. Whole core XRF scans show substantial manganese spikes in a unit of stromatolitic dolomite in cores AGP-1 and AGP-2.

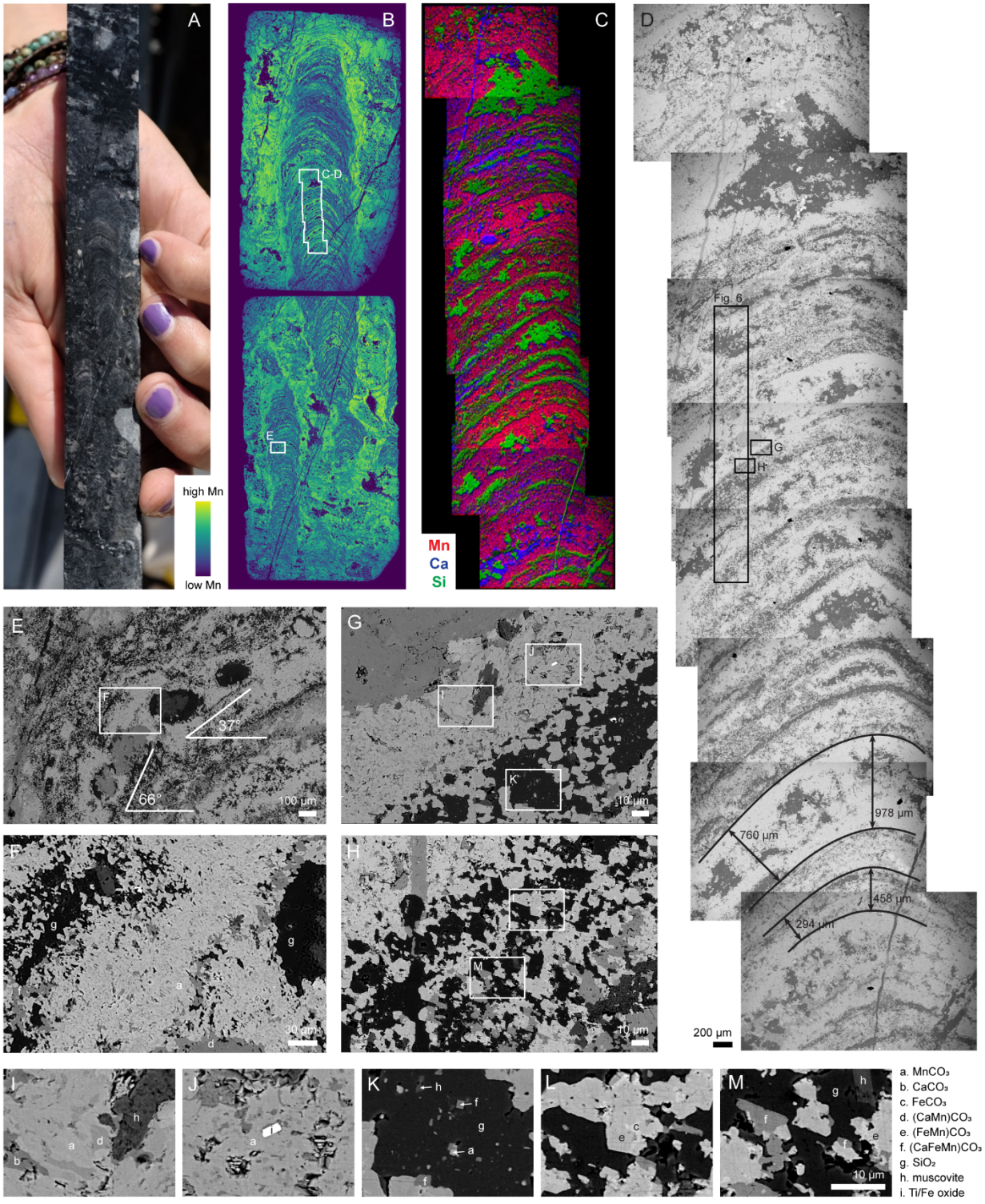

Figure 3. Manganese stromatolites of the Duitschland Formation. ***A.*** Sample from core AGP-2, 125.67 m depth. ***B.*** Synchrotron XRF map of manganese distribution. ***C-D.*** Backscatter SEM images (***D***) and EDS maps (***C***), showing laminae defined by chemical composition (***C***) that thicken towards the apex of the stromatolite column (***D***). ***E-M.*** Backscatter SEM images showing grains trapped and bound above the

angle of repose (***E***), EDS points identifying mineral phases (***F***, ***I***-***M***; representative spectra shown in Fig. S4), and fabrics characterized by diagenetic textures and low-grade metamorphism.

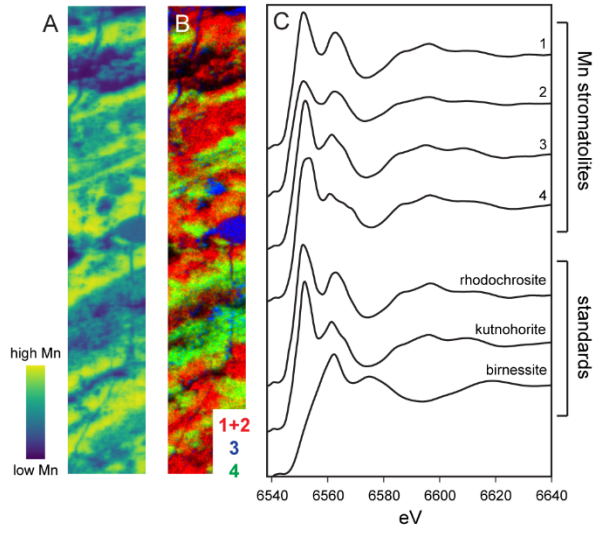

Figure 4. Synchrotron characterization of manganese stromatolites. ***A.*** Microprobe XRF map of manganese distribution, region shown in Fig. 3*D*. ***B.*** Manganese speciation map, fit with endmember spectra shown in ***C***. ***C.*** Manganese K-edge XANES spectra, showing four endmembers from the manganese stromatolites, along with standard spectra for rhodochrosite ($MnCO_3$), kutnohorite ($[CaMn]CO_3$), and birnessite (MnO_2) for comparison.

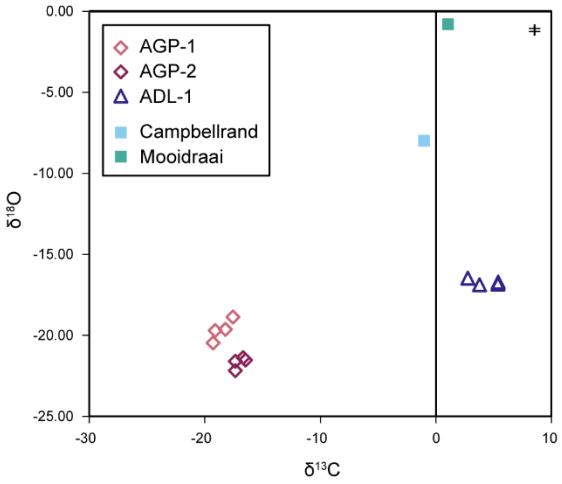

Figure 5. Carbonate isotopic composition of manganese stromatolites, presented as isotope ratios relative to Vienna Pee Dee Belemnite (VPDB). Inset error bars in the upper right corner show average standard deviation, which ranges from 0.03 to 0.09‰ for $\delta^{13}C$ and 0.05 to 0.16‰ for $\delta^{18}O$. Average isotopic compositions of the Campbellrand and Mooidraai platforms (reported by Fischer *et al*, 2009 and Bau *et al*, 1999, respectively) included to represent contemporaneous seawater DIC, along with measurements of other, non-manganiferous stromatolitic carbonates from the Upper Duitschland Formation from core ADL-1 for contrast.

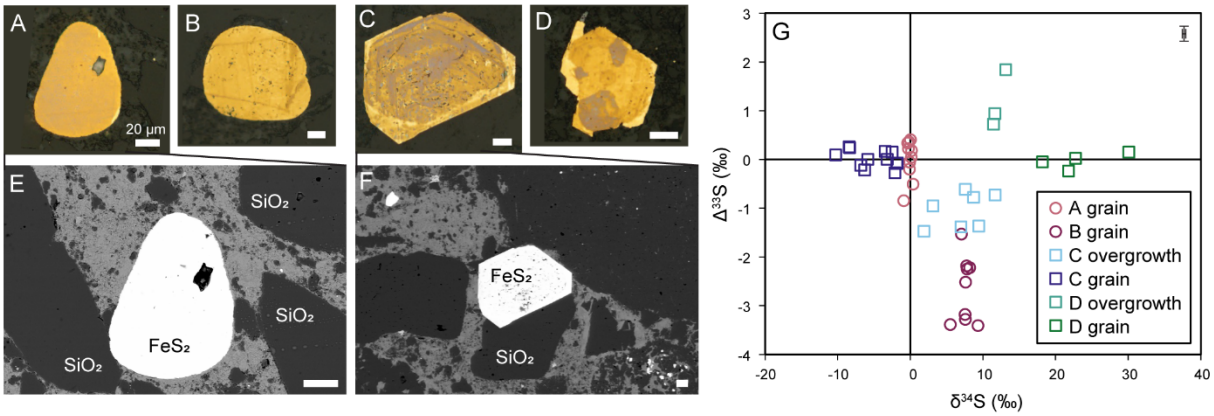

Figure 6. Detrital pyrite grains in the Makganyene Formation from core Erin-3. ***A-D.*** Reflected light images. ***E-F.*** Backscatter SEM images annotated with phases identified by EDS; a representative pyrite EDS spectrum is shown in Fig. S5. ***G.*** Multiple sulfur isotopes measured by SIMS and presented as isotope ratios relative to Vienna Cañon Diablo Troilite (VCDT). Inset error bars in the upper right corner show average 2σ uncertainty, which ranges from 0.27 to 0.36‰ for $\Delta^{33}S$ and 0.34 to 0.69‰ for $\delta^{34}S$. Datapoints are colored by grain, and in the case of the grains in ***C*** and ***D***, further separated into the primary grain and post-depositional overgrowth.

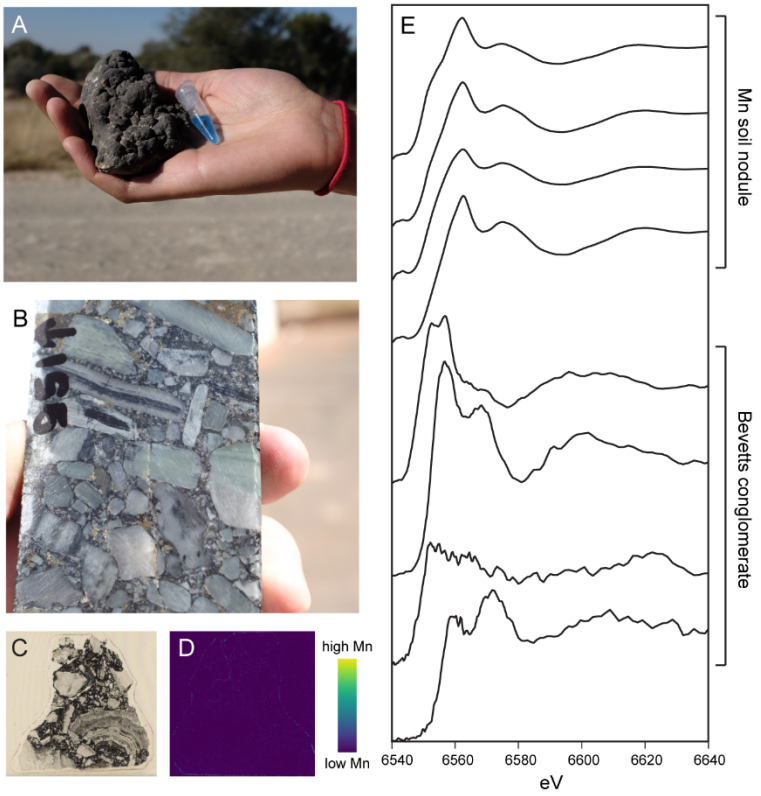

Figure 7. The behavior of manganese during weathering. ***A*.** Modern supergene manganese soil nodule collected near outcrop of the Campbellrand platform. The tube in the picture contains leucoberbelin blue, a colorimetric dye used to detect high valent manganese; the strong blue color demonstrates the substantial manganese oxide content of the sample. ***B*.** Bevetts conglomerate sample from core AGP-1. ***C*.** Bevetts conglomerate sample from core ANW-1 in thin section, featuring a silicified stromatolite. ***D*.** Synchrotron XRF map of the thin section in ***C*** showing undetectably low manganese content. ***E*.** Manganese K-edge XANES spectra showing manganese oxides from the modern soil nodule and trace manganese in silicate minerals from Bevetts.

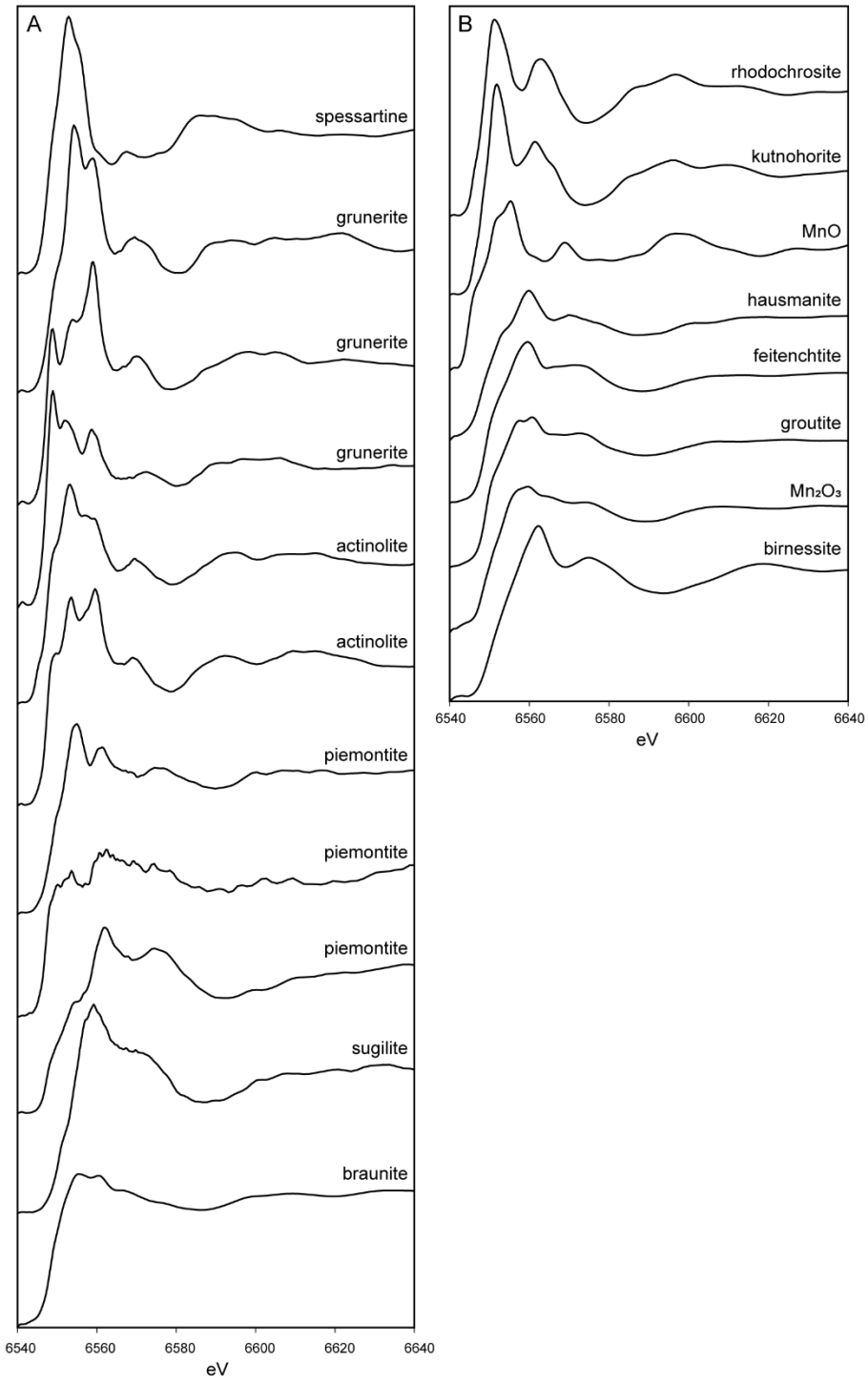

Figure S1. Manganese K-edge XANES standard spectra. ***A.*** Silicates. ***B.*** Carbonates and oxides.

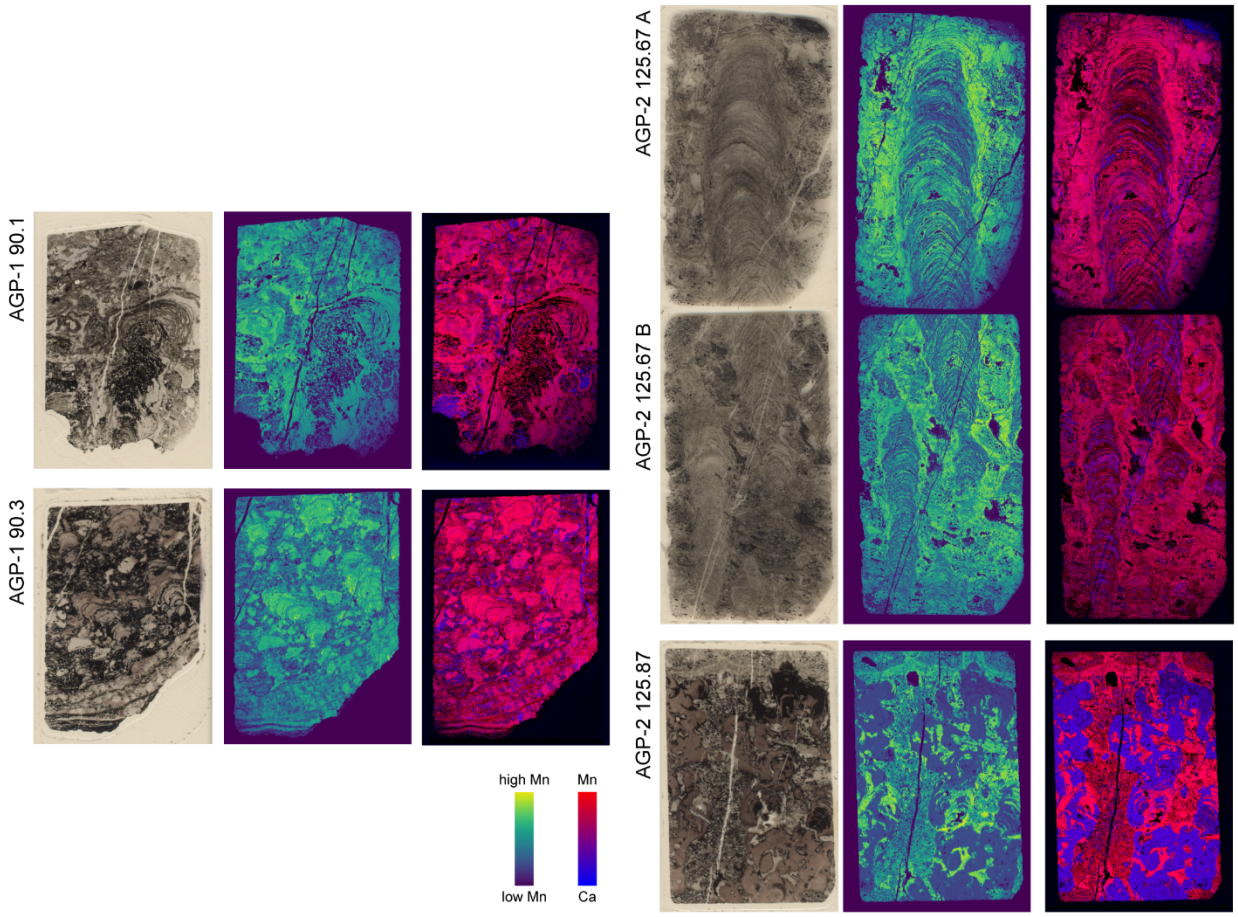

Figure S2. More manganese stromatolites of the Duitschland Formation. Shown here are petrographic thin sections alongside synchrotron XRF maps of manganese and calcium distributions. In both cores, the stromatolites further down core are more segregated into larger domains of Mn^{2+}-dominated vs. Ca^{2+}-dominated carbonate.

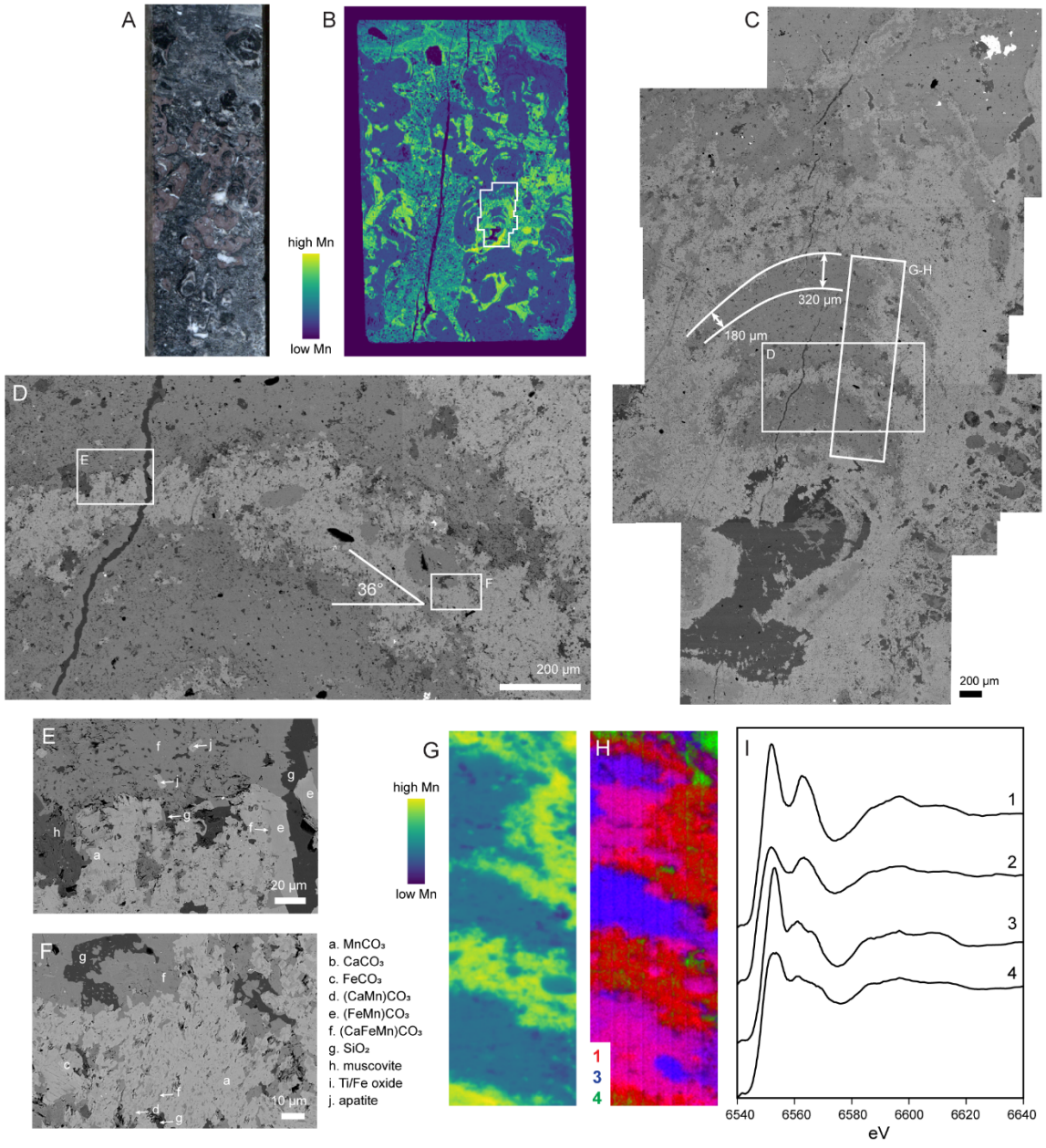

Figure S3. Manganese stromatolites, down core version. ***A.*** Sample from core AGP-2, 125.87 m depth. ***B.*** Synchrotron XRF map of manganese distribution. ***C-F.*** Backscatter SEM images showing laminae that thicken towards the apex of the stromatolite column (***C***), grains trapped and bound above the angle of repose (***D***), EDS points identifying mineral phases (***E-F***; representative spectra shown in Fig. S4), and fabrics characterized by diagenetic textures. ***G-H.*** Synchrotron microprobe XRF maps showing manganese distribution (***G***) and speciation (***H***). ***I.*** Manganese K-edge XANES spectra, showing a similar set of endmembers to the up core sample.

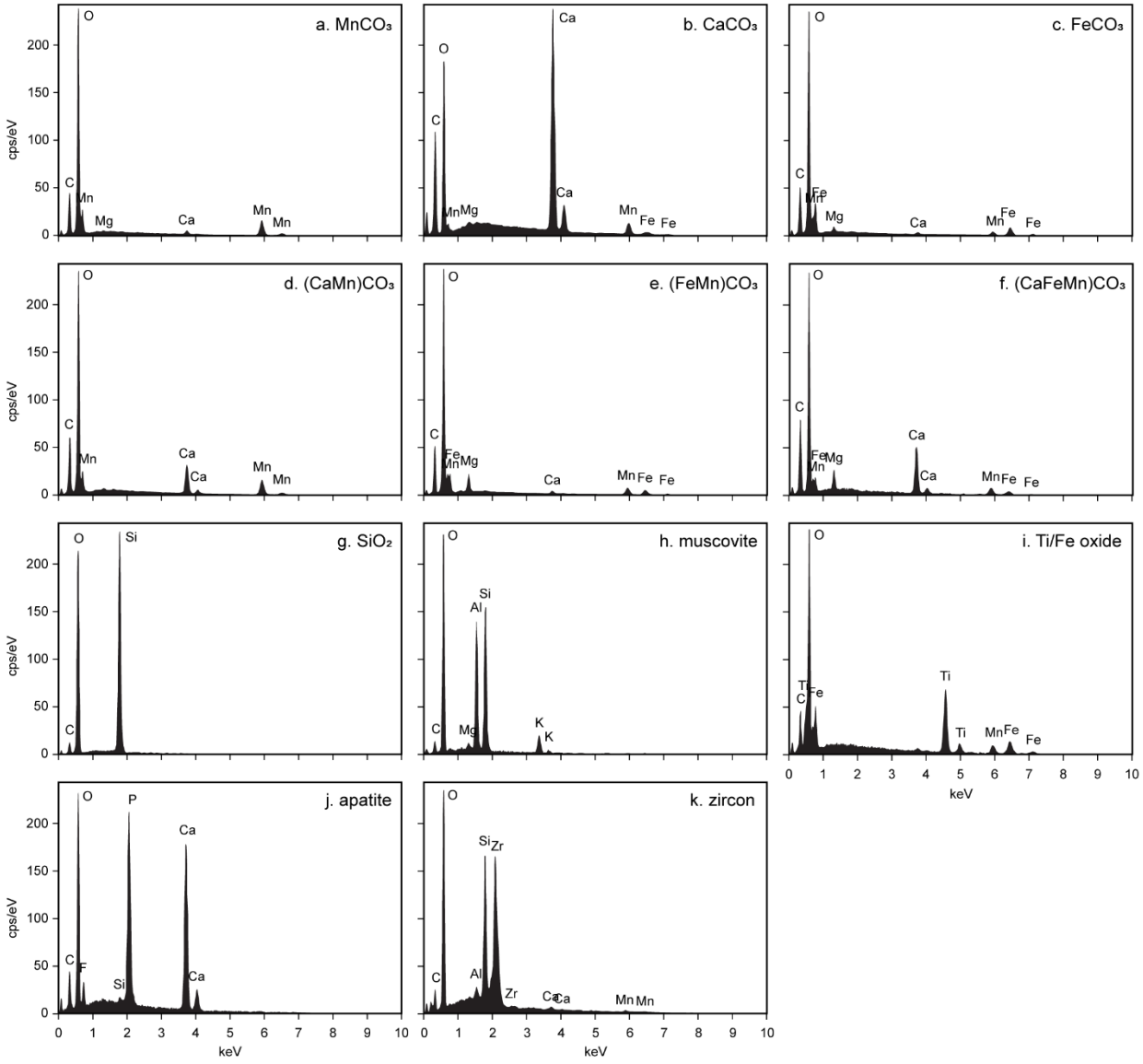

Figure S4. Representative EDS spectra identifying the phases found in the Duitschland Formation manganese stromatolites, shown in Figures 3 & S3.

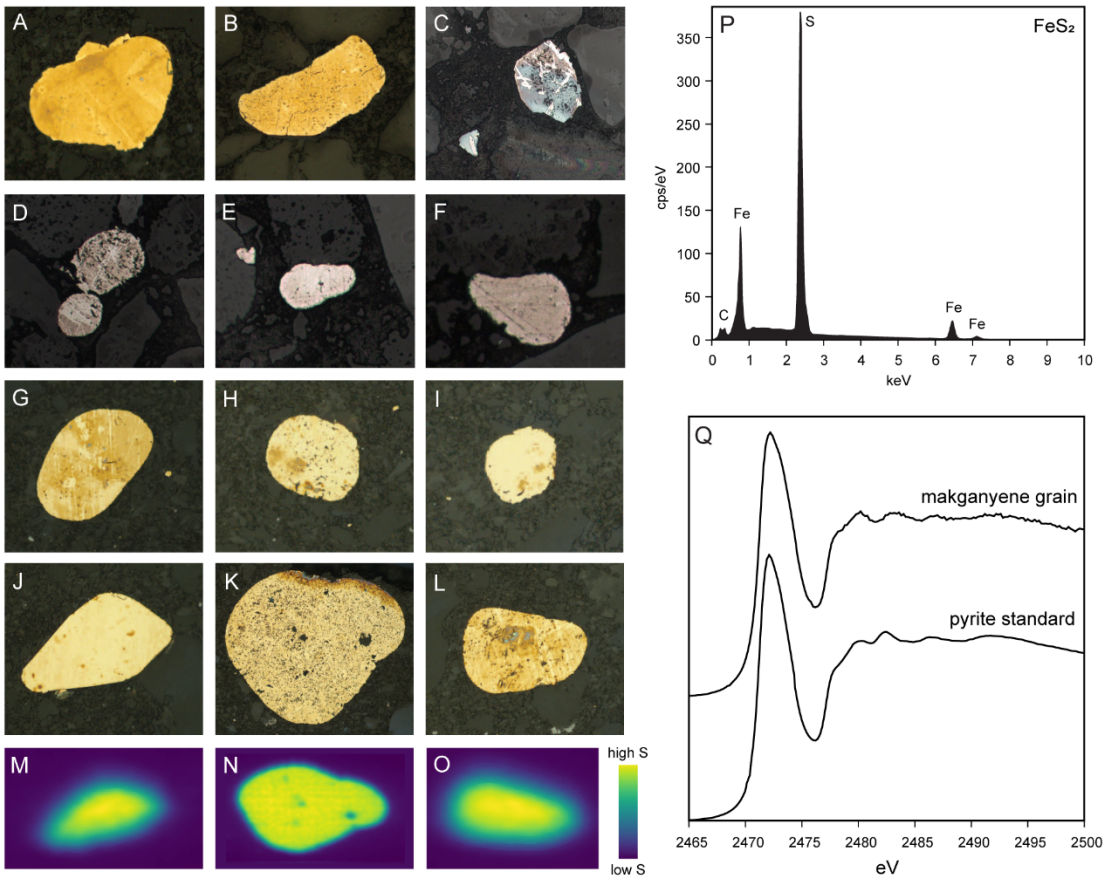

Figure S5. Detrital pyrite in the Makganyene Formation continued. ***A-F.*** Additional images of detrital pyrite grains from core Erin-3. ***G-L.*** Detrital pyrite in the Makganyene Formation from core GTF01. ***M-O.*** Synchrotron XRF maps of the grains in ***J-L*** showing sulfur distribution. ***P.*** A representative EDS spectrum identifying the grains from Erin-3 as pyrite. ***Q.*** A representative sulfur K-edge XANES spectrum identifying the grains from GTF01 as pyrite.

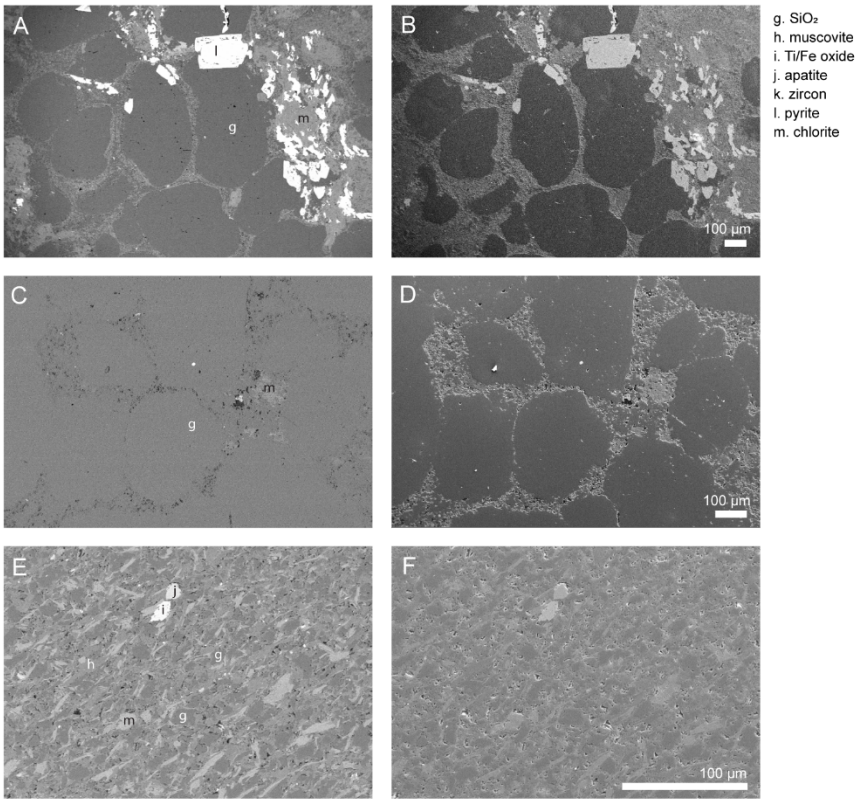

Figure S6. Representative backscatter (***A***, ***C***, ***E***) and secondary electron (***B***, ***D***, ***F***) SEM images of Duitschland Formation sandstones/shales. ***A-B.*** AGP-1 88.0 m. ***C-D.*** ANW-1 46.95 m. ***E-F.*** AGP-1 137.2 m. While some samples exhibited late, post-depositional pyrites (e.g., ***A***), detrital pyrite and/or uraninite grains were not observed in any of the sandstone and siltstone samples examined, including along heavy mineral laminae.

CHAPTER IV

An ecophysiological explanation for manganese enrichment in rock varnish

Usha F. Lingappa[1], Chris M. Yeager[2], Ajay Sharma[3], Nina L. Lanza[2], Demosthenes P. Morales[2], Gary Xie[2], Ashley D. Atencio[2], Grayson L. Chadwick[1], Danielle R. Monteverde[1], John S. Magyar[1], Samuel M. Webb[4], Joan Selverstone Valentine[1,5], Brian M. Hoffman[3], Woodward W. Fischer[1]

1. Division of Geological and Planetary Sciences, California Institute of Technology, Pasadena, CA 91125, USA

2. Los Alamos National Laboratory, Los Alamos, NM 87545, USA

3. Department of Chemistry, Northwestern University, Evanston, IL 60208, USA

4. Stanford Synchrotron Radiation Lightsource, Stanford University, Menlo Park, CA 94025, USA

5. Department of Chemistry and Biochemistry, University of California Los Angeles, Los Angeles, CA 90095, USA

Abstract

Desert varnish is a dark rock coating that forms in arid environments worldwide. It is highly and selectively enriched in manganese, the mechanism for which has been a long-standing geological mystery. We collected varnish samples from diverse sites across the western United States, examined them in petrographic thin section using microscale chemical imaging techniques, and investigated the associated microbial communities using 16S amplicon and shotgun metagenomic DNA sequencing. Our analyses described a material governed by sunlight, water, and manganese redox cycling that hosts an unusually aerobic microbial ecosystem characterized by a remarkable abundance of photosynthetic Cyanobacteria in the genus *Chroococcidiopsis* as the major autotrophic constituent. We then showed that diverse Cyanobacteria, including the relevant *Chroococcidiopsis* taxon, accumulate extraordinary amounts of intracellular manganese—over two orders of magnitude higher manganese content than other cells. The speciation of this manganese determined by advanced paramagnetic resonance techniques suggested that the Cyanobacteria use it as a catalytic antioxidant—a valuable adaptation for coping with the substantial oxidative stress present in this environment. Taken together, these results indicated that the manganese enrichment in varnish is related to its specific uptake and use by likely founding members of varnish microbial communities.

Significance statement

Rock varnish is a prominent feature of desert landscapes and the canvas for many prehistoric petroglyphs. How it forms—and in particular, the basis for its extremely high manganese content—has been an enduring mystery. The work presented here establishes a biological mechanism for this manganese enrichment, underpinned by an apparent antioxidant strategy that enables microbes to survive in the harsh environments where varnish forms. The understanding that varnish is the residue of life using manganese to thrive in the desert illustrates that even in extremely stark environments, the imprint of life is omnipresent on the landscape.

Introduction

Rock varnish (also called desert varnish) is a thin, dark coating found on exposed surfaces of rocks in arid environments, comprised primarily of clay minerals and manganese and iron oxides (1–3). It has long been recognized as a geochemical puzzle (4–6) and has received considerable scientific and popular interest due to its widespread occurrence (7), association with archaeological petroglyphs (8–10), use in age dating (11–17), potential as a paleoclimate proxy (16, 18–20), and comparisons to rock coatings on Mars (21–24). However, many interpretations and applications of varnish hinge on understanding the mechanism of its formation, which remains unknown.

The most perplexing aspect of varnish is its extremely high enrichment in manganese. Varnish characteristically contains 10 to 30 wt% MnO—two to three orders of magnitude higher manganese content than typical underlying rocks or the surrounding dust from which much of the mass comprising varnish originates (2, 3, 25). Other major elements including iron, silicon, aluminum, magnesium, sodium, and titanium, though abundant, are not enriched.

Diverse microorganisms are known to be associated with varnish, but whether or not they play a role in its origin has been fiercely debated (26). Numerous processes, both abiotic (e.g., dust deposition, water leaching, photochemical manganese oxidation) and biological (e.g., microbial mediation of binding and cementation, microbial manganese oxidation), have been proposed to contribute (summarized in *SI* text), but since varnish grows very slowly—at most tens of microns over a thousand years (27)—empirical demonstration has not been attainable. While many of these processes may be relevant to varnish formation, none of them satisfactorily explains the highly and selectively enriched manganese content in varnish.

In this paper, we stepped back from the various paradigms that have been previously proposed and considered varnish formation from a new perspective. Synthesizing results from physical, chemical, and biological analyses, we reevaluated the relationship between varnish microflora and their environment and developed a hypothesis linking specific manganese accumulation to environmental adaptations of major members of the varnish microbial community.

Results

Varnish is governed by sunlight, water, and manganese redox cycling

We collected varnish on a range of rock types from seven field areas across the western United States (Fig. S1). Varnish occurs on diverse lithologies in different settings, yet there are some common developmental patterns. A close relationship between varnish and sunlight has been established—varnish develops preferentially on lit rather than shaded surfaces (28–30). Although found in arid environments, therein varnish develops preferentially with the availability of water, such as in shallow depressions on rock surfaces where dew accumulates (31) and along runoff streaks down cliff faces (32). These observations provided circumstantial evidence that light and water play important roles in varnish formation.

To understand better the physical processes controlling varnish development, we examined depositional textures in petrographic thin sections using backscatter scanning electron microscopy (SEM). Varnish cross sections revealed micron-scale, sub-horizontal laminations that reflect its accretionary mode of growth (Fig. 1*B*, Fig. S2) (3). In all varnish samples examined, we observed laminae with crinkly to columnar or domal textures that mark an emergent topography similar to that of stromatolites—macroscopic sedimentary structures commonly understood as mineralized residue of ancient microbial mats (33). In certain stromatolites, these textures have been interpreted in terms of light-dependent growth, models of which come from studies of coral growth (34). On a topographically irregular surface, relative highs receive more light while relative lows get shaded, thus the highs grow higher forming columnar features. In varnish, these microtextures supported the relationship with sunlight that has been documented with macroscale field observations and strengthened the evidence for a role for light in varnish genesis.

Textural data also supported the previously documented relationship with water by suggesting that varnish formation involves manganese redox cycling through a soluble phase. Desert dust samples that we collected at varnish sites contained manganese as both trace Mn^{2+} in igneous minerals and

manganese oxide particles (Fig. S2*E*). We observed detrital particles embedded in varnish, but high-resolution chemical imaging by energy dispersive spectroscopy (EDS) and nanoscale secondary ion mass spectrometry (NanoSIMS) showed that these particles are largely silicate minerals, while the manganese-rich oxide material that characterizes varnish is in the laminated cement itself (Figs. S3-4). Since manganese is water soluble in its divalent form but not as higher-valent oxides, redox cycling is required to mobilize and reprecipitate the manganese oxide in dust to form the accreting oxide cements.

The manganese oxide mineral phase in varnish has been described as poorly crystalline birnessite (2)—a phase comprised of manganese octahedra organized in layers (35); it is formally $Mn^{4+}O_2$, but can incorporate a substantial fraction of Mn^{3+} instead of Mn^{4+} when accompanied by charge balance with heteroatoms (Na^+, K^+, Ba^{2+}, etc.) between the layers (36). Using synchrotron X-ray absorption near-edge structure (XANES) spectroscopy and multiple-energy 'redox' mapping at the manganese K-edge, we found that varnish birnessite is not homogenous in its redox properties. Although predominantly Mn^{4+}, it contains common discrete microscale domains with variable and considerable mixtures of Mn^{3+} (Fig. 1*C-E*, Fig. S2). This heterogeneity is consistent with the view that manganese redox cycling occurs within varnish, and the distribution of these domains indicates that such cycling is not restricted to surficial processes contributing to the ongoing accretion of varnish, but rather also characterizes the ecosystem that exists within well-developed varnish.

Numerous manganese redox cycling processes occur in Earth surface environments. Manganese oxidation with atmospheric O_2 is thermodynamically favorable and can be catalyzed by metal oxide surfaces or bacterial and fungal enzymes (37–40). Manganese reduction can also be catalyzed by microbial processes, notably anaerobic respiration (41), and with an appropriate electron donor present (e.g., organic carbon) photochemical reduction of manganese oxides occurs readily even in aerobic settings (42–44). While any of these processes might contribute to varnish development and the manganese redox heterogeneity we observed, the relationship between varnish and sunlight raised the hypothesis that photochemistry—and perhaps photobiology—might play particularly important roles.

To visualize organic matter in varnish, we used NanoSIMS imaging of sulfur. ^{32}S appeared throughout varnish, notably concentrated in micron-scale particles that sit along varnish laminations and are distinct from detrital grains observed in the ^{28}Si and ^{57}Fe mass channels (Fig. S4*A*). To confirm that this sulfur reflects organics rather than just sulfur-bearing mineral phases, we used XANES spectroscopy to assess electronic structure at the sulfur K-edge. The sulfur in varnish displayed complex speciation; sulfur is present in organic forms observed in biological material (variable mixtures of thiols with disulfides, sulfoxides, and sulfonates) as well as sulfate salts (Fig. S4*B*). The fact that varnish is rich in organics and exposed to light—conditions that promote manganese photoreduction—and yet the manganese is maintained largely as Mn^{4+} oxides supports the view that dynamic redox cycling occurs within varnish.

The varnish microbial community is characterized by Cyanobacteria

To investigate the microbial diversity in varnish, we extracted DNA from varnish samples along with samples of surrounding surface soils for comparison. 16S rRNA gene amplicon sequencing revealed a varnish-specific microbial community that is distinct from surrounding soils, but common among varnishes from different rock types and locations (Figs. S5-7). The taxa we recovered are consistent with previous studies of varnish microbiology (45–48), with the bacterial families Xenococcaceae, Rubrobacteraceae, Acetobacteraceae, Sporichthyaceae, and Gemmatimonadaceae distinguishing the varnish community.

The most striking observation from our community analyses was the high abundance of Cyanobacteria associated with varnish, specifically members of *Chroococcidiopsis*—a genus of the family Xenococcaceae noted for its ability to live in extreme environments, with high tolerance for radiation and desiccation (49–52) (Fig. 2). 16S sequences assigned to the Xenococcaceae (either *Chroococcidiopsis* or unassigned below the family level) were recovered from 48 out of 49 varnish samples and accounted for 25.9% of all sequence reads and 98.7% of cyanobacterial reads recovered from varnish. In contrast, the Xenococcaceae represented only 0.06% of all reads and 1.4% of cyanobacterial

reads from soil. The single most abundant unique *Chroococcidiopsis* sequence variant accounted for 8% of all reads from varnish and was completely absent from soil samples. Top BLAST hits for this sequence in the NCBI nr database included a remarkable representation of hits from previous varnish studies, and 99.6% identity with isolate Ryu 1-3 from the University of the Ryukyus in Okinawa (53), which we obtained for further study. Additionally, epifluorescence microscopy on varnish flakes revealed sarcinoid clusters of cells that are morphologically characteristic of baeocystous *Chroococcidiopsis* cells (Fig. 2*D*).

Shotgun metagenomic sequencing of select samples further emphasized the importance of these Cyanobacteria in the varnish community. 21.9% of raw metagenome reads were assigned to Cyanobacteria, corroborating their high abundances in the 16S amplicon data (Fig. S6*C*). We recovered six high-quality cyanobacterial metagenome-assembled genomes (MAGs), all belonging to members of the Chroococcidiopsidaceae (Fig. S8). These Cyanobacteria appeared to be the main primary producers of the varnish community—of nine MAGs containing genes for the Calvin-Benson-Bassham cycle, six were Cyanobacteria, with three others representing considerably less abundant taxa (of Armatimonadota, Rhodobacteraceae, and Beijerinckiaceae). No MAGs appeared to encode alternative carbon fixation pathways. Furthermore, we only recovered one additional MAG with phototrophic reaction center genes (an aerobic photoheterotroph of the Acetobacteraceae), indicating that the Cyanobacteria are the only taxa in varnish capable of using light as an energy source for autotrophic growth. Sulfur K-edge spectra of *Chroococcidiopsis* cells were similar to the organic content we observed within varnish (Fig. S4), supporting the interpretation that these taxa are the main primary producers of the ecosystem.

By both abundance and function, we concluded that *Chroococcidiopsis* are extremely important taxa in varnish and are likely founding autotrophic members of the community. When considered in this context, the physical evidence that sunlight and water play important roles in varnish development can be interpreted to suggest that these Cyanobacteria, which grow with light and water, might be involved in the formation of varnish itself.

Metagenomic data also revealed that the varnish microbial communities mark a highly aerobic ecosystem, far more so than typical sediments or soils. No obligate anaerobic metabolisms were

represented by the gene content of our MAGs—consistent with the known physiologies of the major taxa identified in our 16S analysis. Indeed, nearly all MAGs contained high-potential bioenergetic systems utilized in aerobic respiration as well as reactive oxygen species detoxification systems. Of the 38 MAGs we recovered from varnish samples, we observed heme-copper O_2 reductase and/or *bd* O_2 reductase complexes in 37 of them, a superoxide dismutase in 34 of them, and a catalase in 24 of them. These aerobic adaptations are perhaps unsurprising considering the proximity of this community to atmospheric O_2 and exposure to solar irradiation; they are biochemical attestations to the high degrees of oxidative stress encountered in this harsh environment.

Cyanobacteria accumulate manganese likely as a non-enzymatic antioxidant system

The significance of cyanobacterial taxa as abundant keystone members of the varnish ecosystem suggested to us a previously unexplored connection between the microbial community and the manganese content of varnish. The model freshwater cyanobacterium *Synechocystis* sp. PCC 6803 has been shown to accumulate a massive pool of intracellular Mn^{2+}, up to 10^8 atoms per cell, which when averaged over cell volume is the equivalent concentration of 100 mM manganese—four orders of magnitude higher than their growth medium (54). We hypothesized that if this hyper-accumulation of manganese occurs broadly in the Cyanobacteria—particularly those taxa that are dominant members of the varnish community—then this physiological peculiarity might underpin varnish development.

We examined two strains of *Chroococcidiopsis* (PCC 7433 and Ryu 1-3, the closest cultured relative to the varnish sequences), *Synechocystis* sp. PCC 6803, and *Gloeobacter violaceous* PCC 7421, a very deep branching member of the photosynthetic Cyanobacteria (Fig. S9), along with non-cyanobacterial model organisms *Escherichia coli* K12 and *Shewanella oneidensis* MR-1 for comparison. Using inductively coupled plasma mass spectrometry (ICP-MS) to measure total cellular manganese, we observed dramatic manganese accumulation in all cyanobacterial strains; the highest values were seen in Ryu 1-3, with over two orders of magnitude greater manganese content than that seen in *E. coli* or *S. oneidensis* (Fig. 3*A*).

To probe the speciation of this copious intracellular manganese, we combined electron paramagnetic resonance (EPR), electron nuclear double resonance (ENDOR), and electron spin echo envelope modulation (ESEEM) spectroscopies. The EPR spectra of all Cyanobacteria examined showed that the majority of the Mn^{2+} pool exists in soluble high symmetry complexes with low molecular weight ligands (denoted H-Mn^{2+}) and not in low symmetry complexes with strongly chelating ligands or bound to proteins (denoted L-Mn^{2+}) (Fig. 3*B*, Fig. S10*A-B*). ^{31}P, ^{1}H ENDOR and ^{14}N ESEEM measurements along with ^{13}C ENDOR on labeled cells further revealed that this manganese binds undetectably low amounts of phosphate and nitrogenous ligands, and is instead predominantly bound to carboxylato ligands (Fig. 3*C*, Fig. S10*C-D* and *SI* text). Notably, previously studied organisms with abundant cellular H-Mn^{2+} exhibited significant contributions from phosphate and nitrogenous ligands (55, 56); this difference makes the Mn^{2+} pool in Cyanobacteria unique.

This speciation data implied the functional role for Mn^{2+} in cyanobacterial physiology as a small molecule antioxidant system. Certain H-Mn^{2+} complexes are known to act as effective catalytic antioxidants of superoxide and peroxide (57, 58), and accumulation of H-Mn^{2+} has been shown to predict oxidative stress resistance (55, 59). This physiology is well documented in radiation-resistant taxa such as *Deinococcus radiodurans* (60, 61), but was not previously known in Cyanobacteria. The H-Mn^{2+} accumulation shown here helps explain how the Cyanobacteria in varnish cope with the extremely aerobic, arid, and irradiated environments where varnish is found. Taken together with the high abundance of cyanobacterial taxa associated with varnish, the establishment of this cyanobacterial manganese-based antioxidant system provides an adaptive biological mechanism behind the enrichment of manganese in rock varnish.

Discussion

Varnish develops in environments that are extremely harsh, where protective strategies against irradiation and oxidative stress are essential for life to survive. The presence of the varnish microbial community has been noted in such terms; for example, varnish provides a habitat for microbial life

shielded by oxide minerals that absorb UV radiation (62). However, up until now, how and why the varnish—with its high and specific enrichment in manganese—got there in the first place was a mystery. Based on the data presented here, we propose that *varnish itself is a hallmark of life prevailing in these extreme environments*.

We showed that Cyanobacteria of the genus *Chroococcidiopsis* are intimately and abundantly associated with varnish. Moreover, being the main primary producers of the ecosystem, these organisms must establish prior to heterotrophic taxa that depend upon them for organic substrates, implicating them as likely founding members of the microbial community. Evidence tying sunlight and water to varnish development provided further, albeit circumstantial, evidence that photosynthetic Cyanobacteria play a fundamental role. We then demonstrated that diverse Cyanobacteria, including *Chroococcidiopsis*, accumulate substantial quantities of H-Mn^{2+}. This phenomenon is well established as an antioxidant strategy that enables tremendous oxidative stress resistance (58, 59, 63); indeed, there is no other known physiological purpose for such elevated manganese concentrations. The cyanobacterial H-Mn^{2+} pool that we observed is comparable in magnitude to the most radiation resistant organisms known (60).

Many previous studies have focused on a mechanism of manganese oxidation as the key to varnish formation. However, in such aerobic environments, manganese oxidation may proceed through numerous pathways with both biological (*SI* text and Fig. S8) and abiotic (including photochemical and autocatalytic) mechanisms. Rather than oxidation, it is the selective enrichment of manganese that represents a process of singular importance to the development of varnish. The manganese hyper-accumulation that we observed in *Chroococcidiopsis* provides a simple and effective, ecologically relevant, physiological explanation for this manganese enrichment.

Thus, we propose a new hypothesis for varnish formation (Fig. 4). These Cyanobacteria grow on sunlit rock surfaces with intermittent access to water, sequestering high concentrations of manganese in their cells and exploiting the unique redox chemistry of manganese complexes as a catalytic antioxidant system that enables their survival in such a harsh environment. When they die, the residue from their biomass provides an enriched manganese source that is ultimately oxidized to form the oxide mineral

cements that comprise varnish. Since varnish forms over timescales of millennia, a well-developed varnish sample represents the time integrated manganese accumulation of many, many generations of cells, which are sparsely distributed at any given time. This was demonstrated in our analyses of varnish samples in petrographic thin section—the Mn^{2+} content of any living cells is negligible next to thousands of years of accumulated Mn^{3+}/Mn^{4+} mineral. In addition to solving the mystery of manganese enrichment, cyanobacterial exudates and necromass also supply fresh organic carbon to the varnish ecosystem. This provides a growth substrate for the heterotrophic microbes that inhabit varnish, as well as an effective electron donor for photochemical manganese reduction. Taken together, our results place the activity of extremophilic Cyanobacteria as a key driver of both the physical and biological development of varnish ecosystems.

Methods

Study locations & sampling

Samples were taken from seven field locations across the southwestern United States, ranging from arid to semiarid climates, corresponding to rock varnish Type I and Type II designated by Macholdt *et al.* (64) (Fig. S1). Underlying lithologies including mafic, felsic, and sedimentary rocks. Varnished rocks were collected with ethanol-sterilized gloves into Whirl-Pak sample bags, and surface soil samples were collected using sterile spatulas into falcon tubes. Ultrathin sections cut orthogonal to the varnished surface were prepared by David Mann at High Mesa Petrographics (Los Alamos, NM). The thin sections revealed varnishes ranging in thickness from ~5 μm to ~100 μm, likely representing hundreds to thousands of years of development (27). For DNA sampling, varnished rocks were returned to the lab, gently rinsed with sterile nanopure water using a 50 mL syringe and 16-gauge needle, and allowed to dry. For DNA extraction, varnish was removed from rock surfaces by scraping with flame-sterilized steel brushes, spatulas, and dental picks, and collected in a weigh boat. Each varnish sample was obtained from a separate rock. Dust analysis was conducted on a fine grained (clay-silt sized) fraction of surface soil from the Barstow field location.

SEM/EDS/NanoSIMS

SEM and EDS analyses were conducted in the Caltech Geological and Planetary Sciences Division Analytical Facility on a ZEISS 1550VP Field Emission SEM, with a Robinson-type backscatter electron detector and an Oxford X-Max SDD X-ray EDS system. Varnish was imaged at 10 to 20 kV with working distances of 7 to 10 mm and magnifications of 500 to 4500 x. NanoSIMS analyses were conducted in the Caltech Microanalysis Center, on a Cameca NanoSIMS 50L using a Cs^+ primary ion beam with 50 nm resolution, primary ion current of 1 pA, and dwell time of 3.5 ms/pixel. The masses of ^{12}C, $^{12}C^{14}N$, ^{32}S, ^{31}P, ^{18}O, ^{28}Si, $^{55}Mn^{16}O$, and $^{57}Fe^{16}O$ were collected. Petrographic thin sections were coated with 20 nm graphite using a Turbo carbon evaporator for SEM/EDS, and with 40 nm gold using a Cressington HR metal sputtering coater for NanoSIMS. EDS and NanoSIMS images were examined using ImageJ.

Synchrotron X-ray spectroscopy

Synchrotron analyses were conducted at the Stanford Synchrotron Radiation Lightsource, on X-ray microprobes at beamlines 2-3 for the manganese K-edge and 14-3 for the sulfur K-edge. The 2-3 beam was energy calibrated using the pre-edge feature of $KMnO_4$ at 6543.34 eV, and 14-3 was calibrated using the pre-edge feature of $Na_2S_2O_3$ at 2472.02 eV. Multiple energy maps for producing images of manganese redox state were collected at 6553, 6557, 6559, 6562, and 6570 eV, with 3 µm resolution. For both spectra and maps, least squares fitting was done using a spessartine standard spectrum (65) representative of igneous Mn^{2+}, manganic oxide (65) and feitknechtite (66) standard spectra as two different Mn^{3+}-bearing phases, and an internal endmember spectrum for $Mn^{4+}O_2$. Spectra and maps were reduced and fit using the SIXPACK (67) and SMAK (68) software packages respectively (https://www.sams-xrays.com/). Colormaps were converted to viridis using fixthejet (https://fixthejet.ecrlife.org/).

DNA extraction & sequencing

Genomic DNA was extracted from 10-50 mg varnish scrapings or soil using the FastDNA™ SPIN kit for soil (MP Biomedicals). DNA yields were quantified using a Qubit 2.0 fluorometer with the HS dsDNA assay kit (ThermoFisher Scientific).

To generate 16S rRNA gene libraries, the V3-V4 hypervariable region of the 16S gene was amplified using degenerate primers (341-806 pair) from ~12.5 ng genomic DNA with KAPA HiFi HotStart ReadyMix (denaturation at 95 °C for 3 minutes, 20 cycles of 95 °C for 30 seconds, 55 °C for 30 seconds, and 72 °C for 30 seconds, and a final extension of 72 °C for 5 minutes before holding at 4 °C). A second round of PCR added Nextera XT v2 indexes (Illumina) (denaturation at 95 °C for 3 minutes, 8 cycles of 95 °C for 30 seconds, 55 °C for 30 seconds, and 72 °C for 30 seconds and a final extension of 72 °C for 5 minutes before holding at 4 °C). The amplicons were cleaned up using AMPure XP beads (Beckman Coulter). A no template control was processed, and did not show a band in the amplicon region. The amplicons were pooled and sequenced on the Illumina MiSeq platform generating paired end 301 bp reads using the MiSeq reagent kit v3 (600 cycles) (Illumina).

Two representative varnish DNA samples (sample 24, sandstone from Babbitt Ranch, AZ and sample 41, basalt from Mesa Prieta, NM) were selected for metagenomic sequencing. These samples were selected based on 16S amplicon data as likely candidates to recover high quality genomes for the major taxa in the varnish community. No aspects of the communities in these two samples were outliers, and together they represent samples from two different locations and very different rock types.

Illumina shotgun libraries were prepared using the Next Ultra DNA II library preparation kit (New England Biolabs). DNA was fragmented using a Covaris E220; the ends were made blunt and adapters and indexes added onto the fragments to generate Illumina libraries, which were eluted in DNA elution buffer (Zymo). Libraries were quantified using the KAPA Illumina/Universal library quantification kit, normalized based on qPCR results, and sequenced on the Illumina NextSeq platform generating paired end 151 bp reads using the NextSeq 500/550 high output kit v2.5 (300 cycles) (Illumina).

16S data processing

16S amplicon sequence reads from 61 varnish samples and 19 soil samples were processed using QIIME2 (69) to generate feature tables containing the frequencies of each unique sequence variant per sample. Quality filtering, denoising, merging of paired end reads, and chimera removal were done using DADA2 (70). The QIIME2 q2-feature-classifier plugin was used to align the sequences against the Greengenes 13.8 database (71) and assign taxonomy. 1 sample which returned < 2000 total reads was omitted from downstream analyses. NMDS & ANOSIM analyses were done by calculating a Bray dissimilarity matrix using the vegan ecology package in R (72). LEfSe analysis was done using the Microbiome Analyst tool (73) with default settings. For the phylogenetic tree presented in this paper, sequences were aligned with the SINA aligner (74) and converted from fasta format to phylip format with SEAVIEW (75). The phylogenetic tree was constructed using PhyML (76) implemented on the website http://www.atgc-montpellier.fr/phyml/ with default settings, and the resulting tree was visualized using FigTree.

Metagenomic data processing

Taxonomic assignments of raw metagenome reads were done using the MG-RAST analysis platform(77). Metagenome sequence read quality control, *de novo* assembly, and binning of metagenome assembled genomes (MAGs) was performed largely on the KBase platform(78). Combinations of read pre-processing, assembly, and binning methods were tested and evaluated based on the quality and quantity of final MAGs. Read pre-processing included no processing (raw reads), Bloom Filter Read Error Correction (79) v. r181 (drop_unique_kmer_reads = 1, kmer_size = 33), Trimmomatic (80) v. 0.38 (LEADING:3 TRAILING:3 SLIDINGWINDOW:4:15 MINLEN:125), BBMap (81) v37.93 (bbduk.sh -Xmx1g, k=15, mink=10, ktrim=r, tbo). Processed reads were assembled with MEGAHIT (82) v2.4.2 (meta-large), MetaSPAdes (83) v1.2.4 (K-mer sizes 33, 55, 77, 99, and 127), or IDBA-UD (84) v1.0.4. Assemblies were performed with minimum contig size of 2000 bp. MAGs were constructed with two

automated binning tools, MaxBin2 (85) v2.2.4 and MetaBAT2 (86) v1.7 with default settings except for minimum contig lengths of 2500 bp. All MAGs from combinations of the above setting were evaluated for quality using the CheckM software v1.0.18 on KBase with default settings. Sufficiently high-quality bins were defined using the Parks *et al.* cutoff of completeness – 5*contamination > 50 (87). Bin taxonomy was assigned using GTDB-Tk v0.3.2 using gtdbtk release 89 (88). The number of bins passing this cutoff and their phylogenetic affiliations were used to compare between the different parameters described above. The greatest number of quality bins was achieved with Trimmomatic, MetaSPAdes and MetaBAT2 for sample 41 and Trimmomatic + BBmap mink, MetaSPAdes and MetaBAT2 for sample 24. Other combinations of parameters produced a subset of less complete versions of the final bins, not completely different MAGs. Genome annotation was conducted using the RASTtk algorithm (89) v.0.1.1 in KBase, as well as a local implementation of the KOfamScan (90) software for the KEGG database. The canonical metabolic pathways encoded by these genomes were parsed using KEGG-decoder (91), and additional analyses of genes of interest, including MCOs and pili, were done using local BLAST searches for known systems (see supplementary material). Cytochromes *c* were identified by counting heme-binding domains (CxxCH motifs), and beta barrels were predicted using the PRED-TMBB tool (92).

Fluorescence microscopy

Fluorescence microscopy was performed at the Center of Integrated Nanotechnologies at Los Alamos National Laboratory. Cavity well microscope slides (Globe Scientific) were used to mount varnish flakes and fitted with #1.5 coverslips. Imaging was conducted on a Zeiss Axio Observer D1 inverted microscope equipped with a 100x, 1.3 NA oil immersion objective and a BP 640/30 excitation and BP 690/50 emission filter set to observe chlorophyll autofluorescence.

Culture conditions

Synechocystis sp. PCC 6803 (obtained from Richard Debus, University of California Riverside), *Gloeobacter violaceous* PCC 7421 (obtained from ATCC), *Chroococcidiopsis cubana* PCC 7433

(obtained from ATCC), and Ryu 1-3 (obtained from Shoichiro Suda, University of the Ryukyus), were grown in liquid BG11 medium (93) which contains 9 μM $MnCl_2$. 6803 and Ryu 1-3 were kept in a 30°C shaking incubator under white fluorescent lights, 7421 and 7433 were kept at room temperature with natural light on a windowsill. *Escherichia coli* and *Shewanella oneidensis* were grown in liquid LB medium, in a 30°C shaking incubator. Cells were harvested after 24 hours growth for *E. coli* and *S. oneidensis*, ~1 week for 6803, and ~1 month for 7421 and 7433. Ryu 1-3 was sufficiently slow growing that once a month all biomass in the culture was transferred to fresh medium.

ICP-MS

Harvested cells were washed in sterile nanopure water to remove residual media and any extracellular material, and then frozen at -80°C. Frozen cells were lyophilized in a SpeedVac vacuum concentrator, and the dried cell pellet was transferred to a 50 mL DigiTUBE (SCP Science). The dry cell pellet was digested for two hours at 95 °C in 3 mL concentrated (70%) nitric acid purified by distillation at Caltech. The digested cell pellet was then diluted to 50 mL with nanopure water. ICP-MS analysis was conducted in the Caltech Environmental Analysis Center on an Agilent 8800 ICP-MS Triple Quad using a collision/reaction cell with O_2 as the reaction gas. Sulfur was analyzed as $^{32}S^{16}O$ (mass 48). Measurements were calibrated using a multielement standard (Inorganic Ventures, IV-ICPMS-71A, Lot M2-MEB658498). Due to the extremely clumpy phenotype of the *Chroococcidiopsis* cells hindering accurate cell counts, manganese content was reported as a ratio to sulfur content as a proxy for normalizing to biomass. Cell-specific manganese abundance was determined for *Synechocystis* by cell counts in a Petroff Hausser counting chamber (Hausser Scientific).

EPR/ENDOR/ESEEM spectroscopy

Concentrated cell suspensions in 40% glycerol were loaded into custom-made quartz EPR tubes, and then flash frozen in liquid N_2. Paramagnetic resonance spectroscopy was conducted in the Hoffman Laboratory at Northwestern University. 35 GHz continuous-wave (CW) EPR spectra were recorded using

a lab-built EPR spectrometer (94). Absorption-display EPR spectra of frozen cells and manganese standards were collected in the "rapid passage" mode at 2 K as previously described (56, 59) (MW frequency 34.9 GHz, MW power 1 mW, temperature 2 K, modulation amplitude 1 G, time constant 64 ms, scan rate 1 kG/min).

Pulsed ENDOR/ESEEM spectra were recorded using a lab-built 35 GHz pulsed EPR spectrometer (95). All spectra were recorded at 2 K using an immersion helium cryostat. ^{31}P, ^{1}H Davies ENDOR spectra were recorded using the pulse sequence $\pi - T_{rf} - \pi/2 - \tau - \pi - \tau -$ echo, where T_{rf} is the time interval for the radio-frequency (RF) pulse, which is randomly hopped (96) (MW frequency 34.8 GHz, temperature 2 K, magnetic field ~ 12.5 kG, $t_{\pi/2}$ = 60 ns, τ = 400 ns, T_{rf} = 160 µs, repetition time 10 ms). The ENDOR response is enhanced by broadening the frequency-bandwidth of the RF pulse using a 100 kHz white noise source (97). ^{13}C Mims ENDOR spectra were recorded using the pulse sequence $\pi/2 - \tau - \pi/2 - T_{rf} - \pi/2 - \tau -$ echo (MW frequency 34.8 GHz, temperature 2 K, magnetic field ~ 12.5 kG, $t_{\pi/2}$ = 50 ns, τ = 400 ns, T_{rf} = 20 µs, repetition time 10 ms). 3-Pulse ESEEM spectra were recorded using the pulse sequence, $\pi/2 - \tau - \pi/2 - T - \pi/2 - \tau -$ echo where T is the time varied between second and third microwave pulses, with four-step phase cycling to suppress unwanted Hahn and refocused echoes (96) (MW frequency 34.8 GHz, temperature 2 K, magnetic field ~ 12.5 kG, $t_{\pi/2}$ = 30 ns, τ = 400 ns, T = 1 µs with 20 ns step size, repetition time 10 ms).

Data availability

Sequence data are available as FASTQ files on the Sequence Read Archive (SRA), under BioProject ID PRJNA630476. Binned genomes from samples 24 and 41 are provided as supplemental files.

Acknowledgments

This research was supported by NSF grant IOS-1833247 (UFL and WWF), NSF GRFP (UFL), NIH grant GM111097 (BMH), NASA Exobiology grant 18-EXO18-0040 (WWF and NLL), and LANL LDRD project 20170414ER (CMY and NLL). Use of the Stanford Synchrotron Radiation Lightsource, SLAC National Accelerator Laboratory, was supported by the DOE Office of Basic Energy Sciences under Contract No. DE-AC02-76SF00515, and the SSRL Structural Molecular Biology Program supported by the DOE Office of Biological and Environmental Research and the NIH, NIGMS (P41GM103393). This project benefited from the use of instrumentation made available by the Caltech Environmental Analysis Center, Caltech Microanalysis Center, and Caltech Geological and Planetary Sciences Division Analytical Facility. Fieldwork for this project was conducted on ancestral lands of the Hopi, Pueblo, Ute,

Apsáalooke, and Serrano peoples. We thank George Rossman, Hope Johnson, Jared Leadbetter, and Yonaton Goldsmith for helpful discussions and insight; Chi Ma, Yunbin Guan, and Nathan Dalleska for help with SEM, NanoSIMS, and ICP-MS analyses; Nick Edwards and Sharon Bone for support at SSRL; Babbitt Ranches for allowing us to sample; Shoichiro Suda for supplying the Ryu 1-3 strain; and Jason Tor and the environmental microbiology class at Hampshire College for sparking UFL's interest in rock varnish research.

Author contributions

UFL, WWF, CMY, NLL, and JSV designed research. UFL, WWF, CMY, and NLL collected samples. UFL, WWF, JSM, and SMW performed SEM/EDS, NanoSIMS, and synchrotron analyses on petrographic thin sections. UFL, CMY, and ADA extracted DNA. UFL, CMY, GX, and GLC performed bioinformatic analyses. DPM performed fluorescence microscopy. UFL grew cyanobacterial cultures. JSM and DRM performed ICP-MS analyses. AS and BMH performed paramagnetic resonance analyses. UFL wrote the manuscript with input from WWF and JSV. All co-authors edited and approved the manuscript.

References

1. R. M. Potter, G. R. Rossman, Desert Varnish: The Importance of Clay Minerals. *Science* **196**, 1446–1448 (1977).

2. R. M. Potter, G. R. Rossman, The manganese- and iron-oxide mineralogy of desert varnish. *Chem. Geol.* **25**, 79–94 (1979).

3. R. S. Perry, J. B. Adams, Desert varnish: evidence for cyclic deposition of manganese. *Nature* **276**, 489–491 (1978).

4. von Humboldt, A., *Personal narrative of travels to the quinoctial regions of America during the years 1799-1804 by Alexander von Humboldt and Aime Bonpland* (London, Bell, 1812).

5. Darwin, C. R., *Journal of researches into the natural history and geology of the countries visited during the voyage of H.M.S. Beagle round the world, under the Command of Capt. Fitz Roy, R.N.*, 2d edition (London, John Murray, 1845).

6. A. Lucas, *The blackened rocks of the Nile cataracts and of the Egyprian deserts* (National Printing Department, 1905).

7. C. G. Engel, R. P. Sharp, Chemical Data on Desert Varnish. *Geol. Soc. Am. Bull.* **69**, 487–518 (1958).

8. M. Dietzel, H. Kolmer, P. Pölt, S. Simic, Desert varnish and petroglyphs on sandstone – Geochemical composition and climate changes from Pleistocene to Holocene (Libya). *Geochemistry* **68**, 31–43 (2008).

9. D. S. Whitley, C. M. Santoro, D. Valenzuela, Climate Change, Rock Coatings, and the Archaeological Record. *Elements* **13**, 183–186 (2017).

10. D. S. Whitley, *Cave paintings and the human spirit: the origin of creativity and belief* (Prometheus Books, 2009).

11. R. I. Dorn, Cation-Ratio Dating: A New Rock Varnish Age-Determination Technique. *Quat. Res.* **20**, 49–73 (1983).

12. R. I. Dorn, P. B. Clarkson, M. F. Nobbs, L. L. Loendorf, D. S. Whitley, New Approach to the Radiocarbon Dating of Rock Varnish, with Examples from Drylands. *Ann. Assoc. Am. Geogr.* **82**, 136–151 (1992).

13. P. R. Bierman, A. R. Gillespie, Evidence Suggesting That Methods of Rock-Varnish Cation-Ratio Dating Are neither Comparable nor Consistently Reliable. *Quat. Res.* **41**, 82–90 (1994).

14. W. Beck, Ambiguities in Direct Dating of Rock Surfaces Using Radiocarbon Measurements. *Science* **280**, 2132–2139 (1998).

15. A. Watchman, A review of the history of dating rock varnishes. *Earth-Sci. Rev.* **49**, 261–277 (2000).

16. T. Liu, W. S. Broecker, Millennial-scale varnish microlamination dating of late Pleistocene geomorphic features in the drylands of western USA. *Geomorphology* **187**, 38–60 (2013).

17. D. S. Whitley, Rock Art Dating and the Peopling of the Americas. *J. Archaeol.* **2013**, 1–15 (2013).

18. T. Liu, W. S. Broecker, J. W. Bell, C. W. Mandeville, Terminal Pleistocene wet event recorded in rock varnish from Las Vegas Valley, southern Nevada. *Palaeogeogr. Palaeoclimatol. Palaeoecol.* **161**, 423–433 (2000).

19. T. Liu, W. S. Broecker, Rock varnish evidence for latest Pleistocene millennial-scale wet events in the drylands of western United States. *Geology* **36**, 403–406 (2008).

20. Y. Goldsmith, Y. Enzel, M. Stein, Systematic Mn fluctuations in laminated rock varnish developed on coeval early Holocene flint artifacts along a climatic transect, Negev desert, Israel. *Quat. Res.* **78**, 474–485 (2012).

21. R. S. Perry, V. M. Kolb, From Darwin to Mars: desert varnish as a model for preservation of complex (bio)chemical systems in R. B. Hoover, A. Y. Rozanov, Eds. (2004), pp. 136–144.

22. D. Krinsley, R. I. Dorn, B. DiGregorio, Astrobiological Implications of Rock Varnish in Tibet. *Astrobiology* **9**, 551–562 (2009).

23. N. L. Lanza, *et al.*, Examining natural rock varnish and weathering rinds with laser-induced breakdown spectroscopy for application to ChemCam on Mars. *Appl. Opt.* **51**, B74–B82 (2012).

24. N. L. Lanza, *et al.*, Understanding the signature of rock coatings in laser-induced breakdown spectroscopy data. *Icarus* **249**, 62–73 (2015).

25. Y. Goldsmith, M. Stein, Y. Enzel, From dust to varnish: Geochemical constraints on rock varnish formation in the Negev Desert, Israel. *Geochim. Cosmochim. Acta* **126**, 97–111 (2014).

26. R. I. Dorn, "Rock Varnish" in *Geochemical Sediments & Landscapes*, (Blackwell, 2007), pp. 246–297.

27. T. Liu, W. S. Broecker, How fast does rock varnish grow? *Geology* **28**, 183 (2000).

28. X. Xu, *et al.*, Characteristics of desert varnish from nanometer to micrometer scale: A photo-oxidation model on its formation. *Chem. Geol.* **522**, 55–70 (2019).

29. T. Waragai, Effects of Rock Surface Temperature on Exfoliation, Rock Varnish, and Lichens on a Boulder in the Hunza Valley, Karakoram Mountains, Pakistan. *Arct. Alp. Res.* **30**, 184 (1998).

30. A. Lu, *et al.*, Photoelectric conversion on Earth's surface via widespread Fe- and Mn-mineral coatings. *Proc. Natl. Acad. Sci.* **116**, 9741–9746 (2019).

31. C. E. Jones, Characteristics and Origin of Rock Varnish from the Hyperarid Coastal Deserts of Northern Peru. *Quat. Res.* **35**, 116–129 (1991).

32. P. H. Larson, R. I. Dorn, Painting Yosemite Valley: A Case Study of Rock Coatings Encountered at Half Dome. *Phys. Geogr.* **33**, 165–182 (2012).

33. T. Bosak, A. H. Knoll, A. P. Petroff, The Meaning of Stromatolites. *Annu. Rev. Earth Planet. Sci.* **41**, 21–44 (2013).

34. R. R. Graus, I. G. Macintyre, Light Control of Growth Form in Colonial Reef Corals: Computer Simulation. *Science* **193**, 895–897 (1976).

35. J. E. Post, Manganese oxide minerals: Crystal structures and economic and environmental significance. *Proc. Natl. Acad. Sci.* **96**, 3447–3454 (1999).

36. F. T. Ling, J. E. Post, P. J. Heaney, E. S. Ilton, The relationship between Mn oxidation state and structure in triclinic and hexagonal birnessites. *Chem. Geol.* **479**, 216–227 (2018).

37. B. M. Tebo, *et al.*, Biogenic Manganese Oxides: Properties and Mechanisms of Formation. *Annu. Rev. Earth Planet. Sci.* **32**, 287–328 (2004).

38. U. F. Lingappa, D. R. Monteverde, J. S. Magyar, J. S. Valentine, W. W. Fischer, How manganese empowered life with dioxygen (and vice versa). *Free Radic. Biol. Med.*, 113–125 (2019).

39. K. J. Parchert, M. N. Spilde, A. Porras-Alfaro, A. M. Nyberg, D. E. Northup, Fungal Communities Associated with Rock Varnish in Black Canyon, New Mexico: Casual Inhabitants or Essential Partners? *Geomicrobiol. J.* **29**, 752–766 (2012).

40. J. J. Morgan, Kinetics of reaction between O2 and Mn(II) species in aqueous solutions. *Geochim. Cosmochim. Acta* **69**, 35–48 (2005).

41. C. R. Myers, K. H. Nealson, Bacterial Manganese Reduction and Growth with Manganese Oxide as the Sole Electron Acceptor. *Science* **240**, 1319–1321 (1988).

42. T. David. Waite, I. C. Wrigley, Ron. Szymczak, Photoassisted dissolution of a colloidal manganese oxide in the presence of fulvic acid. *Environ. Sci. Technol.* **22**, 778–785 (1988).

43. F. F. Marafatto, *et al.*, Rate and mechanism of the photoreduction of birnessite (MnO_2) nanosheets. *Proc. Natl. Acad. Sci.* **112**, 4600–4605 (2015).

44. W. G. Sunda, S. A. Huntsman, G. R. Harvey, Photoreduction of manganese oxides in seawater and its geochemical and biological implications. *Nature* **301**, 234–236 (1983).

45. N. Lang-Yona, *et al.*, Insights into microbial involvement in desert varnish formation retrieved from metagenomic analysis: The desert varnish microbiome. *Environ. Microbiol. Rep.* **10**, 264–271 (2018).

46. A. Esposito, *et al.*, Comparison of Rock Varnish Bacterial Communities with Surrounding Non-Varnished Rock Surfaces: Taxon-Specific Analysis and Morphological Description. *Microb. Ecol.* **70**, 741–750 (2015).

47. D. E. Northup, *et al.*, Diversity of rock varnish bacterial communities from Black Canyon, New Mexico. *J. Geophys. Res. Biogeosciences* **115**, G02007 (2010).

48. K. R. Kuhlman, P. Venkat, M. T. La Duc, G. M. Kuhlman, C. P. McKay, Evidence of a microbial community associated with rock varnish at Yungay, Atacama Desert, Chile. *J. Geophys. Res. Biogeosciences* **113** (2008).

49. C. S. Cockell, A. C. Schuerger, D. Billi, E. I. Friedmann, C. Panitz, Effects of a Simulated Martian UV Flux on the Cyanobacterium, *Chroococcidiopsis* sp. 029. *Astrobiology* **5**, 127–140 (2005).

50. D. Billi, E. I. Friedmann, K. G. Hofer, M. G. Caiola, R. Ocampo-Friedmann, Ionizing-Radiation Resistance in the Desiccation-Tolerant Cyanobacterium Chroococcidiopsis. *Appl. Environ. Microbiol.* **66**, 1489–1492 (2000).

51. C. Fagliarone, *et al.*, Avoidance of protein oxidation correlates with the desiccation and radiation resistance of hot and cold desert strains of the cyanobacterium Chroococcidiopsis. *Extremophiles* **21**, 981–991 (2017).

52. D. C. Lacap-Bugler, *et al.*, Global Diversity of Desert Hypolithic Cyanobacteria. *Front. Microbiol.* **8**, 867 (2017).

53. X. Nguyen, S. Sumimoto, S. Suda, Unexpected High Diversity of Terrestrial Cyanobacteria from the Campus of the University of the Ryukyus, Okinawa, Japan. *Microorganisms* **5**, 69 (2017).

54. N. Keren, M. J. Kidd, J. E. Penner-Hahn, H. B. Pakrasi, A light-dependent mechanism for massive accumulation of manganese in the photosynthetic bacterium Synechocystis sp. PCC 6803. *Biochemistry* **41**, 15085–15092 (2002).

55. A. Sharma, *et al.*, Responses of Mn2+ speciation in Deinococcus radiodurans and Escherichia coli to -radiation by advanced paramagnetic resonance methods. *Proc. Natl. Acad. Sci.* **110**, 5945–5950 (2013).

56. M. Tsednee, *et al.*, Manganese co-localizes with calcium and phosphorus in *Chlamydomonas* acidocalcisomes and is mobilized in manganese-deficient conditions. *J. Biol. Chem.* **294**, 17626–17641 (2019).

57. K. Barnese, E. B. Gralla, J. S. Valentine, D. E. Cabelli, Biologically relevant mechanism for catalytic superoxide removal by simple manganese compounds. *Proc. Natl. Acad. Sci.* **109**, 6892–6897 (2012).

58. V. C. Culotta, M. J. Daly, Manganese Complexes: Diverse Metabolic Routes to Oxidative Stress Resistance in Prokaryotes and Yeast. *Antioxid. Redox Signal.* **19**, 933–944 (2013).

59. A. Sharma, *et al.*, Across the tree of life, radiation resistance is governed by antioxidant Mn^{2+}, gauged by paramagnetic resonance. *Proc. Natl. Acad. Sci.* **114**, E9253–E9260 (2017).

60. M. J. Daly, Accumulation of Mn(II) in Deinococcus radiodurans Facilitates Gamma-Radiation Resistance. *Science* **306**, 1025–1028 (2004).

61. M. J. Daly, *et al.*, Small-Molecule Antioxidant Proteome-Shields in Deinococcus radiodurans. *PLoS ONE* **5**, e12570 (2010).

62. K. H. Nealson, Ex-phot: a new take on primitive utilization of solar energy. *Environ. Microbiol. Rep.* **7**, 33–35 (2015).

63. F. S. Archibald, I. Fridovich, Manganese and defenses against oxygen toxicity in Lactobacillus plantarum. *J. Bacteriol.* **145**, 442–451 (1981).

64. D. S. Macholdt, *et al.*, Characterization and differentiation of rock varnish types from different environments by microanalytical techniques. *Chem. Geol.* **459**, 91–118 (2017).

65. J. E. Johnson, S. M. Webb, C. Ma, W. W. Fischer, Manganese mineralogy and diagenesis in the sedimentary rock record. *Geochim. Cosmochim. Acta* **173**, 210–231 (2016).

66. J. E. Johnson, *et al.*, Real-Time Manganese Phase Dynamics during Biological and Abiotic Manganese Oxide Reduction. *Environ. Sci. Technol.* **50**, 4248–4258 (2016).

67. S. M. Webb, SIXPack a Graphical User Interface for XAS Analysis Using IFEFFIT. *Phys. Scr.*, 1011 (2005).

68. S. M. Webb, I. McNulty, C. Eyberger, B. Lai, The MicroAnalysis Toolkit: X-ray Fluorescence Image Processing Software. *AIP Conf. Proc.* **1365**, 196–199 (2011).

69. E. Bolyen, *et al.*, Reproducible, interactive, scalable and extensible microbiome data science using QIIME 2. *Nat. Biotechnol.* **37**, 852–857 (2019).

70. B. J. Callahan, *et al.*, DADA2: High-resolution sample inference from Illumina amplicon data. *Nat. Methods* **13**, 581–583 (2016).

71. T. Z. DeSantis, *et al.*, Greengenes, a Chimera-Checked 16S rRNA Gene Database and Workbench Compatible with ARB. *Appl. Environ. Microbiol.* **72**, 5069–5072 (2006).

72. J. Oksanen, *et al.*, *Vegan: Community Ecology Package, R package, v. 2.4–6* (2018).

73. A. Dhariwal, *et al.*, MicrobiomeAnalyst: a web-based tool for comprehensive statistical, visual and meta-analysis of microbiome data. *Nucleic Acids Res.* **45**, W180–W188 (2017).

74. E. Pruesse, J. Peplies, F. O. Glöckner, SINA: Accurate high-throughput multiple sequence alignment of ribosomal RNA genes. *Bioinformatics* **28**, 1823–1829 (2012).

75. N. Galtier, M. Gouy, C. Gautier, SEAVIEW and PHYLO_WIN: two graphic tools for sequence alignment and molecular phylogeny. *Bioinformatics* **12**, 543–548 (1996).

76. S. Guindon, *et al.*, New algorithms and methods to estimate maximum-likelihood phylogenies: assessing the performance of PhyML 3.0. *Syst. Biol.* **59**, 307–321 (2010).

77. F. Meyer, *et al.*, The metagenomics RAST server – a public resource for the automatic phylogenetic and functional analysis of metagenomes. *BMC Bioinformatics* **9**, 386 (2008).

78. A. P. Arkin, *et al.*, KBase: The United States Department of Energy Systems Biology Knowledgebase. *Nat. Biotechnol.* **36**, 566–569 (2018).

79. H. Li, BFC: correcting Illumina sequencing errors. *Bioinformatics* **31**, 2885–2887 (2015).

80. A. M. Bolger, M. Lohse, B. Usadel, Trimmomatic: a flexible trimmer for Illumina sequence data. *Bioinformatics* **30**, 2114–2120 (2014).

81. B. Bushnell, BBMap: A Fast, Accurate, Splice-Aware Aligner.

82. D. Li, C.-M. Liu, R. Luo, K. Sadakane, T.-W. Lam, MEGAHIT: an ultra-fast single-node solution for large and complex metagenomics assembly via succinct de Bruijn graph. *Bioinformatics* **31**, 1674–1676 (2015).

83. S. Nurk, D. Meleshko, A. Korobeynikov, P. A. Pevzner, metaSPAdes: a new versatile metagenomic assembler. *Genome Res.* **27**, 824–834 (2017).

84. Y. Peng, H. C. M. Leung, S. M. Yiu, F. Y. L. Chin, IDBA-UD: a de novo assembler for single-cell and metagenomic sequencing data with highly uneven depth. *Bioinforma. Oxf. Engl.* **28**, 1420–1428 (2012).

85. Y.-W. Wu, B. A. Simmons, S. W. Singer, MaxBin 2.0: an automated binning algorithm to recover genomes from multiple metagenomic datasets. *Bioinformatics* **32**, 605–607 (2016).

86. D. D. Kang, J. Froula, R. Egan, Z. Wang, MetaBAT, an efficient tool for accurately reconstructing single genomes from complex microbial communities. *PeerJ* **3**, e1165 (2015).

87. D. H. Parks, *et al.*, Recovery of nearly 8,000 metagenome-assembled genomes substantially expands the tree of life. *Nat. Microbiol.* **2**, 1533–1542 (2017).

88. P.-A. Chaumeil, A. J. Mussig, P. Hugenholtz, D. H. Parks, GTDB-Tk: a toolkit to classify genomes with the Genome Taxonomy Database. *Bioinformatics*, btz848 (2019).

89. T. Brettin, *et al.*, RASTtk: A modular and extensible implementation of the RAST algorithm for building custom annotation pipelines and annotating batches of genomes. *Sci. Rep.* **5**, 8365 (2015).

90. T. Aramaki, *et al.*, KofamKOALA: KEGG ortholog assignment based on profile HMM and adaptive score threshold. *Bioinformatics*, btz859 (2019).

91. E. D. Graham, J. F. Heidelberg, B. J. Tully, Potential for primary productivity in a globally-distributed bacterial phototroph. *ISME J.* **12**, 1861–1866 (2018).

92. P. G. Bagos, T. D. Liakopoulos, I. C. Spyropoulos, S. J. Hamodrakas, PRED-TMBB: a web server for predicting the topology of -barrel outer membrane proteins. *Nucleic Acids Res.* **32**, W400–W404 (2004).

93. R. Carpentier, *Photosynthesis Research Protocols* (Humana Press, 2004).

94. M. M. Werst, C. E. Davoust, B. M. Hoffman, Ligand spin densities in blue copper proteins by q-band proton and nitrogen-14 ENDOR spectroscopy. *J. Am. Chem. Soc.* **113**, 1533–1538 (1991).

95. C. E. Davoust, P. E. Doan, B. M. Hoffman, Q-Band Pulsed Electron Spin-Echo Spectrometer and Its Application to ENDOR and ESEEM. *J. Magn. Reson. A* **119**, 38–44 (1996).

96. A. Schweiger, G. Jeschke, *Principles of pulse electron paramagnetic resonance* (Oxford University Press, 2001).

97. B. M. Hoffman, V. J. Derose, J. L. Ong, C. E. Davoust, Sensitivity Enhancement in Field-Modulated CW ENDOR via RF Bandwidth Broadening. *J. Magn. Reson. A* **110**, 52–57 (1994).

Supplemental text

Building on previous hypotheses of varnish formation

Varnish genesis is the topic of a substantial body of previous work, which has shed important light on a wide range of sedimentary, geochemical, and biological factors. Analyses of accretionary microtextures (1–3) and trace element and isotopic compositions (4–7) demonstrated that the material comprising varnish originates from dust external to the host rock, mediated by atmospheric precipitation. Other studies examined the importance of silica in the varnish material, proposing processes of silica dissolution, gelling, condensing, and hardening as controlling the development of such rock coatings (8, 9). The presence of biology in varnish has been documented by various techniques including culturing (10, 11), DNA analyses (10, 12–16), and SEM imaging of filamentous and coccoidal forms (2, 10, 17); and a role for microbes in binding together the oxides and clay minerals that comprise varnish has been suggested (18).

Several different mechanisms for the enrichment and oxidation of manganese have been proposed; this includes both biological and abiotic processes. Hypotheses attributing the manganese in varnish to biological activity generally invoke microbial manganese oxidation (10, 11, 19–22). Model organisms like *Bacillus* sp. SG-1 and *Pseudomonas putida* MnB-1 strains are known to oxidize Mn^{2+} extracellularly (Fig. S8*E*)—generating manganese oxides that accumulate on their exosporia or glycocalyx, respectively (23). Previous studies have isolated similar bacteria from varnish (10, 11), and suggested that manganese oxide encrusted microbes could provide the manganese source for the varnish cement (18). Fungi are also known to oxidize manganese (24, 25), and have similarly been implicated in varnish (20, 26). In contrast, abiotic models of varnish formation have advocated thermodynamic arguments for the preferential mobility of manganese at certain pH regimes, enabling the enrichment of manganese from dust deposited on the rock surface through water leaching (7). The abiotic oxidation of manganese can be catalyzed by either mineral surface coordination (27) or photochemistry (28), both of which have been invoked in varnish hypotheses. Many of these processes could contribute to varnish

accretion and manganese oxidation, however, none of them entirely explain the high concentrations and specific enrichment of manganese in this material.

It has been argued that the very slow rate of varnish formation rules out mechanisms based on biological processes that are known from laboratory experiments to proceed at more rapid rates (7, 18, 29). However, it is important to note that rates of microbial activities under idealized laboratory conditions are not necessarily representative of the natural environment (30). Most cells in the environment are not actively growing exponentially most of the time. Especially in harsh environments, such as those relevant to varnish formation. In this context microbial growth can be very slow, and limited by water availability or nutrient availability, or inhibited by excessive heat or radiation. The relatively rapid growth rates we can sometimes achieve in the laboratory enable us to study processes that might otherwise happen too slowly to capture on experimental timescales—but this has very little bearing on how quickly such processes might be occurring in the environment.

Genomic insights into manganese cycling in the varnish ecosystem

Our synchrotron data indicated that manganese redox cycling (both oxidation and reduction) not only contributes to the formation of varnish, it continues in well-developed varnish—hinting that the varnish is characterized by unique opportunities biology to interface with manganese redox cycling. Biological processes can catalyze both reductions and oxidations of manganese. In order to better understand which manganese redox reactions might be mediated by varnish community members, we searched for genomic hallmarks of known biological metal cycling processes in our varnish metagenomic datasets. This included both reactions that could be directly coupled to cellular energy conservation, and reactions catalyzed by enzymes but not directly involved in energy metabolism.

Coupling metabolic processes to redox reactions of insoluble, extracellular metal oxides requires the ability to transport electrons into or out of cells. This process has been best studied in the model systems for dissimilatory metal oxide reduction—*Shewanella* and *Geobacter*, that use large multiheme cytochromes (MHC) embedded in outer membrane beta barrel porins as conduits between their electron

transport chains and extracellular electron acceptors (Fig. S8*B*) (31). A similar biochemical strategy for extracellular electron transfer (EET) has been identified in organisms with metabolisms based on both iron and manganese oxidation (32, 33). None of our varnish MAGs were phylogenetically associated with known EET capable organisms, however this trait is broadly distributed throughout many bacterial phyla. Therefore, we used a gene-centric method to assess EET capability—an approach similar to the strategy employed in a recent survey of neutrophilic iron oxidizer genomes (32). We specifically screened for the porin proteins from known MHC-porin complexes MtrB (*Shewanella oneidensis*) (34), MtoB (*Sideroxydans lithotrophicus*) (35), and PioB (*Rhodopseudomonas palustrus*) (36), along with PCC3 and PCC4, hypothetical porin-cytochrome complex gene clusters from other known iron oxidizers (32). We also screened more generally for any MHCs by counting the occurrence of heme binding domains (CxxCH motifs), and determined whether or not these fell within gene clusters that also contained predicted beta barrel porins. Notably, we did not detect any MHCs with greater than 10 hemes—a characteristic of many organisms capable of EET—and none of our predicted MHCs resided in porin-MHC gene clusters. This suggested that microbial metabolisms based on EET via large MHCs are uncommon in varnish—far rarer than in soils and sediments.

The dearth of organisms exploiting the oxides in varnish for dissimilatory metal reduction is understandable given that varnish appears to be a thoroughly aerobic environment—O_2 will always be a better electron acceptor for respiration. Unlike the anaerobic sediment environments wherein dissimilatory metal reduction is an important biogeochemical process, varnish may present a habitat with different opportunities for metal cycling. In this setting, biological manganese reduction might be more likely to occur via processes aimed at mobilizing and assimilating manganese rather than for core energy metabolism.

Pili have been implicated in metal reduction in *Geobacter* (Fig. S8*D*), and a pilin system in Cyanobacteria—homologous to the one from *Geobacter*—has been proposed to allow *Synechocystis* sp. PCC 6803 to grow on manganese oxides as their sole manganese source, presumably via reductive dissolution (37). While the role of pili in metal reduction has been the topic of some controversy (38), it is

worth noting the presence of these pilin proteins (COG2165) in several of our varnish MAGs, including 5 of the 6 Chroococcidiopsiaceae MAGs.

Not all known iron oxidizing organisms use large MHCs—another strategy for EET involves an outer membrane cytochrome with a single heme bound in the center of a beta barrel porin that transfers electrons from iron to other small periplasmic cytochromes (Fig. S8*C*). In principle, an analogous system can be imagined for manganese, though one has not as yet been identified. We used BLAST to search for the outer membrane cytochromes Cyc2 (*Acidothiobacillus ferrooxidans*) (39), Cyt572 (*Leptospirillum* spp.) (40), and Cyc2PV-1 (*Mariprofundus ferrooxydans* PV-1) (41), all distant homologs broadly found in iron oxidizers. No significant hits for these proteins were identified in any of our MAGs.

We also counted total putative *c*-type cytochrome encoding genes in each MAG, because it has been observed that organisms involved in metal redox cycling tend to have an abundance of these genes (e.g. 111 in *Geobacter sulfurreducens* and 42 in *Shewanella oneidensis*) (42, 43). Some of our MAGs were comparably rich in *c*-type cytochromes, including some MHCs with up to 7 CxxCH motifs. One MAG of the Chitinophagaceae had 52 cytochromes, the largest with 7 heme binding domains; and one MAG of the Armatimonadota had 48 cytochromes, the largest with 5 heme binding domains. Our Chroococcidiopsiaceae MAGs were fairly rich in cytochromes as well—the 4 Chroococcidiopsiaceae MAGs with > 93% completeness had 32, 32, 41, and 44 cytochrome genes, respectively.

Other known modes of microbial manganese oxidation use extracellular or outer membrane multicopper oxidase (MCO) enzymes to catalyze manganese oxidation (Fig. S8*E*) (44). This reaction is not coupled to metabolic energy conservation, and therefore does not require a mechanism of EET. A hypothetical porin-MCO complex has been proposed, suggested to function similarly to the porin-MHC complexes known to engage in EET, but currently lacks experimental support (Fig. S8*F*) (32). This hypothetical system is homologous to PcoAB, a periplasmic copper detoxification system. We specifically screened for MnxG (*Pseudomonas putida* GB-1) (45), CotA (*Bacillus pumilus* WH4) (46), MoxA (*Pedomicrobium* sp. ACM 3067) (47), McoA (*Pseudomonas putida* GB-1) (45), and MofA (*Leptothrix discophora*, with high homology to OmpB from *Geobacter sulfurreducens*), as MCOs

implicated in manganese oxidation, along with PcoAB; we also screened for MCOs more generally, as determined by cupredoxin domains annotated in KBase. We identified MoxA, a protein known to exhibit manganese oxidation and laccase activity, in 5 of our MAGs, and PcoAB in two of them. Other MCOs are present in many of our MAGs (including 5 of the 6 Chroococcidiopsiaceae MAGs), but given the catalytic breadth of this diverse family of enzymes, we hesitated to draw definitive conclusions about their specific functions based on genomic data alone.

The Cyanobacteria provide an additional mechanism for manganese oxidation that has not previously been discussed in the context of varnish—photosystem II oxidizes manganese (Fig. S8*G*), as exemplified by the photoassembly of the Mn_4CaO_5 cluster that enables water oxidation (48). There are several lines of evidence that oxygenic photosynthesis evolved in the ancestors of the Cyanobacteria from a version of anoxygenic photosynthesis based on manganese oxidation (49, 50), and it is possible this metabolism still exists in their modern decedents. Oxygenic phototrophs are often thought of as having an unlimited electron donor for photosynthesis, but under arid conditions water is scarce, and maintaining the ability to use manganese as an alternative electron donor might be useful. Thus, we propose an additional potential function for cyanobacterial manganese accumulation, particularly in the extremophilic, desiccation-resistant *Chroococcidiopsis*: these taxa might stockpile an electron reservoir to enable photosynthetic electron transport without using up water. This, along with the observations of a H-Mn^{2+} antioxidant system, suggests two potential physiological reasons that extreme manganese accumulation could be a useful ecological strategy for cyanobacterial survival in the arid, oxidizing environments where varnish forms.

Mn^{2+} speciation probed by paramagnetic resonance techniques

The EPR spectra of H-Mn^{2+} complexes discussed here are characteristic of an S = 5/2 ion with small zero-field splitting (ZFS), with the principal ZFS parameter, D, much less than the microwave quantum (hv) (51). Such spectra show a central ^{55}Mn (I = 5/2) sextet arising from hyperfine interactions, A ~ 90 G, that is associated with transitions between the $m_s = +1/2$ and $-1/2$ electron-spin substates.

These features ride on, and are flanked by, significantly broader wings—signals from the four satellite transitions involving the other electron-spin substates (m_s ±5/2 ⇔ ±3/2; ±3/2 ⇔ ±1/2). The net absorption spectrum is the sum of the five envelopes of these five transitions among substates. The cellular Mn^{2+} EPR spectra of all Cyanobacteria showed a resolved six-line ^{55}Mn hyperfine pattern centered at g-2 (~12 kG) riding on relatively narrow wings extending to both high and low magnetic field with a total field span of 4 kG, features which are suppressed in the derivative-mode CW EPR spectra (Fig. 3*B*). Frozen standard solutions of Mn^{2+} complexed with orthophosphate, polyphosphate, and bicarbonate show similar high-symmetry EPR spectra with relatively narrow wings (Fig. S10*A*). Much broader wings are seen in low-symmetry complexes with chelating ligands (such as EDTA) and proteins (such as MnSOD) (Fig. S10*A-B*).

The frozen solution ENDOR spectrum of an I = 1/2 nucleus, such as ^{31}P, ^{13}C, ^{1}H, coupled to S = 5/2 Mn^{2+} comprises a set of doublets centered at the nuclear Larmor frequency, each split by a multiple of the electron-nuclear hyperfine coupling (A). The primary doublet is associated with the $m_s = \pm 1/2$ electron spin sublevels of Mn^{2+} and is split by A; weaker satellite doublets associated with the $m_s = \pm 3/2$ and ±5/2 sublevels are split by 3A and 5A. All spectra in this study displayed ^{1}H signals that could be assigned to the protons of bound water (Fig. 3*C*). For a phosphate moiety bound to a Mn^{2+} center we focused on the sharp $m_s = \pm 1/2$ ^{31}P doublet. The relative intensities of ^{31}P and ^{1}H signals provided a means of assessing Mn^{2+} speciation (52).

A ^{14}N nucleus (I = 1) directly coordinated with Mn^{2+} creates modulation in the electron spin echo decay, which is dominated by ^{14}N hyperfine interaction (53). To quantitate ^{14}N ESEEM responses from cellular Mn^{2+}, we chose as a standard the ^{14}N response from the Mn-imidazole complex, which binds one imidazole and (presumably) five waters. Mn-imidazole showed a strong time dependent modulation signal; no such signal was observed in any of the cyanobacterial samples (Fig. S10*C*). The absence of such a signal indicated that manganese resides in locations without a significant pool of nitrogenous ligands.

Cell biological insights suggest the cyanobacterial Mn^{2+} pool is periplasmic

The massive pool of manganese that we observed to accumulate in cyanobacterial cells is unlikely to be either cytoplasmic or extracellular. In the cytoplasm, where the cyanobacterial carbon concentrating mechanism accumulates substantial HCO_3^- (54), such a high abundance of Mn^{2+} would precipitate $MnCO_3$ minerals. Furthermore, the cytoplasm contains polyphosphate granules, which have a high affinity for Mn^{2+} (55–58). We did not observe such minerals, nor any manganese complexed by phosphates, in any of the cyanobacterial strains we examined. The manganese speciation that we did see —manganese complexed by small organic acids—is unlikely to be extracellular. Thus, we concluded that this manganese pool is most likely periplasmic.

Building on this is another line of evidence; this manganese pool cannot be disrupted by a vigorous water wash, supporting the interpretation that it is intra rather than extracellular. However, ~80% of it can be extracted with an EDTA wash, which is consistent with a periplasmic pool but not a cytoplasmic pool (59). Furthermore, a transporter that keeps manganese in the periplasm rather than the cytoplasm is known to be an essential aspect of manganese homeostasis in Cyanobacteria (60).

Relevance to Mars and astrobiological implications

Many previous studies have highlighted the resemblance of varnish to phenomena observed on Mars (9, 17). However, while many dark, shiny rocks have been observed on Mars, these are largely ventifacted rather than coated. Varnish itself (defined as a mixture of manganese and iron oxides and clay minerals) has not been definitively identified on Mars, and indeed only one instance of a potentially high-manganese surface coating has been found (61). The definitive manganese oxide phases that have been discovered on Mars do not appear to be associated with surface exposures, rather they precipitated in the subsurface (62). Therefore, we hesitate to assert any strong astrobiological interpretations for biological processes underpinning terrestrial varnish.

Supplemental references

1. R. S. Perry, J. B. Adams, Desert varnish: evidence for cyclic deposition of manganese. *Nature* **276**, 489–491 (1978).

2. D. Krinsley, Models of rock varnish formation constrained by high resolution transmission electron microscopy. *Sedimentology* **45**, 711–725 (1998).

3. L. A. J. Garvie, D. M. Burt, P. R. Buseck, Nanometer-scale complexity, growth, and diagenesis in desert varnish. *Geology* **36**, 215 (2008).

4. N. Thiagarajan, C.-T. Aeolus Lee, Trace-element evidence for the origin of desert varnish by direct aqueous atmospheric deposition. *Earth Planet. Sci. Lett.* **224**, 131–141 (2004).

5. M. Fleisher, T. Liu, W. S. Broecker, W. Moore, A clue regarding the origin of rock varnish. *Geophys. Res. Lett.* **26**, 103–106 (1999).

6. H. Bao, G. M. Michalski, M. H. Thiemens, Sulfate oxygen-17 anomalies in desert varnishes. *Geochim. Cosmochim. Acta* **65**, 2029–2036 (2001).

7. Y. Goldsmith, M. Stein, Y. Enzel, From dust to varnish: Geochemical constraints on rock varnish formation in the Negev Desert, Israel. *Geochim. Cosmochim. Acta* **126**, 97–111 (2014).

8. R. S. Perry, *et al.*, Baking black opal in the desert sun: The importance of silica in desert varnish. *Geology* **34**, 537 (2006).

9. R. S. Perry, V. M. Kolb, From Darwin to Mars: desert varnish as a model for preservation of complex (bio)chemical systems in R. B. Hoover, A. Y. Rozanov, Eds. (2004), pp. 136–144.

10. D. E. Northup, *et al.*, Diversity of rock varnish bacterial communities from Black Canyon, New Mexico. *J. Geophys. Res. Biogeosciences* **115**, G02007 (2010).

11. F. E. Palmer, J. T. Staley, R. G. E. Murray, T. Counsell, J. B. Adams, Identification of manganese-oxidizing bacteria from desert varnish. *Geomicrobiol. J.* **4**, 343–360 (1986).

12. K. R. Kuhlman, *et al.*, Diversity of Microorganisms within Rock Varnish in the Whipple Mountains, California. *Appl. Environ. Microbiol.* **72**, 1708–1715 (2006).

13. K. R. Kuhlman, P. Venkat, M. T. La Duc, G. M. Kuhlman, C. P. McKay, Evidence of a microbial community associated with rock varnish at Yungay, Atacama Desert, Chile. *J. Geophys. Res. Biogeosciences* **113** (2008).

14. N. Lang-Yona, *et al.*, Insights into microbial involvement in desert varnish formation retrieved from metagenomic analysis: The desert varnish microbiome. *Environ. Microbiol. Rep.* **10**, 264–271 (2018).

15. A. Esposito, *et al.*, Comparison of Rock Varnish Bacterial Communities with Surrounding Non-Varnished Rock Surfaces: Taxon-Specific Analysis and Morphological Description. *Microb. Ecol.* **70**, 741–750 (2015).

16. A. Esposito, L. Borruso, J. E. Rattray, L. Brusetti, E. Ahmed, Taxonomic and functional insights into rock varnish microbiome using shotgun metagenomics. *FEMS Microbiol. Ecol.* **95**, fiz180 (2019).

17. D. Krinsley, R. I. Dorn, B. DiGregorio, Astrobiological Implications of Rock Varnish in Tibet. *Astrobiology* **9**, 551–562 (2009).

18. R. I. Dorn, "Rock Varnish" in *Geochemical Sediments & Landscapes*, (Blackwell, 2007), pp. 246–297.

19. W. E. Krumbein, Über den Einfluß der Mikroflora auf die exogene Dynamik (Verwitterung und Krustenbildung). *Geol. Rundsch.* **58**, 333–363 (1968).

20. G. Grote, W. E. Krumbein, Microbial precipitation of manganese by bacteria and fungi from desert rock and rock varnish. *Geomicrobiol. J.* **10**, 49–57 (1992).

21. R. I. Dorn, T. M. Oberlander, Microbial Origin of Desert Varnish. *Science* **213**, 1245–1247 (1981).

22. B. Hungate, *et al.*, Characterization of manganese-oxidizing (MnII→MnIV) bacteria from Negev Desert rock varnish: implications in desert varnish formation. *Can. J. Microbiol.* **33**, 939–943 (1987).

23. B. M. Tebo, *et al.*, Biogenic Manganese Oxides: Properties and Mechanisms of Formation. *Annu. Rev. Earth Planet. Sci.* **32**, 287–328 (2004).

24. C. M. Hansel, C. A. Zeiner, C. M. Santelli, S. M. Webb, Mn(II) oxidation by an ascomycete fungus is linked to superoxide production during asexual reproduction. *Proc. Natl. Acad. Sci. U. S. A.* **109**, 12621–12625 (2012).

25. N. Miyata, Y. Tani, K. Iwahori, M. Soma, Enzymatic formation of manganese oxides by an Acremonium-like hyphomycete fungus, strain KR21-2. *FEMS Microbiol. Ecol.* **47**, 101–109 (2004).

26. K. J. Parchert, M. N. Spilde, A. Porras-Alfaro, A. M. Nyberg, D. E. Northup, Fungal Communities Associated with Rock Varnish in Black Canyon, New Mexico: Casual Inhabitants or Essential Partners? *Geomicrobiol. J.* **29**, 752–766 (2012).

27. J. J. Morgan, Kinetics of reaction between O2 and Mn(II) species in aqueous solutions. *Geochim. Cosmochim. Acta* **69**, 35–48 (2005).

28. X. Xu, *et al.*, Characteristics of desert varnish from nanometer to micrometer scale: A photo-oxidation model on its formation. *Chem. Geol.* **522**, 55–70 (2019).

29. D. H. Krinsley, B. DiGregorio, R. I. Dorn, J. Razink, R. Fisher, Mn-Fe-Enhancing Budding Bacteria in Century-Old Rock Varnish, Erie Barge Canal, New York. *J. Geol.* **125**, 317–336 (2017).

30. M. Bergkessel, D. W. Basta, D. K. Newman, The physiology of growth arrest: uniting molecular and environmental microbiology. *Nat. Rev. Microbiol.* **14**, 549–562 (2016).

31. D. J. Richardson, *et al.*, The “porin-cytochrome” model for microbe-to-mineral electron transfer. *Mol. Microbiol.* **85**, 201–212 (2012).

32. S. He, R. A. Barco, D. Emerson, E. E. Roden, Comparative Genomic Analysis of Neutrophilic Iron(II) Oxidizer Genomes for Candidate Genes in Extracellular Electron Transfer. *Front. Microbiol.* **8**, 1584 (2017).

33. H. Yu, J. Leadbetter, in review. *Nature* (2020).

34. A. S. Beliaev, D. A. Saffarini, Shewanella putrefaciens mtrB encodes an outer membrane protein required for Fe(III) and Mn(IV) reduction. *J. Bacteriol.* **180**, 6292–6297 (1998).

35. J. Liu, *et al.*, Identification and Characterization of MtoA: A Decaheme c-Type Cytochrome of the Neutrophilic Fe(II)-Oxidizing Bacterium Sideroxydans lithotrophicus ES-1. *Front. Microbiol.* **3**, 37 (2012).

36. Y. Jiao, D. K. Newman, The pio operon is essential for phototrophic Fe(II) oxidation in Rhodopseudomonas palustris TIE-1. *J. Bacteriol.* **189**, 1765–1773 (2007).

37. J. J. Lamb, M. F. Hohmann-Marriott, Manganese acquisition is facilitated by PilA in the cyanobacterium Synechocystis sp. PCC 6803. *PLOS ONE* **12**, e0184685 (2017).

38. F. Wang, *et al.*, Structure of Microbial Nanowires Reveals Stacked Hemes that Transport Electrons over Micrometers. *Cell* **177**, 361-369.e10 (2019).

39. C. Castelle, *et al.*, A New Iron-oxidizing/O_2-reducing Supercomplex Spanning Both Inner and Outer Membranes, Isolated from the Extreme Acidophile *Acidithiobacillus ferrooxidans*. *J. Biol. Chem.* **283**, 25803–25811 (2008).

40. C. Jeans, *et al.*, Cytochrome 572 is a conspicuous membrane protein with iron oxidation activity purified directly from a natural acidophilic microbial community. *ISME J.* **2**, 542–550 (2008).

41. R. A. Barco, *et al.*, New Insight into Microbial Iron Oxidation as Revealed by the Proteomic Profile of an Obligate Iron-Oxidizing Chemolithoautotroph. *Appl. Environ. Microbiol.* **81**, 5927–5937 (2015).

42. T. E. Meyer, *et al.*, Identification of 42 Possible Cytochrome C Genes in the *Shewanella oneidensis* Genome and Characterization of Six Soluble Cytochromes. *OMICS J. Integr. Biol.* **8**, 57–77 (2004).

43. B. A. Methe, Genome of Geobacter sulfurreducens: Metal Reduction in Subsurface Environments. *Science* **302**, 1967–1969 (2003).

44. A. V. Soldatova, *et al.*, Mn(II) oxidation by the multicopper oxidase complex Mnx: A coordinated two-stage Mn(II)/(III) and Mn(III)/(IV) mechanism. *J. Am. Chem. Soc.* (2017) https:/doi.org/10.1021/jacs.7b02772.

45. K. Geszvain, J. K. McCarthy, B. M. Tebo, Elimination of Manganese(II,III) Oxidation in Pseudomonas putida GB-1 by a Double Knockout of Two Putative Multicopper Oxidase Genes. *Appl. Environ. Microbiol.* **79**, 357–366 (2013).

46. J. Su, *et al.*, CotA, a Multicopper Oxidase from Bacillus pumilus WH4, Exhibits Manganese-Oxidase Activity. *PLoS ONE* **8**, e60573 (2013).

47. J. P. Ridge, *et al.*, A multicopper oxidase is essential for manganese oxidation and laccase-like activity in Pedomicrobium sp. ACM 3067. *Environ. Microbiol.* **9**, 944–953 (2007).

48. H. Bao, R. L. Burnap, Photoactivation: The Light-Driven Assembly of the Water Oxidation Complex of Photosystem II. *Front. Plant Sci.* **7** (2016).

49. J. E. Johnson, *et al.*, Manganese-oxidizing photosynthesis before the rise of cyanobacteria. **110**, 11238–11243 (2013).

50. W. W. Fischer, J. Hemp, J. E. Johnson, Manganese and the Evolution of Photosynthesis. *Orig. Life Evol. Biosphere J. Int. Soc. Study Orig. Life* **45**, 351–357 (2015).

51. A. Sharma, *et al.*, Responses of Mn2+ speciation in Deinococcus radiodurans and Escherichia coli to -radiation by advanced paramagnetic resonance methods. *Proc. Natl. Acad. Sci.* **110**, 5945–5950 (2013).

52. R. L. McNaughton, *et al.*, Probing in vivo Mn2+ speciation and oxidative stress resistance in yeast cells with electron-nuclear double resonance spectroscopy. *Proc. Natl. Acad. Sci. U. S. A.* **107**, 15335–15339 (2010).

53. K. M. Salikhov, Schweiger, A., Jeschke, G.:Principles of pulse electron paramagnetic resonance: XXVI, 478 pp. Oxford University Press, Oxford 2001. Hardcover GBP 95.00. *Appl. Magn. Reson.* **22**, 319–319 (2002).

54. N. M. Mangan, A. Flamholz, R. D. Hood, R. Milo, D. F. Savage, pH determines the energetic efficiency of the cyanobacterial CO_2 concentrating mechanism. *Proc. Natl. Acad. Sci.* **113**, E5354–E5362 (2016).

55. M. Tsednee, *et al.*, Manganese co-localizes with calcium and phosphorus in *Chlamydomonas* acidocalcisomes and is mobilized in manganese-deficient conditions. *J. Biol. Chem.* **294**, 17626–17641 (2019).

56. R. Docampo, "Acidocalcisomes and Polyphosphate Granules" in *Inclusions in Prokaryotes*, Microbiology Monographs., J. M. Shively, Ed. (Springer-Verlag, 2006), pp. 53–70.

57. S. P. Santos, *et al.*, The interplay between Mn and Fe in Deinococcus radiodurans triggers cellular protection during paraquat-induced oxidative stress. *Sci. Rep.* **9**, 17217 (2019).

58. M. Hauck, Effects of manganese on the viability of vegetative diaspores of the epiphytic lichen Hypogymnia physodes. *Environ. Exp. Bot.* **47**, 127–142 (2002).

59. N. Keren, M. J. Kidd, J. E. Penner-Hahn, H. B. Pakrasi, A light-dependent mechanism for massive accumulation of manganese in the photosynthetic bacterium Synechocystis sp. PCC 6803. *Biochemistry* **41**, 15085–15092 (2002).

60. F. Brandenburg, *et al.*, The *Synechocystis* Manganese Exporter Mnx Is Essential for Manganese Homeostasis in Cyanobacteria. *Plant Physiol.* **173**, 1798–1810 (2017).

61. N. L. Lanza, *et al.*, High manganese concentrations in rocks at Gale crater, Mars. *Geophys. Res. Lett.* **41**, 5755–5763 (2014).

62. N. L. Lanza, *et al.*, Oxidation of manganese in an ancient aquifer, Kimberley formation, Gale crater, Mars: Manganese Fracture Fills in Gale Crater. *Geophys. Res. Lett.* **43**, 7398–7407 (2016).

Figures

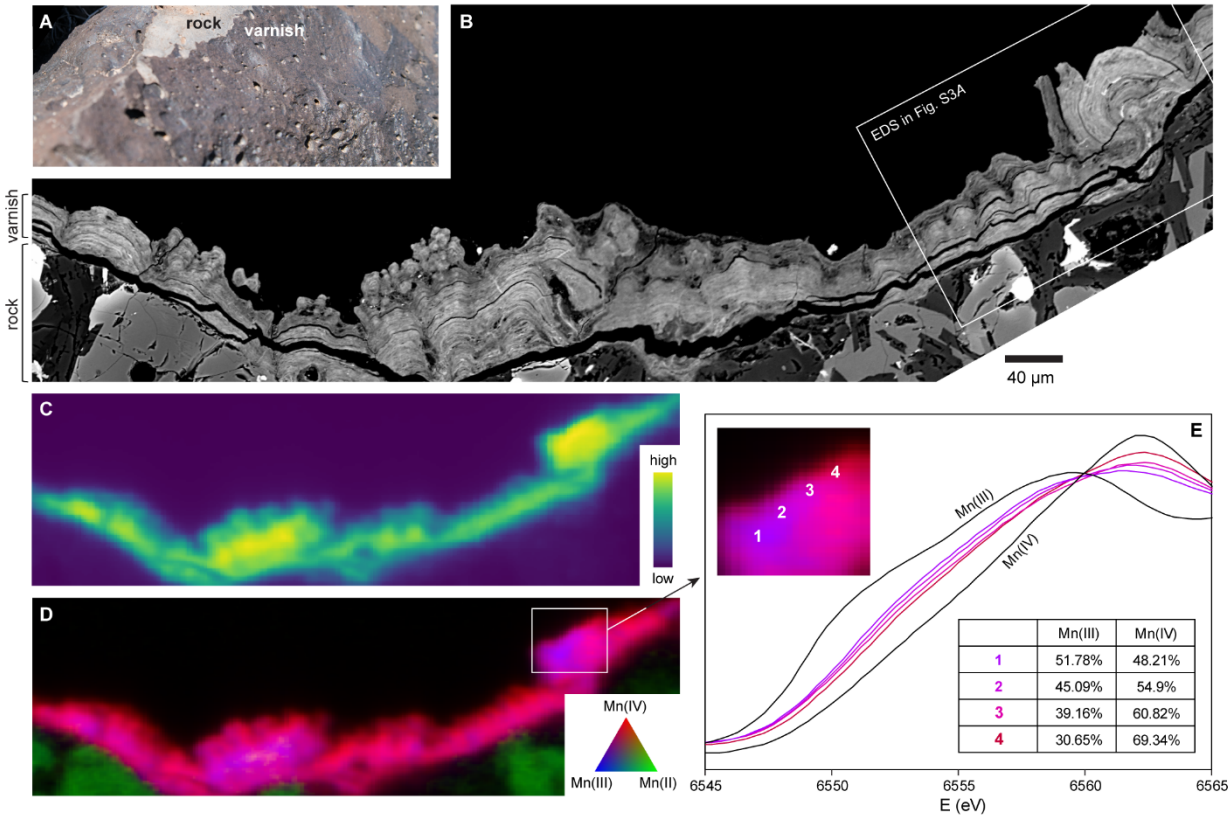

	Mn(III)	Mn(IV)
1	51.78%	48.21%
2	45.09%	54.9%
3	39.16%	60.82%
4	30.65%	69.34%

Figure 1: Stromatolitic microtextures and manganese redox states in varnish developed on a basalt flow at Babbitt Ranch, AZ. (*A*) Photograph of varnished surface with a freshly broken face revealing underlying rock. (*B*) SEM image of a cross section through the varnish-rock interface showing accretionary laminations that establish stromatolitic columns and domes. (*C*) Synchrotron X-ray microprobe map showing manganese distribution. Varnish is massively enriched in manganese relative to underlying rock. (*D*) Manganese redox map. Manganese in basalt is entirely Mn^{2+}, while varnish is predominantly Mn^{4+} with spatially varying domains richer in Mn^{3+}. (*E*) Point spectra taken across a manganese redox gradient. Inset table shows least squares fits quantifying the components of each spectrum.

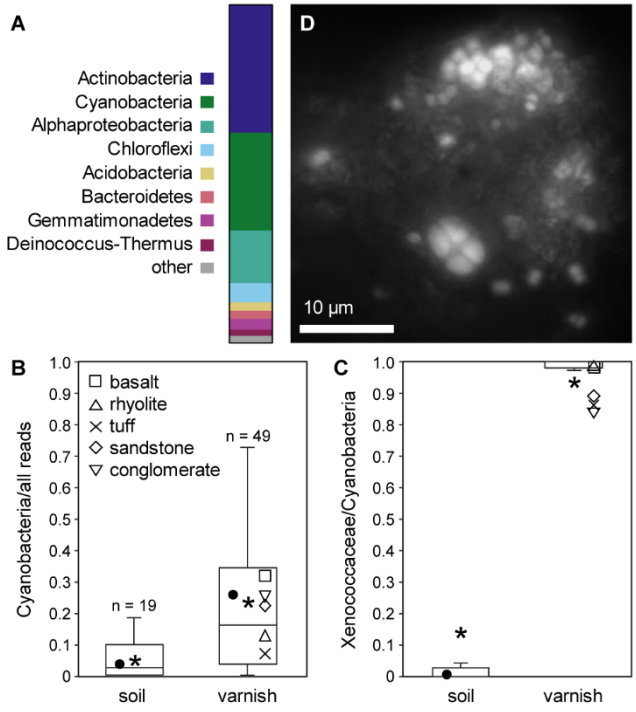

Figure 2: Cyanobacteria of the family Xenococcaceae are a major and specific constituent of the varnish microbial community. (*A*) Average taxonomic composition of varnish communities by 16S rRNA gene amplicon sequencing. (*B*-*C*) Box and whisker plots showing the abundance of Cyanobacteria (*B*) and family Xenococcaceae within the Cyanobacteria (*C*) in 16S reads from varnish vs. neighboring soil samples. Filled circles indicate fraction of all reads, asterisks indicate average relative abundance of all samples, other shapes indicate average relative abundance of each varnished rock type. (*D*) Fluorescence microscopy highlighting cells with the characteristic sarcinoid morphology of *Chroococcidiopsis* in varnish.

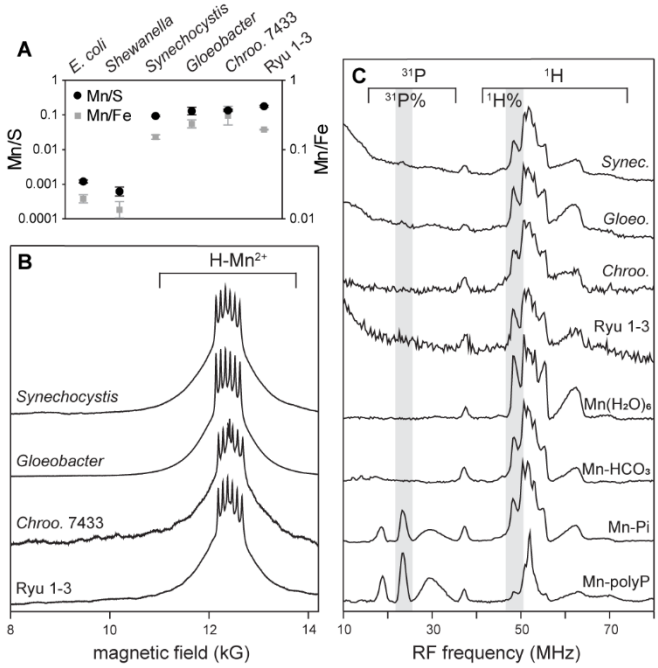

Figure 3: Cyanobacteria accumulate substantial intracellular Mn^{2+}, predominantly coordinated by small molecule carboxylato ligands. (*A*) Cellular manganese abundance measured by ICP-MS, reported as a ratio to sulfur as a proxy for normalizing to biomass, and to iron—a metric commonly associated with oxidative stress tolerance. Results are means of measurements from three independent cultures; error bars reflect standard error. (*B*) Absorption-display 35 GHz 2 K CW EPR spectra showing that > 95% of cyanobacterial Mn^{2+} exists as H-Mn^{2+} complexes. (*C*) 35 GHz 2 K $^{31}P/^{1}H$ Davies pulsed ENDOR spectra of Cyanobacteria and Mn^{2+} standards. Braces represent spans of ^{31}P and ^{1}H ENDOR responses; ^{31}P% and ^{1}H% represent absolute ENDOR responses (gray highlight). The negligible ^{31}P% ENDOR signals and diminished ^{1}H% ENDOR responses of Cyanobacteria versus hexaquo Mn^{2+} indicate that > 90% of the cyanobacterial Mn^{2+} is bound to ENDOR-silent carboxylato ligands (represented by Mn-HCO_3 standard), which was confirmed by ENDOR measurements of ^{13}C-labelled cells (Fig. S10*D*).

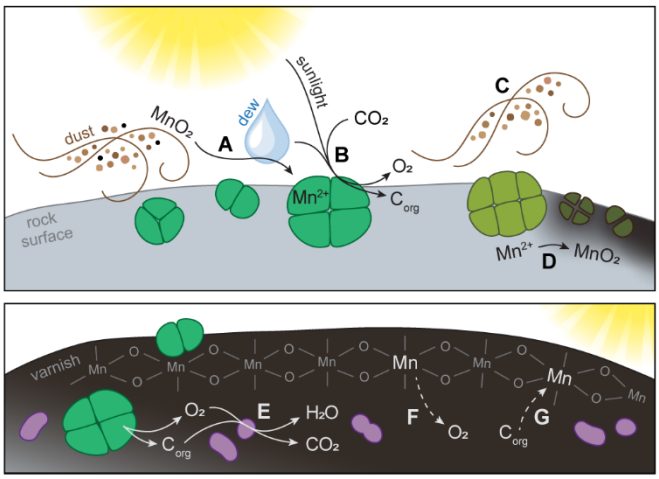

Figure 4: Natural history of varnish. (*A*) Manganese is delivered largely as oxide particles in windborne dust, reduced by either photochemical or biological processes, and taken up by *Chroococcidiopsis* cells for use as a catalytic antioxidant. (*B*) *Chroococcidiopsis* grows with light and water, fixing carbon and trapping accumulated manganese. (*C*) Dust material not adhered to the rock surface is removed by wind or precipitation. (*D*) When *Chroococcidiopsis* cells die, the manganese-rich residue left behind by their biomass is oxidized to generate the manganese oxides that comprise varnish. This oxidation could be biologically catalyzed and/or abiotic. (*E*) Products from cyanobacterial photosynthesis serve as substrates for heterotrophic community members. (*F*-*G*), manganese redox cycling continues in developed varnish, with abundant O_2 as an electron acceptor (*F*) and organic matter as an electron donor (*G*).

Supplemental figures

B

location	rock type collected	GPS coordinates	elevation (m)	average temp. (°C)	average rainfall (mm/year)
Barstow, CA	rhyolite	34°37'44.3"N 116°57'05.0"W	676	18.4	134
Babbitt Ranch, AZ	basalt, sandstone	35°40'59.9"N 111°24'13.3"W	1281	15.1	141
Black Canyon, NM	rhyolite	33°59'7.802"N 106°58'41.413"W	1656	13.7	260
Mesa Prieta, NM	basalt	36°8'13.099"N 106°1'20.129"W	1781	10.75	260
White Rock, NM	tuff	35°48'24.848"N 106°12'1.734"W	1845	9.1	479
Green River, UT	sandstone, conglomerate	38°52'50.094"N 110°12'23.797"W	1291	12	180
Basin, WY	sandstone	44°24'25.214"N 108°6'23.797"W	1224	7.6	175

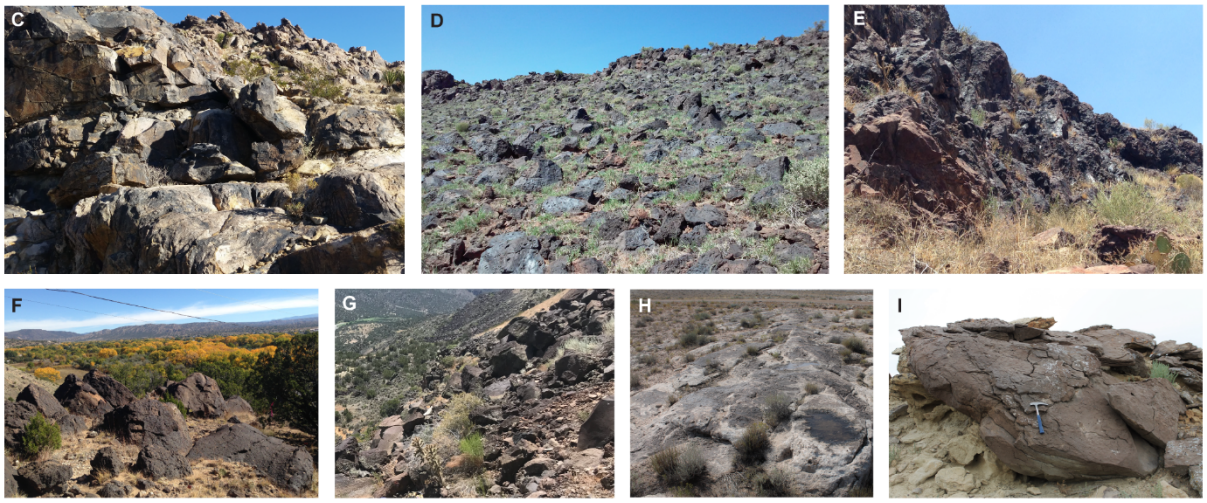

Figure S1: Field areas in this study. (*A*) Map of the western United States, with varnish sampling locations indicated. (*B*) Field area metadata. Average temperature and rainfall from nearest weather station on US Climate Data. (*C-I*) Context photos showing varnish from Barstow (*C*), Babbitt Ranch (*D*), Black Canyon (*E*), Mesa Prieta (*F*), White Rock (*G*), Green River (*H*), and Basin (*I*) sampling locations.

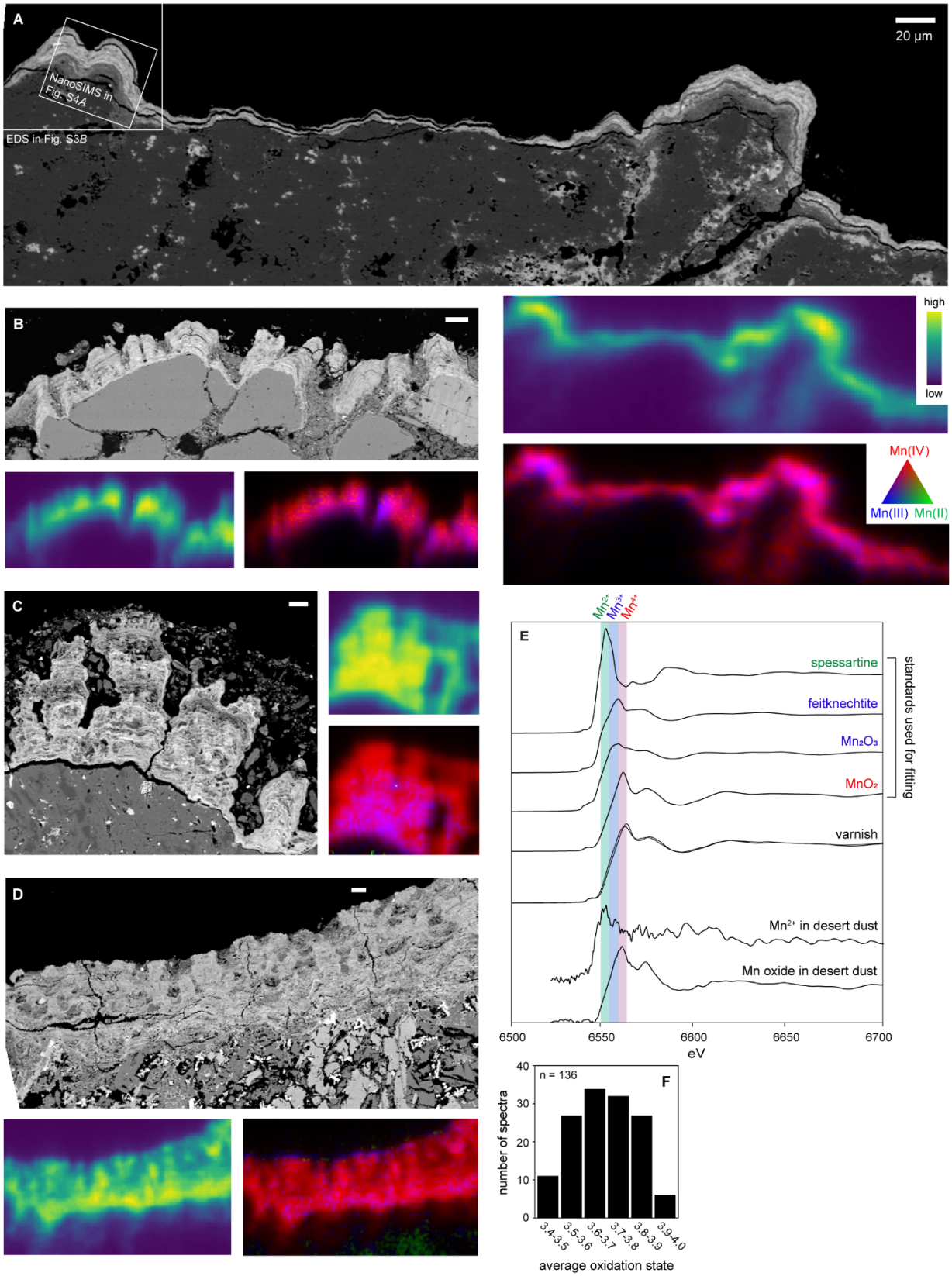

Figure S2: Extended SEM and synchrotron data. (*A-D*) Additional examples of SEM images showing

accretionary laminations with stromatolitic textures and manganese K-edge maps showing manganese distribution and redox heterogeneity in varnish thin sections. (*A*) Rhyolite from Black Canyon, NM. (*B*) Sandstone from Babbitt Ranch, AZ. (*C*) Rhyolite from Black Canyon, NM. (*D*) Basalt from Mesa Prieta, NM. (*E*) Manganese K-edge XANES spectra. For standards we employed spectra from spessartine for Mn^{2+}, both feitknechtite (β-MnOOH) and Mn_2O_3 as options for Mn^{3+}, and an internal endmember for Mn^{4+}. The two varnish spectra shown here plotted on top of each other represent the first and third quartile of our varnish dataset, with average oxidation states of 3.6 and 3.8 respectively. The desert dust spectra demonstrate the presence of manganese oxides in addition to trace igneous Mn^{2+} in surrounding dust that supplies the source of the material for varnish formation. (*F*) Histogram showing distribution of manganese redox states of all varnish spectra collected, including basalt, rhyolite, and sandstone samples.

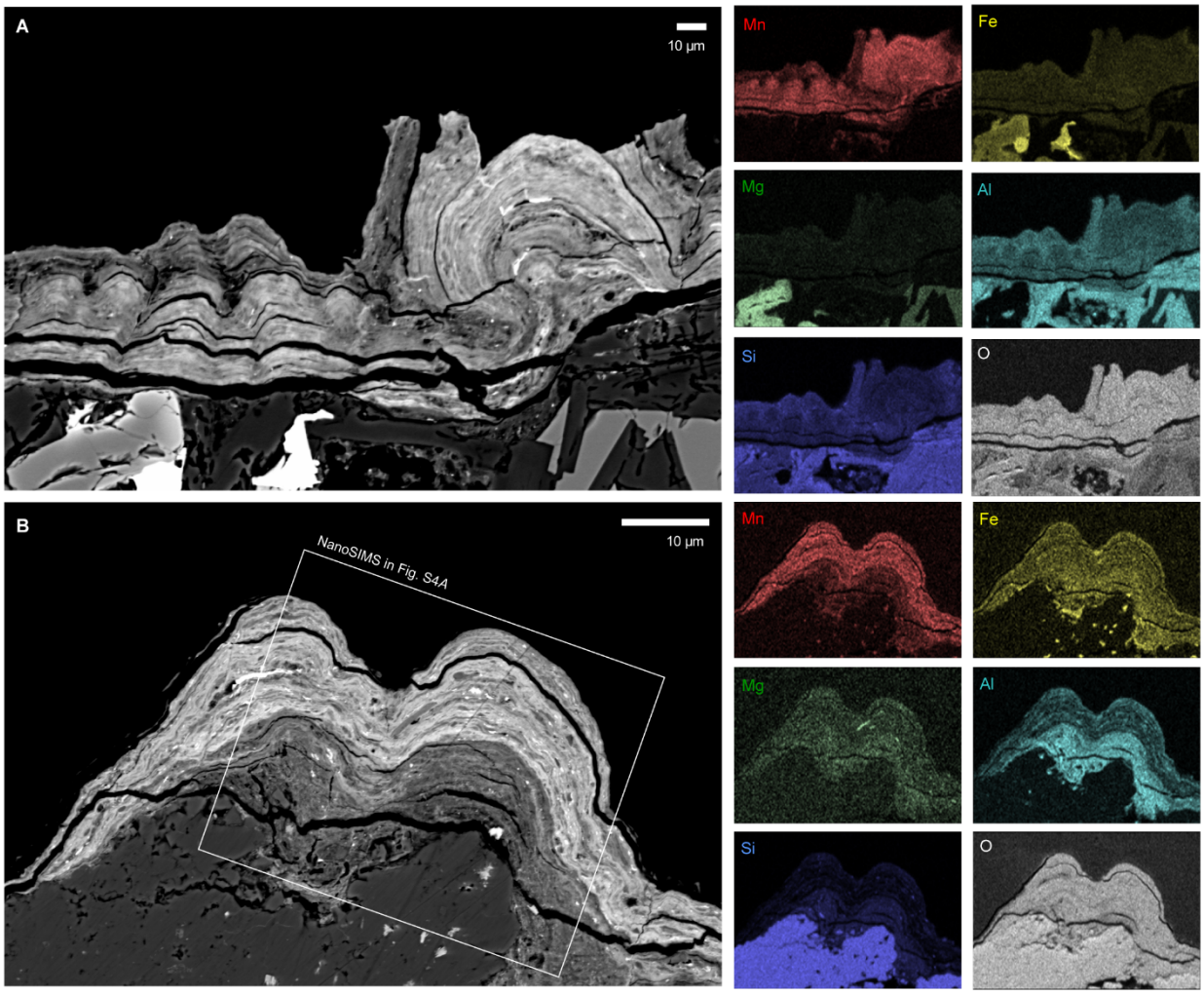

Figure S3: Backscatter SEM images with EDS chemical maps showing the distribution of major elements in varnish and underlying rock. (*A*) A mafic example, basalt from Babbit Ranch, AZ; the sample shown in Fig. 1. (*B*) A felsic example, rhyolite from Black Canyon, NM; the sample shown in Fig. S2*A*. Varnish is comprised primarily of manganese and iron oxides (reflected in the Mn and Fe channels, respectively) and clay minerals (reflected in the Si, Al, and Mg channels). Detrital grains are embedded in the laminated cement. The high manganese content occurs in the cement itself, not the detrital grains.

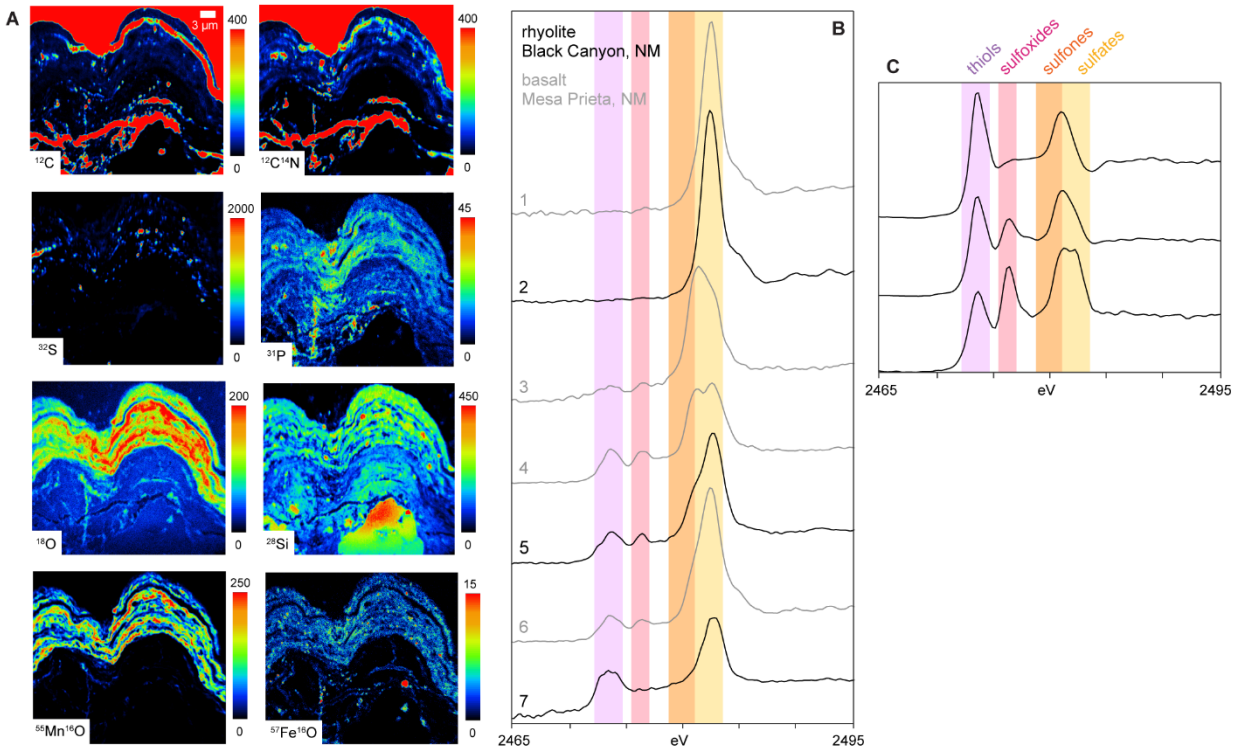

Figure S4: Sulfur distribution and speciation as a biosignature in varnish. (*A*) NanoSIMS images of the sample shown in Figs. S2*A* and S3*B*, to visualize the distribution of lighter elements indicative of biomass. Of the major biological elements, carbon and nitrogen signals are overwhelmed by background resin, but the resin is extremely poor in sulfur content; that, plus the high ion-yield of organic matter enables ^{32}S ion images to provide a measure of organic matter native to the varnish. (*B*) Sulfur K-edge XANES spectra from two varnish thin sections. These spectra demonstrate complex sulfur speciation in varnish, with both oxidized and reduced organic species that are consistent with biological material, in addition to sulfate salts. (*C*) Sulfur K-edge spectra taken on *Chroococcidiopsis* cells, representing the dominant source of biomass in varnish, exhibit the same organic sulfur moieties we observed in varnish.

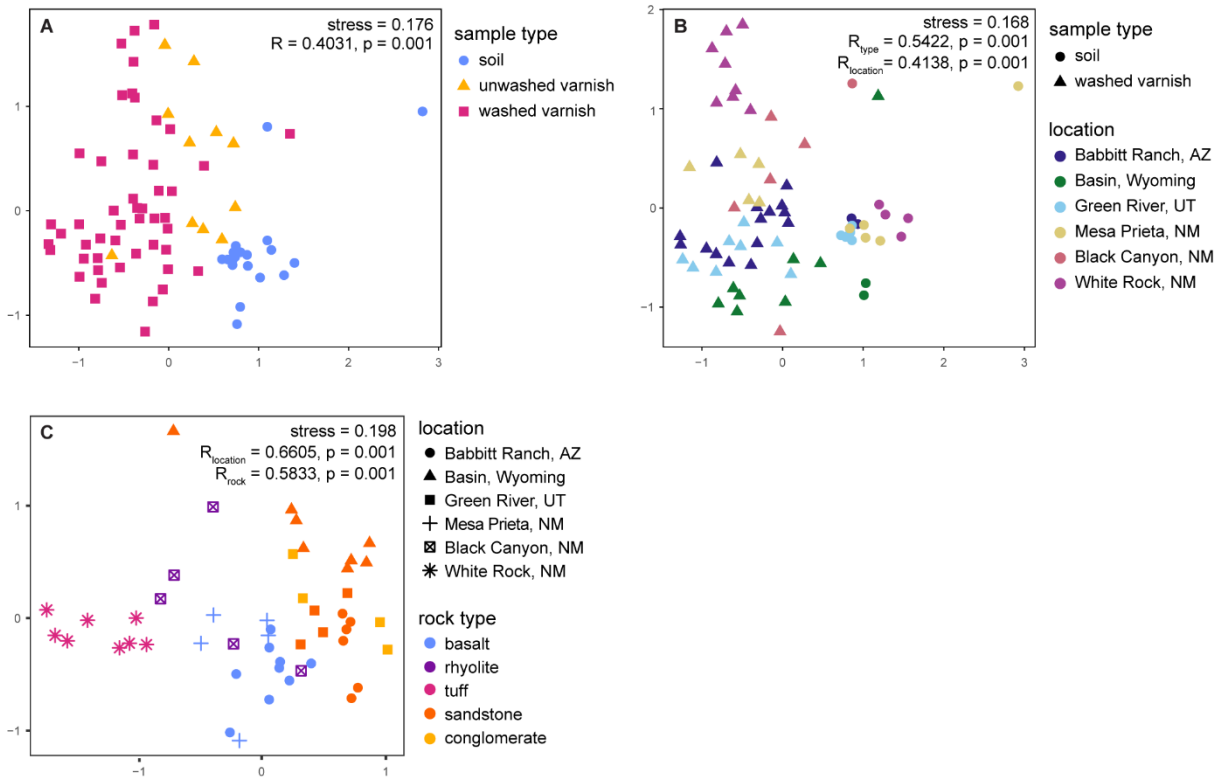

Figure S5: Nonmetric multidimentional scaling (NMDS) ordination analyses of 16S rRNA gene amplicon data to visualize variance. Each point represents the microbial community recovered from a sample; relative proximity between points indicates their similarity. (*A*) The varnish microbial community is distinct from that in surrounding soils, regardless of sample location or rock type. Rinsing the varnished rocks with sterile water to remove surficial dust further increased NMDS separation between varnish and soils. Thus, the remainder of our DNA analyses focused on washed varnish samples, to more accurately target taxa endemic to varnish. The analysis of similarities (ANOSIM) statistic *R* for soil vs. unwashed varnish = 0.4265, $p = 0.001$; and soil vs. washed varnish = 0.5442, $p = 0.001$. (*B*) Washed varnish and surrounding soil samples colored by sample location. (*C*) Washed varnish samples alone, colored by rock type. Among varnish samples, we observed some higher order clustering based on rock type and location.

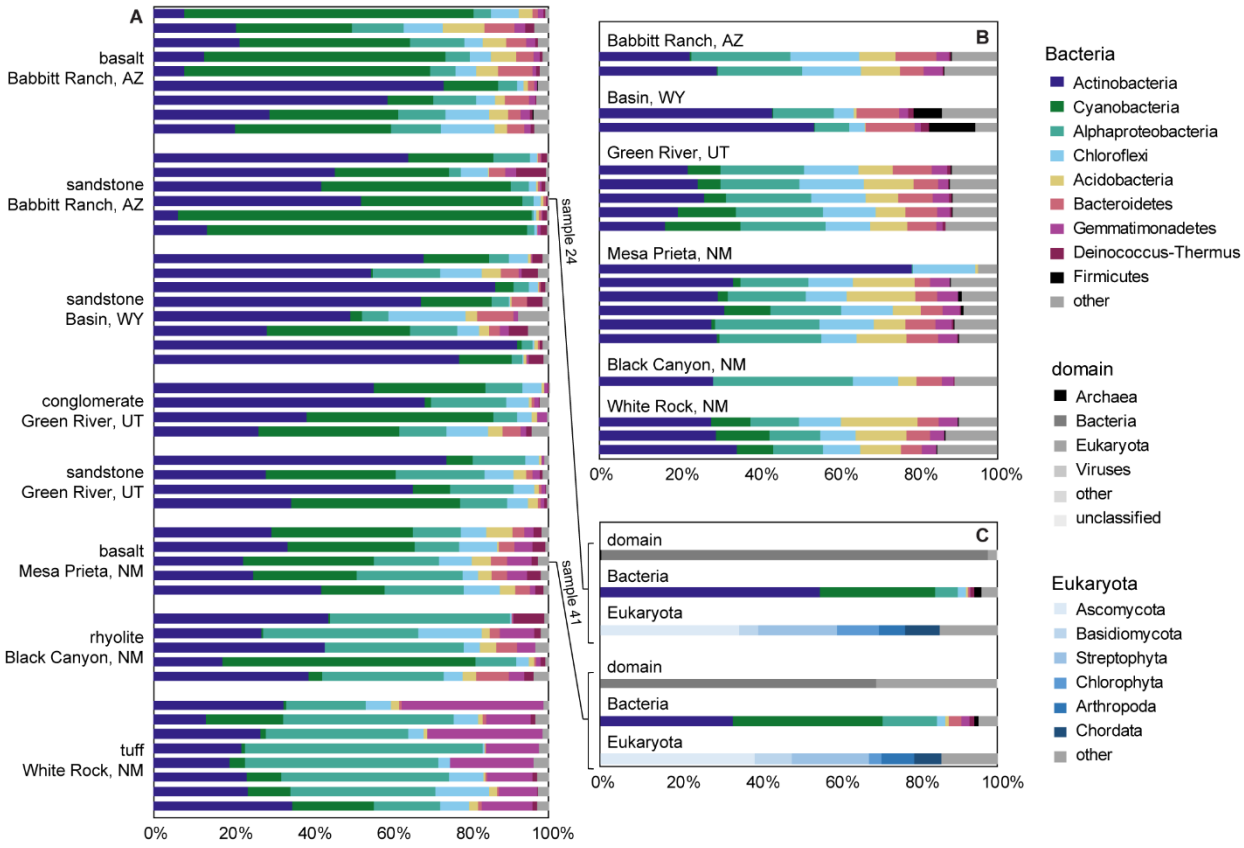

Figure S6: Phylum level community composition of (*A*) varnish 16S rRNA gene amplicon reads, (*B*) surrounding desert soil 16S rRNA gene amplicon reads, and (*C*) varnish shotgun metagenome reads. The varnish community is dominated by bacteria, with eukaryotes comprising 2.4% and 30.5%, and archaea comprising <0.5% of metagenome reads.

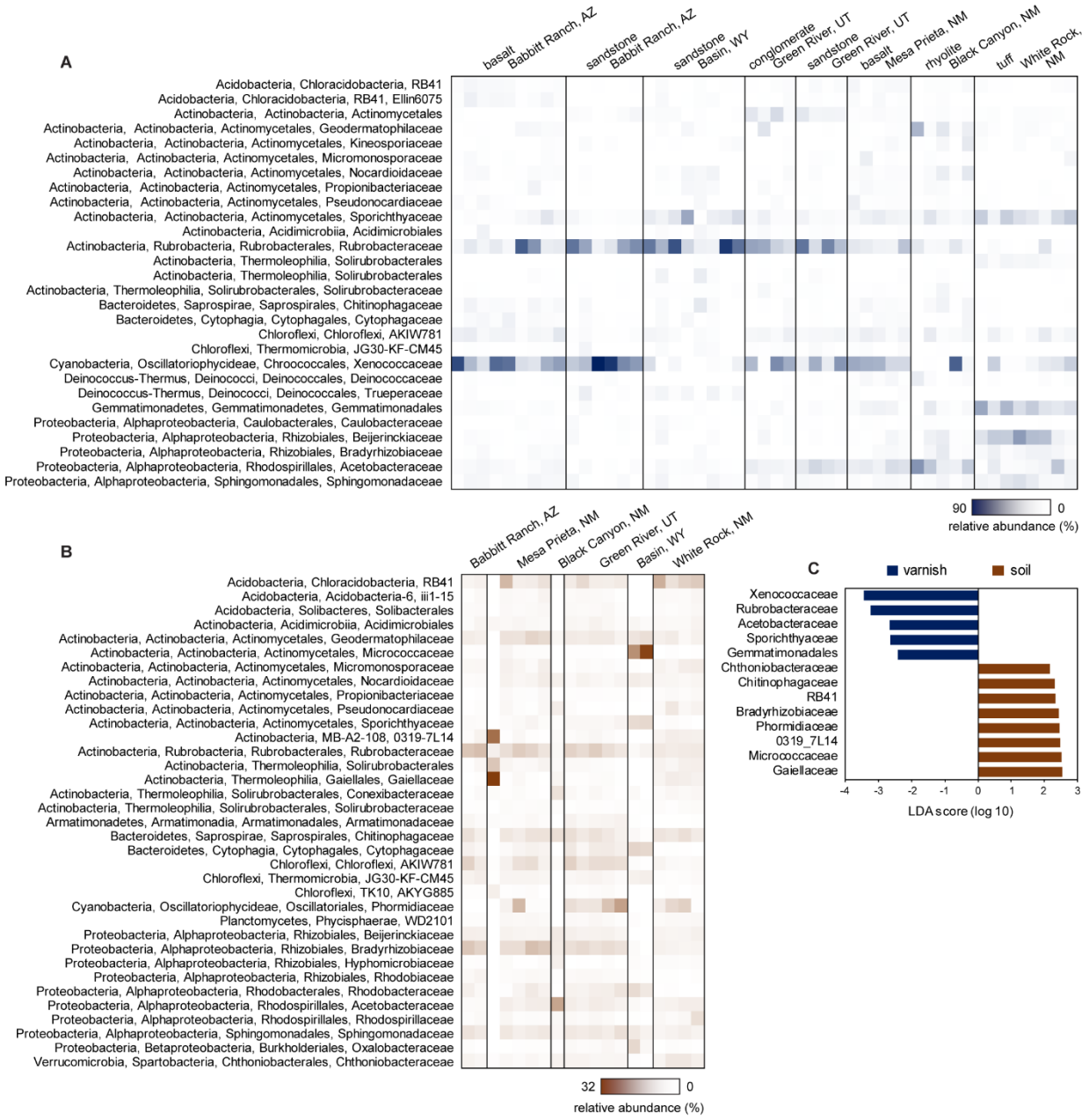

Figure S7: Major families characterizing the varnish microbial community. (*A-B*) The most abundant families (average relative abundance > 0.5%) identified in 16S rRNA gene amplicon reads from varnish (*A*) and surrounding desert soils (*B*). (*C*) Linear discriminant analysis effect size (LEfSe) identifying families that contributed most strongly to the distinction between the microbial communities of varnish vs. soil. The family Xenococcaceae was a major constituent of the varnish microbial community across all rock types and locations examined, and was the strongest contributor identified by LEfSe as characterizing varnish relative to soil.

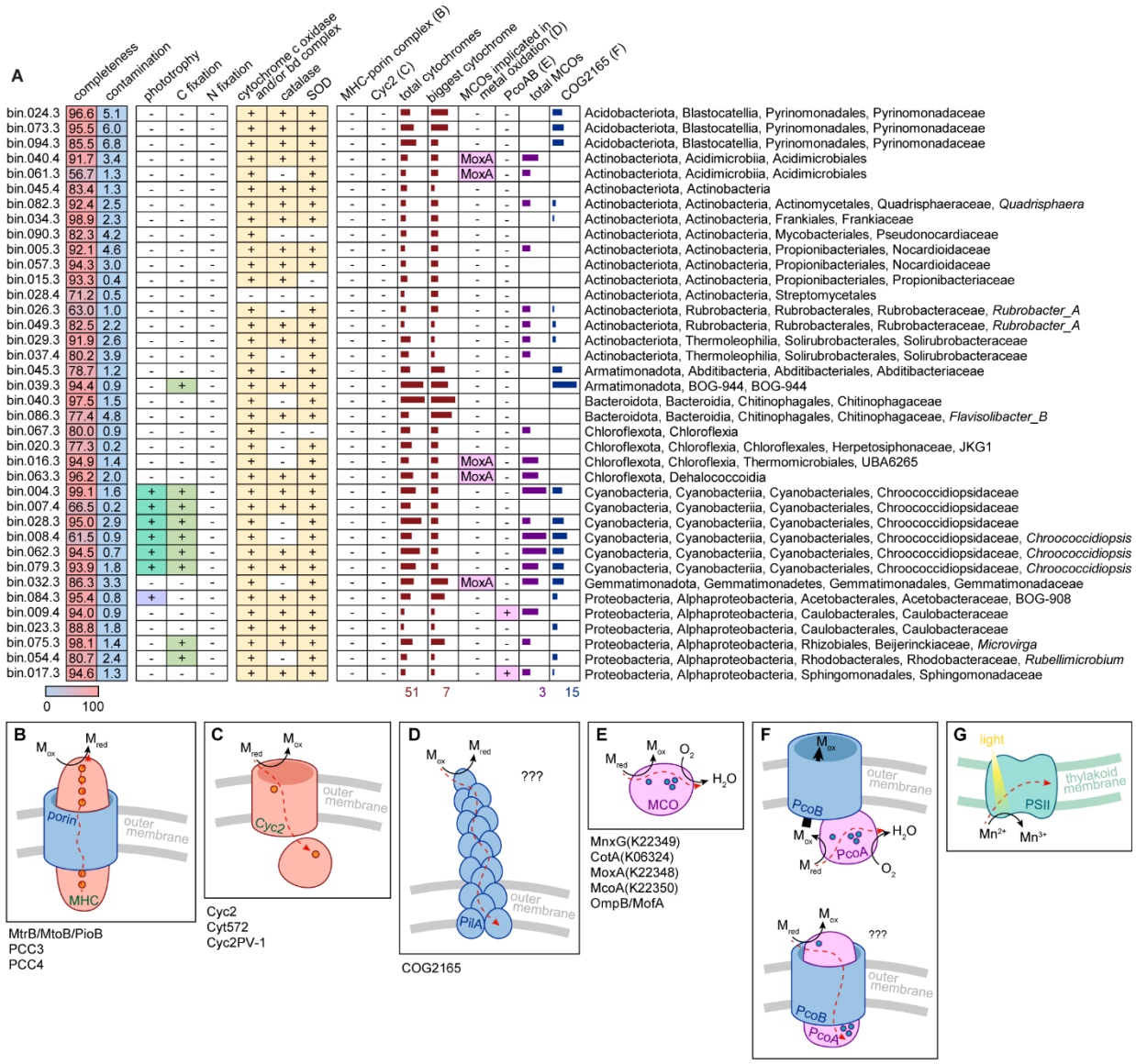

Figure S8: Metagenomic insights into varnish ecology. (*A*) We recovered 38 high quality MAGs from varnish shotgun metagenomes, 6 of which belonged to the Chroococcidiopsidaceae. Genes indicative of autotrophy are highlighted in green, showing that the Chroococcidiopsidaceae are the main primary producers and therefore keystone members of the ecosystem. Genes indicative of interactions with O_2 and reactive oxygen species (heme-copper O_2 reductase and/or *bd* O_2 reductases, catalase, and superoxide dismutase) are highlighted in yellow, demonstrating the strikingly aerobic nature of this ecosystem. Genes implicated in metal cycling processes, including MHC-porin complexes (*B*), Cyc2 homologs (*C*), high-potential MCOs (*D*), putative MCO-porin complexes (*E*), the COG2165 pilin system (*F*), and photosystem II (*G*), were also catalogued, along with counts of total cytochromes, largest MHC, and total MCOs in each genome bin. Dashed red arrows indicate electron flow.

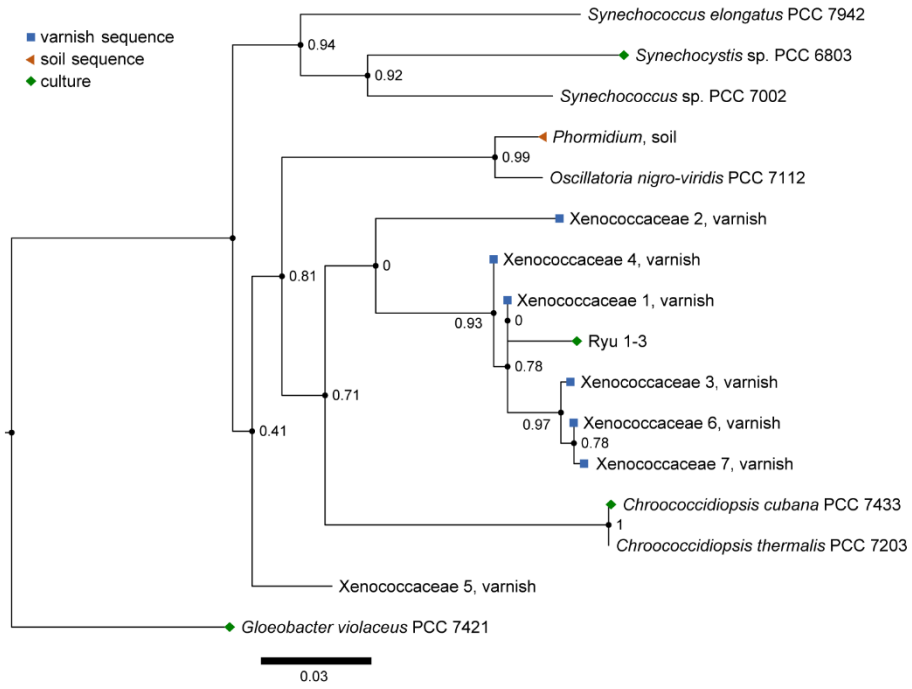

Figure S9: Phylogenetic tree showing relationships between the Cyanobacteria examined in this study. Tree includes cultured strains we used to investigate intracellular manganese accumulation and speciation (model organism *Synechocystis* sp. PCC 6803, *Chroococcidiopsis* strains Ryu 1-3 and PCC 7433, and the deep branching *Gloeobacter violaceous* PCC 7421), along with the most abundant 16S sequences recovered from varnish and soil (Xenococcaceae and Phormidium, respectively).

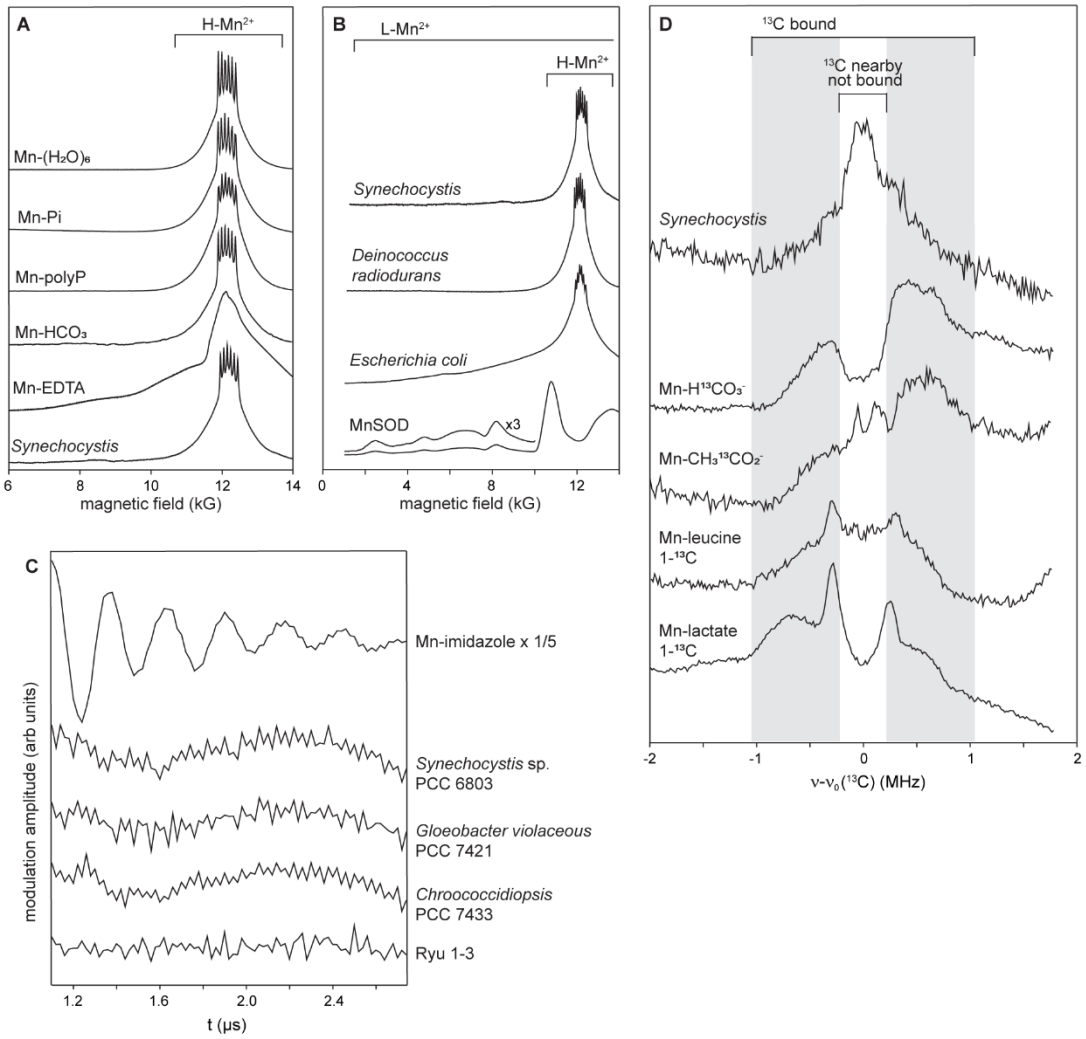

Figure S10: Additional paramagnetic resonance data. (*A*-*B*) Absorption display CW EPR spectra. The frozen solution EPR spectra of Mn-$(H_2O)_6$, Mn-HCO_3, Mn-Pi, and Mn-polyP are representative exemplars for H-Mn^{2+} complexes with six sharp Mn^{2+} hyperfine lines riding on a ~4 kG 'skirt'. Both *Deinococcus radiodurans* and all of our cyanobacterial strains (*Synechocystis* included as representative example) displayed cellular Mn EPR spectra indicative of this type of manganese speciation. In contrast, L-Mn^{2+}, including strongly chelated (e.g. Mn-EDTA) and protein-bound (e.g. MnSOD) Mn^{2+} display spectra which go well beyond the "H" 4 kG skirt, both at low and high magnetic fields. In *Escherichia coli*, the much broader skirt around the Mn^{2+} hyperfine lines relative to *Deinococcus* and *Synechocystis* indicates significantly more manganese bound to strongly chelating ligands or proteins. (*C*) 3-pulse ESEEM timewaves, which show modulations arising from ^{14}N hyperfine coupling, as observed in a frozen solution of Mn-imidazole. None of the cyanobacterial strains examined here displayed ^{14}N modulaton, indicating a negligible population of nitrogenous ligands in the manganese environment. (*D*) ^{13}C Mims ENDOR, characterizing Mn-^{13}C coupling in ^{13}C-labelled *Synechocystis*. The region centered around the ^{13}C Larmor frequency shown with two gray stripes (denoted as "^{13}C bound") is similar to that observed for standard Mn^{2+} complexes with ^{13}C-labelled bicarbonates and organic molecules, and is indicative of manganese bound to carboxylate ligands. The high central peak at the ^{13}C Larmor frequency (denoted "^{13}C nearby, not bound") arises from the nearby ^{13}C nuclei that are not coordinated to manganese, suggesting that these ligands might be multi-C molecules such as small organic acids.

CHAPTER V

Manganese oxidation by Cyanobacteria

Usha F. Lingappa[1], Hope A. Johnson[2], Yvonne Dimagiba[2], Lindsay Kane Barnese[2,3], Joshua Phelan[2], William Kim[2], Sam Webb[4], James Hemp[5], Joan Selverstone Valentine[1,6], Woodward W. Fischer[1]

1. Div. of Geological & Planetary Sciences, California Institute of Technology, Pasadena, CA 91125, USA

2. Dept. of Biological Science, California State University Fullerton, Fullerton, CA 92831, USA

3. School of Arts & Sciences, Concordia University Irvine, Irvine, CA 92612, USA

4. Stanford Synchrotron Radiation Lightsource, Stanford University, Menlo Park, CA 94025, USA

5. Department of Gastroenterology, Hepatology, & Nutrition, University of Utah, Salt Lake City, UT 84132, USA

6. Dept. of Chemistry & Biochemistry, University of California Los Angeles, Los Angeles, CA 90095, USA

Abstract

Oxygenic photosynthesis is thought to have evolved from a version of anoxygenic phototrophy based on manganese oxidation in the ancestors of the Cyanobacteria. Here we investigated whether their modern descendants remain capable of this metabolism. We demonstrated that manganese oxidation catalyzed by Cyanobacteria is a robust, bulk phenomenon. To constrain mechanism, we examined this phenomenon under a suite of different inhibition conditions, at different levels of biochemical complexity, and with PSII mutants. We resolved three distinct pathways of manganese oxidation: a primary mechanism directly catalyzed by PSII, a secondary mechanism that was O_2 dependent and PSII independent, and a third indirect mechanism driven by pH. The manganese oxidation product that we observed was a transient Mn(III) complex (putatively Mn(III)-citrate), suggesting a role for Cyanobacteria in producing soluble Mn(III) in the environment. While all three mechanisms could contribute to such fluxes, the PSII mechanism is especially notable—it represents the only known mechanism of biological manganese oxidation that does not require O_2 or other reactive oxygen species, and the first demonstration of bulk manganese oxidation with live cells possibly coupled to phototrophic energy conservation.

Introduction

The element manganese is geologically most abundant in its reduced form, Mn(II). However, oxidized manganese species—both insoluble Mn(III)/(IV) oxide minerals and soluble Mn(III)-ligand complexes—play unique and valuable roles in the environment (1, 2). As exceptionally strong and reactive oxidants, oxidized manganese species drive redox processes central to the biogeochemical cycles of many other major elements (carbon, sulfur, iron, etc.). Given this notability, understanding the processes that generate oxidized manganese is important.

The uncommonly high reduction potentials of manganese redox couples necessitate even higher potential oxidants for their oxidation; chemically, this is limited to dioxygen (O_2) and other reactive oxygen species such as superoxide (O_2^-) and hydrogen peroxide (H_2O_2). Although abiotic manganese oxidation with these oxidants does occur, biological catalysis is thought to contribute much more

substantial manganese oxidation fluxes (3). Many different bacteria and fungi that oxidize manganese have been identified (4–16), all of which do so via mechanisms that exploit the thermodynamically favorable reactions between Mn^{2+} and $O_2/O_2^-/H_2O_2$. With the single exception of a recently discovered chemolithoautotrophic metabolism (14), all other recognized modes of microbial manganese oxidation are not coupled to cellular energy conservation. A microbial metabolism based on phototrophic manganese oxidation has been hypothesized and searched for but never identified (17).

Phototrophic manganese oxidation is the use of manganese as the electron source for a reaction center that harnesses light energy to power an electron transport chain. Many different phototrophic metabolisms exist, exploiting a wide range of different electron sources (H_2O, Fe^{2+}, H_2, S^0, HS^-, $S_2O_3^{2-}$, NO_2^-, AsO_3^{3-}, various organics) (17, 18). However, aside from photosystem II (PSII)—the reaction center that oxidizes H_2O to O_2 in Cyanobacteria, algae, and plants—all known reaction centers have lower reduction potentials than most manganese species, making manganese oxidation inaccessible.

The ability of PSII to obtain electrons from manganese has been well documented. The active site of PSII hosts a Mn_4CaO_5 cofactor known as the water oxidizing complex (WOC) (19, 20). The biogenesis of this cofactor occurs *in situ* via a process known as photoassembly (21), wherein Mn^{2+} ions are directly oxidized by PSII to generate the $Mn(III)_3Mn(IV)$ baseline state of the cluster, which is subsequently further oxidized and then regenerated during the catalytic cycle. A vast body of work aimed at elucidating the mechanics of photoassembly has demonstrated the robustness of PSII as a manganese oxidase; perturbations ranging from mutagenesis of the residues coordinating the WOC, incomplete post-translational cleavage of the C-terminus, removal of calcium, and removal of extrinsic subunits all eliminate the ability to assemble and stabilize the cluster, but do not eliminate manganese oxidation activity (21–32). Furthermore, purified PSII protein from spinach has recently been shown to catalyze manganese oxidation beyond the four atoms required to assemble the WOC (33). The reduction potentials required for manganese oxidation are generated through photochemical charge separation; thus, PSII catalyzes the only known mode of manganese oxidation that does not involve O_2 or reactive oxygen species.

The understanding that PSII can oxidize manganese has been invoked in support of the hypothesis that phototrophic manganese oxidation was an evolutionary precursor to oxygenic photosynthesis in the ancestors of the Cyanobacteria (2, 17, 34–37), which provides an explanation for evidence of manganese oxide deposition observed in the geological record from prior to the rise of O_2 (34). However, the idea that phototrophic manganese oxidation by modern Cyanobacteria might still be ecologically important today has not been explored. Here we present experimental data demonstrating cyanobacterial manganese oxidation across several different levels of complexity. This work suggests that manganese oxidation by PSII is an important aspect of both manganese biogeochemistry and cyanobacterial ecophysiology in modern environments.

Results

Cyanobacteria oxidize manganese using PSII

We began investigating the ability of Cyanobacteria to oxidize manganese using cultures of the model organism *Synechocystis* sp. PCC 6803, a genetically tractable cyanobacterium that is capable of growing heterotrophically on glucose. This metabolic flexability enables inhibition and/or mutagenesis of PSII that would be fatal in an obligate autotroph. We incubated *Synechocystis* cells with reduced manganese (aqueous Mn^{2+} as a manganese chloride solution) and assayed for the production of oxidized manganese along an experimental timecourse using the colorimetric indicator leucoberbelin blue (LBB) (38). Parallel reactions without cells were run as abiotic controls.

We did not observe any manganese oxidation, either abiotic or biologically catalyzed, in experiments provided with only manganese chloride. However, with the addition of sodium citrate—citrate is known to chelate Mn^{2+} and Mn^{3+} ions and stimulate biological manganese oxidation (39)—we observed robust biological manganese oxidation under conditions in which abiotic manganese oxidation was minimal (Fig. 1*A*). This phenomenon was unique to citrate; other ligands that we tried under various conditions (including tartrate, succinate, fumarate, acetate, malate, lactate, oxalate, formate, pyruvate, histidine, ethylenediaminetetraacetic acid, nitrilotriacetic acid, bicarbonate, phosphate, pyrophosphate,

hexametaphosphate, and undefined humic acids) stimulated little to no manganese oxidation. The citrate dependence along with the fact that we did not observe oxide precipitation suggested that the product in these experiments was a Mn(III)-citrate complex.

Having established a phenomenon, we conducted manganese oxidation experiments under a suite of conditions designed to constrain different possible mechanisms—with and without light; with and without 3-(3,4-dichlorophenyl)-1,1-dimethylurea (DCMU), a specific inhibitor of PSII; and with and without superoxide dismutase (SOD) or catalase, enzymes that quench O_2^- and H_2O_2, respectively (Fig. 1*A*). Manganese oxidation did not occur in the dark or with the addition of DCMU, which suggested a light dependent, PSII dependent mechanism. Furthermore, this manganese oxidation was only slightly diminished by the addition of SOD or catalase, which suggested a mechanism not involving O_2^- or H_2O_2—implicating PSII itself as the most likely oxidant.

Mutant studies provided an additional line of evidence for this interpretation. D1 is the core subunit of PSII that hosts the active site. We utilized two D1 mutants—D1-Δ (40) and D1-D170A (25). In the D1-Δ mutant, the D1 protein is knocked out, resulting in no functional PSII. In the D1-D170A mutant, a single amino acid change in the D1 protein prevents it from assembling the WOC; it is therefore incapable of oxygenic photosynthesis, but otherwise contains a complete PSII. In our experiments, the D1-Δ mutant did not oxidize manganese, while the D1-D170A mutant did, as would be expected from a PSII dependent mechanism distinct from O_2 production (Fig. 1*B*).

Definitive demonstration of photosynthetic energy conservation coupled to manganese oxidation by PSII is unattainable with wildtype (WT) cells, as electrons derived from manganese oxidation are indistinguishable from electrons derived from water oxidation and manganese oxidation did not appear to inhibit water oxidation. However, the D1-D170A mutant provided a system where manganese oxidation could be observed in the absence of water oxidation. This mimics the hypothesized ancestral PSII that oxidized manganese prior to the evolution of oxygenic photosynthesis, and potentially enables the demonstration of energy conservation. Unfortunately, confounding variables including toxicity

engendered by high manganese concentrations have hindered these efforts (Fig. S1). Therefore, it remains unclear whether the manganese oxidation we observed formally provides electrons for photosynthesis.

To further pinpoint the mechanism of manganese oxidation to PSII, we conducted experiments in increasingly reductionist systems—first isolated photosynthetic membranes and then pure PSII protein—to methodically separate PSII activity from the complexity of live cells. Membrane preparations provided an intermediate system with the photosynthetic electron transport chain in a more physiologically faithful context than purified protein. In the membrane system, we observed a similar manganese oxidation phenomenon to our whole cell experiments (Fig. 2*A*-*C*). D1-Δ membranes did not oxidize manganese while both WT and D1-D170A membranes did, in a manner that was light dependent and largely inhibited by DCMU but only slightly inhibited by SOD. The addition of catalase mildly enhanced this manganese oxidation, suggesting a role for H_2O_2 as a manganese reductant instead of or in addition to an oxidant. Manganese oxidation in the membrane system exhibited Michaelis-Menten kinetic behavior, consistent with catalytic enzyme activity rather than a stoichiometric chemical reaction (Fig. 2*D*-*E*).

PSII protein purified from a WT strain with a hexahistidine tag fused to the C-terminus of CP47 (41) also exhibited light dependent manganese oxidation activity that was not inhibited by SOD or catalase (Fig. 2*F*). While DCMU inhibition was incomplete, a dose dependent titration effect indicated that this was likely due to insufficient DCMU concentrations relative to the much higher PSII concentrations in the membrane and pure protein systems than whole cell experiments. The pure protein system also exhibited a decrease in O_2 production under manganese oxidizing conditions accompanied by an increase in the reduction of 2,6-dichlorophenolindophenol (DCIP), an artificial electron acceptor used to measure photosynthetic activity, consistent with the interpretation that manganese is serving as an alternative to water as the electron donor for PSII (Fig. 2*G*).

Additional pathways of manganese oxidation

During the course of our whole cell experiments, cells would settle out of solution onto the bottom of the tube. At each timepoint, we shook them up in order to remove a homogenous aliquot for

our assay. After several years of conducting these experiments, we realized that the frequency with which timepoints were sampled—and therefore shaken—was impacting the results. To eliminate this variability, we switched the format of our experiments from culture tubes to Erlenmeyer flasks that were shaken continuously throughout the duration of the experiment. In the flask format, DCMU no longer inhibited manganese oxidation, suggesting a PSII independent mechanism under these conditions (Fig. 3*A*-*B*).

Aside from PSII, the only plausible oxidants for manganese are O_2 and other reactive oxygen species derived from O_2 such as O_2^-. This suggested that the key difference in the DCMU condition between the tube and flask formats could be O_2 availability—in the presence of DCMU, cells are unable to produce O_2, but still consume it; therefore, unless aerated by shaking, O_2 availability is limited by diffusion. Conductivity measurements of O_2 saturation confirmed that the DCMU conditions went anaerobic in the tube format and remained saturated with O_2 in the flask format (Fig. 3*C*). In striking contrast to our original tube format experiments, the manganese oxidation observed in the flask format with DCMU was almost entirely inhibited by the addition of SOD, suggesting that O_2^- played a key role in the oxidation occurring under these conditions (Fig. 3*D*). Therefore, we suspect distinct mechanisms of manganese oxidation—a PSII dependent, O_2 independent pathway seen in the absence of DCMU, and a PSII independent, O_2 dependent pathway seen in the presence of DCMU when aerated. Importantly, the membrane system did not exhibit a difference between the tube and flask formats (Figs. 2*A* vs. 3*E*). This further strengthened evidence that this O_2 dependent manganese oxidation was a separate phenomenon from the PSII dependent mechanism by suggesting that when we fractionated the cells to isolate photosynthetic membranes, the biochemical factors required for this O_2 dependent mechanism were lost with the soluble fraction.

A third mechanism of manganese oxidation that we investigated was the possibility of photosynthetic activity increasing the solution pH (42)—a consequence of cyanobacterial autotrophy effectively consuming protons (43)—and thereby driving abiotic manganese oxidation (42). We showed that unbuffered *Synechocystis* WT cultures increased the pH of their medium dramatically during growth (Fig. 4*A*) and medium in which cells were grown and then removed by centrifugation catalyzed

substantially more abiotic manganese oxidation than starting medium (Fig. 4*B*). Thus, this indirect mechanism is a valid pathway by which Cyanobacteria can catalyze manganese oxidation.

To tease out the threshold of pH dependence in our experimental system, we conducted carefully buffered experiments that were continuously mixed to minimize the buildup of local pH or O_2 gradients around cells. Both the biological and abiotic reactions proceeded more readily with increasing pH (Fig. 4*C*); this suggested that slight variations in pH might contribute to inconsistencies in the magnitude of our phenomenon between different experiments. Nonetheless, the biological reaction was clearly separable from any abiotic artifact due to pH—in reaction solutions between pH 7.4 and 7.8, the biological reaction proceeded while the abiotic reaction did not. Therefore, this indirect pathway cannot explain the majority of the manganese oxidation observed in our experiments.

Manganese oxidation product is transient

In addition to the confounding effects of multiple different manganese oxidation pathways, a further complication was presented by the nature of the manganese oxidation product itself. The oxidized manganese product observed in our experiments was highly unstable and short lived; in reactions from which the cells were removed via centrifugation or moved to the dark—in either case ceasing the flux of product being generated—the accumulated product disappeared rapidly (Fig. 5). This suggested that substantial invisible manganese cycling could be occurring in our experiments and the product concentrations captured by our assay represented momentary snapshots of a dynamic, transient product, accumulated in a steady-state pool only through high fluxes of formation. Taken together with a growing appreciation for the importance of transient Mn(III)-ligand complexes (44), this understanding has profound implications for the role of cyanobacterial manganese oxidation in the environment.

***Chroococcidiopsis* provides a different window into cyanobacterial manganese oxidation**

Since it is known that electrons derived from manganese during photoassembly enter the cyanobacterial electron transport chain, it is likely that bulk manganese oxidation by PSII provides useful

metabolic energy. While our efforts to demonstrate energy conservation with *Synechocystis* were inconclusive, it occurred to us that this phenomenon might be more valuable—and therefore possibly more readily apparent—in organisms adapted to extremely arid environments, where water scarcity could promote the use of an alternative electron donor. Accordingly, we examined *Chroococcidiopsis* sp. PCC 7433, a highly desiccation tolerant cyanobacterium (45–47) isolated from a dried up pond (48).

We grew *Chroccoccidiposis* cultures in two different settings—at room temperature under natural light on a windowsill, and in a 30°C shaking incubator under constant illumination (the same growth conditions as *Synechocystis*). The windowsill cultures grew slowly and were extremely clumpy, a consequence of baeocystous reproduction (Fig. 6*B*), while the incubator cultures grew faster and reached a high-density growth stage dominated by free floating vegetative cells (Fig. 6*C*).

Using synchrotron X-ray absorption near edge structure (XANES) spectroscopy at the manganese K-edge, we examined the redox state of manganese associated with biomass from *Synechocystis*, windowsill *Chroococcidiopsis*, and incubator *Chroococcidiopsis* cultures (Fig. 6*D*). In addition to cultures grown in standard BG11 (9 μM $MnCl_2$), we examined cultures supplemented with 100 μM $MnCl_2$ to amplify the total manganese signal. The manganese content of *Synechocystis* has been previously described as predominantly Mn(II) (49). Our data corroborated this earlier work, however, we note that spectral fits suggested a minor component (~25%) of Mn(III) (Fig. S2). Incubator grown *Chroococcidiopsis* exhibited a similar XANES profile. For both *Synechocystis* and incubator *Chroococcidiopsis*, the manganese content appeared homogeneous and supplemental manganese increased signal strength but did not appear to change the speciation. In contrast, windowsill *Chroococcidiopsis* exhibited variable XANES spectra with considerable oxidized content in standard BG11 (~40-60% Mn(III)) that increased with supplemental manganese (~60% Mn(III) and ~5-15% Mn(IV)). Since all manganese supplied to these cultures is Mn(II), the presence of oxidized species can be interpreted as a signal of manganese oxidation.

To test the hypothesis that manganese oxidation could be an important strategy for desiccation survival, we grew windowsill cultures of *Chroococcidiposis* under manganese starved (BG11 without any

$MnCl_2$), standard (9 μM $MnCl_2$), and manganese replete (100 μM $MnCl_2$) conditions, and examined whether manganese availability impacted their tolerance for desiccation. Using chlorophyll fluorescence quenching as a measure of function, we found that the manganese replete cultures were able to maintain some degree of activity following a period of desiccation that abrogated both the manganese starved and normal BG11 cultures (Fig. 7).

Discussion

Different aspects of the link between PSII and manganese oxidation have been previously recognized by different scientific communities. In the biogeochemistry literature, connections between oxygenic phototrophs (largely algae) and manganese oxidation have been documented, but previous interpretations were limited to indirect mechanisms such as pH increase and extracellular enzymatic O_2^- production (42, 50). In the photosynthesis protein biochemistry literature, manganese oxidation by PSII has been understood through the lens of WOC photoassembly (21–32). In the historical geobiology literature, phototrophic manganese oxidation has been considered an evolutionary precursor to oxygenic photosynthesis that left its mark in the geological record through the deposition of manganese oxides prior to the rise of O_2 (33–35, 37). Here we bridged the gap between these existing bodies of knowledge by experimentally interrogating cyanobacterial manganese oxidation at multiple different levels of complexity and mechanistic detail to build a holistic understanding of this phenomenon.

Our data demonstrated that manganese oxidation by PSII is an important bulk process occurring with live cyanobacterial cells, not limited to WOC photoassembly or isolated protein removed from physiological context. While the PSII pathway was the dominant route of manganese oxidation in our experiments, we also observed pathways driven by pH and O_2^-. The co-occurrence of these multiple mechanisms suggested a complicated relationship between Cyanobacteria and manganese oxidation; future work is required to further tease apart its nuances. However, the possibility of contributions from multiple separate pathways suggests that cyanobacterial manganese oxidation in the environment may contribute disproportionately large fluxes relative to its physiological role(s). Since Cyanobacteria are

essentially ubiquitous in any photic environment—they are found in marine, freshwater, and terrestrial settings, from the poles to the tropics (51)—the phenomenon presented here likely represents a major branch of environmental manganese cycling.

The nature of the labile Mn(III)-citrate product generated in our experiments raised further environmental implications for this manganese oxidation phenomenon. Soluble Mn(III)-ligand complexes have received growing recognition as important and dynamic players in biogeochemistry (44, 52–61) and likely remain underappreciated due to their lability hindering their detection and quantification (44). As extremely reactive oxidants they can degrade otherwise refractory molecules ranging from recalcitrant plant matter such as lignin (16) to steroids derived from anthropogenic pollution (59). Indeed, manganese content has been implicated as the strongest correlate to leaf litter decomposition rate in forest ecosystems (56). While previous studies have largely focused on manganese oxidation by fungi as the source of reactive Mn(III) complexes, our data suggested that Cyanobacteria may also supply such complexes. This implies that the involvement of Cyanobacteria in carbon cycling may extend beyond their role as primary producers by contributing to manganese oxidation that mediates carbon breakdown.

While all of the manganese oxidation pathways we observed could contribute to such biogeochemical processes, the PSII pathway has unique evolutionary and physiological implications. The understanding that this phenomenon can operate on a bulk level with live cultures strengthens existing evidence (33, 37) for the viability of the hypothesized manganese oxidizing phototrophy that led to the evolution of oxygenic photosynthesis. It also fills in an important hole in the landscape of modern microbial metabolic diversity—the absence of known manganese oxidizing phototrophs. In searches for such organisms, DCMU is typically added to intentionally exclude oxygenic phototrophs (17); the possibility that the oxygenic phototrophs *are* the manganese oxidizing phototrophs has not been previously explored. The apparent lack of other organisms adapted to carry out phototrophic manganese oxidation may be due to Cyanobacteria catalyzing bulk manganese oxidation through a variety of pathways while also outcompeting other organisms thanks to their ability to perform oxygenic

photosynthesis, effectively eliminating the ecological niche once occupied by their evolutionary progenitors.

Unlocking the ability to use water as the electron donor for photosynthesis was one of the most transformative evolutionary innovations of all time, not only because it produced O_2, but also because it enabled levels of primary productivity that would not have been attainable with other, less abundant electron sources. Even today, oxygenic phototrophs are generally considered to be fundamentally electron unlimited; their growth is limited due to lack of nutrients, not electrons. This raised an interesting ecological perspective—retaining the ability to use manganese as an electron donor for photosynthesis might be uniquely important for Cyanobacteria adapted to extremely arid environments, the one ecological context where water might not be the most advantageous electron source. During periods of desiccation, the ability to maintain photosynthetic electron transport without consuming what little water you have could be fundamental to survival. Consistent with this hypothesis, we observed that replete manganese improved the ability of *Chroococcidiopsis* to survive desiccation. The manganese concentrations required to observe this benefit greatly exceed the manganese concentrations required for growth.

Synechocystis and *Chroococcidiopsis* each provided different windows into cyanobacterial manganese oxidation. *Synechocystis* was amenable to carefully controlled timecourse experiments and genetic manipulation, allowing us to tease apart some of the mechanistic details underpinning this phenomenon. However, as a non-extremophilic freshwater organism, *Synechocystis* did not offer much insight into desiccation resistance. In contrast, *Chroococcidiopsis* was less amenable to laboratory growth and manipulation, but has been recognized for its remarkable desiccation tolerance (45–47) and association with manganese biogeochemistry in the context of desert varnish (62). By XANES spectroscopy, we observed clear signatures of manganese oxidation in *Chroococcidiopsis* biomass, while such signatures with *Synechocystis* were much subtler. The difference between windowsill and incubator grown *Chroococcidiopsis* cultures suggested that this manganese oxidation occurs preferentially under slower growth regimes.

Taken together, the work presented here sheds new light on the intimate connections between Cyanobacteria and manganese biogeochemistry. Phototrophic manganese oxidation by ancestral PSII led to the origin of the WOC and oxygenic photosynthesis, a critical evolutionary innovation that is continuously played back, not only through photoassembly, but also through bulk manganese oxidation. This interaction between Cyanobacteria and manganese—which transformed the face of the Earth with the Great Oxygenation Event ~2.4 billion years ago—continues to play a crucial role in our biosphere through its control on manganese redox cycling.

Methods

Culture conditions

Synechocystis sp. PCC 6803 strains (WT, CP47-his, D1-Δ, and D1-D170A) were obtained from Richard Debus, University of California Riverside. Cultures were grown in liquid BG11 medium (63) supplemented with 5 mM glucose along with 25 μg/mL erythromycin for the D1-Δ mutant and kanamycin for the D1-D170A mutant. Cultures were kept in a 30°C shaking incubator under constant illumination with white fluorescent lights. Growth was measured by optical density at 730 nm. Experiments were conducted with cultures at mid to late exponential growth stage.

Chroococcidiopsis sp. PCC 7433 was obtained from the ATCC and grown in liquid BG11 without glucose, with normal 9 μM $MnCl_2$, no $MnCl_2$, or 100 μM $MnCl_2$. Cultures were kept either in a 30°C shaking incubator under white fluorescent lights or at room temperature with natural light on an east-facing, southern California windowsill. For desiccation experiments, cells were grown in either regular BG11 medium, BG11 medium with no $MnCl_2$, and BG11 supplemented with 100 μM $MnCl_2$.

Cultures were imaged by light microscopy using a B120 LED microscope equipped with an MD500 eyepiece camera (Amscope).

Manganese oxidation experiments

Manganese oxidation experiments were conducted in either culture tube or Erlenmeyer flask formats. The tube formats contained 1-2 mL volume and were kept stationary, while the flask formats contained 4-5 mL volume and were kept shaking at ~120 rpm. In either format, experiments were conducted with and without 1 mM $MnCl_2$, 20 mM Na citrate, 10 µM DCMU, 400 µg/mL SOD, 100 µg/mL catalase, and 50 mM HEPES buffer. Unless otherwise specified, experiments were buffered at pH 7.6 or 7.8. Experiments were incubated at 30°C under constant illumination with white fluorescent lights. Dark conditions were wrapped in aluminum foil.

For the LBB assay we used a 0.04% LBB solution in 0.2% acetic acid. At each timepoint, 50 µL aliquots were taken from manganese oxidation experiments and added to 250 µL of LBB solution. After allowing 15 minutes for the reaction to proceed to completion, cells were removed by centrifugation at 16,000 *g* for 1 minute. 250 µL of supernatant was transferred to a 96-well plate and quantified by absorbance at 620 nm with a Cytation 5 plate reader (BioTek). $KMnO_4$ standard curves were used to translate LBB absorbance into concentrations, under the assumption that the product measured is Mn(III)-citrate and not MnO_2.

Membrane and pure protein preparations

Photosynthetic membranes were isolated following the protocol described by Norling *et al* (64). Liter-scale cultures were harvested by centrifugation at 5,000 *g* for 5 minutes. Pellets were resuspended in 20 mM $K_xH_xPO_4$ buffer, pH 7.8. Cells were lysed with 0.17-0.18 mm glass beads by 3 sets of vortexing for 2 minutes followed by 1 minute of resting on ice. The resulting lysate was centrifuged at 3,300 *g* for 1 minute, and the supernatant was collected. To salvage any unlysed cells, an additional buffer aliquot was added to the pelleted material/beads, and vortexed and centrifuged again. Pooled supernatants were centrifuged at 3,300 *g* for 10 minutes to remove any remaining debris and beads. The resulting supernatant was ultracentrifuged at 103,000 *g* for 30 minutes in a TLA-120.2 fixed angle rotor (Beckman Coulter). Pelleted membranes were resuspended in 25 M sucrose, 5 mM potassium phosphate, pH 7.8.

His-tagged PSII protein was purified following the protocol described by Vavilin (65). Harvested cell pellets were resuspended in 50 mM 2-(4-morpholino)ethanesulfonic acid (MES)-NaOH buffer, pH 6.0, with 10 mM $MgCl_2$, 5 mM $CaCl_2$, 20% glycerol, and 1 mM phenylmethylsulfonyl fluoride. Cells were lysed with glass beads in a BeadBeater chamber (Biospec Products) by 15 sets of 15 seconds of bead beating followed by 2 minutes of cool down. To solubilize membrane bound PSII, 100 µL/mL of 10% dodecyl ß-D-maltoside (DoDM) detergent was added to the lysate and mixed by gently pipetting up and down for 20 minutes. The lysate was then ultracentrifuged at 40,000 *g* for 20 minutes in a 50 Ti fixed angle rotor (Beckman Coulter). Supernatants were collected for PSII purification by nickel affinity chromatography. 5 mL gravity flow columns were loaded with 2 mL of 50% nickel nitrilotriacetic acid agarose beads and briefly allowed to settle. Beads were washed with 5 column volumes of milli-Q water and then equilibrated with 5 mL 50 mM MES-NaOH buffer, pH 6.0, with 10 mM $MgCl_2$, 5 mM $CaCl_2$, 20% glycerol, and 0.04% DoDM. The PSII-containing supernatant was applied to the column, washed with the same buffer, and then eluted with the same buffer supplemented with 50 mM histidine. Purity of eluted PSII was confirmed by UV-vis spectroscopy. To exchange the histidine elution buffer, an equal volume of 50 mM MES-NaOH, pH 6.0, with 15% glycerol, 15 mM $CaCl_2$, 5 mM $MgCl_2$, 0.03% DoDM, and 20% polyethylene glycol (PEG)-8000 was added for PEG precipitation of PSII. The mixtures were incubated on ice for 30 minutes and then centrifuged at 40,000 *g* for 30 minutes. Pelleted protein was resuspended in 50 mM MES-NaOH, pH 6.0, with 15% glycerol, 15 mM $CaCl_2$, 5 mM $MgCl_2$, 0.03% DoDM.

Synchrotron X-ray spectroscopy

Synchrotron analyses were conducted at the Stanford Synchrotron Radiation Lightsource on X-ray microprobe beamline 2-3. Live cells were pelleted by centrifugation and washed with sterile milli-Q water. Dense cell slurries were spotted onto glass slides. XANES spectra at the manganese K-edge were collected from 6300 to 7100 eV. The beam was energy calibrated using the pre-edge feature of $KMnO_4$ at 6543.34 eV. Spectra were reduced and fit using SIXPACK (66) (https://www.sams-xrays.com/). Fits were

calculated on the region from 6530 to 6590 eV using standard spectra of $MnCl_2$, feitknechtite, and birnessite as Mn(II), Mn(III), and Mn(IV) components, respectively.

Other measurements

Chlorophyll fluorescence measurements were conducted in a cuvette format with an AquaPen-C AP-C 100 (Photon Systems Instruments) using the 620 nm excitation light and predefined NPQ1 protocol. Photochemical quenching (*qP*) was calculated as $F_m'-F_t'/F_m'-F_0'$, where F_m' is the maximum fluorescence upon a saturating flash in the light adapted state, F_t' is the transient fluorescence in the light adapted state, and F_0' is the minimal fluorescence in the light adapted state.

Measurements of culture O_2 saturation were made at room temperature using a microsensor monometer system with an OX-500 oxygen microsensor (Unisense). Conductivity was translated to O_2 saturation using a standard curve generated from deionized water bubbled for 30 minutes with air or N_2 for 100% or 0% saturation, respectively.

For labelled carbon fixation experiments, 166 µM $H^{13}CO_3^-$ was added to manganese oxidation incubations. At the 48 hour timepoint, cells were pelleted by centrifugation, washed, and lyophilized. The bulk carbon isotope composition of dry biomass was measured with an elemental analyzer isotope ratio mass spectrometer (ThermoFischer Scientific). Instrument precision on standards was ± 0.2‰.

For *Synechocystis* survivability experiments, cells were pelleted by centrifugation and resuspended in fresh BG11 medium +/- glucose, $MnCl_2$, and Na citrate. Experiments were conducted in both tube and flask formats and incubated at 30°C under constant illumination with white fluorescent lights. At each timepoint, 1 µL was spotted onto BG11 agar plates with glucose.

For *Chroococcidiopsis* desiccation experiments cells were pelleted by centrifugation to remove medium and avoid salt crystallization during drying. Cell pellets were resuspended in a small amount of sterile milli-Q water and transferred to a 24-well plate where they were left to dry. Plates were stored at room temperature with natural light on a windowsill. After four days, cells were rehydrated in the same

medium they were originally grown in. After allowing 1 hour for rehydration, survival was assessed by chlorophyll fluorescence induction and quenching.

Acknowledgements
This research was supported by NSF grant IOS-1833247 (HAJ and WWF) and the NSF GRFP (UFL). Use of the Stanford Synchrotron Radiation Lightsource, SLAC National Accelerator Laboratory, was supported by the DOE Office of Basic Energy Sciences under Contract No. DE-AC02-76SF00515, and the SSRL Structural Molecular Biology Program supported by the DOE Office of Biological and Environmental Research and the NIH, NIGMS (P41GM103393). We thank Rick Debus for providing *Synechocystis* strains, Sam Webb, Sharon Bone, and Nick Edwards for support at SSRL, and Kat Dawson for help with isotope ratio measurements. We also thank Jared Leadbetter, Hank Yu, John Magyar, Danie Monteverde, Brian Hoffman, Rick Debus, Rob Burnap, Kevin Redding, Jeff Cameron, and Patrick Shih for helpful discussions and insight.

Author contributions
UFL, HAJ, JH, JSV, and WWF designed research. UFL, HAJ, YD, and LB generated data. UFL wrote the manuscript with input from HAJ, JSV, and WWF.

References

1. J. J. Morgan, Manganese in natural waters and earth's crust: its availability to organisms. *Met. Ions Biol. Syst.* **37**, 1–34 (2000).

2. U. F. Lingappa, D. R. Monteverde, J. S. Magyar, J. S. Valentine, W. W. Fischer, How manganese empowered life with dioxygen (and vice versa). *Free Radic. Biol. Med.*, 113–125 (2019).

3. B. M. Tebo, *et al.*, Biogenic Manganese Oxides: Properties and Mechanisms of Formation. *Annu. Rev. Earth Planet. Sci.* **32**, 287–328 (2004).

4. C. N. Butterfield, A. V. Soldatova, S.-W. Lee, T. G. Spiro, B. M. Tebo, Mn(II,III) oxidation and MnO2 mineralization by an expressed bacterial multicopper oxidase. *Proc. Natl. Acad. Sci.* **110**, 11731–11735 (2013).

5. L. Tao, *et al.*, Mn(II) Binding and Subsequent Oxidation by the Multicopper Oxidase MnxG Investigated by Electron Paramagnetic Resonance Spectroscopy. *J. Am. Chem. Soc.*, 150813153632003 (2015).

6. A. V. Soldatova, C. Butterfield, O. F. Oyerinde, B. M. Tebo, T. G. Spiro, Multicopper oxidase involvement in both Mn(II) and Mn(III) oxidation during bacterial formation of MnO(2). *J. Biol. Inorg. Chem. JBIC Publ. Soc. Biol. Inorg. Chem.* **17**, 1151–1158 (2012).

7. K. Geszvain, J. K. McCarthy, B. M. Tebo, Elimination of Manganese(II,III) Oxidation in Pseudomonas putida GB-1 by a Double Knockout of Two Putative Multicopper Oxidase Genes. *Appl. Environ. Microbiol.* **79**, 357–366 (2013).

8. P. L. A. M. Corstjens, J. P. M. de Vrind, T. Goosen, E. W. de V. Jong, Identification and molecular analysis of the *Leptothrix discophora* SS-1 *mofA* gene, a gene putatively encoding a manganese-oxidizing protein with copper domains. *Geomicrobiol. J.* **14**, 91–108 (1997).

9. J. P. Ridge, *et al.*, A multicopper oxidase is essential for manganese oxidation and laccase-like activity in Pedomicrobium sp. ACM 3067. *Environ. Microbiol.* **9**, 944–953 (2007).

10. K. Nakama, *et al.*, Heterologous Expression and Characterization of the Manganese-Oxidizing Protein from Erythrobacter sp. Strain SD21. *Appl. Environ. Microbiol.* **80**, 6837–6842 (2014).

11. C. R. Anderson, *et al.*, Mn(II) oxidation is catalyzed by heme peroxidases in "Aurantimonas manganoxydans" strain SI85-9A1 and Erythrobacter sp. strain SD-21. *Appl. Environ. Microbiol.* **75**, 4130–4138 (2009).

12. D. R. Learman, B. M. Voelker, A. I. Vazquez-Rodriguez, C. M. Hansel, Formation of manganese oxides by bacterially generated superoxide. *Nat. Geosci.* **4**, 95–98 (2011).

13. P. F. Andeer, D. R. Learman, M. McIlvin, J. A. Dunn, C. M. Hansel, Extracellular haem peroxidases mediate Mn(II) oxidation in a marine Roseobacter bacterium via superoxide production. *Environ. Microbiol.* **17**, 3925–3936 (2015).

14. H. Yu, J. R. Leadbetter, Bacterial chemolithoautotrophy via manganese oxidation. *Nature* **583**, 453–458 (2020).

15. C. M. Hansel, C. A. Zeiner, C. M. Santelli, S. M. Webb, Mn(II) oxidation by an ascomycete fungus is linked to superoxide production during asexual reproduction. *Proc. Natl. Acad. Sci. U. S. A.* **109**, 12621–12625 (2012).

16. M. Hofrichter, Review: lignin conversion by manganese peroxidase (MnP). *Enzyme Microb. Technol.* **30**, 454–466 (2002).

17. W. W. Fischer, J. Hemp, J. E. Johnson, Evolution of Oxygenic Photosynthesis. *Annu. Rev. Earth Planet. Sci.* **44**, 647–683 (2016).

18. R. E. Blankenship, *Molecular Mechanisms of Photosynthesis*, 2nd Ed. (Wiley-Blackwell, 2014).

19. J. P. McEvoy, G. W. Brudvig, Water-splitting chemistry of photosystem II. *Chem. Rev.* **106**, 4455–4483 (2006).

20. Y. Umena, K. Kawakami, J.-R. Shen, N. Kamiya, Crystal structure of oxygen-evolving photosystem II at a resolution of 1.9 \AA. *Nature* **473**, 55–60 (2011).

21. H. Bao, R. L. Burnap, Photoactivation: The Light-Driven Assembly of the Water Oxidation Complex of Photosystem II. *Front. Plant Sci.* **7** (2016).

22. P. J. Nixon, J. T. Trost, B. A. Diner, Role of the carboxy terminus of polypeptide D1 in the assembly of a functional water-oxidizing manganese cluster in photosystem II of the cyanobacterium Synechocystis sp. PCC 6803: assembly requires a free carboxyl group at C-terminal position 344. *Biochemistry* **31**, 10859–10871 (1992).

23. C. Chen, J. Kazimir, G. M. Cheniae, Calcium modulates the photoassembly of photosystem II (Mn)4-clusters by preventing ligation of nonfunctional high-valency states of manganese. *Biochemistry* **34**, 13511–13526 (1995).

24. P. J. Nixon, B. A. Diner, Aspartate 170 of the photosystem II reaction center polypeptide D1 is involved in the assembly of the oxygen-evolving manganese cluster. *Biochemistry* **31**, 942–948 (1992).

25. H. A. Chu, A. P. Nguyen, R. J. Debus, Site-directed photosystem II mutants with perturbed oxygen-evolving properties. 1. Instability or inefficient assembly of the manganese cluster in vivo. *Biochemistry* **33**, 6137–6149 (1994).

26. B. K. Semin, *et al.*, The extrinsic PsbO protein modulates the oxidation/reduction rate of the exogenous Mn cation at the high-affinity Mn-binding site of Mn-depleted PSII membranes. *J. Bioenerg. Biomembr.* **47**, 361–367 (2015).

27. R. J. Boerner, A. P. Nguyen, B. A. Barry, R. J. Debus, Evidence from directed mutagenesis that aspartate 170 of the D1 polypeptide influences the assembly and/or stability of the manganese cluster in the photosynthetic water-splitting complex. *Biochemistry* **31**, 6660–6672 (1992).

28. R. O. Cohen, P. J. Nixon, B. A. Diner, Participation of the C-terminal region of the D1-polypeptide in the first steps in the assembly of the Mn4Ca cluster of photosystem II. *J. Biol. Chem.* **282**, 7209–7218 (2007).

29. K. A. Campbell, *et al.*, Dual-Mode EPR Detects the Initial Intermediate in Photoassembly of the Photosystem II Mn Cluster: The Influence of Amino Acid Residue 170 of the D1 Polypeptide on Mn Coordination. *J. Am. Chem. Soc.* **122**, 3754–3761 (2000).

30. N. Tamura, G. Cheniae, Photoactivation of the water-oxidizing complex in Photosystem II membranes depleted of Mn and extrinsic proteins. I. Biochemical and kinetic characterization. *Biochim. Biophys. Acta* **890**, 179–194 (1987).

31. M. Seibert, N. Tamura, Y. Inoue, Lack of photoactivation capacity in Scenedesmus obliquus LF-1 results from loss of half the high-affinity manganese-binding site. *Biochim. Biophys. Acta BBA - Bioenerg.* **974**, 185–191 (1989).

32. J. L. Roose, H. B. Pakrasi, The Psb27 Protein Facilitates Manganese Cluster Assembly in Photosystem II. *J. Biol. Chem.* **283**, 4044–4050 (2008).

33. P. Chernev, *et al.*, Light-driven formation of manganese oxide by today's photosystem II supports evolutionarily ancient manganese-oxidizing photosynthesis. *Nat. Commun.* **11**, 6110 (2020).

34. J. E. Johnson, *et al.*, Manganese-oxidizing photosynthesis before the rise of cyanobacteria. **110**, 11238–11243 (2013).

35. W. W. Fischer, J. Hemp, J. E. Johnson, Manganese and the Evolution of Photosynthesis. *Orig. Life Evol. Biosphere J. Int. Soc. Study Orig. Life* **45**, 351–357 (2015).

36. U. F. Lingappa, *et al.*, Manganese cycling communities at the dawn of the Great Oxidation Event (in prep).

37. J. Hemp, *et al.*, Mn-oxidizing Phototrophy Was Likely a Direct Precursor to Oxygenic Photosynthesis (in prep).

38. W. E. Krumbein, H. J. Altmann, A new method for the detection and enumeration of manganese oxidizing and reducing microorganisms. *Helgoländer Wiss. Meeresunters.* **25**, 347–356 (1973).

39. M. H. Wright, K. Geszvain, V. E. Oldham, G. W. Luther, B. M. Tebo, Oxidative Formation and Removal of Complexed Mn(III) by Pseudomonas Species. *Front. Microbiol.* **9**, 560 (2018).

40. R. J. Debus, A. P. Nguyen, A. B. Conway, "Identification of Ligands to Manganese and Calcium in Photosystem II by Site-Directed Mutagenesis" in *Current Research in Photosynthesis*, M. Baltscheffsky, Ed. (Springer Netherlands, 1990), pp. 829–832.

41. R. J. Debus, *et al.*, Does Histidine 332 of the D1 Polypeptide Ligate the Manganese Cluster in Photosystem II? An Electron Spin Echo Envelope Modulation Study †. *Biochemistry* **40**, 3690–3699 (2001).

42. L. L. Richardson, C. Aguilar, K. H. Nealson, Manganese oxidation in pH and O_2 microenvironments produced by phytoplankton1,2: Mn oxidation by phytoplankton. *Limnol. Oceanogr.* **33**, 352–363 (1988).

43. F. Garcia-Pichel, Plausible mechanisms for the boring on carbonates by microbial phototrophs. *Sediment. Geol.* **185**, 205–213 (2006).

44. B. Kim, *et al.*, High reactivity confounds measurements of soluble Mn(III) in natural samples (in review).

45. M. G. Caiola, R. Ocampo-Friedmann, E. I. Friedmann, Cytology of long-term desiccation in the desert cyanobacterium Chroococcidiopsis (Chroococcales). *Phycologia* **32**, 315–322 (1993).

46. D. Billi, E. I. Friedmann, K. G. Hofer, M. G. Caiola, R. Ocampo-Friedmann, Ionizing-Radiation Resistance in the Desiccation-Tolerant Cyanobacterium Chroococcidiopsis. *Appl. Environ. Microbiol.* **66**, 1489–1492 (2000).

47. M. Potts, Mechanisms of desiccation tolerance in cyanobacteria. *Eur. J. Phycol.* **34**, 319–328 (1999).

48. J. B. Waterbury, R. Y. Stanier, Patterns of growth and development in pleurocapsalean cyanobacteria. *Microbiol. Rev.* **42**, 2–44 (1978).

49. N. Keren, M. J. Kidd, J. E. Penner-Hahn, H. B. Pakrasi, A light-dependent mechanism for massive accumulation of manganese in the photosynthetic bacterium Synechocystis sp. PCC 6803. *Biochemistry* **41**, 15085–15092 (2002).

50. D. L. Chaput, *et al.*, Mn oxide formation by phototrophs: Spatial and temporal patterns, with evidence of an enzymatic superoxide-mediated pathway. *Sci. Rep.* **9**, 18244 (2019).

51. P. Dvořák, *et al.*, "Diversity of the Cyanobacteria" in *Modern Topics in the Phototrophic Prokaryotes*, P. C. Hallenbeck, Ed. (Springer International Publishing, 2017), pp. 3–46.

52. R. E. Trouwborst, Soluble Mn(III) in Suboxic Zones. *Science* **313**, 1955–1957 (2006).

53. A. S. Madison, B. M. Tebo, A. Mucci, B. Sundby, G. W. Luther, Abundant Porewater Mn(III) Is a Major Component of the Sedimentary Redox System. *Science* **341**, 875–878 (2013).

54. V. E. Oldham, A. Mucci, B. M. Tebo, G. W. Luther, Soluble Mn(III)–L complexes are abundant in oxygenated waters and stabilized by humic ligands. *Geochim. Cosmochim. Acta* **199**, 238–246 (2017).

55. A. Qian, *et al.*, Geochemical Stability of Dissolved Mn(III) in the Presence of Pyrophosphate as a Model Ligand: Complexation and Disproportionation. *Environ. Sci. Technol.* **53**, 5768–5777 (2019).

56. M. Keiluweit, *et al.*, Long-term litter decomposition controlled by manganese redox cycling. *Proc. Natl. Acad. Sci.* **112**, E5253–E5260 (2015).

57. V. E. Oldham, M. R. Jones, B. M. Tebo, G. W. Luther, Oxidative and reductive processes contributing to manganese cycling at oxic-anoxic interfaces. *Mar. Chem.* **195**, 122–128 (2017).

58. E. Hu, *et al.*, Role of dissolved Mn(III) in transformation of organic contaminants: Non-oxidative versus oxidative mechanisms. *Water Res.* **111**, 234–243 (2017).

59. X. Wang, *et al.*, Phototransformation of estrogens mediated by Mn(III), not by reactive oxygen species, in the presence of humic acids. *Chemosphere* **201**, 224–233 (2018).

60. K. L. Johnson, *et al.*, Dissolved Mn(III) in water treatment works: Prevalence and significance. *Water Res.* **140**, 181–190 (2018).

61. M. E. Jones, *et al.*, Manganese-Driven Carbon Oxidation at Oxic–Anoxic Interfaces. *Environ. Sci. Technol.* **52**, 12349–12357 (2018).

62. U. F. Lingappa, *et al.*, An ecophysiological explanation for manganese enrichment in rock varnish (in review).

63. J. J. Eaton-Rye, "Construction of Gene Interruptions and Gene Deletions in the Cyanobacterium Synechocystis sp. Strain PCC 6803" in *Photosynthesis Research Protocols*, Methods in Molecular Biology., R. Carpentier, Ed. (Humana Press, 2011), pp. 295–312.

64. B. Norling, E. Zak, B. Andersson, H. Pakrasi, 2D-isolation of pure plasma and thylakoid membranes from the cyanobacterium Synechocystis sp. PCC 6803. *FEBS Lett.* **436**, 189–192 (1998).

65. D. V. Vavilin, "Methods for the Isolation of Functional Photosystem II Core Particles from the Cyanobacterium Synechocystis sp. PCC 6803" in *Photosynthesis Research Protocols*, Methods in Molecular Biology., R. Carpentier, Ed. (Humana Press, 2011), pp. 29–40.

66. S. M. Webb, SIXPack a Graphical User Interface for XAS Analysis Using IFEFFIT. *Phys. Scr.*, 1011 (2005).

Figures

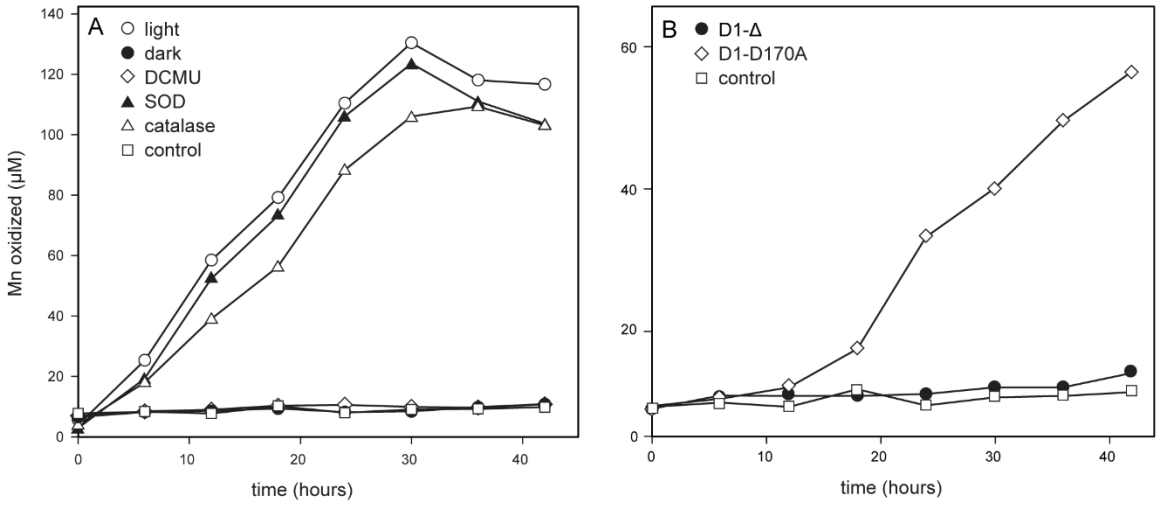

Figure 1. Manganese oxidation by *Synechocystis*. Cells were incubated in culture tubes with manganese chloride, sodium citrate, and HEPES buffer, +/- DCMU, SOD, catalase. At each timepoint, aliquots were removed and assayed for the presence of oxidized manganese by LBB. This experiment has been repeated many times. While it usually follows the pattern shown here, there has been some inconsistency, largely attributable to the confounding pathways illustrated in Figs. 3-5. Therefore, the data presented is a representative example of the phenomenon rather than an average of separate experiments with error bars. ***A.*** Manganese oxidation by WT cells. Manganese oxidation was inhibited in the dark or by addition of DCMU but not inhibited by SOD or catalase, indicative of a mechanism involving PSII and not O_2^- or H_2O_2. ***B.*** Manganese oxidation by D1 mutants. The D1-Δ mutant did not oxidize manganese, while the D1-D170A mutant did, consistent with a PSII dependent mechanism.

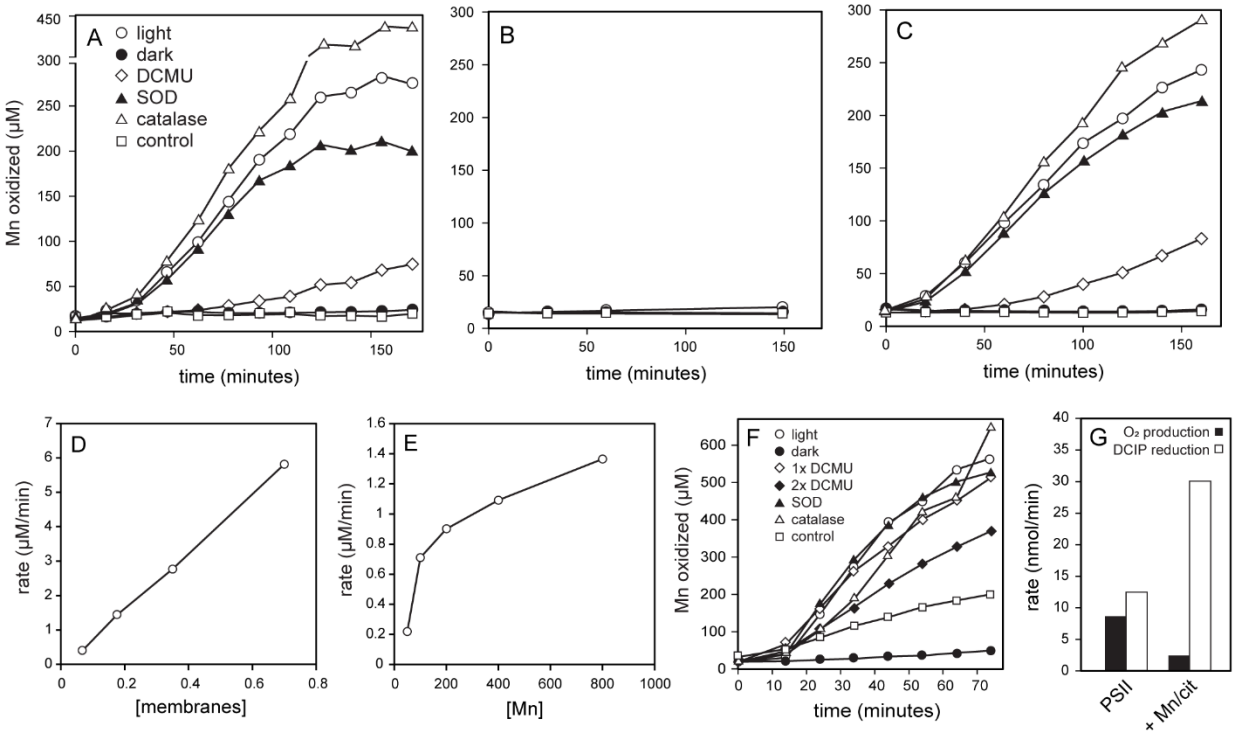

Figure 2. Manganese oxidation by isolated photosynthetic membranes and PSII protein. ***A.*** WT membranes. ***B.*** D1-Δ mutant membranes. ***C.*** D1-D170A mutant membranes. The WT and D1-D170A membranes oxidized manganese and were inhibited in the dark or by addition of DCMU but not by SOD or catalase, while the D1-Δ membranes did not oxidize manganese. ***D-E.*** The rate of manganese oxidation by WT membranes increased linearly with increasing membrane concentration (***D***) but appeared to approach a saturated maximum rate with increasing substrate concentration (***E***), consistent with Michaelis-Menten enzyme kinetics. ***F.*** Purified PSII protein oxidized manganese and was inhibited in the dark but not by SOD or catalase. DCMU inhibition was incomplete but exhibited a dose titration when doubled, suggesting that the incomplete inhibition could be due to insufficient DCMU. ***G.*** Purified PSII exhibited a decrease in O_2 production under manganese oxidizing conditions accompanied by an increase in DCIP reduction, consistent with the manganese serving as an alternative electron donor for PSII. However, we note that the DCIP signal could be confounded by reactivity with the manganese oxidation product.

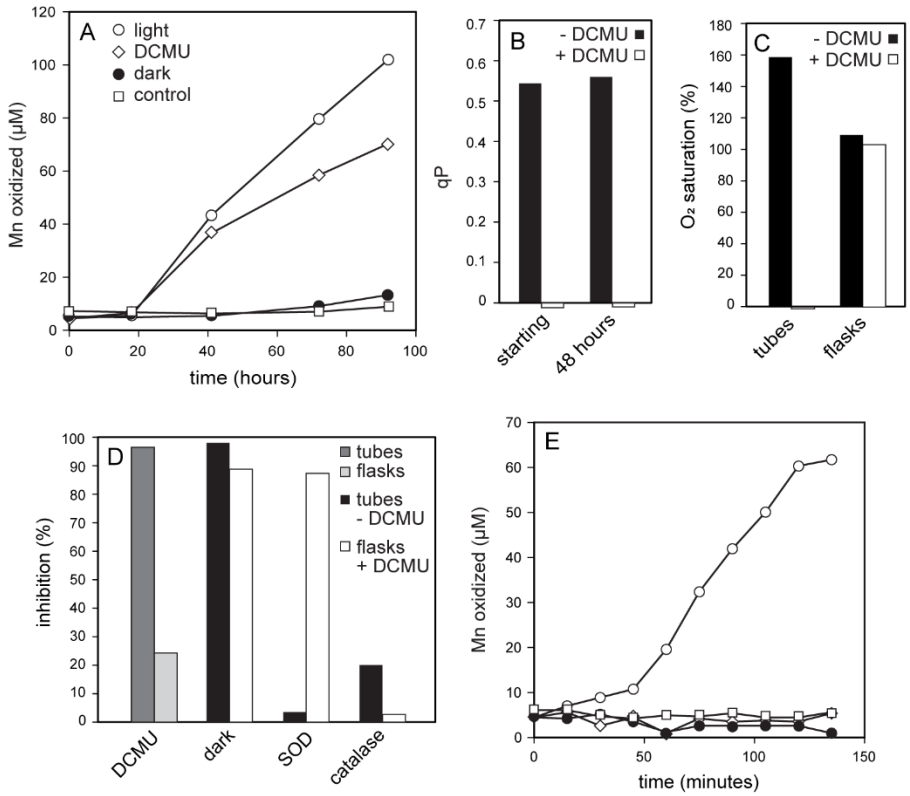

Figure 3. An O_2 dependent pathway of manganese oxidation. ***A.*** Whole cell manganese oxidation experiment conducted in flasks and shaking, in contrast to the experiment shown in Figure 1 which was in tubes and not shaking. In the flask format, DCMU did not inhibit manganese oxidation. ***B.*** Chlorophyll fluorescence data showing DCMU inhibition of PSII photochemical quenching (*qP*), demonstrating no diminution in DCMU efficacy during this timecourse, confirming that the manganese oxidation seen in the presence of DCMU is PSII independent. ***C.*** Conductivity measurements to determine O_2 saturation. Under normal conditions *Synechocystis* cells produce more O_2 than they consume so cultures are supersaturated. In the presence of DCMU, they are unable to produce O_2 but still consume it. In the tube format, external O_2 input was diffusion limited so experimental conditions with DCMU went anaerobic. In the flask format, shaking kept them aerated. ***D.*** Comparison of the manganese oxidation phenomena observed in the tube vs. flask formats. The PSII independent manganese oxidation seen in flasks with DCMU was substantially inhibited by the addition of SOD, while the original manganese oxidation phenomenon in tubes was not, suggesting distinct pathways of biological manganese oxidation—a PSII dependent, O_2 independent pathway and a separate PSII independent, O_2 dependent pathway. ***E.*** Manganese oxidation by WT membranes remained inhibited by DCMU in the flask format, suggesting that this PSII independent pathway was not expressed in the membrane system.

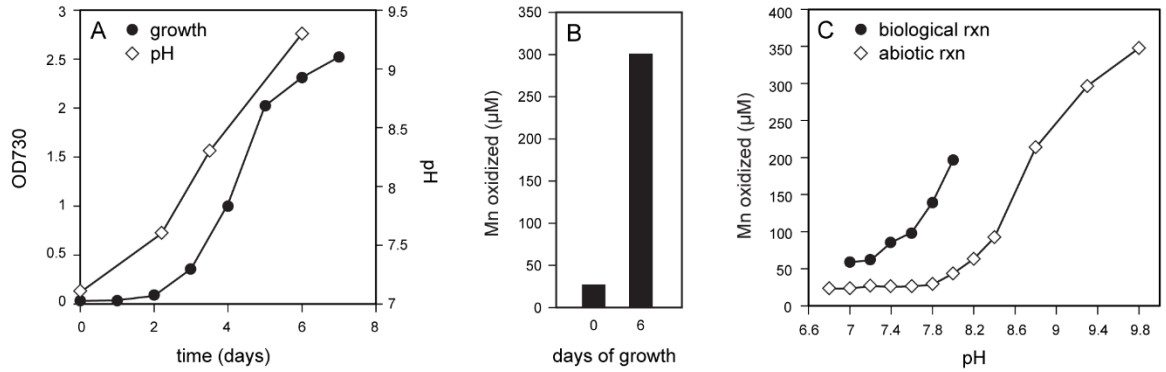

Figure 4. Indirect manganese oxidation driven by pH. ***A.*** WT *Synechocystis* growth curve demonstrating that cyanobacterial autotrophy increases the solution pH. ***B.*** Unbuffered BG11 medium altered by growth (from which cells were removed by centrifugation) catalyzed substantially more abiotic manganese oxidation than starting medium. We attributed this largely to pH, although the presence of biogenic ligands and/or extracellular enzymes may also contribute. ***C.*** Manganese oxidation is pH sensitive—both the biological and abiotic reactions proceeded more rapidly with increasing pH. However, in carefully buffered experiments that were continually mixed to minimize the buildup of local pH or O_2 gradients around cells, the biological reaction was clearly distinguishable from the abiotic one. This suggested that although Cyanobacteria raising their local pH and thereby driving the abiotic reaction could be an important and relevant pathway of manganese oxidation, it cannot explain the full phenomenon observed here.

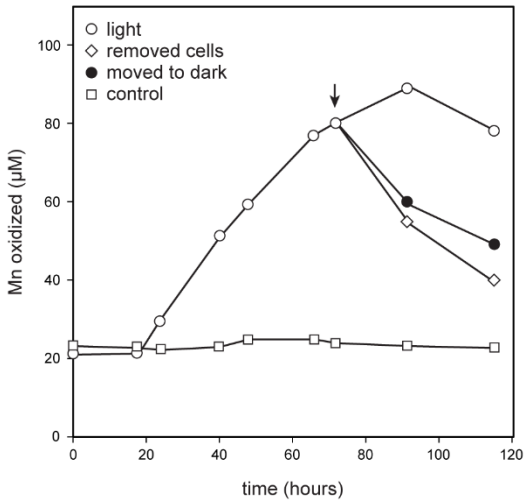

Figure 5. The manganese oxidation product (putatively Mn(III)-citrate) is transient. Manganese oxidation experiments were run normally to build up product, and then stopped (indicated by arrow) by either removing the cells via centrifugation or moving the reactions to the dark. In both cases, the product pool rapidly diminished. This is consistent with the known chemistry of Mn(III) species, which are highly labile and rapidly disproportionate or engage in other redox reactions, making them notoriously short-lived species.

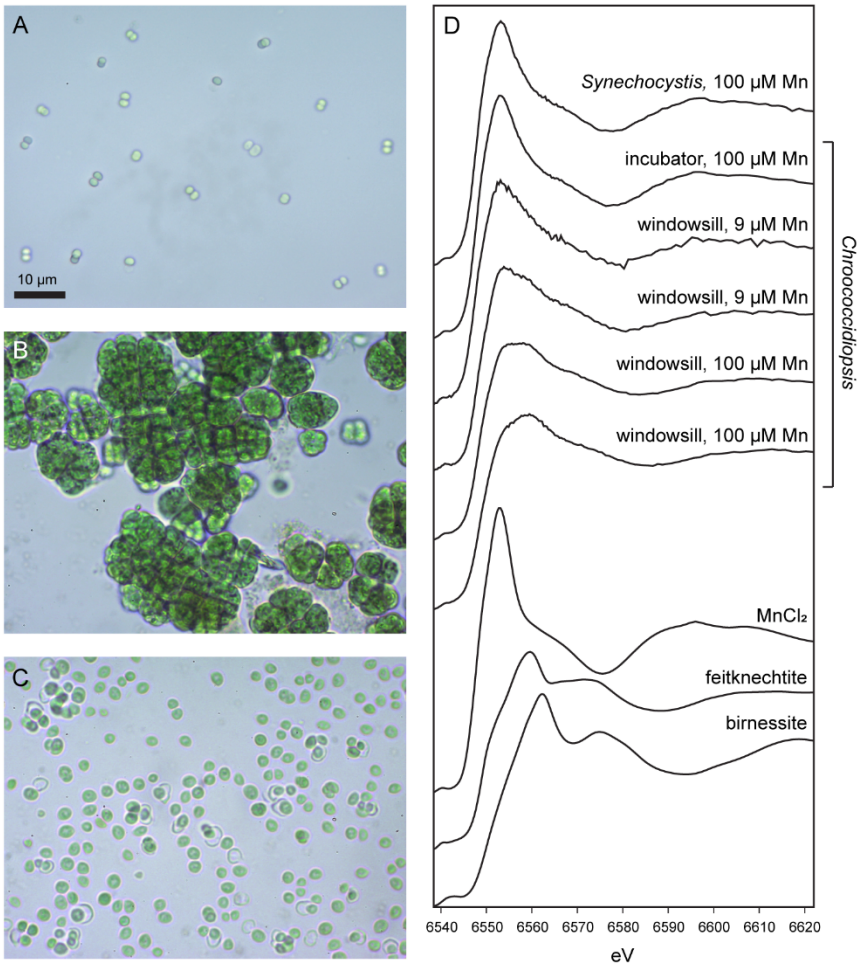

Figure 6. Manganese oxidation signatures in cyanobacterial biomass. ***A.*** *Synechocystis*. ***B.*** Clumpy, baeocystous *Chroococcidiopsis* from windowsill cultures. ***C.*** Non-clumpy vegetative *Chroococcidiopsis* from incubator cultures. ***D.*** Synchrotron XANES spectra at the manganese K-edge showing variable amounts of oxidized manganese associated with *Chroococcidiopsis* cells, increasing with clumpiness and total manganese content. For *Synechocystis* and incubator *Chroococcidiopsis*, the spectra shown are representative examples from cultures supplemented with 100 µM $MnCl_2$ to improve total manganese signal. For windowsill *Chroococcidiopsis* the spectra shown are endmembers demonstrating the range of spectra observed under each $MnCl_2$ concentration. Least squares fits quantifying the components of these spectra can be found in Fig. S2. Standard spectra of $MnCl_2$, feitknechtite, and birnessite are shown as references for Mn(II), Mn(III), and Mn(IV) species, respectively.

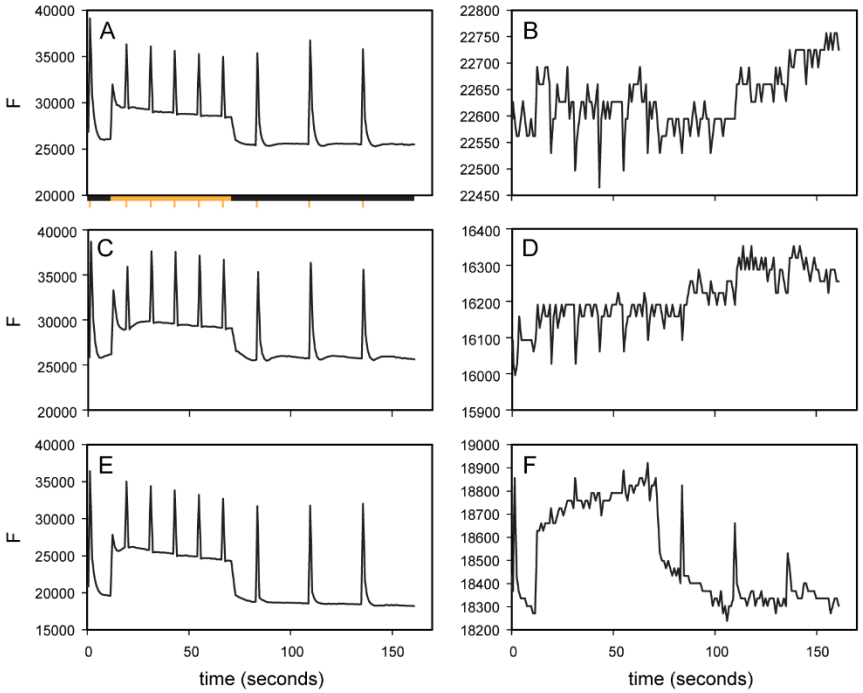

Figure 7. Plentiful manganese improves *Chroococcidiopsis* desiccation tolerance, assayed by chlorophyll fluorescence induction and quenching. *Chroococcidiopsis* cells grown under manganese starved conditions (***A***-***B***), regular BG11 medium with 9 µM manganese (***C***-***D***), and manganese replete conditions with 100 µM manganese (***E***-***F***), were dried for four days, then rehydrated. The chlorophyll fluorescence induction protocol used as a measure of function is illustrated along the x axis of panel *A*; dark bar indicates dark background, yellow bar indicates actinic light background, yellow tick marks indicate saturating pulses. Starting cultures under all three conditions exhibited normal fluorescence quenching patterns (***A***, ***C***, ***E***). By the end of the experiment, the manganese replete condition was the only one that maintained any fluorescence quenching capability (***B***, ***D***, ***F***).

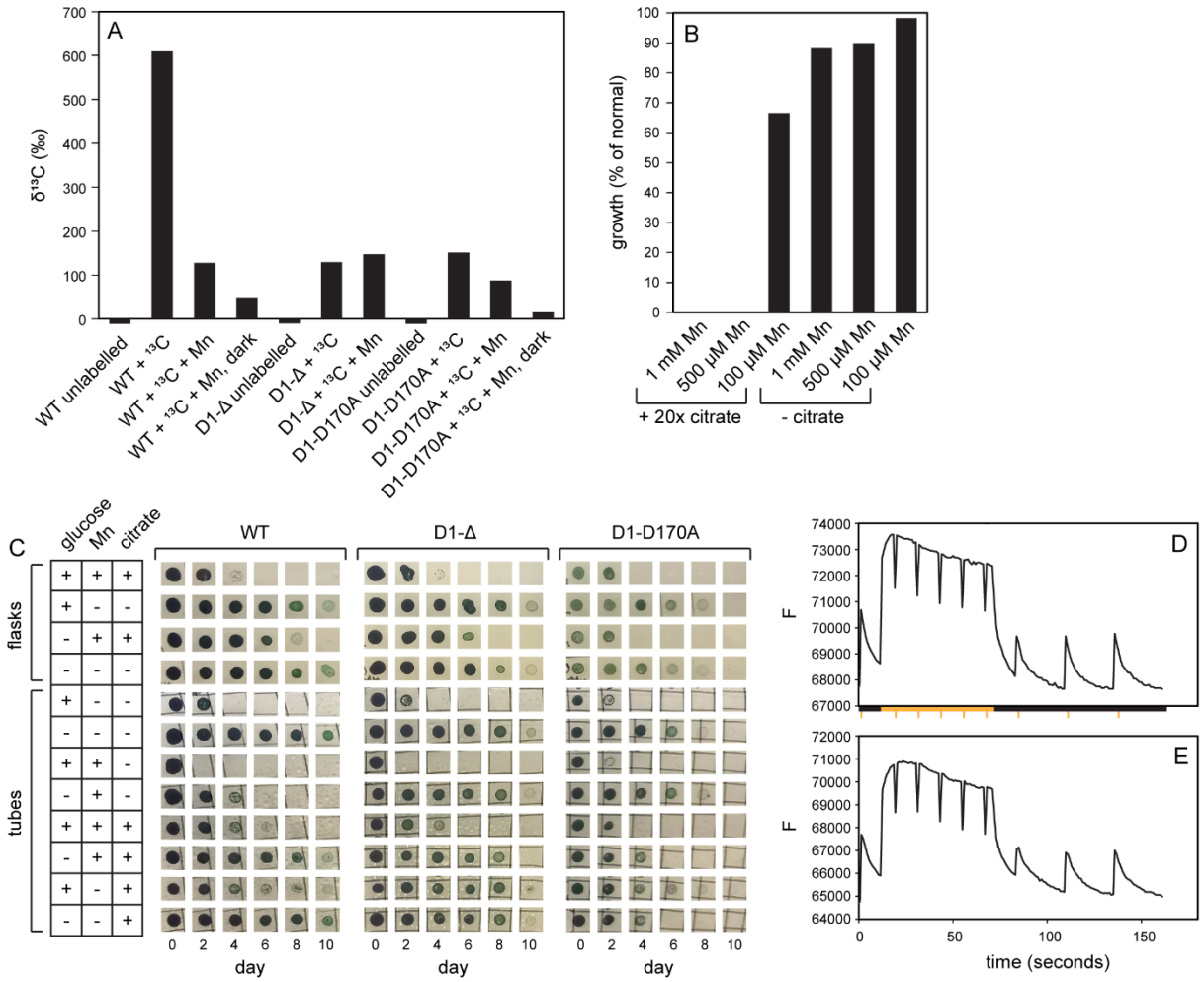

Figure S1. Attempts at demonstrating energy conservation coupled to manganese oxidation by PSII. ***A.*** To investigate carbon fixation coupled to manganese oxidation, we used stable isotope probing with $H^{13}CO_3^-$. Under normal conditions, WT cultures capable of autotrophic growth exhibited robust label uptake, while the D1 mutants exhibited minor amounts due to exchange rather than autotrophy. Under manganese oxidizing conditions, none of the strains exhibited label uptake. ***B.*** The high concentrations of manganese and citrate used in our experiments are incompatible with growth (shown here with WT), explaining the inhibition of carbon fixation seen in *A*. ***C.*** To investigate energy conservation in the absence of growth, we conducted survivability experiments with and without glucose. However, in the flask format, the manganese toxicity signal was a bigger obstacle to survival than lack of glucose. In the tube format, the presence of glucose was the biggest obstacle to survival, presumably related to going anaerobic. ***D-E.*** Attempt at demonstrating photochemical chlorophyll fluorescence quenching coupled to manganese oxidation with the D1-D170A mutant. The chlorophyll fluorescence induction protocol used is illustrated along the x axis of panel *D*; dark bar indicates dark background, yellow bar indicates actinic light background, and yellow tick marks indicate saturating pulses. With (***E***) or without (***D***) added manganese, no photochemical quenching was observed.

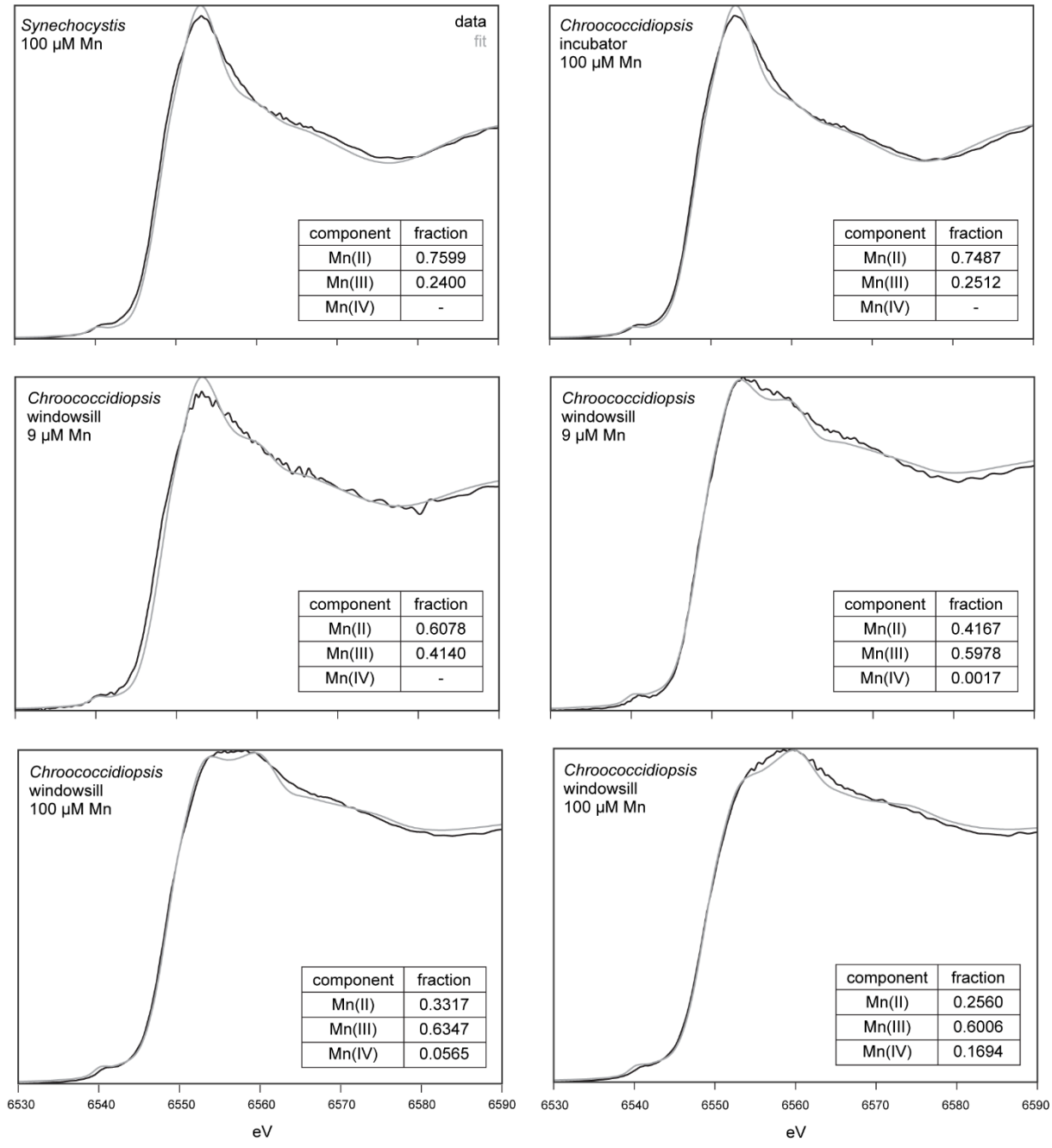

Figure S2. Least squares fits quantifying the components of the cyanobacterial biomass XANES spectra shown in Fig. 6. Fits were calculated using the $MnCl_2$, feitknechtite, and birnessite standards shown in Fig. 6 as Mn(II), Mn(III), and Mn(IV) components, respectively.

CHAPTER VI

High reactivity confounds measurements of soluble Mn(III) in natural samples

Bohee Kim[1a], Usha F. Lingappa[2a], John S. Magyar[2], Danielle R. Monteverde[2], Joan Selverstone Valentine[2,3], Woodward W. Fischer[2], Jaeheung Cho[1,4]

1. Department of Emerging Materials Science, DGIST, Daegu 42988, Korea

2. Division of Geological and Planetary Sciences, California Institute of Technology, Pasadena, CA 91125, USA

3. Department of Chemistry and Biochemistry, University of California Los Angeles, Los Angeles, CA 90095, USA

4. Department of Chemistry, Ulsan National Institute of Science and Technology (UNIST), Ulsan 44919, Korea

[a] *Co-first authors*

Abstract

Soluble Mn(III)-L complexes appear to constitute a substantial portion of manganese in natural environments and serve as critical high potential species for biogeochemical processes. However, the inherent reactivity and lability of these complexes—the same chemical characteristics that make them uniquely important in biogeochemistry—also make them incredibly difficult to measure. Here we present experimental results demonstrating the limits of common analytical methods that have been used to detect and quantify these complexes. Results showed that the leucoberbelin blue (LBB) method was incompatible with a subset of Mn(III) complexes due to their rapid decomposition under low pH conditions—a methodological requirement for the LBB assay—and that the Cd-porphyrin method is not sufficiently accurate for measuring Mn(III) species because additional chemistry occurs that is inconsistent with the proposed reaction mechanism. In both cases, the behavior of Mn(III) species in these methods ultimately stems from inter- and intramolecular redox chemistry that curtails the use of these approaches as a reflection of ligand binding strength. With growing appreciation for the importance of high-valent Mn species and their cycling in the environment, these results underscore the need for additional method development to be able to quantify such species rapidly and accurately in nature.

Introduction

The chemistry of manganese associated with biomass, Earth surface environments, and geological materials is characterized by redox conversions among three common oxidation states (1). The reduced form, Mn(II), is highly soluble in water, but when oxidized it tends to form insoluble Mn(III) and (IV) oxide minerals. In the absence of stabilizing ligand coordination, any Mn(III) in solution will rapidly disproportionate to form Mn(II) and Mn(IV) oxide (2). However, with the coordination of appropriate ligands, this disproportionation reaction can be slowed, allowing Mn(III) to persist in solution long enough to participate in other reactions. Recent years have seen a growing body of work demonstrating that such Mn(III) species constitute a significant proportion of the soluble manganese pool in natural

environments (3–6) and uncovering a broad suite of implications for this element's role in aquatic chemistry and biogeochemistry (7–13).

Mn(III) complexes can be highly reactive, making them important and dynamic players in a myriad of biogeochemical processes. As uniquely high potential, single-electron oxidants, such species contribute to the breakdown of otherwise recalcitrant molecules. For example, Mn(III)-oxalate generated by fungal Mn peroxidases controls lignin decomposition in the leaf litter of forest ecosystems—a critical process in carbon cycling (7, 14). Similarly, Mn(III)-humic acid complexes are likely responsible for the degradation of anthropogenic pollutants including estrogens in natural waters (10). These processes are based on dynamic Mn redox cycling in which the Mn(III) complexes themselves are reactive and transient. They may exist in substantial steady-state concentrations, but only through constant fluxes of formation.

It is important to recognize that Mn(III) complexes behave very differently from similar ligand complexes with ferric iron. Due to the relative energies of their respective di, tri, and tetravalent redox states, Mn(III) is reactive and unstable in ways that Fe(III) is not (13). Mn(III) complexes are susceptible to both inter and intramolecular electron transfer and ligand decomposition and therefore tend to be very short-lived chemical species. The different modes by which Mn(III) complexes decompose were nicely illustrated in a study by Klewicki and Morgan that examined the behavior of the Mn(III) complexes of pyrophosphate (PP), ethylenediaminetetraacetic acid (EDTA), and citrate (15). The Mn(III) complex of PP—a ligand that does not undergo intramolecular redox reactions (6)—displayed the most stability, decomposing slowly by PP hydrolysis and Mn(III) disproportionation on a timescale of months. By contrast, the Mn(III) complexes of EDTA and citrate decomposed readily by internal electron transfer to generate Mn(II) and products of ligand oxidation, on timescales ranging from minutes to days (15, 16). The Mn(III) complex of desferrioxamine B (DFOB) was shown by Duckworth and Sposito to decompose similarly by internal electron transfer to give Mn(II) and an oxidized derivative of DFOB, at rates that rapidly increased with decreasing pH (half-life of ~24 hours at pH 6, but less than one hour at pH 5.7) (17). These studies demonstrated that in addition to bimolecular disproportionation, intramolecular

electron transfer processes are an important aspect of the reactivity of Mn(III) species, particularly when complexed to organic ligands. When conceptualizing fluxes and roles for such complexes in the environment, this chemistry must be taken into account.

Due to this innate reactivity and lability, measuring soluble Mn(III) species in environmental or experimental samples presents a major challenge (18). Transient species can be lost in the time required to transport samples collected in the field back to the laboratory for analysis. Therefore, spectrophotometric methods that are adaptable to rapid, field-based measurements have considerable appeal. Two such methods have been particularly important: one using the dye leucoberbelin blue (LBB), and the other using a Cd(II)-porphyrin, α,β,γ,δ-tetrakis(4-carboxyphenyl)porphyrin (TCPP), complex (Figure 1). It is therefore necessary to understand the degree to which both of these methods have material limitations in their application to quantifying Mn(III) complexes in environmental samples.

The LBB method (Figure 1a and 1c) has been used to detect Mn of any redox state higher than (II), i.e., Mn(III) to Mn(VII) (19–22). With this approach, LBB is oxidized by high valent Mn to form a product with a strong characteristic absorbance at 624 nm. Since the magnitude of this response is stoichiometric with electrons transferred, LBB can be considered a redox titration method. It cannot be used to determine absolute concentrations of Mn species of unknown redox state, but it can provide a measurement of average Mn redox state when combined with other measurements for total Mn concentration (23). In natural environments, the LBB-reactive Mn pool is largely comprised of particulate Mn oxides and soluble Mn(III)-L complexes. Therefore, in samples that are filtered to separate a soluble fraction from a particulate fraction, LBB reactivity has been interpreted to reflect soluble Mn(III) complexes (24). (However, it is important to note that filtration leads to an operational definition of solubility that does not necessarily exclude colloidal or nanoparticulate Mn phases, which may also be biologically and geochemically important, reactive Mn species (25–27).)

The TCPP method (Figure 1b and 1d) has been employed to determine concentrations of both Mn(II) and Mn(III). This method was originally designed to detect Mn(II) (28), and was more recently adapted to simultaneously measure Mn(II) and Mn(III) in the same samples (29). In the case of Mn(II),

Mn(II) reacts with Cd(II)-TCPP by a metal substitution reaction to yield Mn(II)-TCPP. Once complexed by the TCPP, the Mn(II) is rapidly oxidized by ambient O_2 to generate Mn(III)-TCPP, which has a strong characteristic absorbance at 468 nm. In the case of Mn(III), Mn(III) has been proposed to react with the Cd(II)-TCPP by a ligand exchange reaction, also to yield Mn(III)-TCPP. Both of these reactions were considered as (pseudo)first order reactions, but with different rate constants—rapid for Mn(II), and slower for Mn(III), i.e., $k_{Mn(II)} > k_{Mn(III)}$:

$$\frac{d[Mn(III)TCPP]_{from\ Mn(II)}}{dt} = -\frac{d[Mn(II)]}{dt} = k_{Mn(II)}[Mn(II)]$$

$$\frac{d[Mn(III)TCPP]_{from\ Mn(III)}}{dt} = -\frac{d[Mn(III)]}{dt} = k_{Mn(III)}[Mn(III)]$$

Integrating on time yielded:

$$[Mn(III)TCPP]_{from\ Mn(II)} = [Mn(II)]_{initial}(1 - e^{-k_{Mn(II)}t})$$

$$[Mn(III)TCPP]_{from\ Mn(III)} = [Mn(III)]_{initial}(1 - e^{-k_{Mn(III)}t})$$

Which when solved and summed for the total ingrowth of Mn(III)-TCPP over time gave:

$$[Mn(III)TCPP] = [Mn(II)]_{initial}\left(1 - e^{-k_{Mn(II)}t}\right) + [Mn(III)]_{initial}(1 - e^{-k_{Mn(III)}t})$$

The different kinetics of these two different reactions were invoked to justify using this method to quantify simultaneously Mn(III)-TCPP generated from Mn(II) substitution and oxidation and Mn(III)-TCPP generated from Mn(III) exchange (29). In this approach the kinetic profiles are fit and deconvolved, considering them as the weighted sums of two independent exponentials (29). However, this yields a classically ill-posed problem in applied mathematics for which accurate numerical schemes have been challenging to achieve—particularly with experimental data wherein small variations in the data can lead to substantial differences in the parameters achieved by fitting (30, 31). This problem becomes even more acute in samples containing more than one Mn-bearing species if the number of species, their reaction rates, or their concentrations are unknown *a priori*:

$$[Mn(III)TCPP] = [Mn(species_1)]_{initial}\left(1 - e^{-k_1 t}\right) + [Mn(species_2)]_{initial}\left(1 - e^{-k_2 t}\right)$$

$$+[Mn(species_3)]_{initial}\left(1 - e^{-k_3 t}\right) + \ldots$$

$$[Mn(III)TCPP] = \sum_{1}^{n} [Mn(species_n)]_{initial}\left(1 - e^{-k_n t}\right)$$

This method is predicated on the assumption that the only Mn(III) chemistry occurring in these reactions is the proposed mechanism of a simple ligand exchange reaction—and even under that assumption, the challenge of deconvolving reactions from multiple unknown Mn complexes is formidable.

Using both the LBB and TCPP methods, differences in the responses from standard solutions of different Mn(III) complexes have been observed (24, 32). With the TCPP method, it was suggested that the reaction kinetics could be further resolved to distinguish the strength of ligand binding in different Mn(III) complexes based on their rate of exchange (32). With the LBB method, a similar argument based on strong vs. weak ligand binding was suggested to explain the observation that some Mn(III) complexes react readily with LBB, while others do not react at all (24). Building on these interpretations, DFOB has been described as a prototypical "strong ligand", and used for ligand exchange extractions to identify the fraction of soluble Mn(III) that is complexed to a weaker ligand (33).

This "strong ligand" paradigm likely has roots in the use of siderophore complexation reactions (including with DFOB) to determine the concentrations of Fe(III) in natural waters. In such cases, forward and reverse complexation reaction rates can be used to infer conditional equilibrium constants. This relationship has been empirically validated and works well for cases of simple, single step, reversible substitution reactions, which Fe(III) complexations frequently are. However, with multistep complexation reactions, directly relating kinetics to thermodynamics is not possible. For example, the presence of Ca slows down Cu chelation in seawater (34); therefore, inferring the thermodynamics of Cu coordination based on reaction rate in the presence of Ca would not be appropriate. Ca does not affect the equilibrium constant for Cu coordination, it changes the rate by introducing additional steps to the reaction. The fundamental differences in reactivity between Fe(III) and Mn(III) allow such approximations to be accessible for the relatively inert Fe(III) but not for the relatively labile Mn(III). Mn(III) complexation reactions are not the simple, single step reactions that their Fe(III) counterparts would participate in.

Therefore, Mn(III)-L reaction kinetics cannot be used as a reliable indication of ligand binding strength. More broadly, methods, assumptions, and interpretations that are based on the dynamics of Fe(III) should be reevaluated prior to their application to Mn(III).

Here we present the results of a suite of experiments designed to probe the accuracy of these approaches for measuring Mn(III) complexes. Our results indicated important issues with each of these methods and interpretations of the data generated using them. In the case of LBB, we observed that the assay—which requires a low pH solution—is incompatible with Mn(III) complexes that degrade at low pH faster than they can react with LBB; this was illustrated in our experiments by Mn(III)-DFOB. In the case of the TCPP method, we found that the reactivity of Mn(III) species confounded the proposed reaction mechanism, such that fitting different kinetic profiles cannot reliably be used to quantify or draw robust conclusions about the nature of Mn speciation in unknown samples. In the case of ligand exchange extractions, we caution that since DFOB is not a redox stable ligand and its reactivity exhibits a strong pH dependence, this compound (and others like it) should not be used as reference species to examine thermodynamic binding strength of unknown molecules in environmental samples. In all cases, these issues stemmed from the inherent reactivity and lability of Mn(III)-L complexes.

Materials & Methods

Reagents

All chemicals were obtained from Sigma-Aldrich at the best available purity. All solutions were prepared with ultrapure water (UW) obtained from a Merck Millipore MQ Direct 8 water purification system. $MnCl_2$, $KMnO_4$, and Mn(III)-acetylacetonate (acac) solutions were prepared by dissolution in UW. The Mn(III)-PP and Mn(III)-DFOB complexes were synthesized following the protocols from Madison *et al* (29). For electron paramagnetic resonance (EPR) measurements, all Mn solutions were prepared as 1 mM in UW.

LBB method

A 0.04% LBB solution was prepared in UW with 1% glacial acetic acid, equivalent to the primary reagent described in Jones *et al* (24). pH of this solution was ~3. We report LBB concentration as a weight percent rather than molarity as the low purity of commercially available LBB makes precise concentrations of dye content unreliable. Therefore, standard curves with $KMnO_4$ must be employed with each batch of LBB reagent to calibrate quantitation for sample unknowns.

Reactions were performed in a 1 cm UV cuvette to monitor UV-vis spectral changes of reaction solutions. For the cuvette-based assay, similar to that described in Jones *et al.* (24), 40 µL of LBB solution was added to 2 mL of sample solution. For the reaction with Mn(III)-DFOB, we used a 6 µM Mn(III)-DFOB solution and monitored changes in absorbance at 310 nm for [Mn(III)-DFOB] and 624 nm for LBB oxidation. Final pH remained ~3 for reactions with $KMnO_4$ and increased slightly to ~3.5 with Mn(III)-DFOB. To assess the role of the low pH reaction solution in Mn(III)-DFOB decomposition, a similar experiment was conducted with 2 µL of glacial acetic acid added to 2 mL of 6 µM Mn(III)-DFOB (final pH ~3.3).

For a higher throughput (albeit lower sensitivity) LBB assay, reactions can be performed in a 96-well plate. For the plate-based assay, we follow a protocol similar to that described in numerous previous studies (20–22). For samples including biomass, sediment, or other particulate matter, we react 250 µL of LBB solution with 50 µL of sample in a microcentrifuge tube for 15 minutes to allow the reaction to proceed to completion, centrifuge to remove particulate matter, and then transfer 250 µL of supernatant to a plate for quantification. In this study, the plate-based assay was only used with a $KMnO_4$ standard solution and therefore did not require a centrifugation step, so 208.3 µL of LBB solution and 41.6 µL of sample were reacted directly in the plate.

To determine the pH threshold of LBB activity, the LBB reagent solution was diluted 10x and adjusted to pHs ranging from 3 to 8.2, and then reacted with 50 µM $KMnO_4$ in the plate-based assay.

TCPP method

The TCPP method was performed using the protocol from Madison *et al.* (29). A 0.2 mM TCPP solution was prepared in UW with 0.1 M NaOH. To guard against potential photochemistry, the bottle was wrapped in aluminum foil. A 12 mM $CdCl_2$ solution was prepared in UW. The buffer solution was prepared with 0.025 M sodium tetraborate, 0.1 M HCl, and 0.6 M imidazole; the pH was adjusted to 8.0 with 3 M HCl. Reactions were performed in a 1 cm UV cuvette. The precursor, Cd(II)-TCPP, was prepared by addition of 360 μL of TCPP solution, 6 μL of $CdCl_2$ solution, and 120 μL of buffer solution; and then brought up to 3 mL with UW to yield 24 μM Cd(II)-TCPP. 10 μL of 0.54 mM Mn solution was added into the precursor solution for the reaction, for a final concentration of 1.8 μM Mn solution. Changes in absorbance were monitored at 468 nm for [Mn(III)-TCPP]. Reactions were run in triplicate; the data reported are a representative example. For reactions under argon, each solution was purged with stirring for 15 minutes, which scrubs most but not all dissolved O_2 from solution, and reactions were conducted under an argon atmosphere in a two neck UV cell.

Spectroscopy

Cuvette-based UV-vis spectra were recorded on a Hewlett Packard 8454 diode array spectrophotometer. 96-well plates were read with a BioTek Cytation 5 plate reader. EPR spectra were obtained on a JEOL JES-FA200 spectrometer at 113 K. Frequency = 9.155 GHz, microwave power = 0.998 mW, modulation frequency = 100 kHz, and modulation amplitude = 0.6 mT.

Results & Discussion

Limitations of the LBB method

It has been reported that some Mn(III)-L complexes, most notably Mn(III)-DFOB, do not react with LBB (24). This observation was interpreted in thermodynamic terms as a reflection of the binding strength of Mn(III)-L complexes—that weakly bound complexes react readily, while strongly bound complexes react slowly or not at all (24, 29, 32). However, LBB reacts readily with a wide range of solid

Mn oxide phases (23), which are much more stable than any Mn(III)-L complex. Therefore, we investigated an alternative explanation for the reported data.

The LBB method is typically carried out in an acetic acid solution, at pH ~3 (20–22, 24). However, the Mn(III)-DFOB complex is known to only persist in solution within the pH range of ~7-11 (17). We attempted to measure Mn(III)-DFOB using LBB and did not observe the spectral change at 624 nm characteristic of LBB oxidation (Figure 2a), consistent with previous reports that Mn(III)-DFOB does not react with LBB (24). However, by also monitoring the absorbance spectrum at 310 nm for the characteristic absorbance of Mn(III)-DFOB, we found that the Mn(III)-DFOB disappeared on a timescale of seconds upon introduction to the reaction solution of the LBB assay. The same phenomenon occurred when acetic acid without LBB was introduced to the Mn(III)-DFOB solution (Figure 2b). These results demonstrated that the lack of reaction with LBB occurred not because the Mn was so strongly bound that the LBB could not access it, but rather because the complex disintegrated in the low pH reaction solution before it had opportunity to react with LBB. Since the mechanism of decomposition reduces Mn(III) to Mn(II) (17), which does not react with LBB, this explained why the LBB assay does not detect Mn(III)-DFOB.

We further studied the pH dependence of the LBB method using standard solutions of $KMnO_4$ and showed that above pH 5 there is substantial loss of LBB signal (Figure 2c). Therefore, we concluded that since a low pH reaction solution is a methodological requirement, the LBB method is incompatible with Mn(III) complexes that decompose rapidly at low pH. This may include not only Mn(III)-DFOB, but a variety of other Mn(III)-L complexes that could exist the environment. As an example, at the mean pH of Black Sea surface waters (8.38) (35), Mn(III)-DFOB would be stable for weeks. Since complexation to DFOB and other siderophores is thought to increase Mn bioavailability (36), such complexes are likely important players in Mn biogeochemistry. However, any such complexes are undetectable by the LBB method if, like Mn(III)-DFOB, they decompose in the assay faster than the assay can report their presence.

In spite of this limitation, the LBB method remains a very valuable assay, particularly in contexts such as the study of Mn oxidation processes (20–22) or the detection of Mn oxides in unknown materials (23, 33, 37). When using LBB to detect soluble species, it must be understood that since LBB can only access a subset of Mn(III)-L complexes an additional, LBB-invisible pool of Mn(III) may exist. This is not a reflection of ligand binding strength, rather it arises from redox-driven chemical reactions occurring during the assay. Because of this limitation, data quantifying soluble Mn(III) species via the LBB method likely systematically underestimate the true abundance of these species in natural samples.

Behavior of the TCPP method

Use of the TCPP method to measure and distinguish between Mn species was originally shown with standard solutions of $MnCl_2$ as a source of hexaaqua-Mn(II), Mn(III)-PP as a fast-reacting Mn(III) complex, and Mn(III)-DFOB as a slow-reacting Mn(III) complex (29). In the case of hexaaqua-Mn(II), the Mn(III)-TCPP absorption signal fully developed within 1 minute; with the Mn(III) complexes, the signal from Mn(III)-PP developed over several minutes, while the signal from Mn(III)-DFOB developed even more slowly, not reaching the absorbance maximum during the 15 minute time course examined. We reproduced these phenomena and additionally examined the Mn(III)-acac complex, which showed kinetic behavior similar to that of Mn(III)-PP (Figures 1b and 3a).

The reactive nature of Mn(III)-L complexes, in particular the known redox instability of Mn(III) complexed to organic ligands such as DFOB (17), caused us to question the proposed mechanism of this method for detecting Mn(III). If the reaction between Mn(III) complexes and TCPP is well described as a simple ligand exchange, not involving any redox chemistry, it should not be affected by the availability of O_2. Therefore, we performed the same reactions under argon rather than in air. The reaction with Mn(III)-PP behaved consistently with the proposed mechanism, showing no meaningful difference under argon. However, with both Mn(III)-acac and Mn(III)-DFOB, the reaction behaved strangely under argon (Figure 3b). The absorbance fluctuated irregularly with time, and with Mn(III)-DFOB—which in air does not reach its stoichiometric absorbance maximum during the time course examined—the reaction appeared to

proceed at a much higher rate, surpassing the maximum expected absorbance in minutes. These observations appear inconsistent with the idea that the chemistry taking place in these reactions is just a simple substitution reaction.

Use of the TCPP method as a quantitative assay for soluble Mn(III) depends on understanding the reactions taking place in the solution. If additional reactions are occurring here, either instead of or in addition to the proposed mechanism, then caution should be taken when interpreting results based on either the magnitude or rate of Mn(III)-TCPP production. The absorbance changes we observed in the Mn(III)-acac and Mn(III)-DFOB reactions suggest changes in the coordination environment of the Mn in the porphyrin, possibly attributable to ternary complex formation or coordination of exogenous ligands or oxidized ligand fragments. Whatever the mechanism, the chemical complexity implied by these observations undermines this method as an assay for environmental Mn(III). Our data suggested that this method may only be appropriate for Mn(III) complexes with redox stable ligands, such as Mn(III)-PP. Since the identity and distribution of ligands for soluble Mn(III) in natural samples remains largely unknown, this method may not accurately characterize such samples.

Even in the absence of sample unknown materials and with a well behaved Mn(III)-L complex, interactions between Mn(III) and other reagents may complicate the solution chemistry and thereby confound this method. For example, imidazole is used in the method as a buffer to facilitate metal complex substitution. It has been shown that varying the concentration of the imidazole changes the reaction kinetics (38). The fact that the kinetics can be modulated by an additional species demonstrates that the reaction between Mn(III)-L and TCPP cannot be a simple single-step substitution, and therefore inferring thermodynamic properties from kinetic behavior is not appropriate. With both Mn(III)-PP and Mn(III)-acac, we observed absorption changes upon introduction of the Mn species to the imidazole buffer without TCPP, indicating that these Mn(III) complexes reacted in the presence of this reagent.

The TCPP method is predicated on the assumption that the only reaction product is Mn(III)-TCPP. Interactions between Mn materials and additional species—including but not limited to the imidazole buffer—confound interpretation of the data generated by this measurement. With known

materials at least one can constrain the suite of possible reactions occurring during the assay. With natural samples of unknown composition, however, constraining all possible reactions and their products becomes a much bigger challenge.

Reliability of common Mn(III) standards

The inherent lability of Mn(III) complexes not only complicates efforts to understand Mn speciation in natural environments, it also complicates the problem of obtaining reliable Mn(III) standard solutions for method calibration. Even small concentrations of Mn(II) mixed in to Mn(III) solutions could catalyze the reaction between Mn(II) and TCPP, creating a false impression of the Mn speciation in a sample. Mn(II) enters the porphyrin much more readily than Mn(III), where the former is rapidly oxidized; Mn(III) can act as that oxidant, oxidizing the Mn(II)-TCPP to Mn(III)-TCPP and thereby generating more Mn(II) in solution, which can then react with another TCPP. By this mechanism, mixtures of Mn(II) and Mn(III) species could display rapid TCPP reactions, skewing interpretations that are made based on the kinetics of this reaction. Our experimental results illustrated that this chemistry is a concern even in the case of standard solutions of presumptively known Mn(III) complexes, let alone with natural samples of unknown speciation.

To observe and quantify the amount of Mn(II) occurring in our Mn(III) standards, we used EPR spectroscopy. Solutions of our synthesized Mn(III)-PP and Mn(III)-DFOB complexes and commercial Mn(III)-acac all showed a Mn(II) EPR signal at 300 mT. To estimate the abundance of Mn(II) in these materials, we compared the EPR integral value to the integral value from a $MnCl_2$ standard solution (Table 1). We found that these values were slightly higher under argon than under air. We also observed that the Mn(II) EPR signal from dissolved Mn(III)-acac increased over time (41% immediately after dissolution; 49% 1 hour after dissolution; data shown in Table 1 is from experimental solutions, dissolved on a previous day), indicating that this Mn(III) species also reduces to Mn(II) over time in solution.

These results demonstrated that potential interference from Mn(II) is a concern with both commercial and in-house synthesized Mn(III) complex standards. Thus, the presumptively known

concentrations of Mn(III) standard solutions may not reflect the actual concentration of Mn(III) in solution; this constitutes a challenge for the calibration of all existing methods.

Ligand exchange extractions using DFOB

Based on its slow exchange in the TCPP method and lack of reaction with LBB, Mn(III)-DFOB has received attention as a prototypical "strongly binding, non-reactive" Mn(III) complex. However, this interpretive framework does not differentiate between kinetics and thermodynamics—the binding strength is a thermodynamic issue, the rate of exchange or reaction is a kinetic issue. While the Mn(III)-DFOB complex does have a high stability constant, reactivity or perceived lack thereof from unknown complexes in the TCPP or LBB methods does not necessarily indicate ligand binding strength; and known binding strengths do not necessarily predict reaction rates or mechanisms.

As the prototypical strong ligand, DFOB has been used for ligand exchange extractions of soluble Mn(III)-L complexes from natural samples (33). However, we caution that ligand exchange extractions with a ligand that is not redox stable—such as DFOB (17)—may produce misleading results. Furthermore, the products of Mn(III)-DFOB degradation can include chromophores with similar absorption features to Mn(III)-DFOB itself (17); these can additionally confound the measurement.

Implications

Results from these methods for detecting and characterizing soluble Mn(III)-L complexes, the TCPP method in particular, have underpinned the field of Mn aquatic chemistry for the last decade. Although our data raise concerns about the validity of this method, we stress that the work using it to demonstrate the widespread presence of soluble Mn(III) was groundbreaking and instrumental in shifting the field away from the previous paradigm that environmental Mn speciation was a simple dichotomy of soluble Mn(II) and insoluble Mn oxides (3–5). Now that we recognize the potential significance of soluble Mn(III) complexes as reactive intermediates in critical biogeochemical processes, we as a

community have our work cut out for us to understand better their diversity, fluxes, and precise roles in environmental chemistry. In pursuing this better understanding, we must appreciate the highly reactive nature of these complexes, which at once makes them fascinating, important, and so difficult to study. We need to appreciate the limitations of what our current tools can and cannot constrain in order to apply them most effectively, while working to develop better approaches.

Acknowledgements
This work was supported by the NSF GRFP (UFL), NSF IOS grant 1833247 (WWF), and NRF 2017R1A2B4005441 and 2019R1A2C2086249 funded by the Ministry of Science, ICT and Future Planning of Korea (JC). We thank Jim Morgan for invaluable insight on the chemistry of manganese in natural waters and dedicate this work to his memory.

Author contributions
All authors contributed to the study conception and design. BK and UFL generated data. UFL wrote the manuscript with input from all other authors.

References

1. J. J. Morgan, Manganese in natural waters and earth's crust: its availability to organisms. *Met. Ions Biol. Syst.* **37**, 1–34 (2000).

2. G. Davies, Some aspects of the chemistry of manganese(III) in aqueous solution. *Coord. Chem. Rev.* **4**, 199–224 (1969).

3. R. E. Trouwborst, Soluble Mn(III) in Suboxic Zones. *Science* **313**, 1955–1957 (2006).

4. A. S. Madison, B. M. Tebo, A. Mucci, B. Sundby, G. W. Luther, Abundant Porewater Mn(III) Is a Major Component of the Sedimentary Redox System. *Science* **341**, 875–878 (2013).

5. V. E. Oldham, A. Mucci, B. M. Tebo, G. W. Luther, Soluble Mn(III)–L complexes are abundant in oxygenated waters and stabilized by humic ligands. *Geochim. Cosmochim. Acta* **199**, 238–246 (2017).

6. A. Qian, *et al.*, Geochemical Stability of Dissolved Mn(III) in the Presence of Pyrophosphate as a Model Ligand: Complexation and Disproportionation. *Environ. Sci. Technol.* **53**, 5768–5777 (2019).

7. M. Keiluweit, *et al.*, Long-term litter decomposition controlled by manganese redox cycling. *Proc. Natl. Acad. Sci.* **112**, E5253–E5260 (2015).

8. V. E. Oldham, M. R. Jones, B. M. Tebo, G. W. Luther, Oxidative and reductive processes contributing to manganese cycling at oxic-anoxic interfaces. *Mar. Chem.* **195**, 122–128 (2017).

9. E. Hu, *et al.*, Role of dissolved Mn(III) in transformation of organic contaminants: Non-oxidative versus oxidative mechanisms. *Water Res.* **111**, 234–243 (2017).

10. X. Wang, *et al.*, Phototransformation of estrogens mediated by Mn(III), not by reactive oxygen species, in the presence of humic acids. *Chemosphere* **201**, 224–233 (2018).

11. K. L. Johnson, *et al.*, Dissolved Mn(III) in water treatment works: Prevalence and significance. *Water Res.* **140**, 181–190 (2018).

12. M. E. Jones, *et al.*, Manganese-Driven Carbon Oxidation at Oxic–Anoxic Interfaces. *Environ. Sci. Technol.* **52**, 12349–12357 (2018).

13. U. F. Lingappa, D. R. Monteverde, J. S. Magyar, J. S. Valentine, W. W. Fischer, How manganese empowered life with dioxygen (and vice versa). *Free Radic. Biol. Med.*, 113–125 (2019).

14. M. Hofrichter, Review: lignin conversion by manganese peroxidase (MnP). *Enzyme Microb. Technol.* **30**, 454–466 (2002).

15. J. K. Klewicki, J. J. Morgan, Kinetic Behavior of Mn(III) Complexes of Pyrophosphate, EDTA, and Citrate. *Environ. Sci. Technol.* **32**, 2916–2922 (1998).

16. K. A. Schroeder, R. E. Hamm, Decomposition of the Ethylenediaminetetraacetate Complex of Manganese(III). *Inorg. Chem.* **3**, 391–395 (1964).

17. O. W. Duckworth, G. Sposito, Siderophore−Manganese(III) Interactions. I. Air-Oxidation of Manganese(II) Promoted by Desferrioxamine B. *Environ. Sci. Technol.* **39**, 6037–6044 (2005).

18. J. J. Morgan, W. Stumm, Analytical Chemistry of Aqueous Manganese. *J. - Am. Water Works Assoc.* **57**, 107–119 (1965).

19. W. E. Krumbein, H. J. Altmann, A new method for the detection and enumeration of manganese oxidizing and reducing microorganisms. *Helgoländer Wiss. Meeresunters.* **25**, 347–356 (1973).

20. M. Okazaki, *et al.*, Partial purification and characterization of manganese-oxidizing factors of Pseudomonas fluorescens GB-1. *Appl. Environ. Microbiol.* **63**, 4793–4799 (1997).

21. F. C. Boogerd, J. P. de Vrind, Manganese oxidation by Leptothrix discophora. *J. Bacteriol.* **169**, 489–494 (1987).

22. H. A. Johnson, B. M. Tebo, In vitro studies indicate a quinone is involved in bacterial Mn(II) oxidation. *Arch. Microbiol.* **189**, 59–69 (2008).

23. Y. Zhu, *et al.*, Rapid determination of the Mn average oxidation state of Mn oxides with a novel two-step colorimetric method. *Anal. Methods* **9**, 103–109 (2017).

24. M. R. Jones, G. W. Luther, A. Mucci, B. M. Tebo, Concentrations of reactive Mn(III)-L and MnO2 in estuarine and marine waters determined using spectrophotometry and the leuco base, leucoberbelin blue. *Talanta* **200**, 91–99 (2019).

25. S. A. Sañudo-Wilhelmy, I. Rivera-Duarte, A. R. Flegal, Distribution of colloidal trace metals in the San Francisco Bay estuary. *Geochim. Cosmochim. Acta* **60**, 4933–4944 (1996).

26. M. Baalousha, *et al.*, Suspended particulate matter determines physical speciation of Fe, Mn, and trace metals in surface waters of Loire watershed. *Environ. Sci. Pollut. Res.* (2018) https:/doi.org/10.1007/s11356-018-1416-5 (November 27, 2018).

27. C. A. Romano, *et al.*, Biogenic manganese oxide nanoparticle formation by a multimeric multicopper oxidase Mnx. *Nat. Commun.* **8**, 746 (2017).

28. H. Ishii, H. Koh, K. Satoh, Spectrophotometric determination of manganese utilizing metal ion substitution in the cadmium-α,β,-γ,δ -tetrakis(4-carboxyphenyl)porphine complex. *Anal. Chim. Acta* **136**, 347–352 (1982).

29. A. S. Madison, B. M. Tebo, G. W. Luther, Simultaneous determination of soluble manganese(III), manganese(II) and total manganese in natural (pore)waters. *Talanta* **84**, 374–381 (2011).

30. F. S. Acton, *Numerical methods that work* (Mathematical Association of America, 1990).

31. P. De Groen, B. De Moor, The fit of a sum of exponentials to noisy data. *J. Comput. Appl. Math.* **20**, 175–187 (1987).

32. G. W. Luther, A. S. Madison, A. Mucci, B. Sundby, V. E. Oldham, A kinetic approach to assess the strengths of ligands bound to soluble Mn(III). *Mar. Chem.* **173**, 93–99 (2015).

33. M. R. Jones, V. E. Oldham, G. W. Luther, A. Mucci, B. M. Tebo, Distribution of desferrioxamine-B-extractable soluble manganese(III) and particulate MnO2 in the St. Lawrence Estuary, Canada. *Mar. Chem.* **208**, 70–82 (2019).

34. J. G. Hering, F. M. M. Morel, Slow coordination reactions in seawater. *Geochim. Cosmochim. Acta* **53**, 611–618 (1989).

35. A. B. Polonsky, E. A. Grebneva, The Spatiotemporal Variability of pH in Waters of the Black Sea. *Dokl. Earth Sci.* **486**, 669–674 (2019).

36. S. D. Springer, A. Butler, Magnetic susceptibility of Mn(III) complexes of hydroxamate siderophores. *J. Inorg. Biochem.* **148**, 22–26 (2015).

37. A. R. Cavazos, J. B. Glass, Simul-staining manganese oxides and microbial cells. *Limnol. Oceanogr. Methods* **18**, 362–373 (2020).

38. A. Thibault de Chanvalon, G. W. Luther, Mn speciation at nanomolar concentrations with a porphyrin competitive ligand and UV–vis measurements. *Talanta* **200**, 15–21 (2019).

Figures

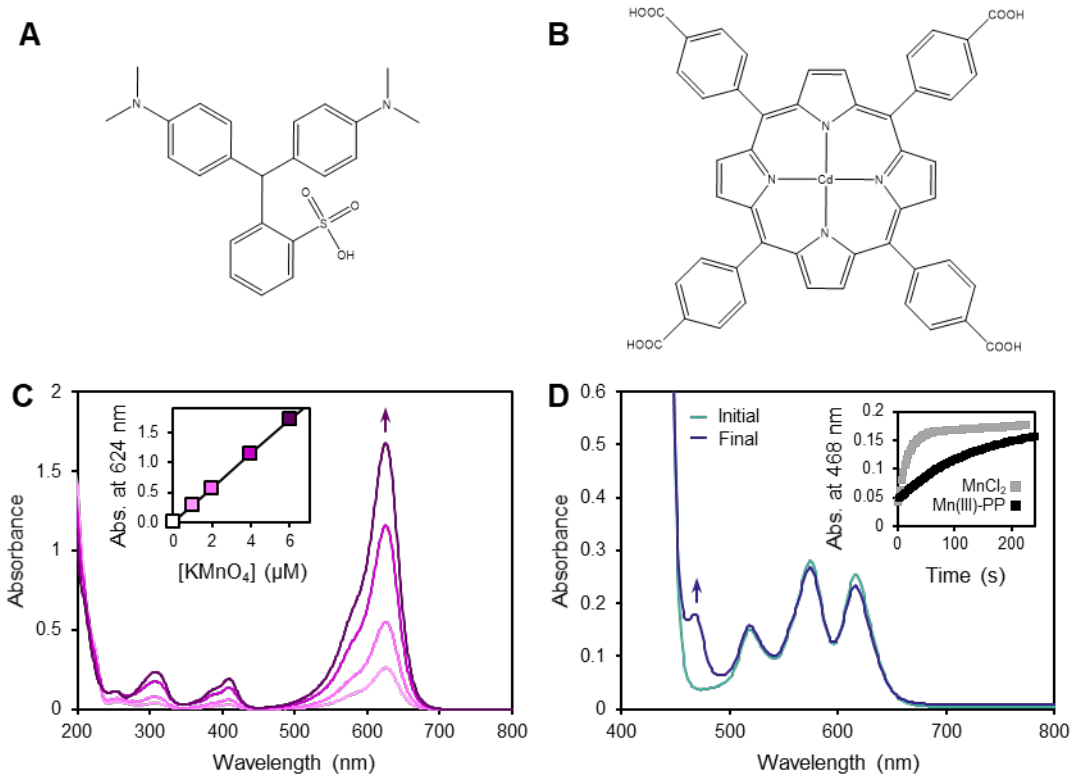

Fig. 1 The leucoberbelin blue (LBB) and Cd-porphyrin (TCPP) spectrophotometric methods for detecting manganese species. (a-b) Chemical structures of the LBB (a) and Cd(II)-TCPP (b) reagents. (c-d) UV-vis absorbance spectra illustrating the application of these methods. (c) The LBB method on a standard curve of $KMnO_4$ solutions, with the inset showing the linear absorbance change at 624 nm with $KMnO_4$ concentration due to oxidation of LBB. (d) The TCPP method on a standard solution of $MnCl_2$ showing the change in absorbance at 468 nm from Mn(II) substitution and oxidation to generate Mn(III)-TCPP. Inset shows the kinetic profile of this reaction along with the Mn(III)-PP ligand exchange reaction to generate Mn(III)-TCPP.

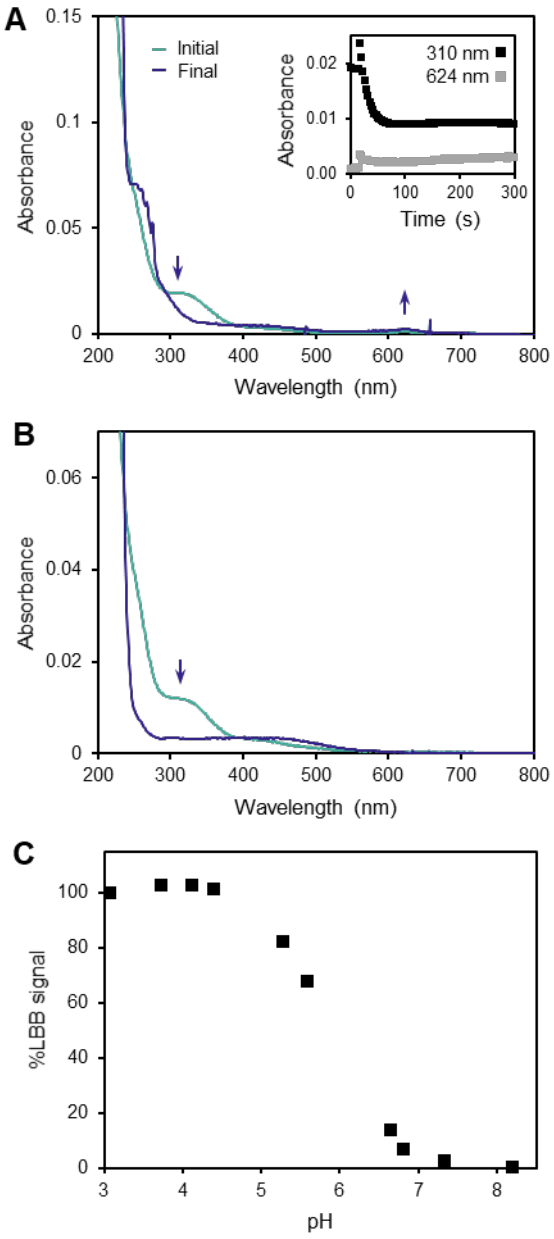

Fig. 2 Mn(III)-DFOB is incompatible with the LBB method due to its rapid decomposition at low pH, a methodological requirement for the LBB assay. (a) LBB solution added to 6 µM Mn(III)-DFOB solution. The characteristic Mn(III)-DFOB band at 310 nm disappeared on a timescale of seconds, and the oxidized LBB band at 624 nm did not appear. (b) Acetic acid without LBB added to 6 µM Mn(III)-DFOB solution. The Mn(III)-DFOB band still disappeared, indicating that the Mn(III)-DFOB decomposition was caused by the change in pH rather than any reaction with LBB. (c) LBB signal with $KMnO_4$ drops off in reaction solutions above pH 5, demonstrating that a low pH reaction solution is required for this method. Percent LBB signal reports the absorbance at 624 nm relative to the reaction at pH 3, the baseline solution pH for this method.

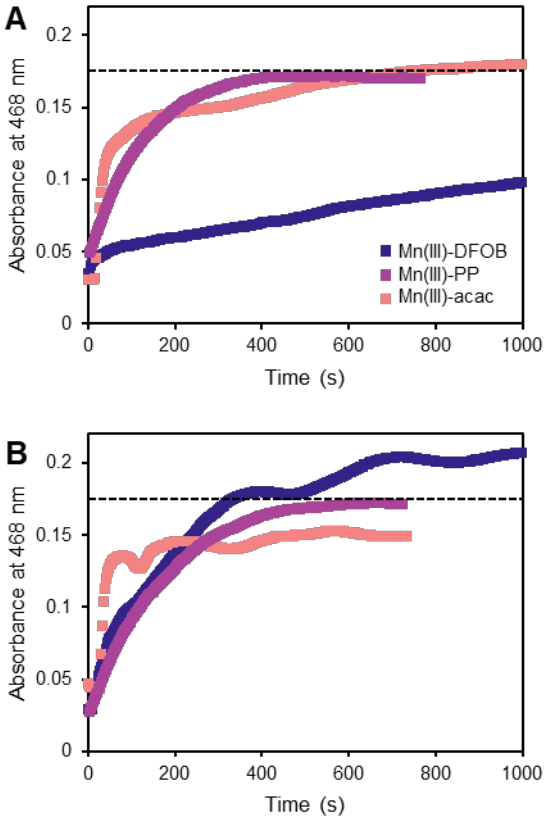

Fig. 3 Reactions of Cd(II)-TCPP with Mn(III) complexes, under air (a) and under argon (b), raise concerns about the proposed mechanism of this method. Dashed lines indicate maximum absorbance expected from 1.8 µM Mn(III)-TCPP. (a) Under air, all three reactions display absorbance increasing with time monotonically. Mn(III)-DFOB reacts much more slowly than Mn(III)-PP, as previously reported. (b) Under argon, the Mn(III)-PP reaction behaves the same as under air. However, the Mn(III)-acac and Mn(III)-DFOB reactions display very different kinetic profiles, casting doubt on the proposed mechanism. With Mn(III)-acac, increase in absorbance is no longer monotonic. With Mn(III)-DFOB, the reaction proceeds far more rapidly, and exceeds the maximum expected absorbance.

Tables

	Air (%)	Ar (%)
Mn(III)-PP	7	11
Mn(III)-DFOB	24	27
Mn(III)-acac	62	69

Table 1. The percent EPR integral value of Mn(II) signal in Mn(III) solutions, calculated as the EPR integral value of Mn(III) solution / EPR integral value of $MnCl_2$ solution x 100.

CHAPTER VII

Early impacts of climate change on a coastal marine microbial mat ecosystem

Usha F. Lingappa[1], Nathaniel T. Stein[1], Kyle S. Metcalfe[1], Theodore M. Present[1], Victoria J. Orphan[1], Andrew H. Knoll[2], John P. Grotzinger[1], Elizabeth J. Trower[3a], Maya L. Gomes[4a], Woodward W. Fischer[1a]

1. Division of Geological and Planetary Sciences, California Institute of Technology, Pasadena, CA 91125, USA

2. Department of Organismic and Evolutionary Biology, Harvard University, Cambridge, MA 02138, USA

3. Department of Geological Sciences, University of Colorado Boulder, Boulder, CO 80309, USA

4. Department of Earth and Planetary Sciences, Johns Hopkins University, Baltimore, MD 21218, USA

[a] *Co-senior authors*

Abstract

Among the earliest consequences of climate change are increasingly extreme weather and rising sea levels—two challenges to which coastal environments are particularly vulnerable. Often found in coastal settings are microbial mats—complex, microbially dominated ecosystems that drive massive nutrient fluxes through biogeochemical cycles and have been important components of the biosphere for eons. Little Ambergris Cay, Turks and Caicos Islands supports extensive mats that vary sharply with relative water level. We began this study by characterizing a baseline condition of the mat microbial communities across this variation. In September 2017, the eyewall of Category 5 Hurricane Irma transited the island. We continued this study to monitor ecosystem recovery from such a catastrophic disturbance. While initial impacts from the storm were severe, new growth of primary mat communities proceeded rapidly and suggested that storm perturbation may facilitate adaptation of these communities to changing sea levels. In contrast, microbial sulfur cycling displayed hysteresis, stalling for > 10 months after the hurricane, with important implications for carbon storage potential through organic matter sulfurization. Full ecosystem recovery was observed in < 2 years, demonstrating considerable ecological resilience in the face of such a dramatic perturbation.

Introduction

Understanding the global implications of climate change requires that we study its consequences for a wide range of ecosystems. Coastal environments are uniquely vulnerable; lying at the interface of land, ocean, and atmosphere, they are directly impacted by sea level rise, extreme weather, and changes in both air and ocean temperature and chemistry. Some coastal ecosystems, e.g. coral reefs and salt marshes, are already suffering devastating losses (1–3), while others, e.g. mangrove forests, appear to be expanding, and even mitigating impacts by providing land stabilization and carbon storage (4–7). Here we examined a predominantly microbial ecosystem facing these challenges: photosynthetic microbial mats, which are often found in close association with mangroves and thought to play major roles in shallow sediment nutrient availability (8).

Photosynthetic microbial mats are assemblies of microbes that form layered, macroscopic structures. Their fabric is commonly built by filamentous Cyanobacteria (9) and the communities that inhabit them rank among the most diverse microbial ecosystems known (10–12). Within a mat, steep physicochemical gradients partition a complex network of niche spaces (13, 14)—sunlight drives phototrophy in the surface layers (15–17); in the subsurface, redox stratification and other chemical gradients support a wide range of anaerobic metabolisms (18–23)—and tightly coupled metabolic interactions fuel rapid and dynamic biogeochemical cycling with a daily diurnal cadence (13, 24). Such ecosystems have been important components of the biosphere since long before the rise of plants and animals (25–27), a history recorded by their mineralized vestiges preserved in ancient sedimentary rocks (28–30).

Little Ambergris Cay is an uninhabited island in the Turks and Caicos with a broad, shallow interior basin widely paved by benthic microbial mats (Fig. 1*A*-*B*). This remote environment is an ideal natural laboratory—both for better understanding modern mat ecosystems and as an analog for the ancient mat ecosystems that dominated the Earth early in its history (31–35). The mats on Little Ambergris exhibit a variety of macroscopic textures (Fig. 1), ranging in thickness from millimeters to decimeters; in consistency from leathery to gelatinous; and in surface character from botryoidal or tufted to smooth. In previous studies, these mats have been categorized into three endmember types (32), termed *blister* mats, *polygonal* (or biscuit (31)) mats, and *smooth* (or flat (31, 33)) mats (Fig. 1*C*-*H*). The basis for this morphological diversity has been of interest to the geobiological community, as mat textures preserved in the geological record provide clues about ancient microbial ecosystems (31, 32).

Previously we conducted a comprehensive mapping effort of these different mat types across Little Ambergris Cay and showed that the primary factors determining their distribution are water depth and tidal exposure time above water (32). The mats exist only within a narrow elevation range; areas higher than 30 cm above mean water level host scrubland rather than mat, lower than 20 cm below mean water level and strong hydrodynamic forces inhibit mat development. Within this range, blister mats occur in the highest, driest areas (subaerial exposure times of 22 to 24 hours per day), polygonal mats in

intermediate areas (subaerial exposure times of 12 to 23 hours per day), and smooth mats in lower, wetter areas (subaerial exposure times of 0 to 12 hours per day). Since small (cm-scale) differences in water level exert such a strong control on mat habitat ranges, this is a system that is acutely sensitive to one of the earliest consequences of global climate change—sea level rise (36). However, observations of ancient mat ecosystems from the geological record demonstrate that mats have persisted across numerous intervals of sea levels rising and falling, with textural changes following changes in water depth (37). This history suggests the hypothesis that while mat ecosystems are finely tuned to water level, they may also be robustly adaptable.

The present study of Little Ambergris Cay microbial mat communities was initiated to better understand the ecological differences between mat types. Our approach combined 16S rRNA gene amplicon sequencing and extensive community analysis with physical, geochemical, and biological field observations. Initial field campaigns were conducted in July 2016 and August 2017, surveying the diversity of microbial mats across the island in 2016, and focusing on the ecosystem structure with depth in 2017.

In September 2017, Little Ambergris Cay experienced a direct hit by the eyewall of Category 5 Hurricane Irma (Fig. 1*I*)—one of the strongest hurricanes ever recorded in the Atlantic—with 920 mb average atmospheric pressure and sustained 170 mph winds accompanied by an estimated 3.2 m storm surge (38, 39). Tropical cyclones of increasing intensity are another impending consequence of climate change (40). While sea level rise, warming, and acidification manifest over timescales of decades, extreme weather events cause dramatic environmental changes over timescales of hours to minutes and therefore can be much more immediately devastating to vulnerable ecosystems (1, 41). In contrast to the adaptability of mat ecosystems to changes in sea level, the geological record demonstrates that sudden blanketing with a sediment layer can terminate mat growth (28). Having characterized the baseline ecosystem just prior to Hurricane Irma, we were uniquely well poised to investigate how the mat communities responded to such a catastrophic disturbance. Follow up studies were conducted in March 2018, July 2018, and June 2019, to document the impact and subsequent recovery.

Results

Profile of a microbial mat ecosystem

To characterize the Little Ambergris mat ecosystems we sampled a depth profile through a polygonal mat in the area designated CC, chosen for being among the lushest (~10 cm thick, well protected by mangroves) mat sites on the island (Fig. 2). The mat communities contained a diverse assemblage of organisms with abundant Cyanobacteria, Chloroflexi, alpha-, gamma-, and delta-Proteobacteria, Planctomycetes, Bacteroidetes, along with forty additional phyla (Fig. 2*B*). Non-metric multidimensional scaling (NMDS) ordination analysis to visualize dissimilarity showed that the surface community is notably distinct, while the subsurface layers displayed a gradual trend of variance with depth (Fig. 2*C*). The strong shift between surface (top cm) and subsurface (> 1.5 cm) communities coincides with the transition from oxic to sulfidic conditions (Fig. 2*F*).

To understand community stratigraphy on a functional level, we examined select groups of organisms whose metabolisms can reasonably be inferred from taxonomy (Fig. 2*D-E*). Among the phototrophs (Fig. 2*D*), sequences associated with oxygenic photosynthetic Cyanobacteria (including abundant members of the genera *Halomicronema, Calothrix,* and other unassigned Cyanobacteria) were recovered only in the uppermost horizon. Genera that likely represent facultatively aerobic anoxygenic photoheterotrophs (*Chlorothrix* of the Chloroflexales and an uncultured member of the Rhodospirillales) were also present at the surface but extended deeper in the mat than the Cyanobacteria. Sulfide-oxidizing anoxygenic phototrophs (*Thioflavicoccus* of the Chromatiales) were absent from the surface layer but found in a near subsurface horizon, co-occurring with the sulfidic chemocline. This distribution of phototrophs demonstrated the presence of both oxic and sulfidic regions within the photic zone of the mat and reflects the ability of different groups to utilize both different wavelengths of light that penetrate the mat to different extents and electron donors that vary with depth (15), consistent with observations from previously characterized mat ecosystems (13).

Different heterotrophic guilds were illustrated by major deltaproteobacterial taxa, which included three genera of sulfate reducers (*Desulfovibrio*, *Desulfomonile*, and Desulfobacteraceae group Sva0081), the genus *Syntrophobacter* (likely fermentative or syntrophic), and an uncultured member of the Myxococcales (aerobic) (42). The Myxococcales were most abundant in the oxic surface layer, while all four anaerobic genera were absent at the surface (Fig. 2*E*). This is notably different from other mat ecosystems wherein sulfate reducers are closely associated with oxygenic Cyanobacteria in the surface layer (43). *Desulfovibrio* and *Syntrophobacter* appeared in the near subsurface, co-occurring with the sulfidic chemocline. ~3 cm below the surface, they were replaced by *Desulfomonile* and Desulfobacteraceae group Sva0081. *Desulfomonile* was only present in a narrow horizon, while Sva0081 persisted throughout the depth of the mat. *Desulfovibro* and *Syntrophobacter* are known to oxidize organic substrates incompletely to acetate, while *Desulfomonile* and most members of the family Desulfobacteraceae can perform complete oxidation of organic substrates, including acetate, to CO_2 (42). Thus, the community stratigraphy reflected a progressive, systematic shift in carbon fixation and remineralization potential along a depth profile through the mat. Microbial diversity was lowest at the surface but increased with depth to a maximum ~4 cm—just below the transition between groups of sulfate reducers (Fig. 2*G-H*). This could reflect the availability of small organic substrates used by a greater diversity of heterotrophs.

Fluorescence microscopy on a mat slice embedded in Steedsman's wax to preserve spatial relationships illustrated its characteristic palisade texture defined by upward radiating sheathes of large filamentous Cyanobacteria with a heterogeneous distribution of other bacteria (Fig. 2*I*). Despite this microscopic heterogeneity, our depth profile resolved clear patterns in mm- to cm-scale ecosystem structure, and replicate samples showed similar trends (Fig. 2*C*). Therefore, while microenvironments undoubtedly control microbial ecology from the perspective of individual cells, many aspects of overall community function can be appreciated from a much coarser picture.

This characterization of microbial community composition with depth provided us a framework for understanding the Little Ambergris Cay mat ecosystem, with niches partitioned along gradients of

light and chemistry. Although we do not have functional insight into much of the extraordinary diversity in these communities, the taxa highlighted here served as windows into processes of carbon, oxygen, and sulfur cycling, providing us with indicators to gauge ecosystem function and recovery in the aftermath of Hurricane Irma.

Community variance across space and time

To understand the biological differences between the range of mats on Little Ambergris Cay, we surveyed the bulk mat communities across different mat morphologies and locations. Two areas featured in this survey, LB and F, included transects across all three mat types (Fig. S1). Broadly, the mat communities across the island were all similar, but NMDS and analysis of similarities (ANOSIM) resolved patterns within the variance observed (Fig. 3). While there was no correlation between community composition and location on the island ($R = 0.0558$, $p = 0.094$) (Fig. S2*B*), there was a clear trend between the different mat types ($R = 0.3772$, $p = 0.001$), corresponding to their relative elevations with polygonal mats sitting between smooth and blister mats (Fig. 3*A*). We repeated this survey ten months (2018) and twenty-one months (2019) following Hurricane Irma, and saw a shift in the mat communities between the pre-hurricane (2016) and 2018 datasets that largely recovered by 2019. The variance between mat types and the variance between years are expressed along different vectors in the NMDS plot, suggesting that different aspects of the community contribute to the between-mat-type differences and the between-year differences.

At the phylum level, the microbial communities of the different mat types are indistinguishable, demonstrating that community differences between mat types occurred only on finer taxonomic scales (Fig. 3*B*-*C*). In contrast, the perturbation in 2018 is quite clear—the Cyanobacteria, Alphaproteobacteria, and Chloroflexi remained abundant, while other major phylum level groups were considerably diminished.

To explore how the variance in this dataset was expressed within major groups, we conducted NMDS and ANOSIM analyses on each phylum level group individually, with a corresponding dataset of

the remainder of the community excluding each group (Fig. S4). By comparing the ANOSIM statistic *R* values calculated with these subsets to those calculated with the full communities, we obtained a measure of which groups contributed most strongly to the differences between mat types and years. The Cyanobacteria were the only group to contribute substantially higher than average to the differences between mat types, with the Cyanobacteria alone exhibiting clear variance between mat types (R = 0.4824, p = 0.001) and the remaining dataset excluding Cyanobacteria exhibiting considerably less variance between mat types (R = 0.2815, p = 0.001) (Fig. 3*D*). The Chloroflexi and Alphaproteobacteria exhibited variance between mat types comparable to the full communities, and all the other groups exhibited considerably less variance between mat types. In contrast, the groups that exhibited differences between years—reflecting the hurricane impact—were almost the inverse of those that exhibited differences between mat types. Cyanobacteria exhibited the least variance between years (R = 0.1514, p = 0.002), the Chloroflexi and Alphaproteobacteria were roughly average again, and the other groups exhibited much higher variance between years, with the highest from the Deltaproteobacteria (R = 0.4709, p = 0.001) (Fig. 3*E*).

Since the distribution of mat types is controlled by exposure time above water, we hypothesized that the aspects of the communities that differed most strongly between the mat types (the Cyanobacteria) reflected those most sensitive to sea level. To investigate the response of these taxa to a change in relative water level, we transplanted a slice of polygonal mat such that its surface sat several cm higher—into the elevation range that tends to host blister mats. One year later, the transplanted mat had developed a hard, darkly pigmented surface, resembling a blister mat (Fig. 4*A*). However, the cyanobacterial communities remained comparable to those found in polygonal mats (Fig. 4*B*). This experiment suggested that although the cyanobacterial populations between blister and polygonal mats are generally distinct, the physical expression of mat morphology primarily reflects environmental context, not microbial community differences. Despite demonstrating clear environmental preference in their naturally occurring distributions, these populations persisted outside of their preferred range over the course of this one year experiment.

Rapid post-hurricane new mat growth

Through both scour and sediment deposition, Hurricane Irma decimated large areas of mat. However, new mat growth developed rapidly over the surfaces exposed or deposited by the hurricane (Fig. 5). We categorized this new growth into three types based on the degree of perturbation—new growth on intact mat surfaces with minimal hurricane sediment (Fig. 5*A*-*B*); new growth on new mat surfaces such as where the old mat surface had been scoured out (Fig. 5*B*) or on intraclasts of ripped up mat that had been redeposited upside down (Fig. 5*C*, *I*); and incipient growth on/in hurricane sediment deposits (Fig. 5*D*), sometimes stabilizing sedimentary bedforms like ripples (Fig. 5*E*). We monitored the development of these post-hurricane growth types six months (March 2018), ten months (July 2018), and twenty-one months (June 2019) after the hurricane.

NMDS analysis showed that the community variance among the post-hurricane growth samples was neatly grouped by the intact/new/incipient types ($R = 0.8189$, $p = 0.001$) (Fig. 5*G*). However, it did not show a trend through time ($R = 0.0898$, $p = 0.081$), which would reflect ecological succession. This suggested that if there was any succession in the establishment of this new growth, it occurred on a timescale not resolved by our field sampling campaigns—within six months after the hurricane. Furthermore, a short-term growth experiment (a biofilm developed on a sheet of plexiglass deployed in the field for one week in 2018 (Fig. 5*F*)) yielded a microbial community very similar to the other new growth samples, demonstrating that this complex community was able to colonize a fresh surface extremely rapidly. However, this experiment did not repeat in 2019 (no visible biofilm developed), suggesting that growth conditions during the aftermath of the hurricane were different from steady state.

Similar to what we observed between the original mat types, we found that the Cyanobacteria exhibited the strongest contribution to the community variance between new growth types ($R = 0.8411$, $p = 0.001$) (Fig. 5*H*). The rapid development of these communities in colonizing new surfaces suggested that they are very robust and dynamic in their ability to respond to environmental disruption. Taken together with their persistence in our transplant experiment, this suggested that the community is highly

resistant to perturbation. Perturbation tolerance is thought to correlate with high biodiversity (44), something these Cyanobacteria exhibited in spades; we recovered over 6000 cyanobacterial OTUs, with abundant representatives from four of the five cyanobacterial subsections documented by both DNA sequence and morphology (Fig. S6).

Slower recovery of the sulfur cycle

Although robust new mat growth was evident as early as six months after the hurricane, it was also clear from field observations that even where the mats remained intact, the hurricane had dramatically impacted their biogeochemistry. Most notably, there was no perceptible odor of sulfide (which can be detected by smell as low as 0.008 ppm (45)), which had been a ubiquitous characteristic of the mats prior to the hurricane. Silver strips inserted into the mats to capture sulfide profiles (22) confirmed the absence of sulfidic porewater (Fig. 6*B*). A sulfide profile similar to the pre-hurricane baseline only returned by our 2019 field campaign (Fig. 6*C*). These observations suggested that the hurricane impact disrupted the sulfur cycle severely, if temporarily.

Using specific taxonomic groups as indicators of ecosystem processes provided another line of evidence for a disrupted sulfur cycle in 2018. Within the Deltaproteobacteria—a group which exhibited particularly high variance between years (Fig. 3*D*)—all three major genera of sulfate reducers were diminished in 2018, while the aerobic Myxococcales remained abundant throughout (Fig. 6*D*). Similarly, among the major phototrophs, the Cyanobacteria and photoheterotrophs (uncultured member of the Rhodospirillales and *Chlorothrix* of the Chloroflexales) remained abundant throughout, while the sulfide oxidizing Chromatiales (*Thioflavicoccus*) were diminished in 2018 (Fig. 6*E*). All of these taxa recovered by 2019, along with the sulfide profile. Taken together, the lack of sulfide and absence of both sulfate reducers and sulfide oxidizers in 2018 demonstrates by both function and community composition that mat sulfur cycling stalled during the year following Hurricane Irma.

Discussion

In ecological theory, perturbations are classified as *pulses*—discrete, relatively instantaneous alterations—or *presses*—sustained, gradual alterations(46, 47). Global climate change is, by definition, a press; but it also increases the frequency and severity of pulses, including but not limited to extreme storm events like Hurricane Irma (40, 48). These different types of perturbation tend to carry different patterns of community response, and the impacts of multiple perturbations may interact with each other in complex ways (49). Therefore, understanding the ecological implications of climate change requires understanding how each type of perturbation affects communities, the extent to which communities can recover from them, and how they might influence each other. The dataset presented here has implications for both pulse (Hurricane Irma) and press (sea level rise) perturbations on a coastal microbial mat ecosystem.

Our depth profile characterization described an ecosystem governed by carbon cycling through primary producers and decomposers (and secondary and tertiary decomposers) and sulfur cycling through both producers and consumers of sulfide. In many ways, this nutrient cycling is the microbial equivalent of the trophic levels that comprise classical macrofaunal ecosystems; rather than predator/prey relationships, species interactions are based primarily on the production and consumption of chemical substrates. The hurricane severely disrupted the chemical gradients that enabled many of those interactions. The rapid development of new growth in the wake of the hurricane reflected the populations not dependent upon those gradients or the buildup of certain substrates—phototrophs, aerobic heterotrophs, metabolically flexible mixotrophs—but lacked many of the niche spaces available in the climax community, exemplified by the absence of sulfur cycling. By analogy to classical ecology, the populations dependent upon an intricate food web (or higher trophic levels) lagged behind the initial community. The subsequent return of sulfur cyclers and a sulfidic chemocline illustrated the recovery of biogeochemical cycling characteristic of a mature mat ecosystem.

The sulfur cycle has important connections to the carbon storage potential of mangrove and mat ecosystems. Reactions between dissolved sulfides and organic matter have been implicated in decreasing organic matter lability and thereby increasing its preservation potential. This phenomenon is known to

occur in the Little Ambergris mats (50) and has been suggested to account for as much as half of the organic matter preservation associated with mangrove forests (51)—ecosystems noted for their disproportionately important contributions to global carbon storage and therefore targeted by restoration and conservation efforts aimed at ameliorating anthropogenic carbon emissions (52). In the absence of sulfides generated by microbial sulfur cycling, such sulfurization reactions are unlikely to occur. Therefore, although mat sulfur cycling ultimately recovered from the hurricane impact, the substantial interruption that we observed likely carries consequences in the form of lost carbon storage potential. This means that the expected increase in extreme storm events due to climate change may have adverse implications for the carbon sequestration capacities of mangrove and mat ecosystems.

Since the sulfur cycle disruption was seen even in mats that remained fully intact, this aspect of the hurricane impact was likely due to the extreme degree of fluid inundation flushing away soluble substrates and overwhelming anaerobic communities with oxic waters rather than physical disruption of mat integrity or burial. That being said, the sediment underlying the Little Ambergris mats is comprised primarily of ooid sand grains, which approximate close packed spheres and therefore accommodate substantial pore space that promotes fluid permeability. This means that significant flushing likely accompanies normal tidal cycles, introducing oxic seawater and moving soluble nutrients (34), and the gradients powering mat biogeochemical function are robust enough to weather that degree of flushing. Therefore, the flushing induced by Hurricane Irma must have exceeded some critical threshold in their buffering capacity. Irma was the strongest hurricane ever to hit Little Ambergris Cay in recorded history, although the island experiences hurricane force winds on average once every 5.5 years, and tropical storms more frequently than that. A better understanding of where this threshold sits on the continuum from normal daily tidal flushing to Hurricane Irma is required to appreciate the severity of these implications for changes going forward.

In contrast to the post-hurricane rapid colonization of fresh surfaces and reestablishment of gradients in surviving mats, adaptation to changing sea level requires mats in a given location to shift from one type to another, as relative water level shifts around them. For the community differences

between mat types to persist, taxa that are specific to a given mat type—and therefore likely well adapted to the narrow habitat ranges that distinguish them—will have to migrate into areas that previously hosted a different mat type. However, our transplant experiment demonstrated impressive persistence of a polygonal mat community in the environmental context of a blister mat. This suggests that although mat morphologies will shift with changing sea level, established mat communities that can tolerate the change may exhibit priority effects, inhibiting the immigration of exogenous taxa that would otherwise be better adapted to that specific environment (47, 53). That being said, we observed post-hurricane new growth analogous to the full range of mat types—with analogous community differences—after the hurricane had scoured out or buried much of the mat area. This new growth occurred at a much higher rate than steady state mat growth, suggesting that the hurricane perturbation enabled the new growth, perhaps by resetting whatever factors limit growth, creating fresh surfaces for colonization, or aiding in dispersal. It is possible that by disrupting the invasion-resistant established mat communities and promoting the redistribution of taxa, such perturbations could facilitate the development of mat communities most optimized to a given habitat range. Therefore, the occurrence of pulse disturbances like a hurricane may enable adjustment to the press disturbance of sea level change for this ecosystem, exemplifying the complex effects of multiple simultaneous forcing factors.

Taken together, this study demonstrates the substantial resilience of Little Ambergris Cay microbial mats in the face of both pulse and press disturbances induced by climate change. The mat communities and putative biogeochemical functions largely recovered from Hurricane Irma—a dramatically destructive perturbation—within two years. In contrast, catastrophic hurricanes threaten extinction for island macrofauna with limited reproduction rates and dispersal abilities (54). While this robustness in the face of environmental perturbation is consistent with the geological record of microbial mat ecosystems persisting through past intervals of climate change, this study resolved a granularity that can only be observed in the modern and rates of both perturbation and recovery that likely exceed most historical examples.

Methods

Fieldwork

We conducted five field campaigns, in July 2016, August 2017, March 2018, July 2018, and June 2019, with an additional campaign limited to drone imaging immediately following the hurricane in September 2017. We conducted an initial bulk mat survey to understand the diversity of microbial mats across the island in July 2016, and focused on the depth profile at a single mat site in August 2017. Following Hurricane Irma, we surveyed new growth types in the March 2018, July 2018, and June 2019 field seasons and repeated the 2016 bulk mat survey in July 2018 and June 2019.

Drone photography

Aerial imaging was done with a DJI Phantom 4 Pro uncrewed aerial vehicle equipped with an inbuilt 12 megapixel CMOS camera. Full island orthomosaics were generated with Agisoft Photoscan software from overlapping nadir images as described by Stein *et al* (32).

Mat sampling

Mat samples were collected using ethanol sterilized razor blades or spatulas into BashingBead lysis tubes containing a DNA preservation buffer (Zymo). Due to manufacturer changes over the course of this study, two different preservation buffers were used. 2016 samples were preserved in Xpedition lysis/stabilization solution, 2017 and 2018 samples were preserved in DNA/RNA Shield. In 2019, we collected a set of samples with replicates in each buffer to constrain artifacts introduced by changing the buffer. See supplemental Figure S7 for a more detailed discussion of this buffer discrepancy.

DNA extraction, amplification, & sequencing

DNA was extracted at Caltech using the Zymo Quick-DNA™ Fecal/Soil Microbe MiniPrep kit. A segment of the V4 to V5 hypervariable region of the 16s rRNA gene was amplified by PCR using the 515f and 926r primer pair (55). PCR reactions were set up in 15 µL volumes with Q5 Hot Start High-

Fidelity 2x Master Mix (New England Biolabs), with annealing at 54 °C and 30 cycles. Amplified products were barcoded with Illumina NexteraXT index 2 primers, and barcoded samples were submitted to Laragen for 2 x 250 bp paired end sequencing on Illumina's MiSeq platform.

Amplicon sequence data processing

Sequence data was processed using QIIME version 1.8.0 (56). Raw sequence pairs were joined and quality trimmed. Sequences were then clustered into operational taxonomic units (OTUs) with 99% similarity using the UCLUST open reference clustering protocol, and the most abundant sequence was chosen as representative for each OTU. Taxonomic identification for each representative sequence was assigned using the Silva-119 database (57), and community composition tables at the OTU, genus, order, and phylum level, with both absolute and relative abundance were generated. Unless otherwise specified, analyses were conducted on the OTU level. OTUs that were taxonomically unassigned, singletons, assigned to the Eukaryota, or likely contaminants indicated by abundance in a negative control were removed. Samples which returned fewer than 1000 sequence reads were not included in analyses. NMDS & ANOSIM analyses were done by calculating a Bray dissimilarity matrix using the vegan ecology package in R (58). Diversity indices were calculated on datasets rarefied to 3000 reads.

Sulfide profiles

Sulfide profiles were captured on clean, polished silver strips inserted into the mats similar to the method described by Fike, *et al* (22). The strips were left to react for 1 hour, and then gently rinsed off and wrapped in kimwipes to avoid disrupting the silver sulfide precipitated on the surface. Upon return to Caltech, the strips were imaged with a flatbed scanner and the profile of captured silver sulfide was quantified by gray value in ImageJ, along a straight vertical path chosen to minimize encounters with bubbles or other anomalies.

Microscopy

Light microscopy was conducted during fieldwork on wet mounts using an Amscope B120 LED microscope equipped with an Amscope MD500 eyepiece camera.

For fluorescence microscopy, slices of mat were fixed in 4% paraformaldehyde in phosphate buffered saline (PBS) for 1 hour, washed in PBS, dehydrated with 15 minute incubations in a series of increasing ethanol:PBS solutions (50:50, 70:30, 90:10), and stored in 100% ethanol. Upon return to the lab at Caltech, the fixed mats were embedded in Steedman's wax, and sliced with a microtome into 5-10 μm sections which were deposited onto Suprafrost Plus microscope slides (Fisher). The wax was dissolved with three 5 minute incubations in 100% ethanol. The remaining biomass was fluorescently labeled with the universal bacterial probe combination EUB338mix (EUB338, -II, and -III) with the FITC fluorophore (Integrated DNA Technologies). FISH hybridization was carried out at 35% formamide concentration as described by McGlynn, *et al* (59). Biomass was also counterstained with DAPI (4.5ng/ul) in Citiflour AF1 Mounting Medium. Tiled fluorescent images were produced on a Zeiss Elyra PS.1 using a Plan-APOCHROMAT 100X/1.46 Oil DIC M27 objective. DAPI, FITC, and cyanobacterial autofluorescence were illuminated 405 nm, 488 nm, and 561 nm laser lines and viewed through BP420-480+LP750, BP495-550+LP750, and BP570-620+LP750 filter sets, respectively.

Transplant experiment

During summer 2018 fieldwork, a several cm thick slice of CC mat (excised to take the evolving depth profile photograph shown in Figure 5) was left sitting on top of the polygonal mat surface, such that the surface of the excised slice was several cm higher than before. When we returned in 2019, this transplanted mat remained undisturbed. We sampled it to explore any changes in the microbial community.

Plexiglass biofilm experiment

During summer 2018 fieldwork, a sheet of plexiglass was deployed at the CC site, secured by zip tie to mangroves and tent stakes. After one week, a biofilm that had developed on the surface was

sampled with an ethanol-sterilized paintbrush. Attempts to repeat this experiment in 2019 failed—no visible biofilm developed.

Acknowledgements
We thank the Agouron Institute for initiating this work through the advanced geobiology field course. This work was funded by the Agouron Institute, NASA Research Opportunities in Space and Earth Science grant 80NSSC18K0278 (EJT & MLG), and the NSF GRFP (UFL). This work was permitted by the Turks and Caicos Islands Dept. of Environment and Coastal Resources. We thank Paul Mahoney, James Seymour, Janice Grancich, and the Tarika family for logistical support. We thank Marjorie Cantine, Emily Orzechowski, Daven Quinn, Cecilia Sanders, Dustin Morris, Sarah Jamison-Todd, Taleen Mahseredijian, Leigh Anne Reidman, Shane O'Reilly, Justin Strauss, Mike Thorpe, Elizabeth Sibert, Anelize Bahniuk, Julien Alleon, Hannah Grotzinger, Max Tarika, Cecilia Howard, Alistair Hayden, Shana Goffredi, Bethany Ehlmann, Rob Phillips, and Mel Simon for participating in field campaigns. We thank Stephanie Connon for help with amplicon preparation and sequencing, Sean Mullin for help with community analyses, Shana Goffredi for help with embedding and sectioning, and Gray Chadwick for help with fluorescence microscopy. We also thank Gray Chadwick and Preston Kemeny for helpful manuscript feedback.

Author contributions
UFL, MLG, EJT, WWF, VJO, JPG, and AHK designed the study. All authors participated in fieldwork. NTS performed drone imaging. UFL and KSM performed DNA extractions and analyses. UFL performed microscopy. UFL wrote the manuscript with input from WWF. All authors edited and approved the manuscript.

References

1. G. De'ath, K. E. Fabricius, H. Sweatman, M. Puotinen, The 27-year decline of coral cover on the Great Barrier Reef and its causes. *Proc. Natl. Acad. Sci.* **109**, 17995–17999 (2012).

2. M. D. Spalding, B. E. Brown, Warm-water coral reefs and climate change. *Science* **350**, 769–771 (2015).

3. K. M. Thorne, J. Y. Takekawa, D. L. Elliott-Fisk, Ecological Effects of Climate Change on Salt Marsh Wildlife: A Case Study from a Highly Urbanized Estuary. *J. Coast. Res.* **285**, 1477–1487 (2012).

4. J. M. Carlton, Land-building and Stabilization by Mangroves. *Environ. Conserv.* **1**, 285–294 (1974).

5. C. L. Doughty, *et al.*, Mangrove Range Expansion Rapidly Increases Coastal Wetland Carbon Storage. *Estuaries Coasts* **39**, 385–396 (2016).

6. D. M. Alongi, The Impact of Climate Change on Mangrove Forests. *Curr. Clim. Change Rep.* **1**, 30–39 (2015).

7. N. Saintilan, N. C. Wilson, K. Rogers, A. Rajkaran, K. W. Krauss, Mangrove expansion and salt marsh decline at mangrove poleward limits. *Glob. Change Biol.* **20**, 147–157 (2014).

8. R. Lee, S. Joye, Seasonal patterns of nitrogen fixation and denitrification in oceanic mangrove habitats. *Mar. Ecol. Prog. Ser.* **307**, 127–141 (2006).

9. L. J. Stal, Physiological ecology of cyanobacteria in microbial mats and other communities. *New Phytol.* **131**, 1–32 (1995).

10. R. E. Ley, *et al.*, Unexpected Diversity and Complexity of the Guerrero Negro Hypersaline Microbial Mat. *Appl. Environ. Microbiol.* **72**, 3685–3695 (2006).

11. H. Bolhuis, L. J. Stal, Analysis of bacterial and archaeal diversity in coastal microbial mats using massive parallel 16S rRNA gene tag sequencing. *ISME J.* **5**, 1701–1712 (2011).

12. M. A. Allen, F. Goh, B. P. Burns, B. A. Neilan, Bacterial, archaeal and eukaryotic diversity of smooth and pustular microbial mat communities in the hypersaline lagoon of Shark Bay. *Geobiology* **7**, 82–96 (2009).

13. D. J. Des Marais, Biogeochemistry of hypersaline microbial mats illustrates the dynamics of modern microbial ecosystems and the early evolution of the biosphere. *Biol. Bull.* **204**, 160–167 (2003).

14. H. L. Wong, D.-L. Smith, P. T. Visscher, B. P. Burns, Niche differentiation of bacterial communities at a millimeter scale in Shark Bay microbial mats. *Sci. Rep.* **5** (2015).

15. M. Stomp, J. Huisman, L. J. Stal, H. C. P. Matthijs, Colorful niches of phototrophic microorganisms shaped by vibrations of the water molecule. *ISME J.* **1**, 271–282 (2007).

16. B. B. Jorgensen, Y. Cohen, D. J. Des Marais, Photosynthetic action spectra and adaptation to spectral light distribution in a benthic cyanobacterial mat. *Appl. Environ. Microbiol.* **53**, 879–886 (1987).

17. N. Finke, T. M. Hoehler, L. Polerecky, B. Buehring, B. Thamdrup, Competition for inorganic carbon between oxygenic and anoxygenic phototrophs in a hypersaline microbial mat, Guerrero Negro, Mexico: Substrate competition between phototrophs. *Environ. Microbiol.* **15**, 1532–1550 (2013).

18. D. E. Canfield, D. J. Des Marais, Biogeochemical cycles of carbon, sulfur, and free oxygen in a microbial mat. *Geochim. Cosmochim. Acta* **57**, 3971–3984 (1993).

19. V. J. Orphan, *et al.*, Characterization and spatial distribution of methanogens and methanogenic biosignatures in hypersaline microbial mats of Baja California. *Geobiology* **6**, 376–393 (2008).

20. J. Kirk Harris, *et al.*, Phylogenetic stratigraphy in the Guerrero Negro hypersaline microbial mat. *ISME J.* **7**, 50–60 (2013).

21. C. E. Robertson, J. R. Spear, J. K. Harris, N. R. Pace, Diversity and Stratification of Archaea in a Hypersaline Microbial Mat. *Appl. Environ. Microbiol.* **75**, 1801–1810 (2009).

22. D. A. Fike, C. L. Gammon, W. Ziebis, V. J. Orphan, Micron-scale mapping of sulfur cycling across the oxycline of a cyanobacterial mat: a paired nanoSIMS and CARD-FISH approach. *ISME J.* **2**, 749–759 (2008).

23. D. Hoffmann, J. Maldonado, M. F. Wojciechowski, F. Garcia-Pichel, Hydrogen export from intertidal cyanobacterial mats: sources, fluxes and the influence of community composition: Hydrogen export in Guerrero Negro intertidal cyanobacterial mats. *Environ. Microbiol.* **17**, 3738–3753 (2015).

24. J. Z. Lee, *et al.*, Fermentation couples Chloroflexi and sulfate-reducing bacteria to Cyanobacteria in hypersaline microbial mats. *Front. Microbiol.* **5** (2014).

25. D. J. Des Marais, Microbial mats and the early evolution of life. *Trends Ecol. Evol.* **5**, 140–144 (1990).

26. H. Bolhuis, M. S. Cretoiu, L. J. Stal, Molecular ecology of microbial mats. *FEMS Microbiol. Ecol.* **90**, 335–350 (2014).

27. P. T. Visscher, J. F. Stolz, Microbial mats as bioreactors: populations, processes, and products. *Palaeogeogr. Palaeoclimatol. Palaeoecol.* **219**, 87–100 (2005).

28. J. P. Grotzinger, A. H. Knoll, Stromatolites in Precambrian carbonates: evolutionary mileposts or environmental dipsticks? *Annu. Rev. Earth Planet. Sci.* **27**, 313–358 (1999).

29. T. Bosak, A. H. Knoll, A. P. Petroff, The Meaning of Stromatolites. *Annu. Rev. Earth Planet. Sci.* **41**, 21–44 (2013).

30. M. D. Cantine, A. H. Knoll, K. D. Bergmann, Carbonates before skeletons: A database approach. *Earth-Sci. Rev.* **201**, 103065 (2020).

31. E. Trembath-Reichert, *et al.*, Gene Sequencing-Based Analysis of Microbial-Mat Morphotypes, Caicos Platform, British West Indies. *J. Sediment. Res.* **86**, 629–636 (2016).

32. N. T. Stein, *et al.*, Geomorphic and environmental controls on microbial mat fabrics on Little Ambergris Cay, Turks and Caicos Islands (in review).

33. M. L. Gomes, et al., Taphonomy of Biosignatures in Microbial Mats on Little Ambergris Cay, Turks and Caicos Islands. *Front. Earth Sci.* **8**, 576712 (2020).

34. T. M. Present, *et al.*, Non-lithifying microbial ecosystem, Little Ambergris Cay, Turks and Caicos Islands (in review).

35. L. M. Ward, U. F. Lingappa, J. P. Grotzinger, W. W. Fischer, Microbial mats in the Turks and Caicos Islands reveal diversity and evolution of phototrophy in the Chloroflexota order Aggregatilineales. *Environ. Microbiome* **15**, 9 (2020).

36. J. A. Church, *et al.*, "Sea Level Change" in *Climate Change 2013: The Physical Science Basis. Contribution of Working Group I to the Fifth Assessment Report of the Intergovernmental Panel on Climate Change*, (Cambridge University Press, 2013).

37. J. P. Grotzinger, Cyclicity and paleoenvironmental dynamics, Rocknest platform, northwest Canada. *GSA Bull.* **97**, 1208–1231 (1986).

38. J. P. Cangialosi, A. S. Latto, R. Berg, National Hurricane Center tropical cyclone report, NOAA. (2018).

39. S. Jamison-Todd, N. Stein, I. Overeem, A. Khalid, E. J. Trower, Hurricane Deposits on Carbonate Platforms: A Case Study of Hurricane Irma Deposits on Little Ambergris Cay, Turks and Caicos Islands. *J. Geophys. Res. Earth Surf.* **125** (2020).

40. T. R. Knutson, *et al.*, Tropical cyclones and climate change. *Nat. Geosci.* **3**, 157–163 (2010).

41. A. J. Cheal, M. A. MacNeil, M. J. Emslie, H. Sweatman, The threat to coral reefs from more intense cyclones under climate change. *Glob. Change Biol.* **23**, 1511–1524 (2017).

42. D. J. Brenner, N. R. Krieg, J. T. Staley, Eds., *Bergey's Manual® of Systematic Bacteriology* (Springer US, 2005) https:/doi.org/10.1007/0-387-29298-5 (July 26, 2020).

43. D. E. Canfield, D. J. Des Marais, Aerobic sulfate reduction in microbial mats. *Science* **251**, 1471–1473 (1991).

44. B. S. Griffiths, *et al.*, Ecosystem Response of Pasture Soil Communities to Fumigation-Induced Microbial Diversity Reductions: An Examination of the Biodiversity - Ecosystem Function Relationship. *Oikos* **90**, 279–294 (2000).

45. National Research Council (U.S.), National Research Council (U.S.), Eds., *Acute exposure guideline levels for selected airborne chemicals* (National Academy Press, 2000).

46. E. A. Bender, T. J. Case, M. E. Gilpin, Perturbation Experiments in Community Ecology: Theory and Practice. *Ecology* **65**, 1–13 (1984).

47. A. Shade, *et al.*, Fundamentals of Microbial Community Resistance and Resilience. *Front. Microbiol.* **3** (2012).

48. R. M. B. Harris, *et al.*, Biological responses to the press and pulse of climate trends and extreme events. *Nat. Clim. Change* **8**, 579–587 (2018).

49. R. T. Paine, M. J. Tegner, E. A. Johnson, Compounded Perturbations Yield Ecological Surprises. *Ecosystems* **1**, 535–545 (1998).

50. M. R. Raven, D. A. Fike, M. L. Gomes, S. M. Webb, Chemical and Isotopic Evidence for Organic Matter Sulfurization in Redox Gradients Around Mangrove Roots. *Front. Earth Sci.* **7**, 98 (2019).

51. D. E. Canfield, B. P. Boudreau, A. Mucci, J. K. Gundersen, The Early Diagenetic Formation of Organic Sulfur in the Sediments of Mangrove Lake, Bermuda. *Geochim. Cosmochim. Acta* **62**, 767–781 (1998).

52. D. M. Alongi, Carbon Cycling and Storage in Mangrove Forests. *Annu. Rev. Mar. Sci.* **6**, 195–219 (2014).

53. M. C. Urban, L. De Meester, Community monopolization: local adaptation enhances priority effects in an evolving metacommunity. *Proc. R. Soc. B Biol. Sci.* **276**, 4129–4138 (2009).

54. D. A. Spiller, Impact of a Catastrophic Hurricane on Island Populations. *Science* **281**, 695–697 (1998).

55. A. E. Parada, D. M. Needham, J. A. Fuhrman, Every base matters: assessing small subunit rRNA primers for marine microbiomes with mock communities, time series and global field samples: Primers for marine microbiome studies. *Environ. Microbiol.* **18**, 1403–1414 (2016).

56. J. G. Caporaso, *et al.*, QIIME allows analysis of high-throughput community sequencing data. *Nat. Methods* **7**, 335–336 (2010).

57. C. Quast, *et al.*, The SILVA ribosomal RNA gene database project: improved data processing and web-based tools. *Nucleic Acids Res.* **41**, D590–D596 (2012).

58. J. Oksanen, *et al.*, *Vegan: Community Ecology Package, R package, v. 2.4–6* (2018).

59. S. E. McGlynn, G. L. Chadwick, C. P. Kempes, V. J. Orphan, Single cell activity reveals direct electron transfer in methanotrophic consortia. *Nature* **526**, 531–535 (2015).

Figures

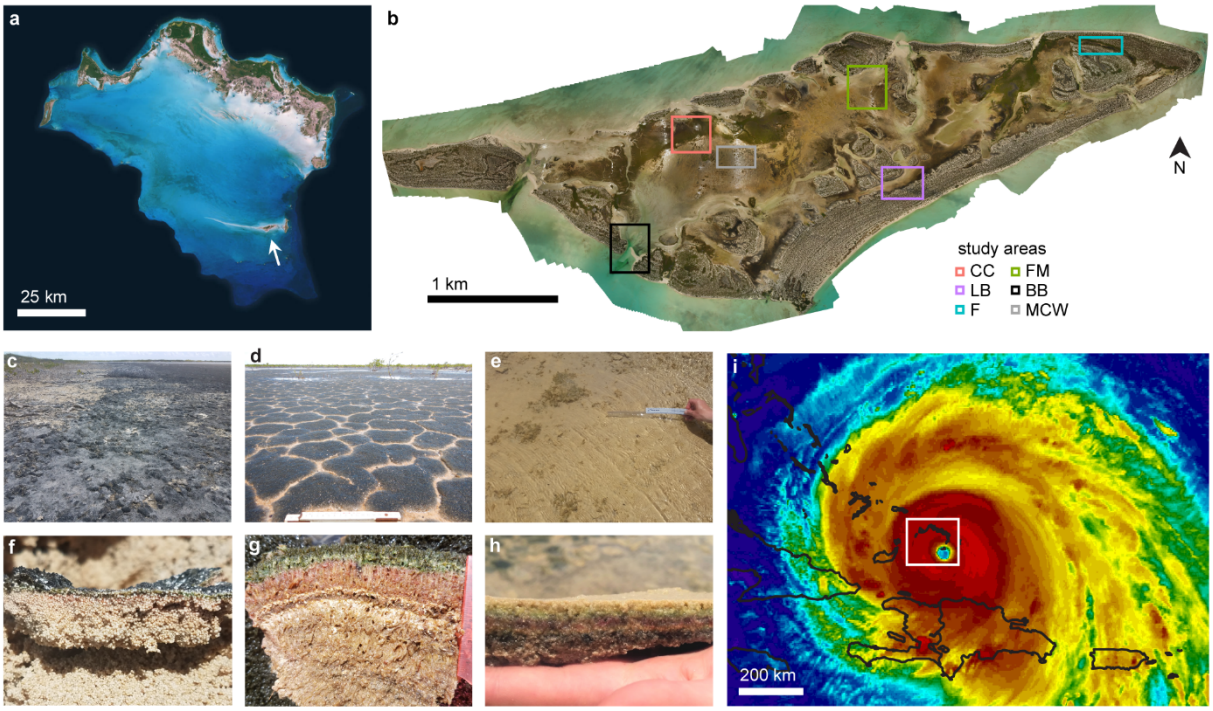

Figure 1. Maps and context images. ***A***, Satellite image of the Caicos carbonate platform, white arrow pointing out Little Ambergris Cay. ***B***, Drone orthomosaic of Little Ambergris Cay with study areas indicated. Aerial images of these regions documenting changes over time and sample details can be found in Figure S1. ***D-I***, Surface (***C-E***) and cross section (***F-H***) photographs of endmember mat types—blister mats, of mm-scale thickness characterized by rough, black or grey surfaces (***C***, ***F***); polygonal mats, of cm- to dm-scale thickness with highly cohesive, often fibrous mat fabric and dark green tufted surfaces characterized by desiccation cracks that delineate polygons (***D***, ***G***); and smooth mats, of generally cm-scale thickness and ranging in consistency from moderately cohesive to loose and goopy, often covered in beige exopolysaccharide material (***E***, ***H***). ***I***, NOAA GOES network infrared image of Hurricane Irma with the eye directly over Little Ambergris Cay on September 7th, 2017, 22:45 UTC. Black traces indicate land masses, white box indicates the area shown in panel ***A***.

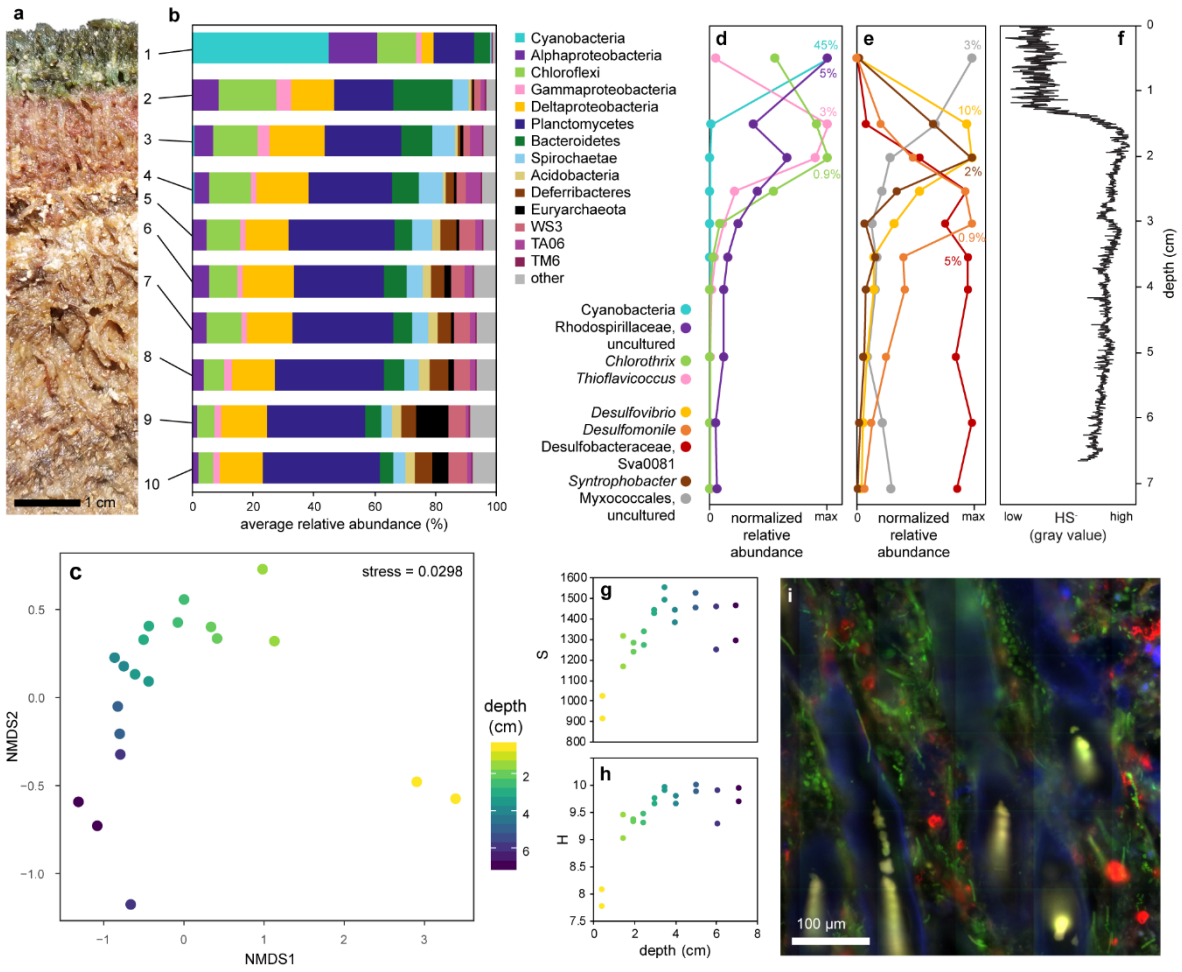

Figure 2. Microbial mat stratigraphy. ***A***, Photograph of CC mat cross section. Each visually distinguishable layer was sampled in replicate for microbial community analysis; the numbers to the right of the photograph indicate the horizons sampled. ***B***, Phylum level community composition of each layer, data shown are the averages of replicates. ***C***, NMDS plot showing variance in the microbial communities with depth. Each point represents a sample; relative proximity between points indicates similarity. Replicate samples are plotted separately, illustrating the minor amount of heterogeneity between replicates. ***D-E***, Normalized relative abundance showing the distribution of major groups of phototrophs (***D***), and Deltaproteobacteria (***E***) with depth, demonstrating the presence of an oxic photic zone, a sulfidic photic zone, and at least four distinct zones of organic carbon breakdown. Percentages indicate the maximum relative abundance of each taxon. ***F***, Sulfide profile captured on a silver strip, illustrating the porefluid chemocline from oxic to sulfidic ~1.3 cm below the mat surface. ***G***, Alpha diversity (observed OTUs) and ***H***, Shannon diversity ($H = -\sum_{i=1}^{s}(p_i\, log_2 p_i)$) of each sample with depth. ***I***, Fluorescence microscopy showing the complexity of spatial relationships and microenvironments in a mat slice. Red is FISH labelling of 16S rRNA with a universal bacterial probe; blue is DAPI, a general DNA stain; green is cyanobacterial autofluorescence.

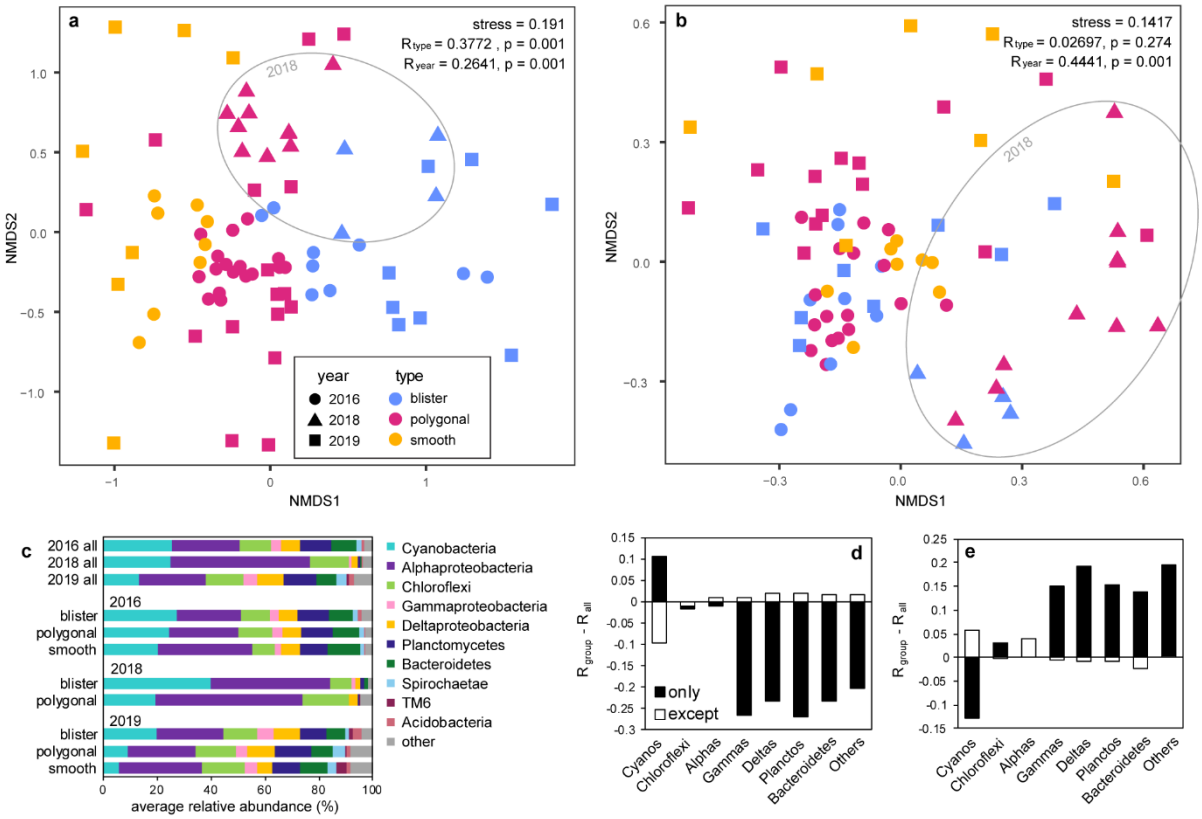

Figure 3. Differences in bulk mat communities across space and time. ***A***, NMDS plot visualizing variance, showing a clear trend between mat types along with a perturbation following the hurricane that largely recovered by 2019. Additional metadata variables can be found in Figures S2 and S7. ***B***, NMDS plot of phylum level rather than OTU level data. At the phylum level, the trend between mat types is lost, but the perturbation in 2018 remains clear. ***C***, Average phylum level community composition of all bulk mat samples from each year, and of each mat type within each year. The individual samples included in these averages can be found in Figure S3. ***D-E***, The contribution of each major group of organisms to the community variance seen between mat types (***D***) and year (***E***), quantified as the difference in ANOSIM statistic *R* between the full dataset and the dataset filtered to include only a specific group of organisms (shaded bars), and also the dataset filtered to exclude that specific group (open bars). NMDS plots accompanying these calculations can be found in Figure S4. The aspects of the community that varied most strongly between mat types and those most strongly perturbed by the hurricane are notably distinct—almost inverse.

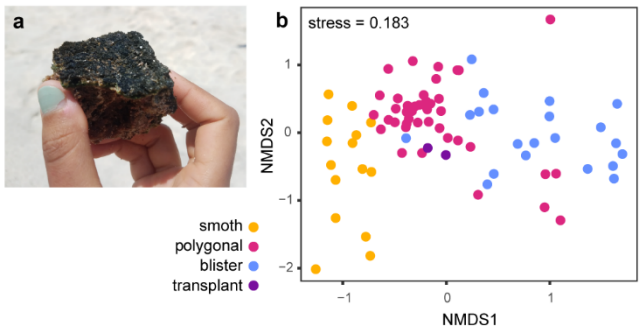

Figure 4. Transplant experiment. ***A***, Photograph of a transplanted slice of polygonal mat, turned dark and hard—reminiscent of blister mat—one year after transplantation. ***B***, NMDS plot of only cyanobacterial OTUs, illustrating their clear pattern of variance between mat types. Transplant samples are more similar to polygonal mats than blister mats, indicating that mat texture reflects environmental factors more than community composition, and demonstrating remarkable tolerance for environmental change from these taxa.

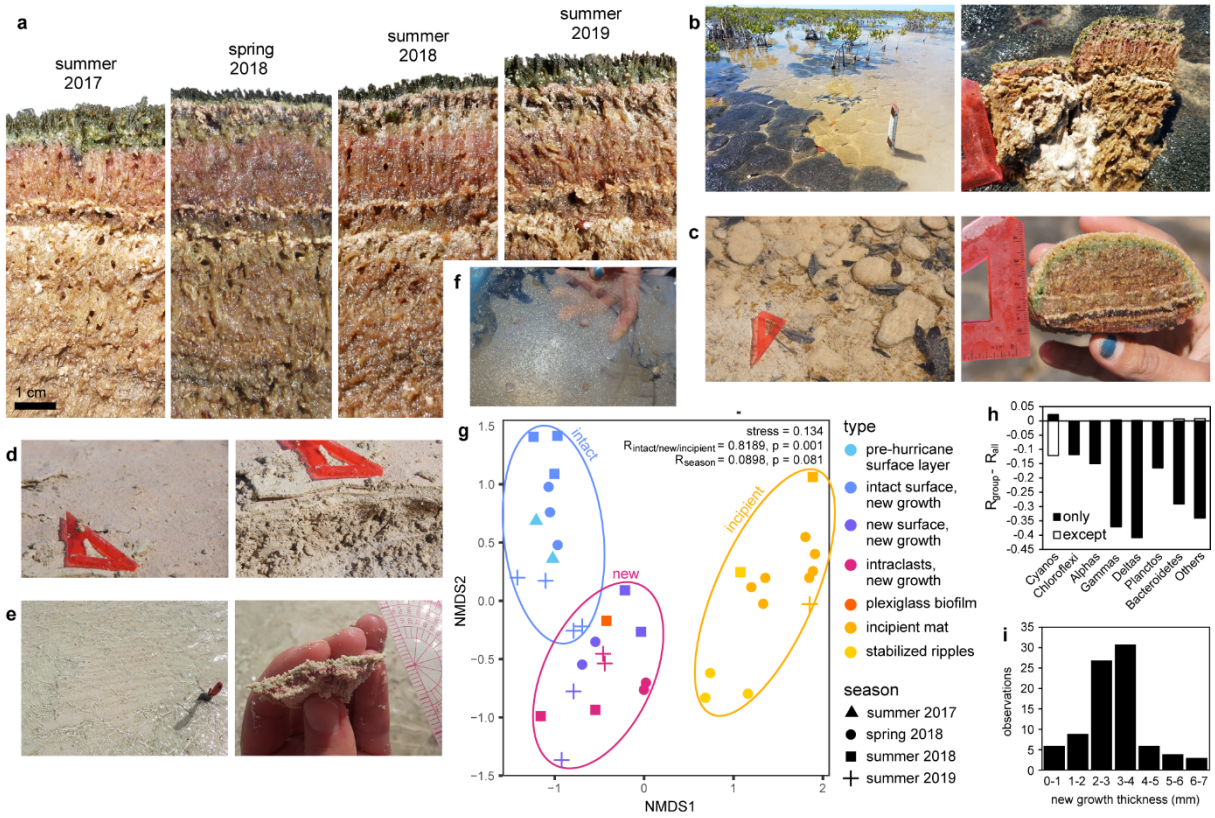

Figure 5. Post-hurricane growth. ***A***, Photographs of the CC mat depth profile through time, beginning one month before the hurricane in August 2017. This area was well protected by mangroves, and therefore impacted minimally. A thin layer of sediment deposited by the storm is visible in all subsequent photographs, with increasing new mat growth above it. Sediment lags several cm below the mat surface could represent previous storm events, possibly Hurricanes Ike in 2008 and Frances in 2004. ***B***, Scoured polygons adjacent to intact polygons in the CC area. New growth is visible on both intact and scoured surfaces. ***C***, Intraclasts of ripped up mat that were rounded during transport and redeposited upside down at MCW. ***D***, Incipient mat on top of hurricane sediment at FM. ***E***, Microbially stabilized ripples at BB. ***F***, Plexiglass biofilm experiment at CC. ***G,*** NMDS plot of post-hurricane growth samples. ***H***, ANOSIM analysis showing the contribution of different groups to the variance between new growth types. ***I***, Histogram showing thicknesses of new growth from 86 measurements of upside down mat intraclasts observed in March 2018, 6 months after the hurricane.

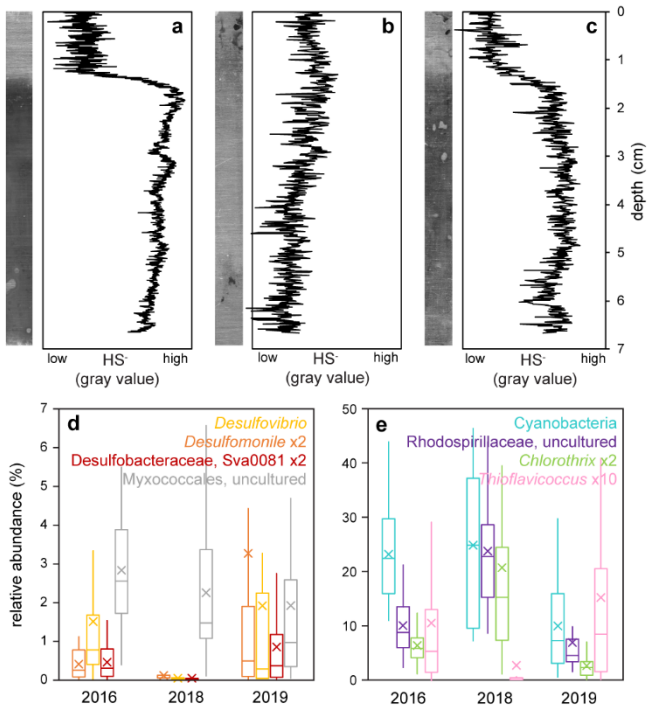

Figure 6. The sulfur cycle recovered on a slower timescale than new mat growth. ***A-C***, Sulfide profiles captured on silver strips at CC depth profile site in ***A***, 2017, ***B***, 2018, and ***C***, 2019, shown as both raw scanned images (left) and quantified by gray value (right). In 2017 and 2019, there was a clear sulfidic zone in the subsurface mat. In 2018, the year following Hurricane Irma, the mats did not appear meaningfully sulfidic at any depth. ***D-E***, Box and whisker plots showing the relative abundances of major Deltaproteobacteria (***D***) and phototrophs (***E***) in bulk mat samples from each year. Boxes denote first and third quartiles, horizontal lines indicate medians, x's indicate averages, whiskers indicate minimum and maximum data points. Taxa implicated in sulfate reduction or sulfide oxidation were substantially diminished in 2018, consistent with an impacted sulfur cycle.

Supplemental figures

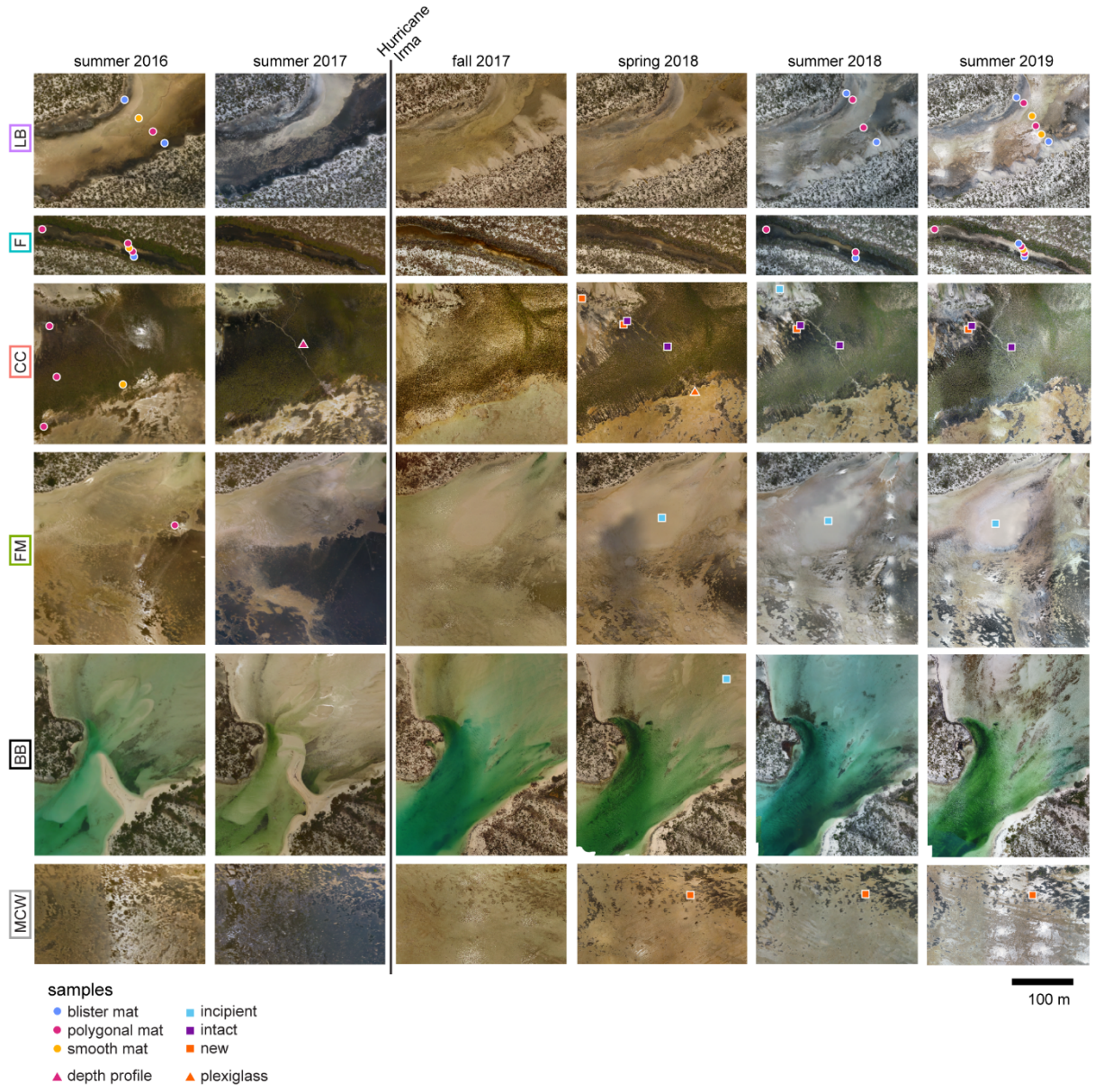

Figure S1. Drone images of mat study areas showing aerially visible changes over time. Specific sample locations from each field season are marked; some markers represent multiple samples of the same type taken in close proximity. The LB and F areas featured all three endmember mat types along transects of varying water depth across channels. The CC area contained thick, lush polygonal mats largely protected by mangrove thickets. The FM area hosted extensive mats prior to Hurricane Irma, most of which were scoured out or buried under a large lobe of sediment deposited during the storm, the surface of which subsequently developed incipient growth. The BB area also experienced massive changes in sedimentation from the hurricane, and transiently featured microbially-stabilized ripples. MCW was one of many areas that accumulated deposits of mat intraclasts after the hurricane.

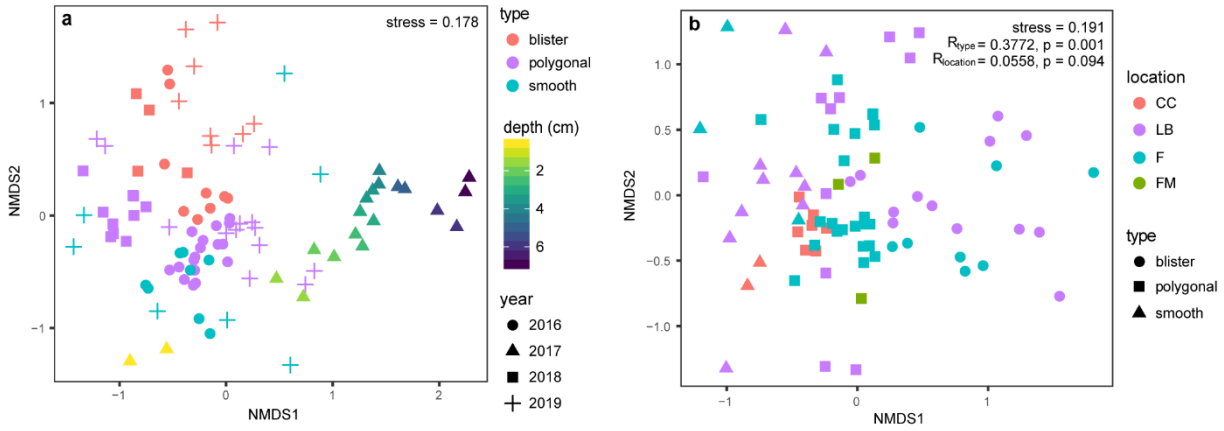

Figure S2. Additional NMDS plots of variance in bulk mat dataset. ***A***, Bulk samples plotted with the depth profile dataset. The variance between bulk mats plotted along a different vector than the variance with depth, indicating that the variance between bulk mats was not merely a reflection of how much of the subsurface community was sampled. ***B***, NMDS plot from Figure 3*A* colored by sample location, which did not exhibit a meaningful trend.

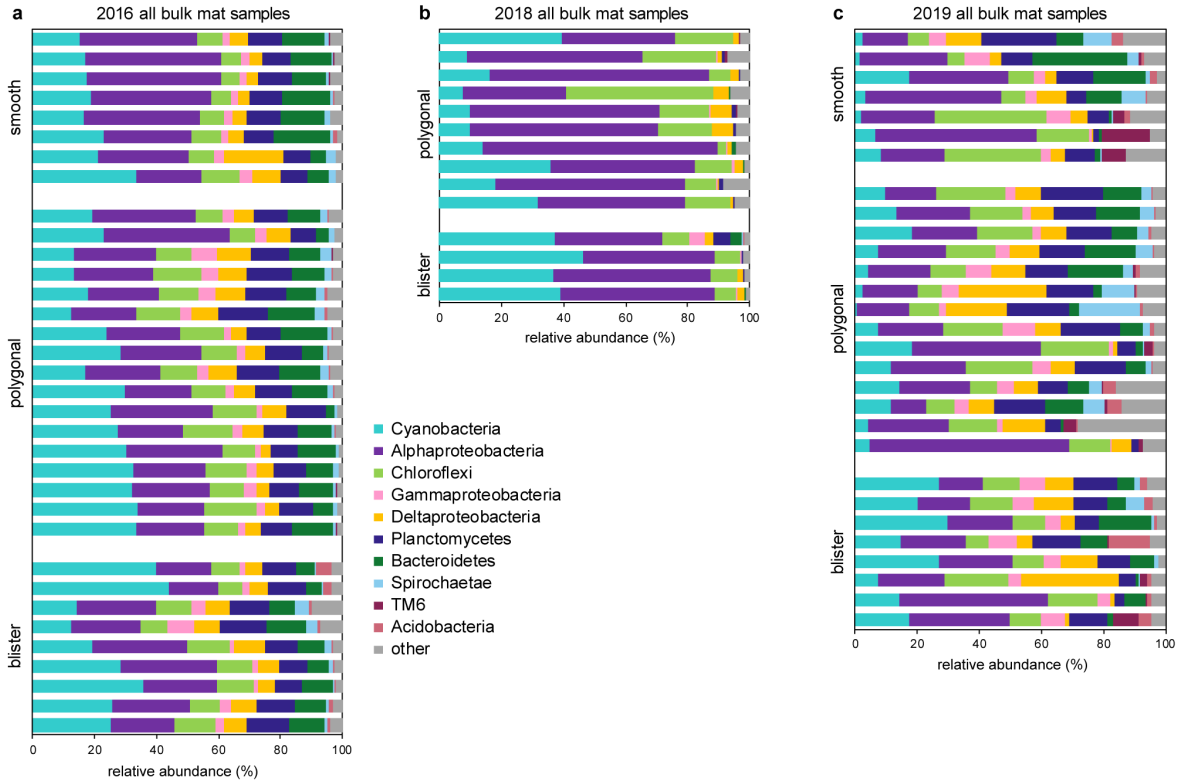

Figure S3. Phylum level community composition of the individual bulk mat samples from ***A***, 2016, ***B***, 2018, and ***C***, 2019 that contributed to the averages shown in Figure 3*C*.

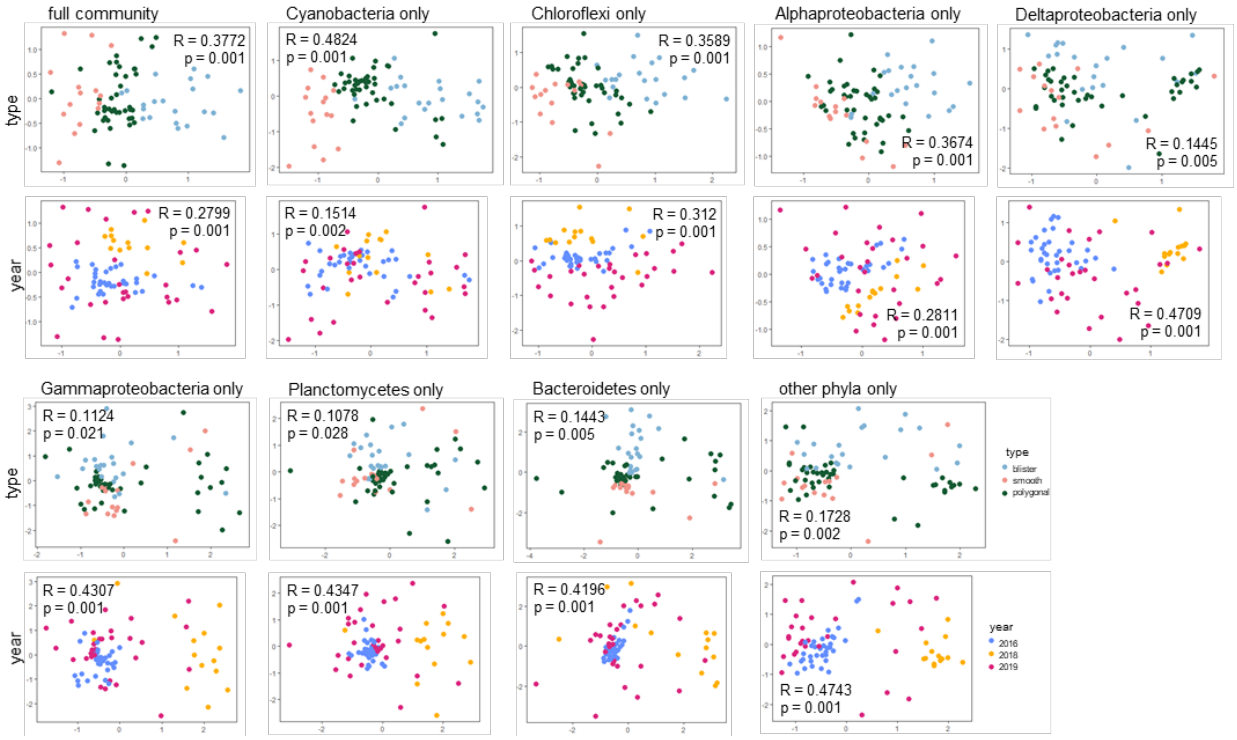

Figure S4. NMDS plots visualizing variance within major groups of organisms from the subsetted datasets used to calculate the ANOSIM values in Figure 3*D-E*. The plot for each group is shown twice with the points colored by mat type or year, to highlight how different groups express patterns in dissimilarity for each variable. ANOSIM statistic *R* values are displayed for the variable in question.

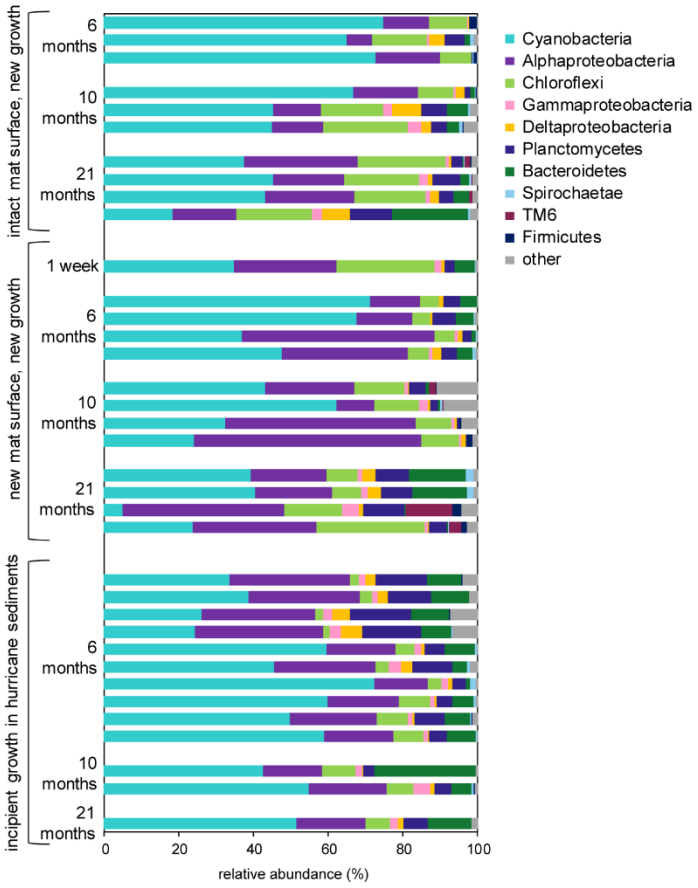

Figure S5. Phylum level community composition of post-hurricane growth samples.

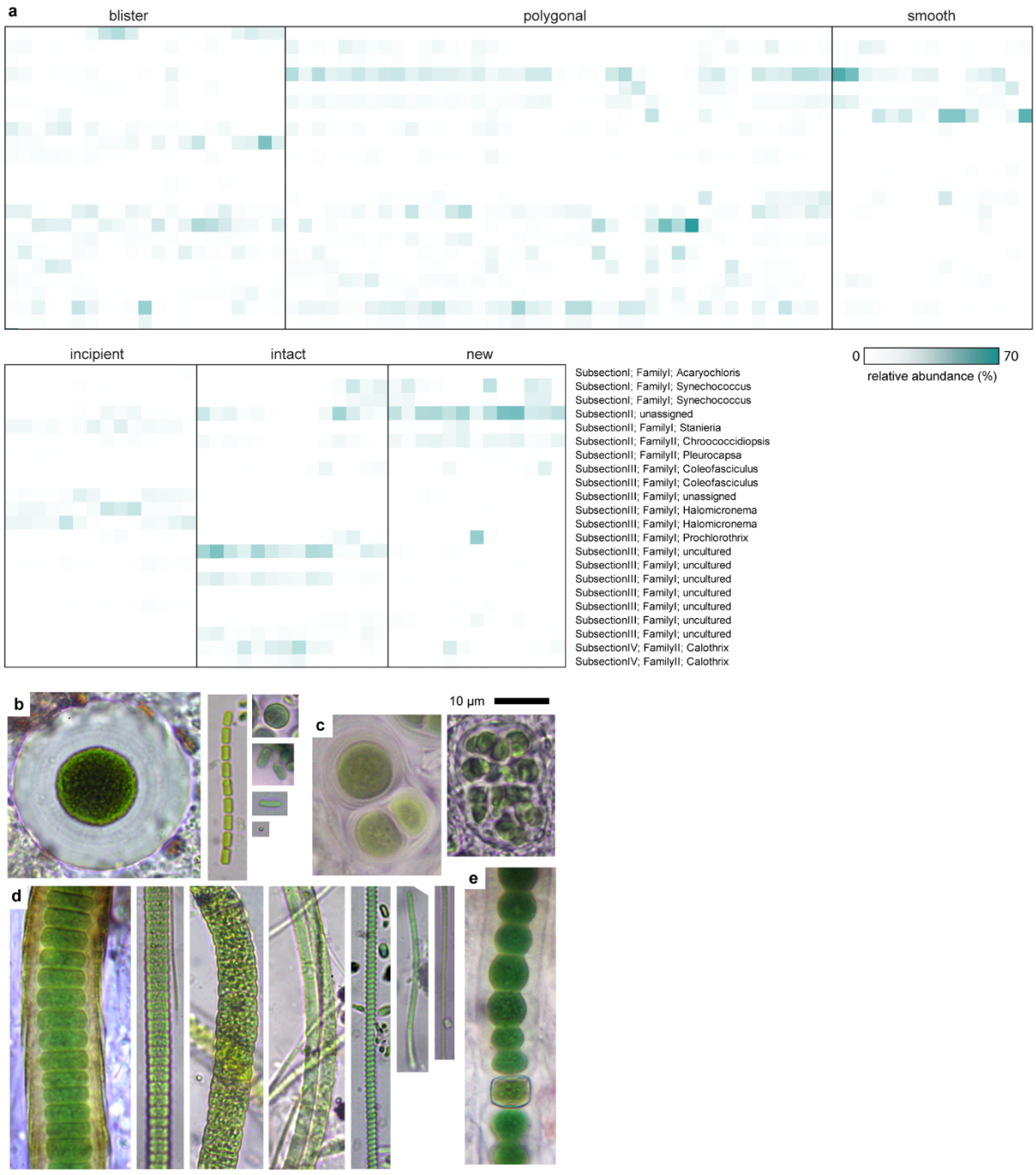

Figure S6. Diversity of Cyanobacteria in the Little Ambergris Cay mats. ***A***, Heat map showing relative abundance of the top cyanobacterial taxa (OTUs with average > 0.5% of cyanobacterial reads in a sample), together accounting for 36% of all cyanobacterial reads. ***B***-***E***, Photomicrographs illustrating the morphological diversity of Cyanobacteria in the Little Ambergris Cay mats, including unicellular (***B***), colonial/baeocystous (***C***), filamentous (***D***), and heterocystous (***E***) representatives.

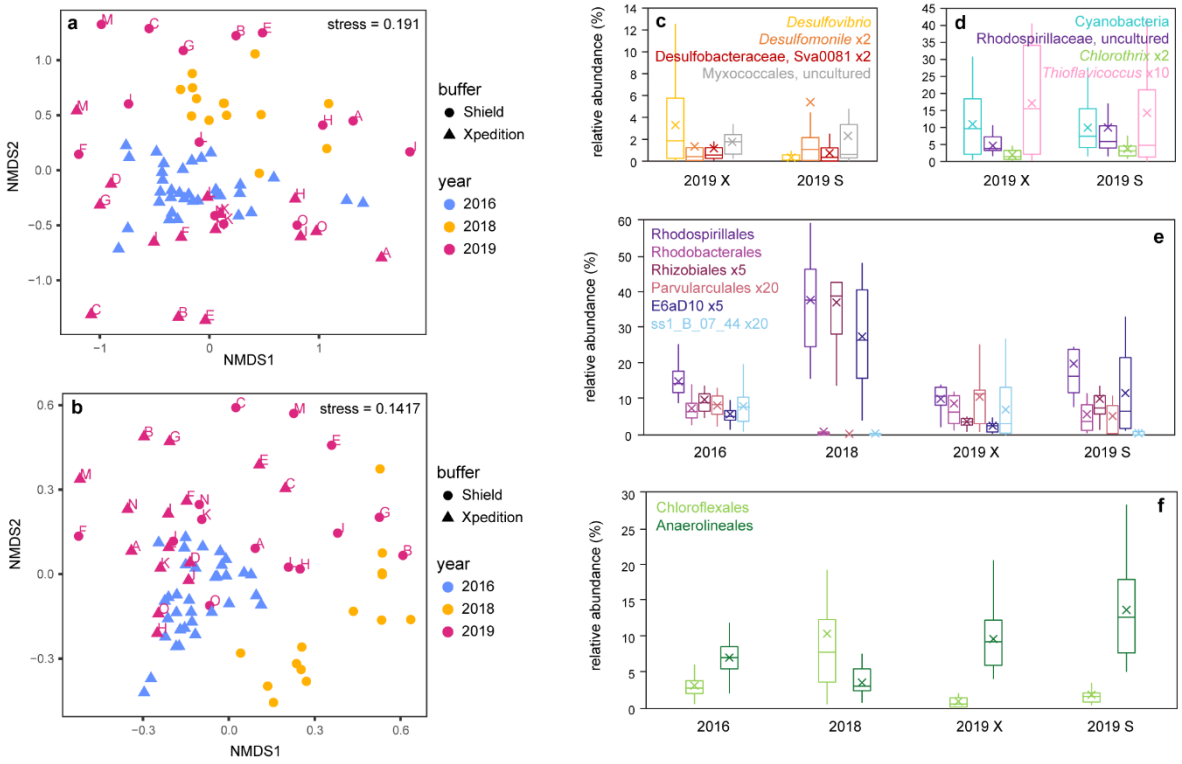

Figure S7. Deconvolving the buffer artifact from the hurricane impact. ***A-B***, NMDS plots from Figure 3 at the OTU (***A***) and phylum (***B***) levels, showing which DNA preservation buffer was used. Letters indicate 2019 replicates. The buffer discrepancy complicated interpretation of the variance between years at the OTU level, but phylum level data showed a clear pattern of hurricane impact and recovery regardless of buffer. ***C-D***, Box and whisker plots of the taxa shown in Figure 6, comparing samples collected in 2019 with the Xpedition (X) buffer used in 2016 and the Shield (S) buffer used in 2018. There was a possible buffer artifact in the Desulfovibrionales, but the remainder of these taxa seemed unaffected by buffer, strengthening our interpretation that the perturbation illustrated with these taxa represented real ecological change. ***E-F***, We also examined major orders within the Alphaproteobacteria and Chloroflexi, two of the most dominant groups across all samples. ***E***, Within the Alphaproteobacteria, some orders were clearly diminished (Rhodobacterales, Parvularculales) while others were enriched (Rhodospirillales, Rhizobiales) in 2018; these taxa did not seem affected by buffer, suggesting that their perturbation also reflected the hurricane impact. However, they are sufficiently functionally diverse that it is inadvisable to draw specific biogeochemical conclusions from their presence or absence. Other groups (E6aD10 and ss1_B_07_44) did exhibit buffer effects. ***F***, Within the Chloroflexi, both the phototrophic Chloroflexales and anaerobic, fermentative Anaerolineae were abundant throughout our timeseries, but their relative dominance was switched in 2018. These taxa did not exhibit a buffer effect.

CHAPTER VIII

Ooids as an eco-friendly exfoliant alternative to plastic microbeads

Usha F. Lingappa[1], Woodward W. Fischer[1], John P. Grotzinger[1], Elizabeth J. Trower[2]

1. Div. of Geological & Planetary Sciences, California Institute of Technology, Pasadena, CA 91125, USA

2. Dept. of Geological Sciences, University of Colorado Boulder, Boulder, CO 80309, USA

Abstract

The pollution caused by plastic microbeads used as exfoliants in facial scrubs and body washes is ecologically devastating. Commonly used natural alternatives such as fragments of walnut shells and stonefruit pits are prone to damaging skin—a serious liability in a skincare product. Here we propose that ooid sand grains present an excellent alternative. We discuss how recent advances in our understanding of ooid formation processes redefined them as a renewable resource. We present size, shape, texture, efficacy, and stability data demonstrating the properties that make ooids an ideal microbead material—both gentle on skin and effective as an exfoliant. Finally, we discuss the fate of ooids after being washed down the drain—dissolution in wastewater or groundwater—which introduces the added benefit of being a CO_2 sink. This dissolution can be catalyzed by endolithic Cyanobacteria, at much faster rates than previously appreciated.

Introduction

Microplastics—plastic particles < 1mm in diameter—are a major and devastating component of plastic pollution. These materials have become the most abundant form of plastic debris in the oceans, found throughout the water column and accumulating in sediment systems around the world (1). Their small size makes them easily ingested, impacting organisms across trophic levels—from filter-feeding zooplankton to top predators (2–6); and the ecological consequences of ingesting these particles are exacerbated by their tendency for toxin sorption (7). Given their persistence in the environment and the impracticality of removing them, the continued release of microplastics represents a lasting ecological threat (5, 8).

Over the past several decades, a major source of microplastic pollution has been the use of plastic microbeads as exfoliants in skincare products (2, 9). The presence of these particles in products designed to be washed down the drain is particularly egregious because wastewater treatment strategies are ineffective at preventing their release into the environment (10). Rising public awareness of the ecological ramifications of microplastics has led to a recent movement away from plastic microbeads; many

countries have adopted legislation banning their use in cosmetic products (11) and corporations have tried to replace the plastics with natural alternatives such as walnut shell or stonefruit pit fragments and jojoba wax beads. Unfortunately, these alternative materials are either more expensive and less effective—i.e. jojoba wax—or have serious liabilities as exfoliants—i.e. walnut shells and stonefruit pits, fragments of which are too jagged and can damage skin (12). Thus, there remains a need for an effective, inexpensive, and environmentally benign microbead material.

Ooids are a type of spherical, concentrically coated carbonate sand grain typically made of the mineral aragonite that form in certain shallow marine and lacustrine environments. Their formation is controlled by dynamic physical and chemical processes of abrasion and precipitation, which operate at near equilibrium with the environment (13). Based on radiocarbon ages, they were previously considered geological products that formed over timescales of millennia. However, recent work documented instantaneous rates of both abrasion and precipitation on the order of 10^4 μm^3/ooid/hour (13)—four orders of magnitude higher than the net growth rates suggested by radiocarbon age (14). These results suggested that the appearance of slow growth is an artifact of natural systems in equilibrium—where abrasion and precipitation are operating at subequal rates—not an inherent property of ooid formation. By extension, if ooid forming environments from which a subset of ooids have been removed are seeded with appropriate nuclei, they can be expected to regenerate sand sized grains on timescales of a few years. This understanding redefined ooids as a renewable resource—a natural product that can be replenished relatively quickly.

Here we propose the use of ooids as a natural alternative to plastic microbeads. Ooid size, shape, and surface texture characteristics along with experimentally demonstrated abrasion efficacy reflect the qualities of an ideal exfoliating material. Furthermore, while they are shelf-stable in facial scrub and body wash matrices, they will dissolve in municipal wastewater systems, and in so doing constitute a net CO_2 sink.

Results & Discussion

Ooids exhibit material properties of an ideal exfoliating microbead

We harvested microbeads from several commercially available facial scrubs and body washes (Table 1, products A-H) and compared them to natural ooid samples from both lacustrine (Great Salt Lake (GSL), USA) and marine (Little Ambergris Cay (LAC), Turks and Caicos Islands, along with commercial aquarium sand composed primarily of ooids sourced from the Bahamas) environments. The microbeads exhibited a wide range of grain sizes, with median diameters ranging from 116 to 791 μm (Fig. 1A). Natural ooids can be sieve sorted to generate populations across the same size ranges (Fig. 1B), demonstrating their versatility as replacements for many different types of microbeads.

To avoid the dermatological damage caused by jagged materials like walnut shells, an ideal microbead glides or rolls across the skin rather than snagging or scraping. This behavior is determined by shape characteristics such as sphericity and roundness, two different measures of how much particle shape deviates from that of a perfect sphere (mathematically defined in Fig. 2 legend). By both of these parameters, natural ooids scored as high or higher than any of the commercial microbeads examined, while walnut shell fragments scored the lowest (Fig. 2).

Scanning electron microscopy (SEM) imaging revealed a wide range of microbead surface textures (Fig. 3). As expected, plastic and wax beads exhibited smoother surfaces, while walnut shell fragments displayed much rougher surfaces (Fig. 3F). The jagged edges that make them prone to tearing skin are defined by plant cell walls and therefore inherent to these and other such plant-derived materials. In contrast, the surfaces of natural ooids are exceptionally smooth, polished by the abrasive forces that contribute to their formation (Fig. 3I).

Their extreme smoothness and roundness demonstrated by both SEM and shape index data made it clear that ooids do not share the liabilities of walnut shells, but raised the concern that perhaps they are too gentle, and therefore insufficiently abrasive to act as effective exfoliants. To test the efficacy of ooids as microabrasive particles, we conducted abrasion experiments comparing ooids to plastic microbeads harvested from a commercial facial scrub (product B) using a low tensile strength polyurethane foam

substrate as a skin simulant. Both sets of particles demonstrated comparable abrasion rates, indicating comparable utility as an exfoliant (Fig. 4).

Taken together, this dataset illustrates the ideal material qualities of ooids for use as an exfoliating microabrasive in cosmetic products. Ooids exist in the same size ranges as commercially used microbeads, their grain shape and surface texture indicates that they will be gentle on skin, and their efficacy as microabrasive particles suggests that they will be effective exfoliants.

Washing ooids down the drain constitutes a net CO_2 sink

Considering the fate of ooids washed down the drain revealed further benefits of using them in cosmetic products. All municipal wastewaters and nearly all non-marine surface, soil, and groundwaters tend to be undersaturated with respect to $CaCO_3$ minerals such as aragonite ($\Omega < 1$) and therefore drive net dissolution of such materials. This means that ooids in products that are ultimately washed down the drain require no special remediation; they will dissolve on their own, at rates determined by grain size and carbonate saturation state (Fig. 5). Furthermore, carbonate can serve as a pH buffer, preventing corrosion and leaching of toxic heavy metals in plumbing systems. If any ooids escape to marine systems, they will contribute to existing natural carbonate sediment that helps buffer against ocean acidification—a challenge for marine fisheries and biodiversity in its own right (15).

Water activity in the detergent matrices of typical microbead-containing products is sufficiently low that ooid dissolution within such products should be minimal. To confirm this, we conducted stability incubations in several facial scrub and body wash products (Table 1, products I-M). After 13 months, ooids did not exhibit any signs of even incipient decomposition (Fig. 6), indicating that dissolution will occur after products containing ooids are used and washed away, but not before.

Ooid dissolution has important environmental implications well beyond mitigating microplastic pollution. Conversions between atmospheric CO_2, dissolved inorganic carbon (DIC), and solid carbonate minerals are central to the Earth's carbon cycle and therefore climate system. CO_2 is a greenhouse gas and major contributor to the increase in Earth's radiative forcing due to anthropogenic emissions. The

equilibrium between atmospheric and dissolved carbon species mitigates this situation; much of our emitted CO_2 is taken up by the oceans as DIC (16). $CaCO_3$ dissolution represents a carbon sink that ties into this equilibrium—the balanced dissolution reaction generates two molar equivalents of dissolved bicarbonate alkalinity for each mole of $CaCO_3$ by pulling one mole of CO_2 out of the atmosphere (equation 1) (17).

1. $CaCO_3 + H_2O + CO_2 \rightarrow Ca^{2+} + 2\ HCO_3^-$

In other words, widespread replacement of plastic microbeads with natural ooids and their subsequent dissolution could constitute a net CO_2 sink. Thus, ooids used as exfoliants are "green" not only in being an alternative to microplastics and a renewable natural resource—they could have a negative carbon footprint.

Boring Cyanobacteria provide a rapid, light-driven mechanism of ooid dissolution

The thermodynamic driving force determined by saturation state is not the only factor controlling ooid dissolution. In certain environments, endolithic Cyanobacteria are known to bore into ooids (18). This occurs even under conditions that are supersaturated with respect to aragonite ($\Omega > 1$), where dissolution is thermodynamically unfavorable. The mechanism by which Cyanobacteria dissolve carbonate was long considered a paradox—as photosynthetic organisms, their primary metabolic activity increases the local pH, thereby facilitating the precipitation rather than dissolution of carbonate minerals. Therefore, in order for Cyanobacteria to bore, their photosynthetic and boring activities must be separated either temporally (such as across the diel cycle), or spatially (such as in different areas of a cyanobacterial cell or filament), or their boring must occur via a mechanism independent of pH (19).

The model organism *Mastigocoleus testarum* strain BC008 has been shown to dissolve carbonate by a mechanism based on active Ca^{2+} transport using a P-type ATPase (20). By pumping Ca^{2+} ions away from the mineral surface these organisms create a steep Ca^{2+} concentration gradient, favoring the

dissolution of the carbonate mineral by a mechanism that is pH independent and therefore not interfered with by photosynthetic activity. There is also evidence that they can obtain the majority of their carbon for autotrophic growth directly from the carbonate mineral (21). This means that these organisms not only facilitate carbonate dissolution and the accompanying CO_2 sink described above, they amplify it—sequestering the carbon liberated from the mineral as biomass, and drawing down *two* molar equivalents of CO_2 from the atmosphere to balance the alkalinity generated by dissolution (equation 2).

2. $CaCO_3 + 2H_2O + 2CO_2 \rightarrow CH_2O + Ca^{2+} + 2\ HCO_3^- + O_2$

Marine ooids, such as those at LAC, often exhibit substantial evidence of boring (Fig. 7A). Like the processes involved in ooid formation, boring was previously thought to occur too slowly to readily study *in situ*. We tested this assumption by deploying polished aragonite stubs in the environment as clean substrates to get colonized and bored, and then collected them and examined them for boring traces by SEM. Even the shortest incubation that we conducted—five days—exhibited boring (Fig. 7B). This remarkably rapid rate suggested that boring controls meaningful fluxes of carbon cycling in shallow marine environments like LAC.

Boring Cyanobacteria exhibit a wide range of both genetic and morphological diversity, and the universality of the *M. testarum* Ca^{2+} pumping mechanism across this diversity remains an open question. While *M. testarum* is sensitive to Ca-ATPase inhibitors, at least one other group of boring Cyanobacteria (of the Pleurocapsales) appear not to be, suggesting the possibility of other boring mechanisms (22). Furthermore, *M. testarum* is unable to bore into dolomite or apatite, although rich endolithic communities exist in dolomitic and phosphatic rocks—another possible indication of mechanistic diversity. Notably, cyanobacterial community members exhibit preferences between mineral substrates only at very high phylogenetic resolution, suggesting very fine niche specialization between closely related organisms (23).

16S rRNA gene amplicon sequencing revealed diverse Cyanobacteria associated with LAC ooids and deployed aragonite stubs (Fig. 8A-B). The stubs represent a much shorter-term colonization window

than the ooids themselves and exhibited much higher dominance of Cyanobacteria relative to other taxa. This observation is consistent with previous work suggesting that cyanobacterial borings are ultimately colonized by a diverse community of other endolithic organisms (24). The identities of the Cyanobacteria that we recovered from the stubs were different from those endemic to the natural ooids, possibly indicating a successional dynamic among the borers themselves. Ongoing work is aimed at elucidating the physiological mechanism, or mechanistic diversity, associated with these boring populations to better understand the role of biological ooid dissolution in the carbon cycle.

Conclusions

This work introduced ooids a replacement for plastic microbeads in cosmetic products that would not only mitigate microplastic pollution but also contribute to CO_2 drawdown via carbonate dissolution. Furthermore, to better understand the landscape of carbonate dissolution processes, we established an experimental system for studying cyanobacterial boring *in situ* and demonstrated that boring occurs incredibly rapidly—on timescales of days—suggesting that photosynthetically-driven carbonate dissolution can control meaningful fluxes of carbon cycling. Many open questions remain concerning the ecology and physiology of boring miocroorganisms. From the basic science perspective, future work on this topic may contribute important insights, not only to our understanding of modern endolithic microbiology, but also to the geological record of endoliths and what their presence or absence from ooids at different periods in Earth history can tell us about paleoenvironment. From the microbead replacement perspective, better understanding ooid microbiology may shed light on important considerations for the material quality of ooids, strategies for sustainably harvesting them from the environment, and implications for their dissolution and CO_2 drawdown capacity following use.

Methods

Ooid and commercial microbead samples

Natural ooids were collected at Little Ambergris Cay, Turks and Caicos Islands and the Great Salt Lake, USA, rinsed with water to remove surficial salts, and allowed to dry. Bahamian ooids sold as aquarium sand were purchased (CaribSea Arag-Alive). For grain size analyses, ooids were sieved to separate different size fractions.

Commercial facial scrub and body wash products containing microbeads were purchased (Walgreens) (Table 1, products A-H). Microbeads were harvested by filtration through nylon mesh cell strainers (VWR), rinsed with water, and allowed to dry.

Size and shape analyses

Grain size and shape characteristics of large populations of grains were determined by dynamic image analysis using a Retsch Camsizer P4.

SEM imaging

Secondary electron SEM imaging of grain surfaces was conducted in the Caltech Geological and Planetary Sciences Division Analytical Facility on a ZEISS 1550VP Field Emission SEM. Samples were mounted on aluminum holders with carbon tape, coated with Pd using a Cressington HR metal sputtering coater, and imaged with accelerating voltages of 10 to 20 kV and working distances of 15 to 25 mm.

Abrasion experiments

To obtain measurable abrasion rates, we used low tensile strength ($\sigma T = 0.32$ MPa) polyurethane foam as a highly abradable skin simulant. Abrasion chambers were constructed by securing a 3.5 cm thick foam disc to the base of a 200 mL beaker, 6.5 cm in diameter. The microabrasive materials being tested were immobilized as a monolayer across a flat surface 4 cm in diameter. The abrasive surfaces were weighted to 80 g, placed in the abrasion chambers, and submerged in water. To insure that any measured abrasion was not merely due to weight, a control was conducted using an identical weighted surface but

without any abrasive material. The chambers were sealed with parafilm and shaken at 230 rmp for 1 – 3 hours. Abrasion was measured as depth scoured in the foam discs by the weighted surfaces.

Stability incubations

Ooids were added to glass vials with commercial facial scrub and body wash products without microbeads but analogous to the types of products that tend to contain them (Walgreens) (Table 1, products I-M). Incubations were kept at room temperature. After 6 months and 13 months, the ooids were filtered out through nylon mesh cell strainers, rinsed, dried, and examined by SEM.

Endolithic microbial community analysis

Aragonite crystals (Jewel Tunnel Imports) were sliced into stubs, polished, and glued to plexiglass sheets that were strapped to cinderblocks and deployed in the environment at LAC to allow colonization by natural microbial communities. After one week, the stubs were collected and either sterilized by submergence in ethanol or sampled for DNA analyses. Upon return to the lab, the sterilized stubs were examined for borings by SEM.

To access endolithic communities for DNA analyses, the surface of a stub was scratched with a sterile dental pick. The scrapings were collected with a sterile paintbrush and deposited in a BashingBead lysis tube containing DNA/RNA Shield (Zymo) for preservation. The endolithic communities of natural ooids were sampled similarly, accessed by grinding ooid grains in a sterile mortal and pestle.

DNA was extracted at Caltech using the Zymo Quick-DNA™ Fecal/Soil Microbe MiniPrep kit. A segment of the V4 to V5 hypervariable region of the 16s rRNA gene was amplified by PCR using the 515f and 926r primer pair (25). PCR reactions were set up in 15 µL volumes with Q5 Hot Start High-Fidelity 2x Master Mix (New England Biolabs), with annealing at 54 °C and 30 cycles. Amplified products were barcoded with Illumina NexteraXT index 2 primers, and barcoded samples were submitted to Laragen for 2 x 250 bp paired end sequencing on Illumina's MiSeq platform. Sequence data was processed using QIIME version 1.8.0 (26). Raw sequence pairs were joined and quality trimmed.

Sequences were then clustered into operational taxonomic units (OTUs) with 99% similarity using the UCLUST open reference clustering protocol, and the most abundant sequence was chosen as representative for each OTU. Taxonomic identification for each representative sequence was assigned using the Silva-119 database (27).

Candidate borer Cyanobacteria were enriched from an LAC ooid sample in PES30 artificial seawater medium (20) and imaged by light microscopy using an Amscope B120 LED microscope equipped with an Amscope MD500 eyepiece camera.

Acknowledgements
We thank our fellow participants of the Agouron Institute's 2016 advanced geobiology field course, during which this idea originated: Marjorie Cantine, Emily Orzechowski, Justin Strauss, Hannah Grotzinger, Maya Gomes, Leigh Anne Riedman, Sophia Roosth, Shane O'Reilly, Daven Quinn, Nathan Stein, Kyle Metcalfe, Andy Knoll, and Mel Simon. We also thank the Caltech Office of Technology Transfer and Corporate Partnerships for helping us develop this concept and patent it. Fieldwork on Little Ambergris Cay was permitted by the Turks and Caicos Islands Dept. of Environment and Coastal Resources.

Author contributions
All authors contributed to idea development. UFL and EJT performed experiments and analyses. UFL wrote the manuscript with input from EJT and WWF.

References

1. M. Cole, P. Lindeque, C. Halsband, T. S. Galloway, Microplastics as contaminants in the marine environment: A review. *Mar. Pollut. Bull.* **62**, 2588–2597 (2011).

2. L. S. Fendall, M. A. Sewell, Contributing to marine pollution by washing your face: Microplastics in facial cleansers. *Mar. Pollut. Bull.* **58**, 1225–1228 (2009).

3. S. E. Nelms, T. S. Galloway, B. J. Godley, D. S. Jarvis, P. K. Lindeque, Investigating microplastic trophic transfer in marine top predators. *Environ. Pollut.* **238**, 999–1007 (2018).

4. E. M. Duncan, *et al.*, Microplastic ingestion ubiquitous in marine turtles. *Glob. Change Biol.* **25**, 744–752 (2019).

5. C. J. Moore, Synthetic polymers in the marine environment: A rapidly increasing, long-term threat. *Environ. Res.* **108**, 131–139 (2008).

6. C. M. Rochman, *et al.*, Anthropogenic debris in seafood: Plastic debris and fibers from textiles in fish and bivalves sold for human consumption. *Sci. Rep.* **5** (2015).

7. R. E. J. Schnurr, *et al.*, Reducing marine pollution from single-use plastics (SUPs): A review. *Mar. Pollut. Bull.* **137**, 157–171 (2018).

8. J. A. Ivar do Sul, M. F. Costa, The present and future of microplastic pollution in the marine environment. *Environ. Pollut.* **185**, 352–364 (2014).

9. W. J. Beach, Skin cleaner.

10. C. M. Rochman, *et al.*, Scientific Evidence Supports a Ban on Microbeads. *Environ. Sci. Technol.* **49**, 10759–10761 (2015).

11. Rep. Pallone, Frank, Jr. [D-NJ-6], H.R.1321 - Microbead-Free Waters Act of 2015 (2015).

12. , Browning et al v. Unilever United States, Inc. (2018).

13. E. J. Trower, M. P. Lamb, W. W. Fischer, Experimental evidence that ooid size reflects a dynamic equilibrium between rapid precipitation and abrasion rates. *Earth Planet. Sci. Lett.* **468**, 112–118 (2017).

14. S. R. Beaupré, M. L. Roberts, J. R. Burton, R. E. Summons, Rapid, high-resolution 14C chronology of ooids. *Geochim. Cosmochim. Acta* **159**, 126–138 (2015).

15. Bhadury, Punyasloke, Effects of ocean acidification on marine invertebrates- a review. *INDIAN J. GEO-Mar. Sci.* **44**.

16. N. Gruber, *et al.*, The oceanic sink for anthropogenic CO_2 from 1994 to 2007. *Science* **363**, 1193–1199 (2019).

17. Z. Liu, J. Zhao, Contribution of carbonate rock weathering to the atmospheric CO 2 sink. *Environ. Geol.* **39**, 1053–1058 (2000).

18. U. F. Lingappa, W. W. Fischer, E. J. Trower, Ecophysiology of Ooid Microborings Excavated by Endolithic Cyanobacteria in *AGU Fall Meeting 2019 Abstract #PP41C-1558*, (2019).

19. F. Garcia-Pichel, Plausible mechanisms for the boring on carbonates by microbial phototrophs. *Sediment. Geol.* **185**, 205–213 (2006).

20. F. Garcia-Pichel, E. Ramirez-Reinat, Q. Gao, Microbial excavation of solid carbonates powered by P-type ATPase-mediated transcellular Ca2+ transport. *Proc. Natl. Acad. Sci.* **107**, 21749–21754 (2010).

21. B. S. Guida, M. Bose, F. Garcia-Pichel, Carbon fixation from mineral carbonates. *Nat. Commun.* **8** (2017).

22. E. L. Ramírez-Reinat, F. Garcia-Pichel, Prevalence of Ca^{2+} -ATPase-Mediated Carbonate Dissolution among Cyanobacterial Euendoliths. *Appl. Environ. Microbiol.* **78**, 7–13 (2012).

23. E. Couradeau, D. Roush, B. S. Guida, F. Garcia-Pichel, Diversity and mineral substrate preference in endolithic microbial communities from marine intertidal outcrops (Isla de Mona, Puerto Rico). *Biogeosciences* **14**, 311–324 (2017).

24. D. Roush, F. Garcia-Pichel, Succession and Colonization Dynamics of Endolithic Phototrophs within Intertidal Carbonates. *Microorganisms* **8**, 214 (2020).

25. A. E. Parada, D. M. Needham, J. A. Fuhrman, Every base matters: assessing small subunit rRNA primers for marine microbiomes with mock communities, time series and global field samples: Primers for marine microbiome studies. *Environ. Microbiol.* **18**, 1403–1414 (2016).

26. J. G. Caporaso, *et al.*, QIIME allows analysis of high-throughput community sequencing data. *Nat. Methods* **7**, 335–336 (2010).

27. C. Quast, *et al.*, The SILVA ribosomal RNA gene database project: improved data processing and web-based tools. *Nucleic Acids Res.* **41**, D590–D596 (2012).

Figures

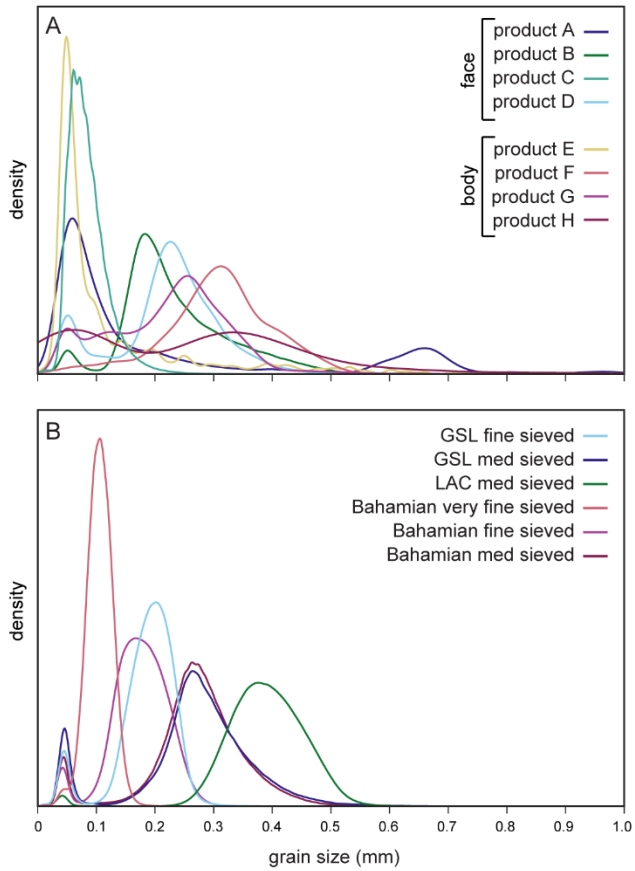

Figure 1. Size distributions of commercial microbeads (A) and natural ooids (B), illustrating that they exist in the same size ranges.

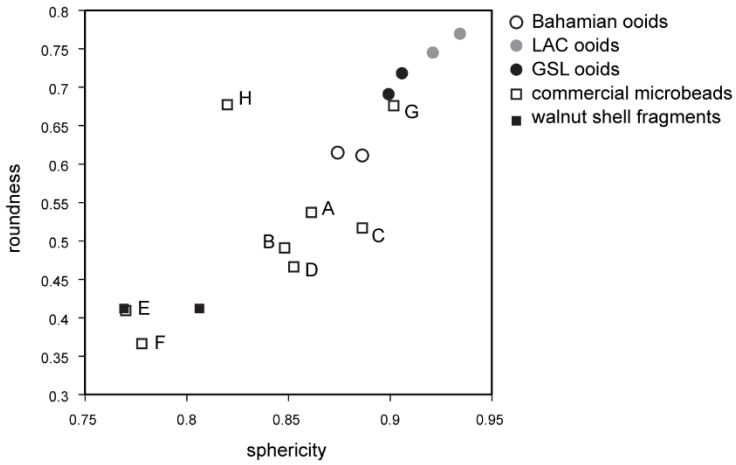

Figure 2. Mean shape indices of commercial microbeads and natural ooids. Sphericity is calculated as $4\pi A/p^2$, where A is the projected area of the particle and p is the perimeter; roundness is calculated with the Wadell roundness index $\Sigma r_i/(nR)$, where r_i are the radii of curvature of particle corners, n is the number of corners measured, and R is the radius of the largest inscribed circle. A perfect sphere has both roundness and sphericity indices of 1. By both of these parameters, ooids scored higher than most of the commercial microbeads examined, while walnut shell and apricot pit fragments scored the lowest.

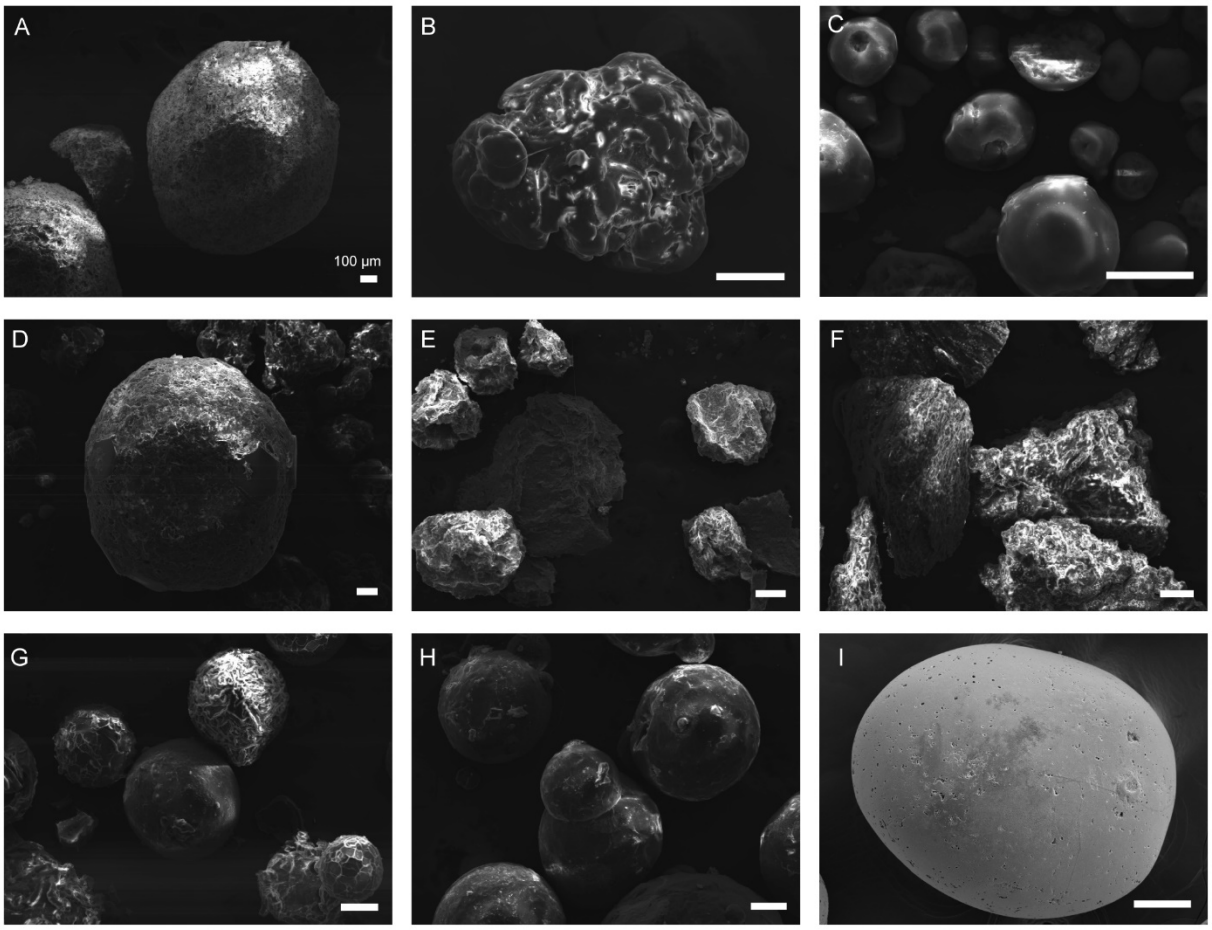

Figure 3. SEM images showing surface textures of commercial microbeads (A-H, products described in Table 1) along with an LAC ooid grain for comparison (I). Note the contrast between the jagged edges of apricot pit fragments (F) and the smooth, well-polished ooid surface (I).

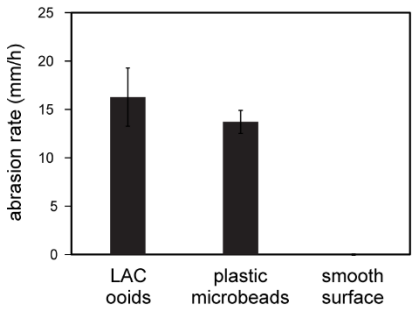

Figure 4. Efficacy of LAC ooids and plastic microbeads as microabrasive particles, determined experimentally on a polyurethane foam substrate. Rates reported here are averages of triplicates, error bars represent standard error. Ooids demonstrated similar abrasion efficacy to plastic microbeads, suggesting they would make an effective exfoliant in skincare products.

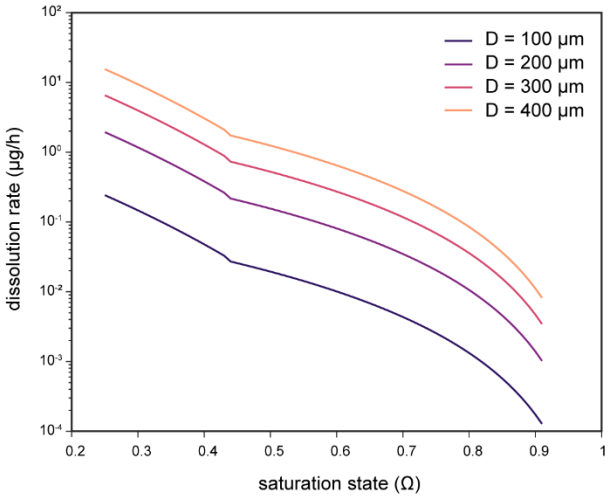

Figure 5. Modelled ooid dissolution rates, calculated based on Morse *et al*, 1979 and Walter and Morse, 1984. Ω is defined as $[Ca^{2+}][CO_3^{2-}]/K_s$. In undersaturated waters, ooids will dissolve, at rates that increase with decreasing saturation state and increasing surface area.

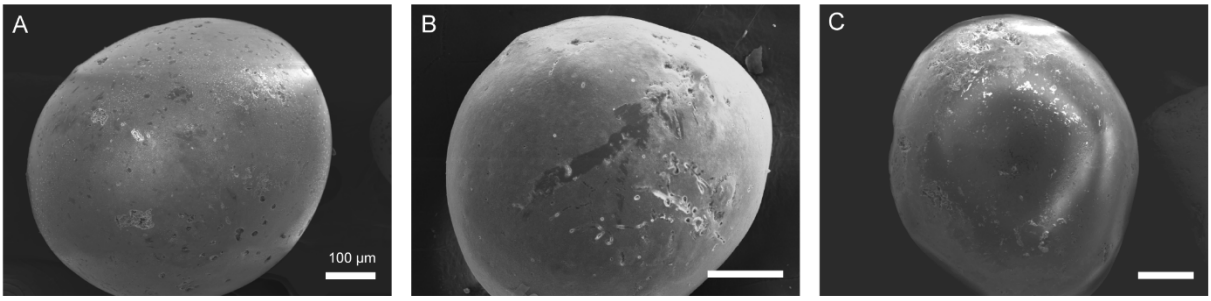

Figure 6. Shelf stability of ooids in a body wash matrix. SEM images of representative ooids incubated in product I and harvested after 6 months (B) and 13 months (C) are indistinguishable from representative starting material (A) and do not display any signs of decomposition. Analogous incubations with products J-M gave similar results.

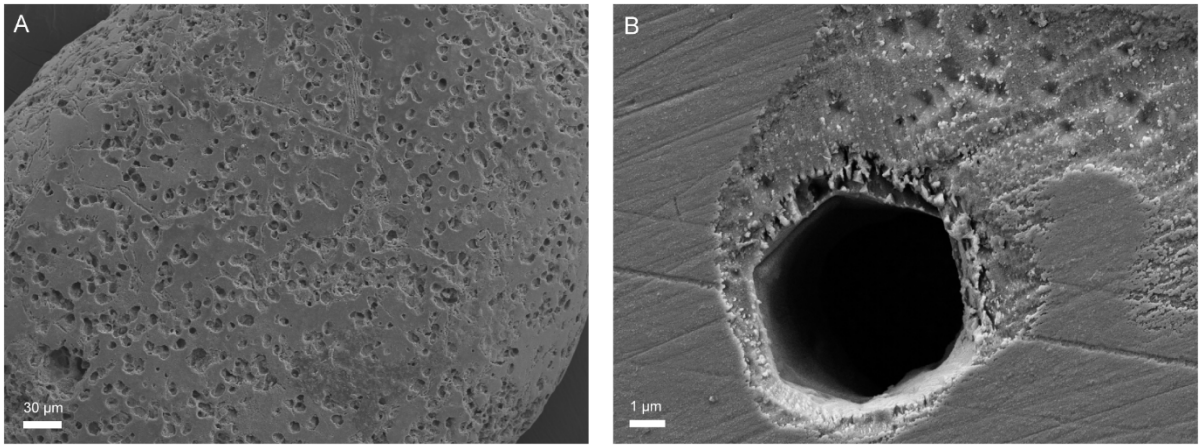

Figure 7. Boring Cyanobacteria facilitate ooid dissolution. A. SEM image showing a heavily bored ooid from LAC. B. SEM image of a hexagonal tunnel rapidly bored into a polished aragonite stub during deployment in the environment for < 1 week.

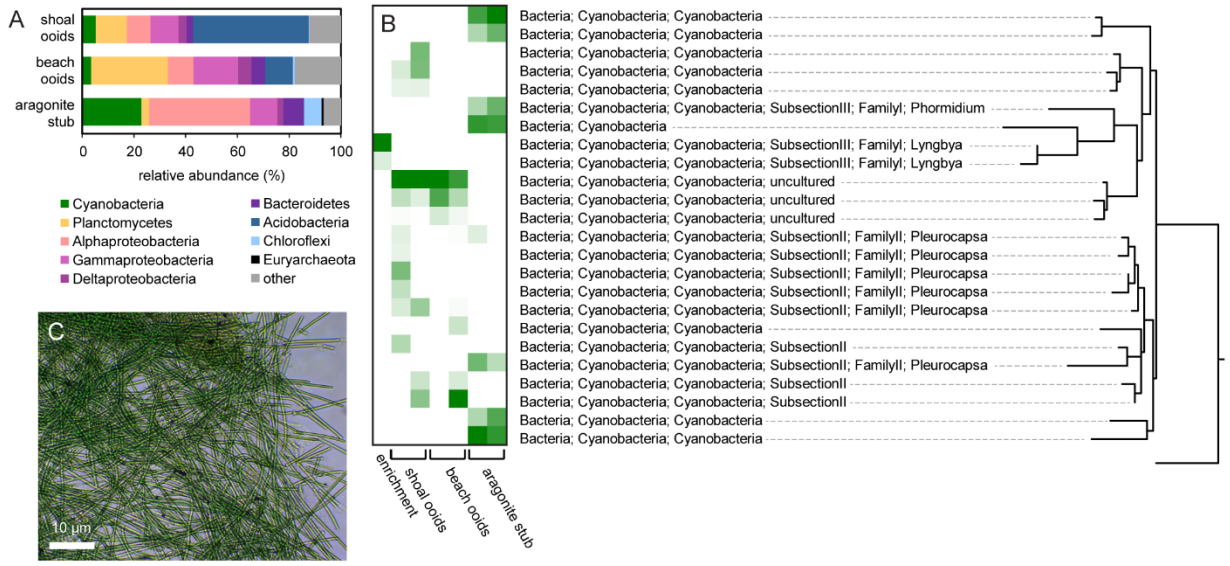

Figure 8. Diverse Cyanobacteira are associated with ooids. A. Phylum-level microbial diversity of communities recovered from LAC ooids and a bored aragonite stub, illustrating the presence of abundant Cyanobacteria. B. Heatmap showing the normalized relative abundances of major cyanobacterial taxa. C. Putative boring cyanobacterium enriched from LAC ooids.

Tables

product ID	brand	description	beads
A	Johnson & Johnson	morning burst facial cleanser	plastic
B	Neutrogena	oil-free acne wash pink grapefruit foaming scrub	plastic
C	St. Ives	nourished & smooth oatmeal scrub	silica and walnut shell
D	Johnson & Johnson	morning burst skin brightening facial scrub	plastic
E	Beauty 360	moisturizing shea butter & almond oil body wash	plastic
F	Beauty 360	exfoliating coconut body wash	apricot pit
G	Beauty 360	radiant sea mineral body wash	plastic
H	Shea Moisture	African black soap body wash	jojoba wax
I	Beauty 360	moisturizing antibacterial body wash	-
J	Dove	sensitive skin nourishing body wash	-
K	Shea Moisture	coconut & hibiscus body wash	-
L	Neutrogena	oil-free acne wash pink grapefruit facial cleanser	-
M	Burt's Bees	sensitive facial cleanser	-

Table 1. Commercial cosmetic products used in this study. Products A-H contain exfoliating particles which were harvested and examined; products I-M do not contain particles and were used for ooid stability incubations.

APPENDIX

Oxygenic photosynthesis

Usha F. Lingappa and Woodward W. Fischer

Div. of Geological & Planetary Sciences, California Institute of Technology, Pasadena, CA 91125, USA

Definition

Photosynthesis is the biological process of converting the energy in visible light into chemical energy available for the cell to fix CO_2 into biomass for growth. Oxygenic photosynthesis is a unique version of photosynthesis that uses water as the electron donor, producing dioxygen as a product.

Chemical Formula

$H_2O + CO_2 + \text{light} \rightarrow O_2 + CH_2O$

Overview

Oxygenic photosynthesis is fundamental to life as we know it today. This metabolism accounts for the vast majority of primary productivity on Earth, and maintains our atmosphere rich in O_2 and far from chemical equilibrium with the solid Earth, thus representing a presumptive biosignature on a planetary scale. It is carried out by members of the bacterial phylum Cyanobacteria and the constitutively related chloroplasts of algae and plants, with major global contributions from both terrestrial and marine ecosystems.

Oxygenic photosynthesis evolved once, roughly 2.4 billion years ago, in the Cyanobacteria and was a key turning point in the history of life on Earth. Unlocking the ability to use the abundant resource of H_2O as an electron donor for photosynthesis allowed for a massive increase in primary productivity and expansion of the biosphere, while the production of O_2 transformed Earth surface environments and led to the evolution of aerobic biochemistries—the latter, by extension, enabled complex multicellular life.

Mechanics

To capture sunlight, photosynthetic organisms use pigment molecules like the tetrapyrrole chlorophyll to absorb light energy, generating an excited state of the pigment molecule. This excited state migrates from pigments in light-harvesting antenna systems to the reaction center—a protein complex

with a pair of pigments that utilizes the excitation energy of the chlorophyll to engender charge separation and electron transfer. When the chlorophyll pair (P) is promoted to the excited state (P*), it moves an electron to an acceptor molecule, simultaneously generating a strong oxidant (P^+) and a strong reductant (A^-) in different parts of the reaction center. The oxidizing power of P^+ is used to pull electrons from an electron donor, and the reducing power of A^- is sent down the electron transport chain—along its path contributing to the transmembrane potential and thereby ATP synthesis, and eventually the generation of low potential reducing power for CO_2 fixation in the form of NADPH.

To span the vast amount of redox space between H_2O and NADPH, oxygenic photosynthesis uses two distinct reaction centers coupled in series—photosystem II (PSII), which oxidizes H_2O to O_2 and donates electrons to the quinol pool, and photosystem I (PSI), which takes electrons that have run through complex III from plastocyanin and donates them to a ferredoxin—which can be used at the start of the process to fix carbon. Part of what makes oxygenic photosynthesis special is the ability derive electrons from water. The key catalyst that enables this is a Mn_4CaO_5 cluster known as the water-oxidizing complex (WOC) or oxygen-evolving complex (OEC), ligated by the PSII complex. The Mn atoms in this cluster cycle through a range of oxidation states, acting as a redox capacitor to bridge the single-electron process of photochemical electron transfer with the four-electron process of oxidizing H_2O to O_2.

The carbon fixation pathway used in oxygenic photosynthesis to convert CO_2 to sugars for various cellular processes is the Calvin cycle, also known as the Calvin-Benson-Bassham cycle or the reductive pentose phosphate cycle. This cycle consumes the reducing power and ATP generated as a part of the photochemical reactions involving the electron transport chain that begins at PSII. The Calvin cycle involves numerous biochemical reactions, but can be summarized as three phases—carboxylation, reduction, and regeneration. In carboxylation, the enzyme RuBisCO—the most abundant protein on the planet—adds a CO_2 molecule to ribulose 1,5-bisphosphate (RuBP), a 5-carbon sugar, to generate two molecules of 3-phosophoglycerate (PGA), a 3-carbon sugar. In reduction, PGA is phosphorylated and reduced to produce glyceraldehyde-3-phosphate (GAP), consuming ATP and NADH. Finally, in regeneration, five molecules of GAP are used to regenerate 3 molecules of RuBP. Thus, for every three

molecules of CO_2 that get fixed, six molecules of GAP are produced, five of which are used to regenerate RuBP, with one remaining GAP exported to other metabolic pathways.

Evolution

Anoxygenic photosynthesis is biochemically simpler than oxygenic photosynthesis; it uses single photochemical reaction centers—rather than the coupled photosystems of oxygenic photosynthesis—and electron donors with much lower reduction potentials rather than H_2O. Anoxygenic phototrophy evolved very early in Earth history; geological data suggest this occurred likely prior to 3.4 billion years ago. Today, anoxygenic phototrophy is known to exist in the bacterial phyla Proteobacteria, Chloroflexi, Chlorobi, Acidobacteria, Firmicutes, Gemmatimonadetes, and the candidate phylum WPS-2; and is known to use electron donors such as H_2, Fe(II), sulfide and other reduced sulfur species, nitrite, arsenite, and organic compounds. However, none of these phyla appear to be ancestrally phototrophic, leaving the identity of the lineage that invented anoxygenic phototrophy an enduring evolutionary mystery. It is possible that this lineage is now extinct.

There is debate about the evolutionary timing of oxygenic photosynthesis, but a wide array of geological observations indicate that it had evolved from an anoxygenic ancestor in the Cyanobacteria by 2.4 billion years ago. This transition involved the evolution of a reaction center with a much higher reduction potential, the innovation of the WOC/OEC to bridge the single electron photochemistry of the reaction center with the requisite four electron chemistry for H_2O oxidation, and the coupling of two separate reaction centers in series in the electron transport chain. With the advent of oxygenic photosynthesis came the first meaningful environmental fluxes of O_2; this transformed Earth surface environments dramatically and irreversibly, impacted all global biogeochemical cycles, and redirected the evolutionary trajectory of life by enabling aerobic metabolisms. This defining moment in Earth history is known as the Great Oxygenation Event (GOE).

All photosynthetic eukaryotes (algae and plants) derived their photosynthetic machinery from Cyanobacteria, as their chloroplasts originated by the endosymbiosis of a Cyanobacterium with a

eukaryotic host cell. The earliest algal fossils date to 1.05 billion years ago, while the first land plants emerged circa 488 million years ago.

Figure

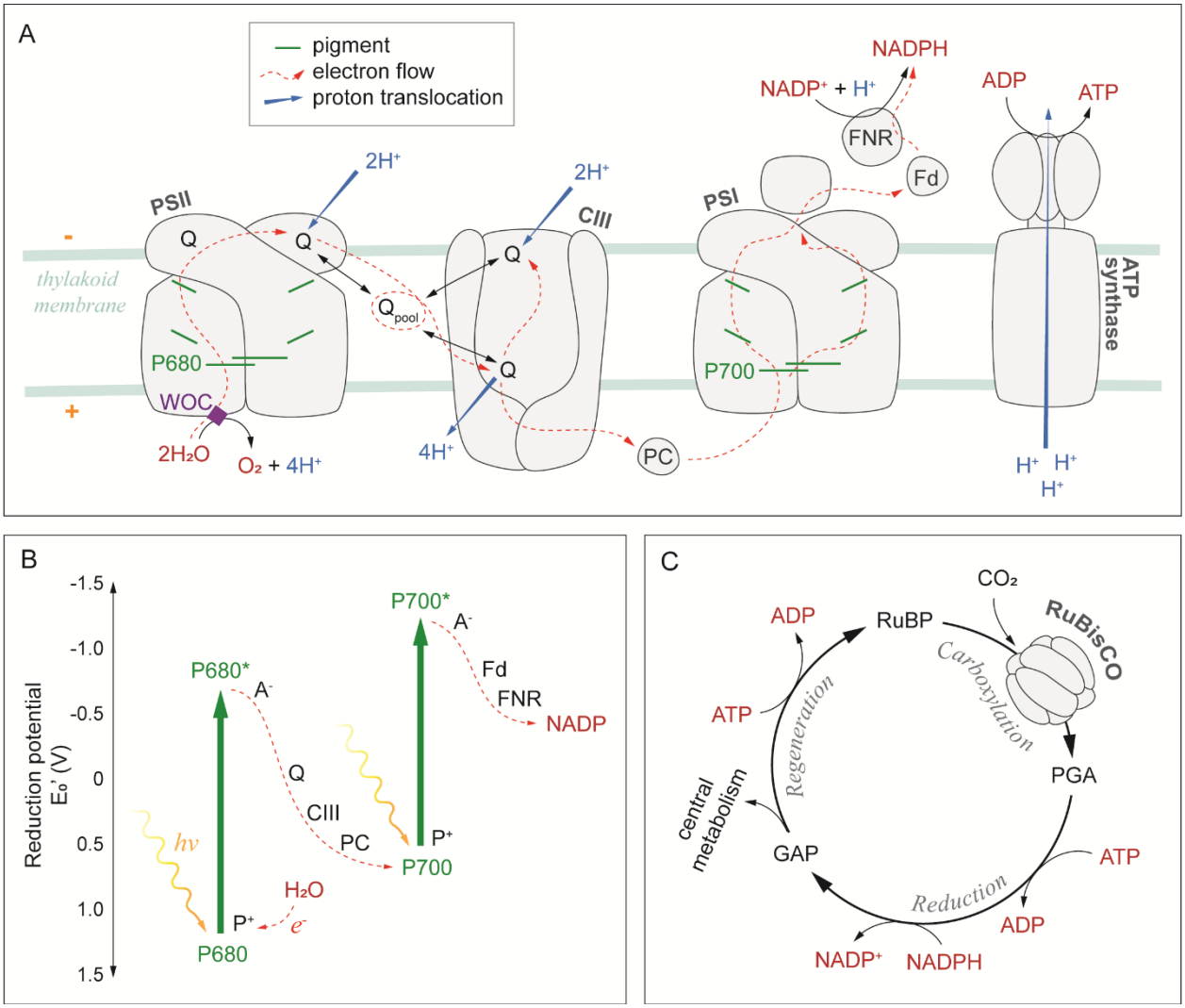

Figure 1. ***A.*** Schematic diagram of the oxygenic photosynthesis electron transport chain. ***B.*** The Z-scheme, depicting the energetics of electron transfer in oxygenic photosynthesis. Electron flow from a lower potential electron donor to a higher potential electron acceptor is thermodynamically favorable. The input of light energy to induce charge separation in the special pair (P680 in the case of PSII, P700 in the case of PSI), generates a very high potential electron acceptor (P^+) and a very low potential electron donor (A^-), allowing for favorable electron flow along the electron transport chain. ***C.*** The Calvin cycle, simplified as three stages—carboxylation, reduction, and regeneration. This pathway uses ATP and NADPH generated by the light-dependent reactions shown in panel *A*. The enzyme RuBisCO catalyzes the key step of CO_2 fixation.